



Schweizerische Eidgenossenschaft
Confédération suisse
Confederazione Svizzera
Confederaziun svizra

Eidgenössisches Departement für Umwelt, Verkehr, Energie und Kommunikation UVEK
Département fédéral de l'environnement, des transports, de l'énergie et de la communication DETEC
Dipartimento federale dell'ambiente, dei trasporti, dell'energia e delle comunicazioni DATEC

Bundesamt für Strassen
Office fédéral des routes
Ufficio federale delle Strade

Modelling of anhydritic swelling claystones

Modellierung von anhydrithaltigen Tonsteinen

Modélisation des roches argileuses contenant de l'anhydride

ETH Zürich, Professur für Untertagbau
Prof. Dr. G. Anagnostou
Dr. K. Serafeimidis
Dr. E. Pimentel
MSc ETH Civ Eng T. Wanninger-Huber
Dipl. Eng. MSc A. Vrakas

**Forschungsprojekt FGU 2010/007 auf Antrag der
Arbeitsgruppe Tunnelforschung (AGT)**

Dezember 2015

1539

Der Inhalt dieses Berichtes verpflichtet nur den (die) vom Bundesamt für Strassen unterstützten Autor(en). Dies gilt nicht für das Formular 3 "Projektabschluss", welches die Meinung der Begleitkommission darstellt und deshalb nur diese verpflichtet.

Bezug: Schweizerischer Verband der Strassen- und Verkehrsfachleute (VSS)

Le contenu de ce rapport n'engage que les auteurs ayant obtenu l'appui de l'Office fédéral des routes. Cela ne s'applique pas au formulaire 3 « Clôture du projet », qui représente l'avis de la commission de suivi et qui n'engage que cette dernière.

Diffusion : Association suisse des professionnels de la route et des transports (VSS)

La responsabilità per il contenuto di questo rapporto spetta unicamente agli autori sostenuti dall'Ufficio federale delle strade. Tale indicazione non si applica al modulo 3 "conclusione del progetto", che esprime l'opinione della commissione d'accompagnamento e di cui risponde solo quest'ultima.

Ordinazione: Associazione svizzera dei professionisti della strada e dei trasporti (VSS)

The content of this report engages only the author(s) supported by the Federal Roads Office. This does not apply to Form 3 'Project Conclusion' which presents the view of the monitoring committee.

Distribution: Swiss Association of Road and Transportation Experts (VSS)



Schweizerische Eidgenossenschaft
Confédération suisse
Confederazione Svizzera
Confederaziun svizra

Eidgenössisches Departement für Umwelt, Verkehr, Energie und Kommunikation UVEK
Département fédéral de l'environnement, des transports, de l'énergie et de la communication DETEC
Dipartimento federale dell'ambiente, dei trasporti, dell'energia e delle comunicazioni DATEC

Bundesamt für Strassen
Office fédéral des routes
Ufficio federale delle Strade

Modelling of anhydritic swelling claystones

Modellierung von anhydrithaltigen Tonsteinen

Modélisation des roches argileuses contenant de l'anhydride

ETH Zürich, Professur für Untertagbau
Prof. Dr. G. Anagnostou
Dr. K. Serafeimidis
Dr. E. Pimentel
MSc ETH Civ Eng T. Wanninger-Huber
Dipl. Eng. MSc A. Vrakas

**Forschungsprojekt FGU 2010/007 auf Antrag der
Arbeitsgruppe Tunnelforschung (AGT)**

Impressum

Forschungsstelle und Projektteam

Projektleitung

Georg Anagnostou

Mitglieder

Erich Pimentel

Konstantinos Serafeimidis

Tara Wanninger-Huber

Apostolos Vrakas

Kooperationspartner EMPA

Pietro Lura

Andreas Leemann

Barbara Lothenbach

Begleitkommission

Präsident

Felix Amberg

Mitglieder

Martin Bosshard

Christian Gammeter

Peter Huggenberger

Jan Carmeliet

KO-Finanzierung des Forschungsprojekts

Schweizerischer Nationalfonds SNF

Antragsteller

Arbeitsgruppe Tunnelforschung (AGT)

Bezugsquelle

Das Dokument kann kostenlos von <http://www.mobilityplatform.ch> heruntergeladen werden.

Inhaltsverzeichnis

Impressum	4
Zusammenfassung	9
Résumé	13
Summary	17
1 Introduction	21
1.1 Context and objectives of the research project.....	21
1.2 Outline of the investigations	21
1.3 Contributions to the project	23
1.4 Publications	24
2 State of research	25
3 Thermodynamic fundamentals	27
3.1 Introduction.....	27
3.2 Basic thermodynamic relations	28
3.2.1 Gibbs free energy.....	28
3.2.2 Chemical potential.....	29
3.2.3 Activity	31
3.2.4 Crystal-liquid interfacial effects	31
3.3 Equilibrium concentrations	33
3.3.1 Gypsum	33
3.3.2 Anhydrite	34
3.4 Anhydrite-gypsum equilibrium relationships	34
3.4.1 General case	34
3.4.2 Simplified model for the conditions in the ground	35
3.5 Comparison between predicted solubilities and published data	36
3.6 Comparison of predicted equilibrium conditions with published data	37
3.6.1 Anhydrite – gypsum equilibrium in pure water	37
3.6.2 Anhydrite – gypsum equilibrium in <i>NaCl</i> solutions	38
3.7 General equilibrium diagram	38
3.8 Conclusions.....	39
4 Time development of sulphate hydration	41
4.1 Introduction.....	41
4.2 Kinetic model.....	41
4.2.1 Dissolution and precipitation rates	41
4.2.2 Sealing of anhydrite by the formed gypsum.....	44
4.2.3 Governing equations for a closed system.....	46
4.3 Comparison of predictions with tests involving simultaneous anhydrite dissolution and gypsum precipitation	48
4.4 Factors governing the time development of hydration	50
4.4.1 Introduction.....	50
4.4.2 Evolution over time.....	50
4.4.3 Limiting mechanism	51
4.4.4 Duration of the hydration process	54
4.5 The effect of sealing	55
4.6 Conclusions.....	58
5 On the role of transport processes	59
5.1 Introduction.....	59
5.2 Governing equations of the advection-diffusion model.....	60
5.2.1 Mass balance and geometric equations	60
5.2.2 Transport.....	62
5.3 The role of diffusion in oedometer tests	63

5.3.1	Introduction	63
5.3.2	Model description and behaviour.....	63
5.3.3	Parametric study.....	65
5.4	The role of advection	67
5.4.1	Problem layout.....	67
5.4.2	Parametric study.....	67
5.4.3	Discussion based on the results of Butscher <i>et al.</i> ([17], [18])	68
5.5	Conclusions	68
6	Anhydrite in Gypsum Keuper at shallow depths	71
6.1	Introduction	71
6.2	The small pore hypothesis.....	75
6.2.1	Introduction	75
6.2.2	Porosity and pore size distribution of anhydritic claystones	76
6.2.3	Discussion.....	77
6.3	The high pressure hypothesis	78
6.3.1	Introduction	78
6.3.2	Required pressure	78
6.3.3	Mechanically possible pressure.....	81
6.3.4	Application to the Belchen and the Chienberg Tunnel	85
6.3.5	Major draw-back of the high pressure hypothesis	87
6.4	The low water activity hypothesis	89
6.5	Conclusions	90
7	Maximum swelling pressure of anhydritic claystones	93
7.1	Introduction	93
7.2	Microscale.....	94
7.2.1	Crystallisation pressure	94
7.2.2	Relationship between crystallisation pressure and concentration.....	95
7.2.3	Ion concentration in a closed system containing anhydrite and gypsum	96
7.2.4	Ion concentration in open systems	99
7.3	Macroscale.....	100
7.3.1	Measured swelling pressures in laboratory tests.....	100
7.3.2	Model for the theoretical estimation of macroscopic swelling pressure	101
7.4	Megascale.....	104
7.5	Conclusions	105
8	Overview of the experimental investigations	107
8.1	Introduction	107
8.2	Description of the experiments	107
8.3	Description of standard analytical testing techniques used.....	108
8.3.1	Thermogravimetric analysis (TGA).....	108
8.3.2	Microscopy.....	108
8.3.3	X-ray diffraction and Rietveld analysis (XRD analysis)	108
8.3.4	Mercury-Intrusion Porosimetry (MIP).....	108
8.3.5	Laserdiffractometry	108
9	Characterization of sample materials.....	111
9.1	Anhydrite.....	111
9.2	Aggregates.....	111
9.3	Anhydritic claystones	112
10	Solubilities.....	113
10.1	Introduction	113
10.2	Experimental procedure.....	113
10.3	Results	114
10.4	Discussion.....	117

11	Sealing.....	119
11.1	Introduction.....	119
11.2	Experimental procedure.....	119
11.3	Results.....	120
11.3.1	Photography.....	120
11.3.2	Microscopy.....	121
11.3.3	Comparison to prediction.....	124
11.4	Discussion.....	124
12	Chemo-mechanical processes.....	127
12.1	Introduction.....	127
12.2	Overview of the experiments.....	129
12.3	Samples and sample preparation.....	129
12.4	Preliminary tests I: free axial swelling tests.....	130
12.4.1	Aim and procedure.....	130
12.4.2	Results.....	131
12.4.3	Discussion.....	133
12.5	Preliminary tests II: Comparison milled natural anhydrite – commercial anhydrite.....	134
12.5.1	Aim and procedure.....	134
12.5.2	Results.....	135
12.5.3	Discussion.....	136
12.6	Oedometer tests.....	136
12.6.1	Aim and procedure.....	136
12.6.2	Results of the first series (various axial loads – steady state).....	137
12.6.3	Results: Various durations (only anhydrite/kaolin samples).....	139
12.6.4	Discussion.....	140
12.7	Investigations of sample structures.....	141
12.7.1	Porosimetry.....	141
12.7.2	Microscopy.....	142
12.8	Ongoing experiments and outlook.....	155
12.8.1	Complete constraint.....	155
12.8.2	Flexible oedometers.....	157
13	Free swelling tests with natural samples.....	159
13.1	Introduction.....	159
13.2	Experimental procedure.....	160
13.2.1	Material and sample preparation.....	160
13.2.2	Testing procedure.....	162
13.3	Results.....	163
13.3.1	Segments.....	163
13.3.2	Disks.....	165
13.4	Discussion.....	166
	Appendix.....	167
	Literaturverzeichnis.....	183
	Projektabschluss.....	193
	Verzeichnis der Berichte der Forschung im Strassenwesen.....	197

Zusammenfassung

Sulfathaltige Tonsteine gehören aufgrund ihrer besonders ausgeprägten Quellfähigkeit zu den problematischsten Gesteinen beim Tunnelbau. Bei zahlreichen Tunnelbauwerken im Gipskeuper lösten sie erhebliche Schäden aus, deren Behebung äusserst kostspielig, zeitaufwändig und oft nur vorübergehender Natur war. Die Rückschläge beim Tunnelbau im Gipskeuper werden unter anderem bedingt durch das beschränkte Wissen über die makroskopischen Gesetzmässigkeiten des Quellvorgangs und deren zugrunde liegenden mikroskopischen Mechanismen.

Quellversuche an natürlichen Gesteinsproben dauern extrem lang – im Minimum 10 Jahre. Zudem sind ihre Resultate aufgrund der Heterogenität natürlicher Proben schwer reproduzierbar. Diese Hindernisse veranlassten die Professur für Untertagbau, komplementär zu den laufenden Langzeitversuchen des Forschungsprojekts FGU 2006/001, das Verhalten von anhydritführenden Tonsteinen anhand von hydraulisch-mechanisch-chemisch gekoppelten mathematischen Modellen zu untersuchen. Letztere sollten die wesentlichen Prozesse der Anhydrit-Gips-Umwandlung erfassen: Lösung des Anhydrits in Porenwasser, Ausfällung von Gipskristallen aus der Lösung, chemisch-mechanische Kopplung zwischen den Sulfaten und der Tonmatrix, Sickerströmung sowie Ionen-transport.

Mit dem vorliegenden Forschungsprojekt sollte der Kenntnisstand bezüglich der oben genannten, dem Quellvorgang zugrunde liegenden, Mechanismen verbessert werden. Zu diesem Zweck wurde eine Serie von theoretischen und experimentellen Untersuchungen zu den Wechselwirkungen zwischen den chemischen Reaktionen, den Transportprozessen und dem mechanischen Verhalten durchgeführt. Ausgangspunkt der Untersuchungen waren im Forschungsantrag ausgewiesene grundlegende Fragestellungen. Diese betreffen die Rolle der Transportprozesse, die Rolle der hydraulischen Randbedingungen, die Rolle der Tonmatrix und die Beziehung zwischen Quelldruck und -dehnung.

Das Quellen anhydritführender Tonsteine ist bedingt durch die chemische Umwandlung von Anhydrit zu Gips und durch die physikalische Wasseraufnahme der Tonmatrix. Ein chemisch-mechanisch gekoppeltes Modell sollte einerseits die umwandlungsbedingten Verformungen abbilden, andererseits die thermodynamischen Bedingungen (Druck, Temperatur usw.), bei denen die chemische Umwandlung stattfindet («chemische Gleichgewichtsbedingungen»), berücksichtigen.

In der Literatur werden die chemischen Gleichgewichtsbedingungen des Anhydrit-Gips-Wasser-Systems üblicherweise unter der Annahme formuliert, dass sich Anhydrit direkt in Gips umwandelt. In Wirklichkeit jedoch erfolgt diese Umwandlung über zwei distinkte chemische Reaktionen, die während der Lösungsphase stattfinden (Anhydritlösung, Gipskristallisation). Die durch die Anhydritlösung entstehenden Sulphationen können dabei advektiv (d.h. mit der Sickerströmung) oder durch Diffusion abtransportiert werden. Da es zu Beginn des Projektes unklar war, ob die Wechselwirkung zwischen den Transportprozessen und den chemischen Reaktionen relevant ist, wurden die chemischen Gleichgewichtsbedingungen unter expliziter Berücksichtigung der zwei Reaktionen hergeleitet. Zudem wurde beim thermodynamischen Modell – neben den üblicherweise berücksichtigten Faktoren wie Temperatur, Porenwasserdruck, Druck auf die Festsubstanzen und Zusammensetzung der Porenlösung – auch der Einfluss der Tonmatrix und der Porengrösse kohärent erfasst. Die Tonmatrix beeinflusst das thermodynamische Gleichgewicht, da die Tonminerale (insbesondere bei Tonsteinen mit sehr niedrigem Wassergehalt) die Aktivität des Porenwassers herabsetzen. Ebenso ist die Porengrösse wichtig, da das Wachstum von Gipskristallen innerhalb der extrem kleinen Poren der anhydritführenden

Tonsteine durch die Oberflächenenergie beeinflusst wird. Ist Ton vorhanden oder ist das Gestein kleinporig, wird das thermodynamische Gleichgewicht zu Gunsten des Anhydrits verschoben.

Anhand des oben skizzierten thermodynamischen Modells wurden zwei Beobachtungen analysiert: das Vorkommen von Anhydrit (anstatt Gips) bei kleinen Überlagerungen im Gipskeuper und die im Verhältnis zum Kristallisationsdruck von Gips niedrigen Quelldrücke von anhydritführenden Tonsteinen. Die Analyse dieser Beobachtungen war aufschlussreich bezüglich der Rolle des Tons.

Nach den herkömmlichen thermodynamischen Modellen, welche weder die Tonmatrix noch die Porengrösse berücksichtigen, sollte in der Tiefenlage des Keupertunnels (50-250 m) kein Anhydrit vorkommen, was den Beobachtungen in der Natur widerspricht. Zur Klärung dieser Beobachtung wurden anhand einer Analyse aller Einflussfaktoren Hypothesen aufgestellt und systematisch auf Plausibilität und Konsistenz geprüft. Einzig die folgende Erklärung hat sich als widerspruchsfrei erwiesen: das Vorkommen von Anhydrit in geringer Tiefe anstatt des zu erwartenden Gipses, ist bedingt durch den thermodynamischen Zustand des Porenwassers in der Tonmatrix. Anhydrit ist trotz geringer Tiefenlage thermodynamisch stabil, weil die Tonminerale die Aktivität des Porenwassers herabsetzen und somit die Löslichkeit von Gips über jene des Anhydrits erhöhen. Dieses Ergebnis liefert eine plausible Erklärung für den Ablauf des Quellvorgangs anhydritführender Tonsteine: Das Quellen beginnt mit der Wasseraufnahme durch die Tonmatrix. Während dieser ersten Phase erhöht sich der Wassergehalt der Tonmatrix und somit auch die Aktivität des Porenwassers. Dadurch wird das chemische Gleichgewicht allmählich zu Gunsten des Gipses verschoben. Die Löslichkeit des Gipses nimmt ab, jene von Anhydrit nimmt zu. Das hat zur Folge, dass ab einem gewissen Zeitpunkt Gips die stabile Phase bildet. In der Folge wandelt sich Anhydrit durch Wasseraufnahme in Gips um. Dadurch wird dem Ton Wasser entzogen und der Quellvorgang des Tons wird aufrechterhalten. Dieser Vorgang hält solange an bis alles Anhydrit in Gips umgewandelt ist. Diese Erkenntnis stützt die Arbeitshypothese des Forschungsprojekts FGU 2012/001 («Quellinhibitoren für anhydritführende Tonsteine»), wonach der Unterbindung der Quellung des Tones eine Schlüsselrolle für die Beherrschung der Quellproblematik zukommt.

Weitere Erkenntnisse bezüglich der Rolle der Tonmatrix konnten aus der Analyse der Beobachtung gewonnen werden, nämlich, dass die im Labor und in-situ beobachteten Quelldrücke um eine bis zwei Grössenordnungen niedriger sind als der thermodynamisch errechnete Kristallisationsdruck von Gips. Dieser Unterschied kann auf die mechanische Wechselwirkung zwischen den in den Poren wachsenden Kristallen, der umgebenden Tonmatrix sowie der Pufferwirkung der letzteren zurückgeführt werden.

Zur Quantifizierung des Beitrags der physikalischen Wasseraufnahme durch die Tonmatrix zur beobachteten Quellung wurden zusätzlich Freiquellversuche mit natürlichen Proben aus dem Belchentunnel durchgeführt. Je nach Entnahmestelle weisen diese Proben eine unterschiedliche Zusammensetzung sowie auch ein unterschiedliches Quellverhalten aus. Bei einer Gruppe von Proben konnte nach etwa einem Jahr (und Quelldehnungen zwischen 20%-40%) ein deutliches Abklingen des Quellvorgangs beobachtet werden. Die Analyse der ausgebauten Proben ergab, dass der Grossteil der gemessenen Verformungen eher auf Bruchvorgänge (Entstehung von Rissen) zurückzuführen ist. Bei einer zweiten Gruppe ist ab dem ersten Halbjahr und nach über zwei Jahren Versuchsdauer weiterhin eine annähernd lineare Zunahme der Quelldehnung bei deutlich niedrigeren Quelldehnungen zu verzeichnen. Da die Versuche noch laufen und die Ergebnisse wegen der Materialheterogenität eine grosse Streuung aufweisen, sind noch keine definitiven Schlussfolgerungen möglich.

Zur Untersuchung der Rolle der Transportprozesse wurde zunächst die Kinetik (d.h. die zeitliche Entwicklung) der chemischen Reaktionen (Anhydritlösung,

Gipsausfällung) untersucht. Die kinetischen Gleichungen wurden der Literatur entnommen und zur Simulation der Vorgänge in einem geschlossenen Anhydrit-Gips-Wasser-System verwendet für welches experimentelle Ergebnisse vorlagen. Letztere stimmten gut mit den theoretischen Prognosen überein. Die kinetischen Gleichungen wurden ferner in einem Modell implementiert, das die Verzögerung der Anhydritlösung durch die im Zuge der Hydratation entstehenden Gipskristallen erfasst. Die aufgrund dieses Modells erhaltenen Berechnungsergebnisse zeigen, dass die Hydratationsverzögerung im Falle von kleinen Anhydritpartikeln oder dünnen Anhydritadern (<1 mm) praktisch unbedeutend ist, bei grösseren Partikeln oder Adern jedoch mehrere Jahrhunderte betragen kann. Somit konnte die allgemeine Beobachtung erklärt werden, dass massiger Anhydrit nur sehr langsam quillt und deshalb für den Tunnelbau irrelevant ist. Zusätzlich zu den numerischen Untersuchungen wurde im Labor eine Serie von Versuchen an natürlichem Anhydrit durchgeführt, bei der die zeitliche Entwicklung der wachsenden Gipschicht fotografisch aufgenommen und im Rasterelektronenmikroskop quantifiziert wurde. Die Ergebnisse zeigen zwar eine starke Streuung der Grenzflächen des Anhydrits und Gipses, die Schichtstärken liegen jedoch innerhalb der mit dem Modell prognostizierten Bandbreite.

Zur Untersuchung des Zusammenspiels der chemischen Reaktion mit dem Ionentransport wurden gekoppelte Advektion-Diffusion-Reaktion-Berechnungen unter Berücksichtigung der oben erwähnten kinetischen Gleichungen durchgeführt. Die Simulationen zeigten, dass der Einfluss der Diffusion vernachlässigbar ist, da sie viel langsamer erfolgt als die chemischen Reaktionen. Das Gleiche gilt auch betreffend der Advektion, sofern die Sickergeschwindigkeiten niedrig sind, was in den gering durchlässigen Tonsteinen des Gipskeupers üblicherweise der Fall ist. Somit kann in den meisten Fällen davon ausgegangen werden, dass die Umwandlung von Anhydrit in Gips einen topochemischen Prozess darstellt, welcher durch eine einzige Reaktion (Anhydrit + Wasser → Gips) beschrieben werden kann. Aufgrund dieser Erkenntnis konnte die Komplexität der mathematischen Erfassung der untersuchten physikalisch-chemischen Prozesse enorm reduziert und somit auf die sehr aufwändige experimentelle Untersuchung der hydraulisch-chemischen Wechselwirkungen verzichtet werden.

Die experimentellen Untersuchungen konzentrierten sich deshalb auf die chemisch-mechanischen Prozesse. Zielsetzung dieser Untersuchungen ist, die Quantifizierung der Spannungen und Dehnungen infolge der Anhydrit-Gips-Umwandlung. Hierfür wurden Serien von Quellversuchen an Mischungen durchgeführt. Die Mischungen bestehen im Wesentlichen aus pulverförmigem industriellem Anhydrit sowie Zuschlagstoffen, welche nicht mit Wasser reagieren. Sie wurden stark verdichtet und unter ödometrischen Bedingungen getestet. Der an diesen Proben experimentell bestimmte Zusammenhang zwischen Quelldehnung und -druck lässt sich – analog zum bekannten Quellgesetz für Tonsteine – sehr gut durch eine Gerade im halblogarithmischen Diagramm approximieren. Dieses Ergebnis ist besonders bemerkenswert, da es sich hierbei um Dehnungen handelt, die ausschliesslich infolge der chemischen Umwandlung (ohne Tonquellung) entstanden. Die mineralogische Zusammensetzung der ausgebauten Proben zeigte jedoch, dass bei einigen Proben die Umwandlung von Anhydrit noch nicht abgeschlossen war, obwohl die Quelldehnung praktisch einen Endzustand erreicht hat. Ferner wurde während weiterer Versuchsserien der Zusammenhang zwischen Quelldehnung und Grad der Anhydrit-Gips-Umwandlung messtechnisch erfasst, indem die Proben vor Erreichen der maximalen Quelldehnung ausgebaut und mineralogisch untersucht wurden. Die Bestimmung des maximalen Quelldrucks dieser Proben erfolgte mit einer Serie von dehnungsbehinderten Quellversuchen.

Die experimentellen Untersuchungen erwiesen sich als äusserst zeitaufwändig und werden auch nach dem formalen Abschluss des Forschungsprojektes fortgesetzt.

Résumé

Les roches argileuses contenant du sulfate - dues à leur capacité de gonflement - font parties des roches les plus problématiques dans la construction des tunnels. Elles ont causé de nombreux dommages dans plusieurs ouvrages de tunnels creusés dans le keuper gypseux et dont la réparation était très coûteuse, longue et souvent seulement de manière temporaire. Les revers dans la construction de tunnels dans le keuper gypseux sont le fait de la connaissance limitée des lois macroscopiques du processus de gonflement et des mécanismes microscopiques sous-jacents.

Les essais de gonflement avec des échantillons naturels se caractérisent par une durée extrêmement longue (de plus de 10 ans par essai). En outre, les résultats sont difficiles à reproduire en raison de l'hétérogénéité des échantillons naturels. Ces obstacles ont poussé notre groupe d'étudier, en plus des essais de longue durée en cours dans le cadre du projet FGU 2006/001, le comportement des roches argileuses contenant de l'anhydrite avec des modèles mathématiques couplés avec l'hydraulique, la mécanique ainsi que la chimie. Ceux-ci doivent prendre en compte les processus essentiels de la transformation de l'anhydrite en gypse : la solution d'anhydrite dans l'eau interstitielle, la cristallisation du gypse, le couplage chimique et mécanique entre les sulfates et la matrice d'argile et le transport des ions par diffusion et advection.

L'objectif de ce projet de recherche est d'améliorer nos connaissances à l'égard des mécanismes de gonflement sous-jacents. Dans ce but, une série d'études théoriques ainsi que expérimentales sur les interactions entre les réactions chimiques, les processus de transport et le comportement mécanique ont été effectués. Le point de départ de ces études était les questions fondamentales identifiées dans la proposition de recherche concernant le rôle du processus de transport, le rôle des conditions aux limites hydrauliques, le rôle de la matrice d'argile ainsi que la relation entre la déformation et la pression de gonflement.

Le gonflement des roches argileuses contenant de l'anhydrite est dû à la transformation de l'anhydrite en gypse et à l'absorption d'eau physique par la matrice d'argile. Un modèle couplé mécaniquement et chimiquement devait d'une part représenter les déformations causées par la transformation, d'autre part prendre en compte les conditions thermodynamiques (pression, température, etc.) dans lesquelles la transformation chimique a lieu (« conditions d'équilibre chimiques »).

Dans la littérature, les conditions d'équilibre chimiques du système anhydrite-gypse-eau sont formulées habituellement en supposant que l'anhydrite se transforme directement en gypse. Cependant, en réalité, cette transformation se produit par la phase de solution (la solution d'anhydrite, la cristallisation du gypse) et par l'intermédiaire de deux réactions chimiques. C'est ainsi que les ions sulfate, se formant par la solution d'anhydrite, peuvent être transportés par l'advection ou par la diffusion. Puisqu'au début du projet il était peu clair, si l'interaction entre les processus de transport et les réactions chimiques étaient pertinents, les conditions d'équilibre ont été obtenues explicitement en prenant compte des deux réactions. En outre, le modèle thermodynamique prend en compte de façon cohérente – en plus de nombres facteurs habituels tels que la température, la pression d'eau interstitielle, la pression agissant sur les substances solides et la composition de l'eau interstitielle – l'influence de la matrice d'argile et la taille des pores. La matrice d'argile influence l'équilibre thermodynamique, parce que les minéraux argileux (existants en particulier dans les roches argileuses ayant une teneur en eau très faible) diminuent l'activité de l'eau interstitielle. Pareillement, la taille des pores est importante, parce que la croissance des cristaux du gypse dans les pores extrêmement petits (des roches argileuses contenant de l'anhydrite) est influencée par l'énergie de surface. En présence de l'argile ou des petits pores, l'équilibre thermodynamique se déplace en faveur de l'anhydrite.

A l'aide du modèle thermodynamique décrit ci-dessus, deux observations ont été analysées : la présence de l'anhydrite (au lieu de gypse) dans le keuper gypseux avec

une petite couverture et la pression de gonflement (des roches argileuses contenant de l'anhydrite) nettement inférieure à celle de cristallisation. L'analyse de ces observations a été très révélatrice concernant le rôle de l'argile.

Selon les modèles thermodynamiques habituelles, qui ne prennent ni en compte la matrice d'argile ni la taille des pores, le gypse situé dans des tunnels à grande profondeur (50-250 m) se situant dans le keuper gypseux devrait être la phase stable, c'est-à-dire qu'aucune anhydrite ne devrait exister. L'observation de la nature contredit ce propos. Afin de clarifier cette observation, en raison d'influences possibles, trois hypothèses ont été établies, examinées systématiquement et vérifiées en fonction de leur plausibilité et consistance. En conséquence, l'explication suivante a prouvé être la seule étant sans contradiction : La présence de l'anhydrite à la place de gypse à faible profondeur est dû à l'état thermodynamique de l'eau interstitielle causée par une matrice d'argile. De ce fait, l'anhydrite est la phase stable, malgré la petite couverture, puisque les minéraux argileux diminuent l'activité de l'eau interstitielle, de sorte que la solubilité de l'anhydrite est inférieure à celle du gypse. Ce résultat fournit une explication plausible pour déroulement du gonflement des roches argileuses contenant de l'anhydrite : Le gonflement commence par l'absorption d'eau par la matrice d'argile. Au cours de cette première phase, le teneur en eau de la matrice d'argile ainsi que l'activité de l'eau interstitielle augmente, de sorte que l'équilibre chimique se déplace en faveur du gypse. La solubilité du gypse diminue, celle de l'anhydrite augmente, de sorte que, à partir d'un certain moment le gypse est la phase stable. En conséquence, l'anhydrite se transforme en gypse en absorbant de l'eau, retirant l'eau à l'argile et maintenant le processus de gonflement de l'argile. Ce processus se poursuit jusqu'à ce que l'anhydrite entière se soit transformée en gypse. Ces résultats sont conformes à l'hypothèse de projet de recherche FGU 2012/001 (« inhibiteurs de gonflement pour les roches argileuses contenant de l'anhydrite »), selon lequel l'empêchement du gonflement de l'argile joue un rôle clé pour maîtriser le problème du gonflement.

Parmi les nouvelles conclusions concernant le rôle de la matrice d'argile ont été obtenues à l'aide de l'analyse des observations : Les pressions de gonflement mesurées en laboratoire ou in-situ sont deux à trois fois inférieures à celles de la cristallisation thermodynamique du gypse calculées de façon thermodynamique. Cette différence peut être attribuée à l'interaction mécanique entre les cristaux croissant dans les pores et à la matrice d'argile - qui entoure les pores – ainsi qu'à l'effet tampon de la matrice d'argile.

En vue de quantifier la déformation en raison du gonflement de l'argile, des essais de gonflement libre ont été menés avec des échantillons naturels du tunnel Belchen. Selon le lieu de prélèvement, les échantillons ont une composition différente et donc un comportement de gonflement différent. Le premier groupe d'échantillons montrait une décroissance significative des soulèvements de gonflement après une année et des déformations de gonflement d'environ 20 à 40%. L'analyse des échantillons prélevés a montré que la majorité des déformations mesurées est probablement due à une rupture (formation de fissures). Le deuxième groupe d'échantillons se déforme en continue depuis le premier semestre et continue de gonfler de façon linéaire après deux ans de durée des essais (mais montrant des déformations de gonflement nettement inférieures). A cause des essais pas encore achevés et de la dispersion importante des résultats – en raison de l'hétérogénéité naturelle des échantillons - il n'est pas encore possible de tirer des conclusions définitives.

En vue des recherches concernant le rôle des processus de transport, premièrement la cinétique (c'est-à-dire l'évolution dans le temps) des réactions chimiques (solution d'anhydrite, précipitation du gypse) a été analysée. Les équations cinétiques (provenant de la littérature) ont été appliquées, pour simuler les processus, dans un système anhydrite-gypse-eau fermé et ultérieurement contrôlés avec les résultats expérimentaux. Ceux-ci sont en bon accord avec les prédictions théoriques. Les équations cinétiques ont été implémentées dans un modèle, qui prend en compte le ralentissement de la solution de l'anhydrite dû à des cristaux de gypse se formant au cours de l'hydratation. Les résultats de cette simulation montrent que le ralentissement de l'hydratation est négligeable pour des particules d'anhydrite très minces ainsi que pour des veines d'anhydrite (< 1 mm), mais peut atteindre plusieurs siècles pour des particules ou des

veines plus grandes. En effet, l'observation générale s'explique principalement par le fait que l'anhydrite massive gonfle très lentement et est donc insignifiant pour la construction des tunnels.

En plus des recherches numériques, un certain nombre d'essais ont été effectués avec de l'anhydrite naturelle, afin de photographier et quantifier l'évolution temporelle de la couche de gypse croissante à l'aide d'un microscope électronique à balayage. Bien que les résultats présentent une dispersion importante des surfaces de séparation de l'anhydrite et du gypse, les épaisseurs des couches se situent dans le domaine pronostiqué par le modèle.

Afin d'étudier l'interaction entre la réaction chimique et le transport d'ions, des calculs couplés - modelant la réaction de l'advection et de la diffusion - ont été effectués en tenant compte des équations cinétiques citées précédemment. Les simulations ont montré que l'influence de la diffusion est négligeable, puisqu'elle est plus lente que les réactions chimiques. Il en est de même pour l'advection, à condition que la vitesse d'infiltration soit basse, ce qui est habituellement le cas dans les roches argileuses du keuper gypseux. En conséquence, il peut être supposé que la transformation de l'anhydrite en gypse se déroule topo-chimiquement dans la plupart des cas et peut ainsi être décrit en une seule réaction chimique (anhydrite + eau \rightarrow gypse). Cette conclusion facilite à la fois la mise en œuvre des modèles, ainsi que la conception et la planification des essais expérimentaux pertinents.

Les études expérimentales se concentrent uniquement sur les modèles couplés mécaniquement et chimiquement. L'objectif de ces études est de quantifier les pressions ainsi que les déformations suite à la transformation de l'anhydrite en gypse. Pour combler cette lacune, des séries d'essais de gonflement ont été effectuées avec des mélanges différents. Les mélanges sont composés essentiellement d'anhydrite industrielle en poudre ainsi que des additifs qui ne réagissent pas avec l'eau. Ils ont été fortement comprimés et testés dans des conditions œdométriques. Pour ces échantillons, une relation linéaire entre les déformations et les pressions de gonflement dans un repère semi-logarithmique a été démontré - analogue à la loi connue de gonflement connue pour les roches argileuses. Ce résultat est remarquable, puisque les déformations sont seulement provoquées par des réactions chimiques (sans gonflement d'argiles). Cependant, la composition minéralogique des échantillons prélevés a montré que quelques échantillons n'avaient pas terminé la transformation de l'anhydrite, bien qu'un état final de déformation de gonflement ait été atteint. En outre, dans d'autres séries d'essais, une relation entre la déformation de gonflement et le degré de transformation d'anhydrite en gypse a été établie en prélevant les échantillons avant d'avoir atteint la déformation de gonflement maximale. La pression de gonflement maximale de ces échantillons a été déterminée en exécutant une série d'essais restreints à la déformation.

Les études expérimentales ont pris beaucoup de temps et se poursuivront après la terminaison officielle du projet de recherche.

Summary

Sulphatic claystones are among the most problematic rocks in tunnelling due to their distinctive swelling behaviour. They are known to have caused severe damage to numerous tunnels excavated in the Gypsum Keuper formation. The repairs were extremely costly and time-consuming, and often provided only a temporary solution. Setbacks experienced in tunnelling through Gypsum Keuper are caused – among other factors – by our limited knowledge of the macroscopic principles governing the swelling process and the underlying microscopic mechanisms.

Swelling tests with natural rock samples are notable for their extremely long duration (over 10 years for a test). Furthermore, the heterogeneity of natural rock samples makes it difficult to obtain reproducible experimental results. This motivated the Chair of Underground Construction to undertake the task – in addition to an ongoing long-term swelling test programme (research project FGU 2006/001) – of investigating the long-term macroscopic behaviour of sulphatic claystones with hydraulic-mechanical-chemical coupled mathematical models. These shall account for the fundamental mechanisms underlying the swelling of anhydritic claystones: anhydrite dissolution and gypsum precipitation; chemo-mechanical coupling between sulphate and clay matrix; seepage flow; and ion transport.

The objective of this research project is to advance the knowledge of these fundamental mechanisms. Towards this end, a series of theoretical and experimental investigations were conducted into the interactions between chemical reactions, transport processes and mechanical behaviour. The starting point of the project was a series of fundamental questions that were identified in the research proposal: the role of transport processes, the role of the hydraulic boundary conditions, the role of the clay matrix and the relationship between swelling strains and stresses.

Swelling of anhydritic claystones occurs due to the chemical transformation of anhydrite to gypsum and water uptake by the clay phase. A chemo-mechanical model should, therefore, consider the thermodynamic conditions (stress, pore pressure, temperature etc.), under which the chemical transformation occurs (*i.e.* the “chemical equilibrium conditions”), as well as the strains caused by this transformation.

In the literature, the chemical equilibrium conditions of the anhydrite-gypsum-water system are formulated under the assumption that anhydrite transforms directly to gypsum. In reality, however, the transformation takes place over the solution phase via two distinct chemical reactions (anhydrite dissolution and gypsum precipitation). The dissolved sulphate ions may be transported via advection (*i.e.* with seepage flow) or via diffusion. Since there was uncertainty at the beginning of the project over the extent to which the transport processes interact with the chemical reactions, the chemical equilibrium conditions had to be derived from an explicit consideration of both reactions. Furthermore, it was necessary to enhance existing thermodynamic models by coherently considering the effects of the clay matrix and the pore size in addition to the other factors usually considered (*i.e.* temperature, pore water pressure, solid pressure and the presence of foreign ions in the pore fluid). The clay matrix influences the thermodynamic equilibrium, since the clay minerals reduce the activity of the pore fluid (particularly if the water content is very low). The pore size is important as well, since it is known that crystal-growth in extremely small pores (which is the case with claystones) is affected by solid-liquid interfacial effects. If clay is present or if the rock contains small pores, the thermodynamic equilibrium shifts in favour of anhydrite.

The thermodynamic model described above was used to shed light on the role of the clay by analysing two observations: the fact that in Gypsum Keuper anhydrite occurs at relatively shallow depths of cover, and the fact that anhydritic claystones exhibit swelling pressures which are significantly lower than the crystallisation pressure of gypsum.

Based on common thermodynamic principles and usual assumptions, the Gypsum Keuper should be free of anhydrite at common tunnel depths (50-250 m), which contradicts observations made *in situ*. In order to clarify the reasons for this apparent contradiction, three hypotheses were formulated, considering all relevant factors, and their plausibility and consistency were examined systematically. According to the investigations, the only consistent - and therefore the most convincing - explanation is that anhydrite rather than gypsum occurs at shallow depths due to the thermodynamic condition of the pore water in the clay matrix. Anhydrite is stable even at shallow depths, due to the fact that the clay minerals reduce the water activity, which in turn shifts the thermodynamic equilibrium in favour of anhydrite, thus preventing its transformation to gypsum. This finding provides an explanation for the processes taking place when anhydritic claystones come into contact with water: Swelling starts with water uptake by the clay minerals. During this first phase, the pore water activity gradually increases with increasing water content. Therefore, the solubility of gypsum decreases, while that of anhydrite increases, until gypsum rather than anhydrite becomes thermodynamically stable. From this point on, anhydrite to gypsum transformation takes place, consuming water and thus maintaining the water deficiency of the clay and sustaining the water uptake until all of the anhydrite is transformed into gypsum. This finding supports the underlying hypothesis of the research project FGU 2012/001 ("Swelling inhibitors for anhydritic claystones"), according to which the swelling of clay plays a key role in the control of swelling when tunnelling through anhydritic claystones.

Further indications about the role of the clay matrix were obtained by analysing the observation that swelling pressures from oedometer tests or *in situ* are lower by one to two orders of magnitude than the thermodynamically calculated crystallisation pressure of gypsum. This observation can be explained by considering the mechanical interaction of the expanding gypsum crystals with the surrounding claystone matrix. The macroscopically observed swelling pressure is lower than the crystallisation pressure, because the clay matrix acts as a buffer.

In order to quantify the amount of swelling due to the physical water uptake by the clay matrix in relation to the total swelling strain, free swelling tests were also performed with natural samples from the Belchen Tunnel. Depending on the origin of the samples (i.e. of the sample composition) different swelling behaviours were observed. With one series, a clear decrease in the rate of swelling strain was observed after about a year, at which point they reached swelling strains of between 20% and 40%. The analysis of the extracted samples led to the assumption that the major part of the deformations can be attributed to cracking of the sample. In another test series, the swelling strain increases linearly after the first half year and the rate of the swelling strain remains constant, even after more than two years. Due to the large scatter of the results, which can be attributed to the heterogeneity of the samples, and the fact that the experiments are still continuing, definitive conclusions cannot be drawn yet.

In order to investigate the role of the transport processes, the kinetic equations that govern the evolution of the chemical reactions (i.e. anhydrite dissolution, gypsum precipitation) were taken from the literature and used to simulate a closed system with simultaneous anhydrite dissolution and gypsum precipitation. The theoretical predictions of the computational model correspond well to the given experimental data. Furthermore, the kinetic equations were implemented in a model which establishes the effect of sealing of anhydrite (i.e. the retardation of the anhydrite hydration due to precipitating gypsum needles). According to the computational results, the gypsum layer does not influence the duration of hydration significantly if the anhydrite particles or veins are small (<1mm). However, the hydration of larger particles or thicker veins can take several centuries. Therefore, the general observation that massive anhydrite swells very slowly and is consequently irrelevant for tunnelling can be explained. In addition to the computational investigations, a series of laboratory experiments were conducted where the development of a growing gypsum layer on massive anhydrite was monitored optically and its thickness quantified with scanning electron microscopy. Although the development of the anhydrite and gypsum surfaces showed some scatter, the thickness of the gypsum layer was within the expected range according to the predictions of the model.

For clarifying the interaction between anhydrite dissolution, gypsum precipitation and transport, it was necessary to quantify the time-development of the individual chemical reactions and to analyse their interplay with the ionic transport by means of a coupled reaction-advection-diffusion model while considering the above mentioned kinetic equations. The numerical simulations showed that diffusion can certainly be disregarded (it occurs very slowly relative to the chemical reactions), while advection may also be neglected, as long as the seepage flow is low, which is usually the case in Gypsum Keuper. Consequently, the anhydrite to gypsum transformation can be considered as a topochemical process in most cases, which can be described by a single reaction (i.e. anhydrite + water \rightarrow gypsum). Based on this conclusion it was possible to reduce the complexity of the mathematical model of the physical-chemical processes under investigation and therefore to abandon the execution of arduous experimental investigations into the hydraulic-chemical coupled processes.

The experimental work therefore focused on the coupled chemo-mechanical processes. The experimental investigations aim to quantify the strains and stresses developing due to the anhydrite to gypsum transformation. For this, a series of swelling tests under oedometric conditions were performed on artificial samples consisting mainly of mixtures of anhydrite and nearly non-reacting powders that were thoroughly compacted. The experimentally-obtained relationship between swelling stresses and strains for these samples can be approximated very well by a straight line in a semi-logarithmic diagram – analogous to the known swelling law for claystones. This result is remarkable, since the swelling strain occurs only due to chemical reactions (not swelling of clay). However, although the swelling strain of each sample appeared to have reached a final value (steady state), the mineralogical composition of the samples post test showed that the hydration of anhydrite was not completed in most cases. With two additional series of experiments, a relationship between the swelling strain and the degree of anhydrite to gypsum transformation was determined by extracting the samples before they reached a steady state in swelling strain. The maximal stress of these samples is determined via a series of tests under complete constraint.

The experimental investigations proved to be very time-consuming and will be continued after the formal completion of this research project.

1 Introduction

1.1 Context and objectives of the research project

Sulphatic claystones belong to the most problematic rocks in tunnelling due to their distinctive swelling behaviour. They are known to have caused severe damage to numerous tunnels excavated in the Gypsum Keuper formation. The repairs were extremely costly and time-consuming, and often provided only a temporary solution. The economic significance of tunnelling through Gypsum Keuper, the repeatedly experienced setbacks and the limited knowledge of the macroscopic principles governing the swelling process and the underlying microscopic mechanisms triggered a series of ASTRA-founded research projects of the Group of Applied and Environmental Geology at the University of Basel (Prof. Huggenberger), of the Chair of Physical Chemistry of Building Materials at ETH Zurich (Prof. Flatt) and of the Chair of Underground Construction at ETH Zurich (Prof. Anagnostou).

The research projects of the University of Basel (projects FGU 2008/004, 2008/005, 2012/004) aim to improve understanding about the influence of the hydrogeological conditions and their tunnelling-induced disturbance on the observed swelling phenomena, addressing the seepage flow processes in the big geological scale. The Chair of Physical Chemistry of Building Materials at ETH Zurich (Project FGU 2012/001) investigates the chemical processes in claystones containing finely distributed anhydrite with the aim to develop swelling inhibitors, *i.e.* materials that could prevent the anhydrite to gypsum transformation. Project FGU 2006/001 of the Chair of Underground Construction investigates by means of a series of long-term swelling tests the relationship between swelling pressure and swelling strain (so-called "swelling law"). Knowledge (even qualitative knowledge) of the swelling law is of paramount importance for the conceptual design of tunnel linings [1].

The extremely long duration of swelling tests (10 to 15 years in the ongoing project FGU 2006/001) in combination with the heterogeneity of natural rock samples (which makes it difficult to obtain reproducible results) motivated our group to undertake the task of estimating the long-term macroscopic behaviour by formulating a hydraulic-mechanical-chemical coupled model, which shall account for the fundamental mechanisms underlying the swelling of anhydritic claystones: anhydrite dissolution and gypsum precipitation; chemo-mechanical coupling between sulphate and clay matrix; seepage flow; diffusive and advective ion transport; and, potentially, evaporation-induced crystal growth in the unsaturated zone.

The objective of the research project FGU 2010/007 is to advance the knowledge of these fundamental mechanisms. Towards this end a series of theoretical and experimental investigations were conducted into the interactions between chemical reactions, transport processes and mechanical behaviour. This report presents the results of these investigations. Since experimental investigations shall continue beyond the project FGU 2010/007, the report is organized in a theoretical part (Sections 3 to 7) and an experimental part (Sections 8 to 13) although the questions under investigation are interconnected.

1.2 Outline of the investigations

Starting point of the project was a series of fundamental questions about the role of transport processes, the role of the hydraulic boundary conditions, the role of the clay matrix and the swelling law [2].

The swelling of anhydritic claystones is due to the chemical transformation of anhydrite to gypsum and to the water uptake by the clay phase. A chemo-mechanical model should, therefore, consider the conditions (stress, pore pressure, temperature etc.), under which

the chemical transformation occurs (*i.e.* the chemical equilibrium conditions), as well as the strains caused by this transformation.

A difficulty, which arises in this respect, is that anhydrite actually does not transform directly to gypsum. The transformation takes place over the solution phase via two distinct chemical reactions: Anhydrite dissolves in the pore water and, once the pore solution becomes oversaturated with respect to gypsum, gypsum crystals start to grow. As this process occurs in general simultaneously with seepage flow and ion diffusion, the dissolved ions may be partially transported away before gypsum precipitates. If anhydrite dissolution and gypsum precipitation occur rapidly relatively to the advective and diffusive transport, then the anhydrite to gypsum transformation could be considered as a single chemical reaction, which would simplify both the continuum-mechanical modelling and the associated experimental investigations considerably. Therefore, clarifying the role of ionic transport and of the hydraulic boundary conditions (which affect the seepage flow rates and thus the advective ionic transport) represents a main task of the project.

Chemical equilibrium conditions

Since it was uncertain at the beginning of the project, to which extent transport interacts with the chemical reactions, the chemical equilibrium conditions had to be studied without making the simplifying assumption of direct anhydrite to gypsum transformation. Contrary to usual thermodynamic analyses of the anhydrite-gypsum-water equilibrium, it was necessary to consider the individual dissolution and precipitation reactions and formulate a thermodynamic model for the estimation of the anhydrite and gypsum solubilities (Sections 3 and 10). In addition, it was necessary to enhance existing thermodynamic models by considering two factors, which are so far neglected in the anhydrite-gypsum literature: the effects of the clay matrix and of the pore size. The clay minerals "attract" the pore water (particularly if the water content is very low), thus reducing its activity and affecting the thermodynamic equilibrium of the anhydrite-gypsum-water system. In addition, claystones contain extremely small pores and it is known that crystal-growth in small pores is affected by solid-liquid interfacial effects. As shown in Section 3 these effects can be taken coherently into account in addition to the other usually considered factors (temperature, pore water pressure, solid pressure and the presence of foreign ions such as NaCl in the pore fluid).

Role of clay

The thermodynamic model of Section 3 is the basis of Sections 6 and 7, which shed light on the role of the clay by analysing two observations: the fact that in Gypsum Keuper anhydrite occurs in relatively shallow depths of cover (Section 6), and the fact that anhydritic claystones exhibit swelling pressures which are significantly lower than the crystallisation pressure of gypsum (Section 7).

Section 6 shows that the only consistent and, therefore, most convincing explanation for the occurrence of anhydrite at shallow depths is associated with the thermodynamic state of the pore water in the clay matrix. More specifically, the very low water content of anhydritic claystones results in a very low water activity, which in turn shifts the thermodynamic equilibrium in favour of anhydrite, thus preventing its transformation to gypsum. This finding, besides being important for the formulation of consistent initial conditions in continuum-mechanical models, shows the role of the clay matrix and provides an explanation of the processes taking place when anhydritic claystones come into contact with water: Swelling starts with water uptake by the clay minerals. During this first phase, the pore water activity gradually increases, eventually reaching the gypsum – anhydrite equilibrium activity. From this point on, anhydrite to gypsum transformation takes place, consuming water and thus maintaining the water deficiency of the clay and sustaining the water uptake until all of the anhydrite is transformed into gypsum. At the end of the swelling process (fully swollen clay) the water activity reaches unity. On-going swelling experiments on natural rock samples (Section 13) are expected to provide more evidence about the interplay of clay swelling and anhydrite transformation.

Further indications about the role of the clay matrix are obtained by analysing swelling pressure data. The swelling pressures observed in oedometer tests or *in situ* are by one to two orders of magnitude lower than the thermodynamically calculated crystallisation pressure of gypsum. Section 7 explains this observation by considering the mechanical interaction of the expanding gypsum crystals with the surrounding claystone matrix. The macroscopically observed swelling pressure is lower than the crystallisation pressure, because the clay matrix acts as a buffer.

Role of transport

For clarifying the interaction between anhydrite dissolution, gypsum precipitation and transport it was necessary to quantify the time-development of the individual chemical reactions (anhydrite dissolution, gypsum precipitation, Sections 4 and 11) and to analyse their interplay with the ionic transport by means of a coupled reaction-advection-diffusion model (Section 5). The numerical simulations showed that diffusion can certainly be disregarded (it occurs very slowly relatively to the chemical reactions), while advection may be significant only in very exceptional cases characterized by high permeability and high hydraulic head gradients. Consequently, the anhydrite to gypsum transformation can be considered as a topochemical reaction in most cases, *i.e.* without considering the intermediate dissolution and precipitation processes.

Role of hydraulic boundary conditions

With the progress of the research project the relevance of the question about the role of the hydraulic boundary conditions was reconsidered and not further investigated. The hydraulic conditions may influence the swelling of anhydritic claystones for the following reasons: (i) they are decisive (together with rock permeability) for the velocity of the seepage flow and thus for the transport processes mentioned above; (ii) they influence the pore pressures in the vicinity of the tunnel and thus the chemical equilibrium conditions; (iii) they determine whether an unsaturated zone develops, inside of which the sulphate concentration increases, thus triggering crystal growth.

Concerning point (i), we could make use of recent results by the University of Basel, which provided the necessary information about the range of the seepage flow velocities in Gypsum Keuper. Furthermore, the thermodynamic equilibrium computations of Section 3 showed that effect (ii) is of minor importance. Finally, hypothesis (iii) was not investigated because it contradicts to the observed pattern of deformations in tunnels through swelling rocks (no swelling is observed in the unsaturated zone above the elevation of the tunnel floor). In addition, this hypothesis was dismissed by recent research by Alonso *et al.* [3].

Chemically-induced strains

Therefore, the experimental works focused mainly on the coupled chemo-mechanical processes rather than on the interaction between seepage flow and chemical reactions. The on-going experimental investigations aim to quantify the strains and stresses developing due to the anhydrite to gypsum transformation (Section 12).

1.3 Contributions to the project

The successful execution of the project was possible thanks to the contribution of several persons from different institutions.

The group Concrete / Construction Chemistry at the EMPA:

Prof. Dr. P. Lura, Dr. A. Leemann and Dr. B. Lothenbach and Dr. M. Wyrzykowski advised us about analytical techniques and performed some analyses and tests for the determination of the chemical composition of water from the Chienberg Tunnel and MIP on samples from the Belchen and from the Chienberg Tunnel.

Chair of Physical Chemistry of Building Materials at the ETH Zurich:

Dr. T. Wangler offered us valuable inputs when discussing our experimental research and advised us on the electrical conductivity experiments and also on usage of thermogravimetry together with T. Keplinger. A. M. Aguilar Sanchez and G. Peschke provided very helpful support and supervision with all microscopic investigations performed.

Institute for Geotechnical Engineering at the ETH Zurich:

Prof. G. Anagnostou and Dr. E. Pimentel supervised the works and co-authored Sections 3 to 7 (with Dr Serafeimidis) and Sections 8 to 13 (with T. Huber), respectively. A. Vrakas contributed with numerical simulations to Sections 6 and 7. Furthermore, several undergraduate students of the Department of Civil Engineering at the ETH Zurich participated to the experimental works either in the framework of their Bachelor theses (M. Kunz with experiments on milled natural or commercial anhydrite; D. Werlen with oedometer tests) or as teaching assistants (M. Kunz, D. Werlen and F. Flütsch).

Dr. M. Plötze and his team (M. Rothaupt, A. Röthlisberger) of the Geo-environmental Engineering and Clay Mineralogy Research Group performed the XRD analysis and porosimetry and supervised the laserdiffractometry on our samples in their laboratories (hereafter referred to as "Clay Lab"). T. Heierli, the technician of the Chair of Underground Construction, built all non-standard apparatuses and components in our workshop (such as the reaction frames for the completely constrained tests, the loading frame and the high-precision measuring chain for swelling tests in flexible oedometers under constant load, oedometer cells and vessels for the free swelling tests etc.). Mr. E. Bleiker, technician in the electronics-workshop, prepared the connections of the sensors to the PCs for the data acquisition.

1.4 Publications

Extensive parts of the present report have already been communicated by means of scientific publications. Sections 3 and 6 are based upon [4] and [5], respectively. Section 4 is based upon [6] and [7]. Section 5 was published in [8]. Section 7 is based upon [9] and [10]. Sections 8 to 13 are largely unpublished with the exception of [11] and [12].

2 State of research

Research on the problem of swelling was triggered in the early 70's by difficulties encountered in two road tunnels, the Wagenburg Tunnel in Germany and the Belchen Tunnel in Switzerland. Since then a series of research projects have been carried out which differ in the questions addressed and therefore also in the methods employed, the scale of the investigation and the scientific disciplines involved. At the microscale, mineralogists have carried out theoretical and experimental studies into the interactions between clay particles, anhydrite and gypsum crystals (*cf.*, *e.g.* [13], [14]). The scale of a geological formation (Dm to km) defines the other end of the spectrum. Here, hydrogeological research by Huggenberger [15], [16] and Butscher *et al.* [17], [18], [19] addresses the question of possible links between regional groundwater circulation systems and the spatial distribution of swelling phenomena observed in tunnelling.

In addition to investigations into processes at the extreme ends of the scale, considerable engineering research has been carried out into phenomena at the scale of the specimens used for geotechnical laboratory testing ('macroscale' *i.e.* some centimetres to decimetres) and at the scale of underground openings ('megascala' *i.e.* some metres to decametres). The following summarises existing theoretical models and experimental investigations, while bearing in mind that interesting research has also been done on concerning the microstructure and mineralogical changes in swelling rocks (*cf.*, *e.g.* [20], [13], [21]).

Theoretical models

Since Grob's semi-logarithmic swelling law [22] many models have been proposed to describe the swelling behaviour of rock in tunnelling and to provide a rational basis for tunnel design. The process began with relatively simple (purely mechanical) analytical ([23], [24]) and numerical ([25], [26]) models and continued with the first attempts to simulate the interaction between mechanical behaviour, seepage flow and chemical reactions.

Bellwald and Einstein [27] proposed a plasticity-based model considering swelling as an inverse consolidation process. This model was extended later by incorporating elastic anisotropy and creep [28] and a swelling-specific term, which assumes a sigmoidal relationship between the excess pore pressure and the volumetric strain ([29], [30], [31]).

Anagnostou [32] developed a fully coupled hydraulic-mechanical model to investigate the effect of seepage flow on the deformation pattern and on the time-development of swelling in tunnelling, while Kiehl [33] addressed the time-dependency of swelling by an elasto-viscoplastic model. Kiehl's model was enhanced later by a time-water absorption relationship based upon Darcy's law [34] or diffusion theory [35].

Alonso and Olivella [36] studied the swelling phenomena in the Lilla Tunnel in Spain and proposed a chemo-mechanical micro-model for crystal growth in a single rock fracture, which is embedded in an elastic continuum element. A basic assumption of this model is that the water in the fracture is always saturated in sulphates and that swelling is triggered by evaporation. This model was improved later by considering a series of mechanisms that might be crucial to the swelling process: evaporation, water seepage flow, stress changes, anhydrite dissolution and gypsum precipitation ([37], [38], [39], [40], [41]). A main conclusion of these works was that evaporation of the ground water is rather insignificant and that the most likely mechanism is the dissolution of anhydrite and the precipitation of gypsum.

Experimental investigations

The goal of the first laboratory tests on samples of swelling rock was to determine their characteristics (magnitude of swelling strain or pressure, relationship between swelling stress and strain) under simple experimental setups (oedometer apparatuses). Huder and Amberg [42] used the conventional oedometer apparatus from soil mechanics for running swelling tests, while special oedometer apparatuses were later developed specifically for rock specimens ([43], [44]). Pimentel ([45], [46]) proposed a modified oedometer that enables the stress - strain relationship to be determined under triaxial conditions and he later improved this technique in order to be able to determine both the maximum swelling stress and the stress-strain relationship with just one test.

The effects of pore water pressure, radial stress and changes in strength and stiffness have been investigated by means of triaxial tests under drained as well as undrained conditions [28]. Pimentel [45] has demonstrated through triaxial tests that claystones experience a considerable loss of strength and stiffness during swelling, while Barla [29] investigated the excess pore pressures developing under triaxial stress conditions.

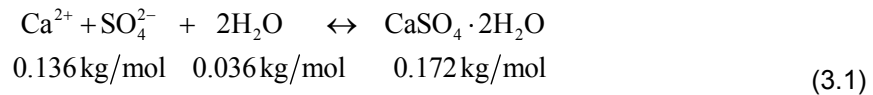
It should be noted that most of the reported laboratory test results concern purely argillaceous rocks. Tests on sulphatic rocks have been carried out mostly within the framework of design activities for tunnelling projects and lack the quality needed for research purposes. As the duration of the swelling process is extremely long even under the optimum watering conditions prevailing in the laboratory, most of the tests were terminated before reaching a steady state. Reliable experimental results for sulphatic rocks are therefore very scarce. Systematic long-term observations are available from only one test series, which was carried out on samples from the Freudenstein railway Tunnel [46]. It is interesting to note that the swelling process did not reach completion even after 20 years. The test results indicated that swelling strain may be largely independent of pressure.

Recent experimental work on anhydritic claystones is that of Oldecop and Alonso [37], who performed nine free-swelling tests and one oedometer test ($\sigma_{ax} = 200$ kPa) with cores from the Lilla Tunnel. After the tests the specimens were broken for further analysis. They observed that the rock volume increased by about 20% during the free swelling tests whereas a large part of the swelling arose from the opening of cracks. Only a small part of the cracks were filled by gypsum crystals. The oedometer test experienced a considerably lower strain (0.7% after five months). The alteration due to anhydrite-gypsum transformation was observed only within a depth of 1mm from the surface. The remaining interior of the specimen showed a completely dry appearance.

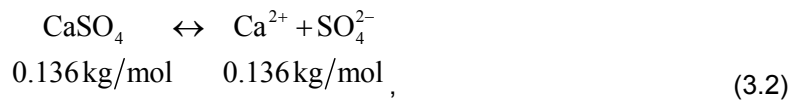
3 Thermodynamic fundamentals

3.1 Introduction

Anhydritic claystones consist of a clay matrix with finely distributed particles, veins and layers of anhydrite ($CaSO_4$). The swelling of anhydritic claystones is attributed mainly to the chemical transformation of anhydrite to gypsum ($CaSO_4 \cdot 2H_2O$), which leads to an increase in the volume of sulphate by 61% (the molar volumes of anhydrite and gypsum are equal to 46 and 74 cm³, respectively). This transformation takes place via the solution phase, *i.e.* via anhydrite dissolution and gypsum precipitation. The chemical dissolution and precipitation reactions of gypsum and anhydrite as well as the masses involved are



and



respectively.

In a system where different minerals co-exist, the mineral with the lower equilibrium concentration (or solubility) represents the stable phase. Thus, the transformation takes place as a result of the anhydrite equilibrium concentration being higher than that of gypsum under the conditions normally prevailing when tunnelling through the Gypsum Keuper formation (rather low temperatures and pressures, *cf.* Section 6.1). More specifically, anhydrite in contact with water starts to dissolve into calcium and sulphate ions until the ionic concentration reaches its equilibrium concentration. Before this happens, however, the concentration reaches the solubility of gypsum with the consequence that gypsum starts to precipitate, thus consuming ions and maintaining a state of undersaturation with respect to anhydrite until all of the anhydrite is dissolved.

Starting with Van't Hoff *et al.* [47], the system $CaSO_4 - H_2O$ has been examined by several authors both experimentally and theoretically based on the thermodynamic concept of Gibbs free energy (see [48], for a review). Nonetheless, most of the studies are outdated and many of them fail to provide all the necessary information. More specifically, the effect of crystal size, which may be particularly important in argillaceous rocks with very small pores, has never been investigated. Additionally, existing research results often appear to be controversial. For instance, the gypsum-anhydrite transition temperature is still quite uncertain, with extreme values of 38 and 63.5 °C proposed by Toriumi and Hara [49] and Van't Hoff *et al.* [47], respectively. However, the following qualitative conclusions are generally accepted: (i) an increase in pressure increases the equilibrium concentrations of anhydrite and gypsum to different extents; (ii) the presence of salts such as $NaCl$ in the solution both increases the equilibrium concentrations and lowers the temperature at which anhydrite and gypsum coexist; (iii), the anhydrite equilibrium concentration decreases with increasing temperature, while the gypsum equilibrium concentration changes only slightly with temperature.

The existing theoretical models for the anhydrite-gypsum equilibrium take into account the temperature, the solid and liquid pressures and the effect of foreign ions in the solution. In the case of small pores, however, the crystal size is an additional important factor ([50], [51], [52]); the equilibrium concentration increases with decreasing crystal size [53]. Another effect which should be considered in the case of claystones with finely distributed anhydrite is that clay minerals lower the chemical potential of the water, thus increasing the solubility of gypsum and shifting the thermodynamic equilibrium in favour of anhydrite. The present work incorporates these effects into the thermodynamic

equations consistently and discusses the effects of clay minerals on water activity (Section 3.2.3).

Almost all theoretical studies deal with the equilibrium between anhydrite and gypsum without investigating the anhydrite-water and the gypsum-water equilibria, *i.e.* without presenting theoretical estimates of the anhydrite and gypsum solubilities. An exception to this is the work of Raju and Atkinson [54], which refers, however, only to sulphate dissolution/precipitation under atmospheric conditions. Here, and in contrast to existing studies, we approach the thermodynamic equilibrium problem starting from the two individual dissolution/precipitation reactions (Eqs. 3.1 and 3.2) and a determination of the equilibrium concentrations of anhydrite and gypsum (Section 3.3).

An analysis only in terms of thermodynamic stability is generally insufficient for investigating the rock-water interaction comprehensively, as the chemical dissolution and precipitation reactions occur simultaneously with diffusive and advective transport (seepage flow through the rock). Nonetheless, consideration of the equilibrium situations constitutes a starting point for further investigations into systems, which are not in equilibrium [55]. The results are thus valuable also as a component of comprehensive claystone-sulphate-water interaction models, which address the chemical dissolution and precipitation reactions simultaneously (*cf.* Section 5).

Starting with an overview of the fundamental thermodynamic principles (Section 3.2), we derive mathematical relationships for the gypsum and anhydrite equilibrium concentrations (Section 3.3) and formulate the anhydrite–gypsum equilibrium condition in terms of temperature, pore water pressure, the pressure in the solid phase and crystal size (Section 3.4). Sections 3.5 and 3.6 compare, respectively, the predicted equilibrium concentrations and equilibrium conditions with existing experimental data and third party computations for pure water and *NaCl* solutions. Finally, Section 3.7 presents and discusses an equilibrium diagram covering a wide range of the parameters that govern the gypsum–anhydrite equilibrium.

In all derivations the geomechanics sign convention is adopted whereby pressures (compressive stresses) are positive. Furthermore, although the equations are given in a general form, attention will be paid to the pressure, temperature and salinity conditions that prevail when tunnelling through the Gypsum Keuper formation.

3.2 Basic thermodynamic relations

3.2.1 Gibbs free energy

According to the first law of thermodynamics (see, *e.g.*, [56]), assuming for simplicity that the product of pressure and volume change is the only mechanical work done by the system, the internal energy differential can be written as

$$dU = dQ - \sum_i P_i n_i dV_i + \sum_i \mu_i dn_i, \quad (3.3)$$

where dQ denotes the energy supplied to the system as heat. The subscript i denotes the i .th constituents of the system. In the present case $i = Ca^{2+}, SO_4^{2-}, H_2O, CaSO_4$ and $CaSO_4 \cdot 2H_2O$. (For the sake of brevity, the subscripts A and G and W will be used in place of the chemical formulae of anhydrite, gypsum and water, respectively.) The second term on the right side of Eq. (3.3) denotes the mechanical work performed when n_i moles of the system-constituent i experience the molar volume change dV_i while being subject to the pressure P_i . The pressure P_i in Eq. (3.3) is equal to $p_W + P_{atm}$ for the water and the ions, and to $p_S + P_{atm}$ for the solid phase, where p_W , p_S and P_{atm} denote the pore water pressure, the macroscopic solid pressure [57] and the atmospheric pressure, respectively. (As usual in geomechanics, the stresses are taken in excess of atmospheric pressure.) The macroscopic solid pressure p_S represents the average pressure experienced by the grains [58] and will be referred to hereafter simply as “*solid pressure*”.

The last term of Eq. (3.3) represents the change in the internal energy due to chemical reactions, *i.e.* due to changes in the molar quantities n_i . The chemical potentials μ_i depend in general on the temperature T and on the pressure P_i (see Section 3.2.2).

According to the second law of thermodynamics,

$$T \sum_i n_i dS_i \geq dQ, \quad (3.4)$$

where the equality sign applies to reversible processes while T and S_i denote the temperature and the molar entropy of constituent i , respectively.

The Gibbs free energy

$$G = U + \sum_i P_i n_i V_i - T \sum_i n_i S_i \quad (3.5)$$

or, after integrating Eq. (3.3) at constant values of the intensive properties,

$$G = \sum_i n_i \mu_i. \quad (3.6)$$

For a reversible process we obtain from Eqs. (3.3), (3.4) and (3.5) the Gibbs free energy increment:

$$dG = \sum \mu_i dn_i + \sum n_i V_i dP_i - \sum n_i S_i dT. \quad (3.7)$$

According to this equation, the chemical potential μ_i of the substance i is equal to the change of the Gibbs free energy G due to the formation of 1 mol of this substance under constant temperature and pressure. The direction of a chemical reaction depends on the difference in the Gibbs free energy G between the products and the reactants: Any transformation in a system takes place in order to minimize G , *i.e.* a chemical reaction will occur spontaneously from a state of high Gibbs free energy G to a state of low G . In a system at equilibrium, the Gibbs free energies G of the products and of the reactants are equal.

3.2.2 Chemical potential

The molar chemical potential μ_i at arbitrary temperature T and pressure P_i can be expressed as a function of T , P_i and the chemical potential $\mu_i|_{T_0, P_{atm}}$ at standard temperature T_0 (298.15 K or 25 °C) and atmospheric pressure P_{atm} . In order to do that, we consider a system consisting of one substance only. In the absence of chemical reactions, we obtain from Eqs. (3.6) and (3.7)

$$d\mu_i = dG = V_i dP_i - S_i dT. \quad (3.8)$$

For a constant molar volume V_i and entropy S_i , which is a reasonable simplification for the constituents of the gypsum–anhydrite–water system (without gases), the integration of Eq. (3.8) leads to

$$\mu_i = \mu_i|_{T_0, P_{atm}} + V_i (P_i - P_{atm}) - S_i (T - T_0). \quad (3.9)$$

Assuming that (i) the water and the dissolved ions are in their standard states and that (ii) liquid-crystal interfacial effects can be neglected for the solids, the chemical potential $\mu_i|_{T_0, P_{atm}}$ at atmospheric pressure and standard temperature is identical to its standard Gibbs energy of formation, $\Delta_f G_i^0$, which can be determined from thermodynamic tables

(see Table 3.1 for the constituents of the gypsum–anhydrite–water system). In general, the chemical potential can be written as

$$\mu_i|_{T_0, P_{atm}} = \Delta_f G_i^0 + RT \ln a_i + \gamma_i \frac{dA_i}{dn_i}, \quad (3.10)$$

where R , a_i , γ_i , and A_i denote the universal gas constant ($R = 8.31$ J/K/mol), the activity of the species i , the surface free energy of the crystal–water interface and the total interfacial area of the species i , respectively. The second and the third term on the right-hand side account for deviations from conditions (i) and (ii), respectively, and will be explained in detail in Sections 3.2.3 and 3.2.4. Inserting $\mu_i|_{T_0, P_{atm}}$ from Eq. (3.10) into Eq. (3.9) leads to the following general expression for the chemical potential of species i :

$$\mu_i = \Delta_f G_i^0 + RT \ln a_i + \gamma_i \frac{dA_i}{dn_i} + V_i (P_i - P_{atm}) - S_i (T - T_0), \quad (3.11)$$

where the second term on the right-hand side is non-zero only for the water and the ions, while the third term is non-zero only for the solid species.

Table 3.1 Parameter values at standard state (after [56], with the exception of $V_{SO_4^{2-}}^0$ and γ_G which are after [59] and Section 3.2.4, respectively)

Molar entropies			Molar volumes		
S_A^0	106.70	J/mol/K	V_A^0	45.94	cm ³ /mol
S_G^0	194.10	J/mol/K	V_G^0	74.30	cm ³ /mol
S_W^0	66.91	J/mol/K	V_W^0	18.00	cm ³ /mol
$S_{Ca^{2+}}^0$	-53.10	J/mol/K	$V_{Ca^{2+}}^0$	-18.40	cm ³ /mol
$S_{SO_4^{2-}}^0$	20.10	J/mol/K	$V_{SO_4^{2-}}^0$	13.98	cm ³ /mol
Anhydrite dissolution			Gypsum dissolution		
$\Delta_{r,A} G^0$	23680	J/mol	$\Delta_{r,G} G^0$	24930	J/mol
$\Delta_{r,A} S^0$	-139.7	J/mol	$\Delta_{r,G} S^0$	-87.28	J/mol
$\Delta_{r,A} V^0$	-50.36	J/mol	$\Delta_{r,G} V^0$	-42.72	J/mol
Anhydrite hydration			Other constants		
$\Delta_{r,GA} G^0$	-1250	J/mol	γ_G	80	mN/m
$\Delta_{r,GA} S^0$	-52.42	J/K/mol	R	8.314	J/K/mol
$\Delta_{r,GA} V^0$	-7.64	cm ³ /mol	T_0	273.15	K
Formation energies					
$\Delta_f G_A^0$	-1321.79	kJ/mol	$\Delta_f G_{Ca^{2+}}^0$	-553.58	kJ/mol
$\Delta_f G_G^0$	-1797.28	kJ/mol	$\Delta_f G_{SO_4^{2-}}^0$	-744.53	kJ/mol
$\Delta_f G_W^0$	-237.12	kJ/mol			

3.2.3 Activity

The activity of a species i is defined as

$$a_i = e^{\frac{\mu_i - \mu_i^\ominus}{RT}} \quad (3.12)$$

where μ_i^\ominus is the chemical potential under standard state conditions. Therefore at standard state, the activity a_i is by definition equal to 1 and the second term in Eq. (3.11) disappears.

For ions and molecules in solutions the activity is related to the molar concentration. As the solution becomes dilute the activity approaches 1, *i.e.* pure or almost pure water has an activity of one. This also applies to a solvent in a solution, where the activity is related to the mole fraction. For pure solids at one bar the activity is equal to 1. Therefore, the second term on the right side of Eq. (3.11) disappears for the anhydrite and gypsum crystals.

The pore water in a clayey material generally has an activity less than unity. The underlying causes on the micro-scale are the increased ionic concentration in the vicinity of the clay platelets and the intermolecular forces acting between the clay surface and the water. In general, water activity can be calculated by using the Kelvin equation (*cf.* [60]):

$$a_w = \exp\left(\frac{\Psi V_w}{RT}\right), \quad (3.13)$$

where $\Psi < 0$ is the soil-water potential, T the temperature in K, R the gas constant and V_w the molar volume of water. The potential Ψ can be defined as *'the work done on a unit mass of water, required to move it from a free water surface to a point in the soil'* [61] and consists of the osmotic potential Ψ_π and the matric potential Ψ_m ([62], [63]).

The osmotic potential Ψ_π is associated with the ionic concentration in the soil water. The clay minerals carry negative electric charges. The pore water between the clay platelets is actually a salt solution in which the cations balance these negative electric charges [64]. The clay platelets thus perform a similar function as a semipermeable membrane in a normal osmotic system, *i.e.* they restrain the ions [65].

The matric potential Ψ_m is made up of two components, the adsorptive component Ψ_a and the capillary component Ψ_c ([66], [67]). In general, when a liquid comes in contact with a solid, a thin liquid film forms around the solid surface and surface forces (suction forces) develop ([68], [69]); the interfacial interactions between the clay surface and the water result in a decrease in the chemical potential of the water in the absorbed film. This decrease induces a further gradient between the chemical potentials of the water in the film and the water in the bulk, which in turn causes an additional water flow in the system and thus also additional swelling [70]. The adsorptive component Ψ_a depends on the thickness of the water layer absorbed. According to Low and Margheim [71], who provided a relationship for the swelling pressure of clays, the thinner the absorbed water layer (*i.e.* the less water), the higher the swelling pressure. The capillary component Ψ_c applies to partly saturated porous media and results from the stresses transmitted to the water phase from the concave menisci at the water–vapour interfaces, causing a decrease in the pore water pressure ([62], [70]).

3.2.4 Crystal-liquid interfacial effects

Solid–liquid interfacial effects increase the chemical potential of crystals. This is taken into account by the third term on the right hand side of Eq. (3.11). This term applies only to the solid species (anhydrite and gypsum crystals in the present case) and corresponds to Eq. (7) of Steiger [72]. Since dA_i/dn_i is directly related to the specific surface of the crystals, this term can be neglected for large crystals or plane interfaces, but is important for crystals with small curvature radii. Under the simplifying assumptions of spherical

particles with radius r_i and isotropic surface free energy γ_i , the third term of Eq. (3.11) is equal to $V_i 2\gamma_i/r_i$ (cf. [50]), which means (as can be confirmed by inspecting Eq. 3.9) that the effect of the surface energy is equivalent to that of the pressure P_i : The surface can be conceived of as a stretched membrane that encloses the crystal and exerts a confining pressure of $2\gamma_i/r_i$ upon it. Figure 3.1 shows this apparent confining pressure $2\gamma_i/r_i$ as a function of the particle radius r_i for the typical range of the interfacial tension γ_i (which is 10 - 150 mN/m, cf. [73]). The apparent confining pressure reaches several MPa at small radii, decreases with increasing radius and becomes negligible for radii greater than $1\mu\text{m}$.

Anhydrite appears in natural rocks either in the form of particles or of layers of different thicknesses and spacings (cf. Section 4.2.1). The shape of the particles may be closer to a sphere, or a rather prismatic form, while their size lies within a wide range, amounting from a few μm to a few cm. The solid-liquid interfacial effects are therefore practically negligible for anhydrite.

However, such effects may be important during gypsum growth inside the pores of anhydritic claystones, since the size of the pores in the rock sets an upper limit to the size of the growing gypsum crystals. According to a literature review [4], both the porosity and the pore size of claystones may be extremely low, while the surface free energy γ_G between gypsum and water is in the range 10 - 120 mN/m. All calculations have been performed for $\gamma_G = 80\text{ mN/m}$.

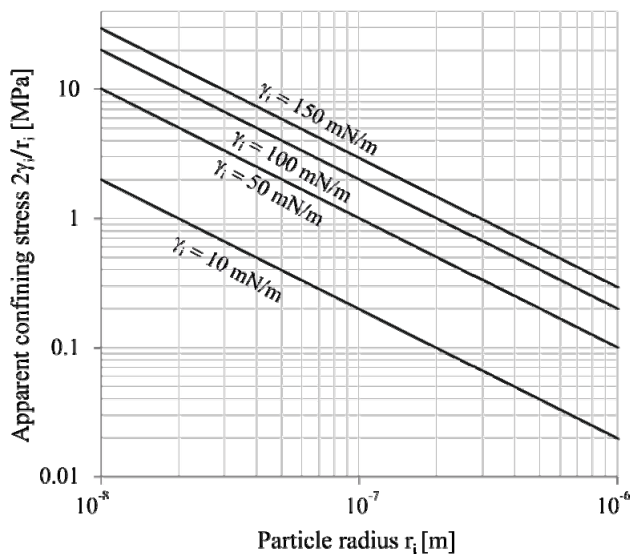


Figure 3.1 Equivalent confining pressure as a function of particle radius.

3.3 Equilibrium concentrations

3.3.1 Gypsum

In order to determine the equilibrium concentration under a given temperature T and pressure P_i , we apply Eq. (3.7) with $dP_i = dT = 0$, with chemical potentials according to Eq. (3.11) and with pressures as introduced in Section 3.2.1. Incorporating the stoichiometric relations $dn_{Ca^{2+}} = dn_{SO_4^{2-}} = 2dn_w = -dn_G$ of the gypsum dissolution/precipitation reaction (Eq. 3.1) as well, we obtain:

$$dG = \left(\mu_{Ca^{2+}} + \mu_{SO_4^{2-}} + 2\mu_w - \mu_G \right) dn_G = \left(\Delta_{r,G}G^0 + RT \ln K_G + p_w (V_G^0 + \Delta_{r,G}V^0) - \left(p_G + \frac{2\gamma_G}{r_G} \right) V_G^0 - (T - T_0) \Delta_{r,G}S^0 \right) dn_G, \quad (3.14)$$

where $\Delta_{r,G}G^0$, $\Delta_{r,G}V^0$, $\Delta_{r,G}S^0$ and K_G are the standard Gibbs energy, the standard volume, the standard entropy and the ion activity product of gypsum dissolution, respectively:

$$\Delta_{r,G}G^0 = \Delta_f G_{Ca^{2+}}^0 + \Delta_f G_{SO_4^{2-}}^0 + 2\Delta_f G_w^0 - \Delta_f G_G^0, \quad (3.15)$$

$$\Delta_{r,G}V^0 = V_{Ca^{2+}}^0 + V_{SO_4^{2-}}^0 + 2V_w^0 - V_G^0, \quad (3.16)$$

$$\Delta_{r,G}S^0 = S_{Ca^{2+}}^0 + S_{SO_4^{2-}}^0 + 2S_w^0 - S_G^0, \quad (3.17)$$

$$K_G = \frac{a_{Ca^{2+}} a_{SO_4^{2-}} a_w^2}{a_G} = \gamma_{Ca^{2+}} \gamma_{SO_4^{2-}} \frac{c_{Ca^{2+}}}{c_0} \frac{c_{SO_4^{2-}}}{c_0} a_w^2. \quad (3.18)$$

(The standard Gibbs energies of formation, molar entropies and molar volumes appearing in these equations are given in Table 3.1.) At equilibrium, $dG/dn_G = 0$ (cf. Section 3.2.1) and, consequently, the last bracketed term in Eq. (3.14) is equal to zero, thus representing the equation for determining the equilibrium solubility product $K_{eq,G}$ as a function of temperature T , pore water pressure p_w , gypsum pressure p_G and grain radius r_G :

$$RT \ln K_{eq,G} = -\Delta_{r,G}G^0 - p_w (V_G^0 + \Delta_{r,G}V^0) + \left(p_G + \frac{2\gamma_G}{r_G} \right) V_G^0 + (T - T_0) \Delta_{r,G}S^0. \quad (3.19)$$

Under the simplifying assumption that the calcium and sulphate ion concentrations are permanently equal during the chemical reaction ($c_{Ca^{2+}} = c_{SO_4^{2-}} = c$), the equilibrium solubility product

$$K_{eq,G} = \left(\gamma_{\pm} \frac{c_{eq,G}}{c_0} a_w \right)^2, \quad (3.20)$$

where $c_{eq,G}$ denotes the gypsum equilibrium concentration and γ_{\pm} the mean activity coefficient of the dissolved ions:

$$\gamma_{\pm} = \sqrt{\gamma_{Ca^{2+}} \gamma_{SO_4^{2-}}}. \quad (3.21)$$

Equation (3.20) is a non-linear equation for the equilibrium concentration $c_{eq,G}$, because the mean activity coefficient γ_{\pm} depends non-linearly on $c_{eq,G}$.

3.3.2 Anhydrite

The anhydrite equilibrium concentration can be calculated analogously to that of gypsum (Section 3.3.1) with some minor modifications. More specifically, Eq. (3.19) becomes

$$RT \ln K_{eq,A} = -\Delta_{r,A} G^0 - p_W \left(V_A^0 + \Delta_{r,A} V^0 \right) + \left(p_A + \frac{2\gamma_A}{r_A} \right) V_A^0 + (T - T_0) \Delta_{r,A} S^0, \quad (3.22)$$

where

$$\Delta_{r,A} G^0 = \Delta_f G_{Ca^{2+}}^0 + \Delta_f G_{SO_4^{2-}}^0 - \Delta_f G_A^0, \quad (3.23)$$

$$\Delta_{r,A} V^0 = V_{Ca^{2+}}^0 + V_{SO_4^{2-}}^0 - V_{CaSO_4}^0, \quad (3.24)$$

$$\Delta_{r,A} S^0 = S_{Ca^{2+}}^0 + S_{SO_4^{2-}}^0 - S_A^0, \quad (3.25)$$

$$K_{eq,A} = \left(\gamma_{\pm} \frac{c_{eq,A}}{c_0} \right)^2. \quad (3.26)$$

and $K_{eq,A}$ and $c_{eq,A}$ denote the equilibrium solubility product and the anhydrite equilibrium concentration.

3.4 Anhydrite-gypsum equilibrium relationships

3.4.1 General case

In order for gypsum and anhydrite to co-exist in a system, their equilibrium concentrations (Eqs. 3.19 and 3.22 with $K_{eq,G}$ and $K_{eq,A}$ according to Eqs. 3.20 and 3.26, respectively) must be equal. This condition leads to the following general equilibrium condition:

$$2RT \ln a_W + (T - T_0) \Delta_{r,GA} S^0 = \Delta_{r,GA} G^0 + p_W \left(V_A^0 - V_G^0 + \Delta_{r,GA} V^0 \right) + \left(p_G + \frac{2\gamma_G}{r_G} \right) V_G^0 - \left(p_A + \frac{2\gamma_A}{r_A} \right) V_A^0, \quad (3.27)$$

where

$$\Delta_{r,GA} G^0 = \Delta_f G_G^0 - \Delta_f G_A^0 - 2\Delta_f G_W^0, \quad (3.28)$$

$$\Delta_{r,GA} V^0 = V_G^0 - V_A^0 - 2V_W^0 \quad (3.29)$$

and

$$\Delta_{r,GA} S^0 = S_G^0 - S_A^0 - 2S_W^0. \quad (3.30)$$

Solving Eq. (3.27) with respect to T yields the equilibrium temperature:

$$T_{eq} = T_{eq}^0 \left(1 + \frac{p_W \left(V_A^0 - V_G^0 + \Delta_{r,GA} V^0 \right) + \left(p_G + \frac{2\gamma_G}{r_G} \right) V_G^0 - \left(p_A + \frac{2\gamma_A}{r_A} \right) V_A^0}{\Delta_{r,GA} G^0 + T_0 \Delta_{r,GA} S^0} \right), \quad (3.31)$$

where T_{eq}^0 denotes the equilibrium temperature under atmospheric pressure ($p_W = p_G = p_A$) without surface tension effects (*i.e.* for sufficiently large crystals):

$$T_{eq}^0 = \frac{\Delta_{r,GA} G^0 + T_0 \Delta_{r,GA} S^0}{2R \ln a_W + \Delta_{r,GA} S^0}. \quad (3.32)$$

At temperatures above the equilibrium temperature T_{eq} , the thermodynamically stable phase is anhydrite. (Gypsum is stable, if $T < T_{eq}$.) According to Eq. (3.31), the equilibrium temperature depends linearly on the pressures of the constituents.

3.4.2 Simplified model for the conditions in the ground

Equation (3.31) will be used in order to determine the equilibrium temperature prevailing at depth H below the surface and to compare it with other theoretical predictions from the literature (Section 3.6). As in Marsal [74] and MacDonald [75], we assume that the solid pressure increases linearly with depth according to the lithostatic gradient (*i.e.* $p_S = \gamma_r H$, where γ_r denotes the unit weight of the rock). According to Dewers and Ortoleva [58], the total pressure p_S acting on a rock volume is undertaken partially by the solid phase and partially by the pores, *i.e.* $p_S = (1-\phi)\gamma_r H + \phi p_W$ where $\gamma_r H$ is the pressure on the solid phase and ϕ the porosity. For very small porosities, which is the case in Gypsum Keuper, $p_S \approx \gamma_r H$. Furthermore, as in the literature, we neglect surface energy effects, which is reasonable for sufficiently large crystals ($r_A, r_G > 1 \mu\text{m}$ according to Fig. 3.1). For the pore water pressure, we will address the two cases investigated in the literature: it will be taken either as hydrostatic (*i.e.* $p_W = \gamma_w H$, where γ_w denotes the unit weight of the water) or equal to the lithostatic pressure ($p_W = p_S$).

Equation (3.31) with $p_A = p_G = p_S = \gamma_r H$, $\gamma_G/r_G = \gamma_A/r_A = 0$ and the constants of Table 3.1 leads to the following expressions for the gradient of equilibrium temperature over depth:

$$\frac{\partial T_{eq}}{\partial H} = T_{eq}^0 \gamma_w \frac{V_G^0 - V_A^0}{\Delta_{r,GA} G^0 + T_0 \Delta_{r,GA} S^0} \left(\frac{\gamma_r}{\gamma_w} - \frac{2V_W^0}{V_G^0 - V_A^0} \right) = -0.005 \frac{T_{eq}^0}{T_0} \left(\frac{\gamma_r}{\gamma_w} - 1.27 \right) \text{ } ^\circ\text{C/m} \quad (3.33)$$

if the pore water pressure is hydrostatic, and

$$\frac{\partial T_{eq}}{\partial H} = T_{eq}^0 \gamma_w \frac{\Delta_{r,GA} V^0}{\Delta_{r,GA} G^0 + T_0 \Delta_{r,GA} S^0} = 0.00135 \frac{T_{eq}^0}{T_0} \text{ } ^\circ\text{C/m} \quad (3.34)$$

if the pore water pressure is equal to the lithostatic pressure. It can easily be verified that in the first case the temperature gradient is negative for the relevant values of γ_r/γ_w , *i.e.* the equilibrium temperature decreases with depth.

3.5 Comparison between predicted solubilities and published data

Figure 3.2a shows the anhydrite equilibrium concentration in pure water under atmospheric pressure ($p_w = p_A = 0$) as a function of the temperature according to Eq. (3.22). The theoretical prediction generally agrees well with the literature data. Greater deviations are observed only at low temperatures, where little data exist (those of Kontrec *et al.* [76]). Similarly, Figure 3.2b shows that the equilibrium concentration computed for gypsum (pure water under atmospheric pressure) is in good agreement with the literature data.

Figure 3.3 shows the gypsum equilibrium concentration as a function of $NaCl$ molality at $T = 30$ °C. Most existing investigations take the molality of $NaCl$ between 0 and 6 mol/l, which is a common range for saline deposits. As the $NaCl$ -molality is relatively low in Gypsum Keuper, the model verification is restricted to low $NaCl$ concentrations in this case. Experimental data for such low molalities exist only for gypsum (in Marshall and Slusher [77]). The predictions of Eq. (3.19) fit the experimental data well.

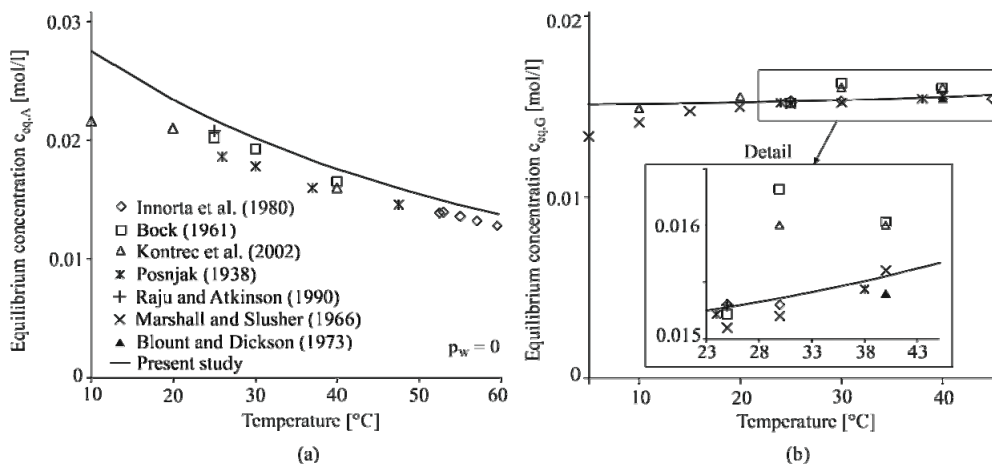


Figure 3.2 (a) Anhydrite and, (b), gypsum equilibrium concentration in pure water at atmospheric pressure as a function of temperature.

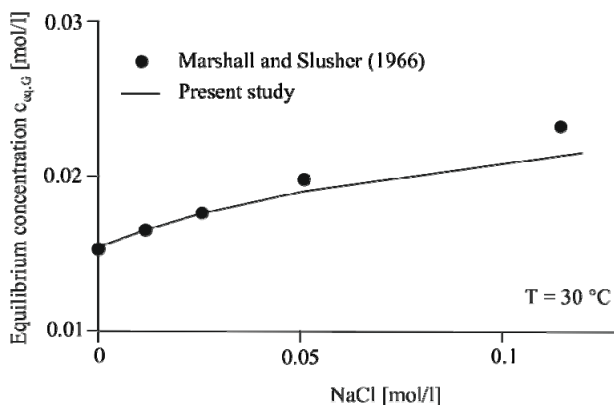


Figure 3.3 Gypsum equilibrium concentration at atmospheric pressure and 30 °C as a function of $NaCl$ -molality.

3.6 Comparison of predicted equilibrium conditions with published data

3.6.1 Anhydrite – gypsum equilibrium in pure water

Figure 3.4 shows the equilibrium temperature between anhydrite and gypsum in pure water ($a_w = 1$, i.e. without foreign ions or interactions with clay minerals) as a function of the depth according to Section 7 as well as according to MacDonald [75] and Marsal [74]. The dashed lines are based on Eq. (3.34), which assumes that the pore water pressure is equal to the lithostatic pressure (Marsal [74] has studied only this case). The solid lines have been computed with Eq. (3.33), which assumes that the lithostatic pressure is higher than the pore water pressure by a factor that is equal to the ratio of the unit weights $\gamma_r/\gamma_w = 2.4$ (cf. [74]).

Marsal [74] determined the equilibrium temperature as a function of depth by using a thermodynamic expression, which accounts for mineral solubilities. MacDonald [75], however, used the empirical relationship of Kelley *et al.* [78], which expresses the change in the Gibbs free energy ΔG of the anhydrite to gypsum transformation as a function of the temperature, and calculated the equilibrium temperature by setting ΔG equal to zero. Furthermore, he employed Eq. (3.7) in order to get the slopes of the lines in Figure 3.4.

All of the model predictions in Figure 3.4 agree well concerning the slope of the equilibrium temperature over depth line, but present differences concerning the equilibrium temperature under atmospheric pressure. According to the relationship used by MacDonald [75], anhydrite and gypsum co-exist under atmospheric pressure at a temperature of $T = 40$ °C, while Marsal [74] suggested a transition temperature of $T = 42$ °C using existing data of Posnjak [79] for his model. The present model predicts a transition temperature of approximately $T = 49$ °C (Eq. 3.32). This value lies in the middle of the range of the transition temperatures usually found in the literature (42 - 60 °C, cf. [48]). The discrepancy between the results of MacDonald [75] and the present model is probably due to the different values that have been used for the thermodynamic parameters (more specifically, the formation of Gibbs free energies and entropies, cf. Eqs. 3.32 and 3.33). Unfortunately, MacDonald [75] does not provide the assumed parameter values. According to Zen [80] the empirical relationship of MacDonald [75] was not consistent, leading to erroneous results. Zen [80] recalculated this relationship but with revised data from Kelley [81] and found a transition temperature of $T = 46$ °C at atmospheric pressure, which is closer to the value proposed in the present study (see lines marked by rhombus in Fig. 3.4).

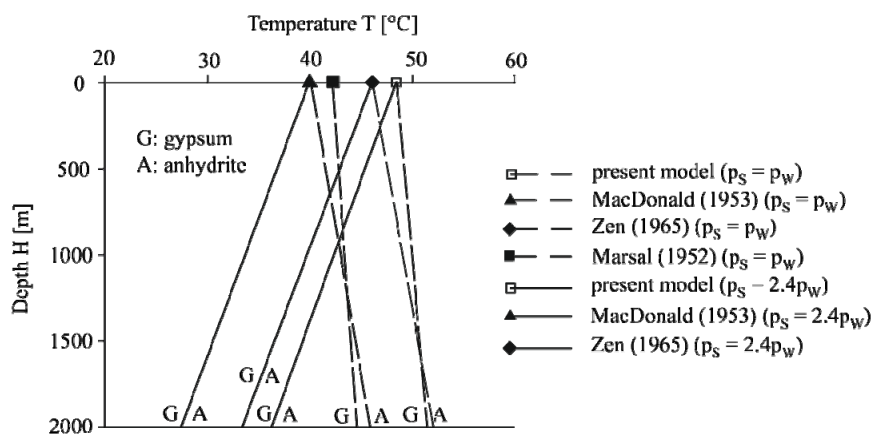


Figure 3.4 Anhydrite – gypsum equilibrium temperature in pure water as a function of depth below surface.

3.6.2 Anhydrite – gypsum equilibrium in NaCl solutions

Figure 3.5 compares the equilibrium temperature in NaCl-solutions according to the model in Section 3.4 with other predictions. For a water activity a_w of 0.75 the prediction of Eq. (3.32) is close to that of Zen [80].

Finally, Figure 3.6 shows the gypsum–anhydrite equilibrium temperature as a function of water activity according to the literature and to the model in Section 3.4. Again, a satisfactory agreement can be observed.

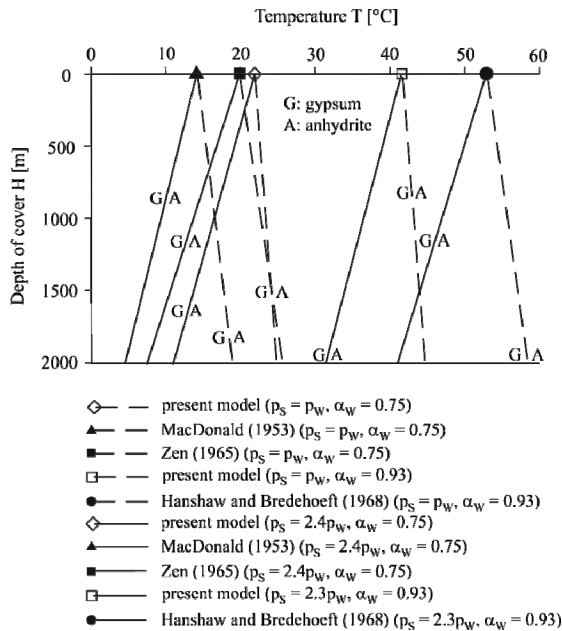


Figure 3.5 Anhydrite – gypsum equilibrium temperature in NaCl solutions as a function of depth below surface.

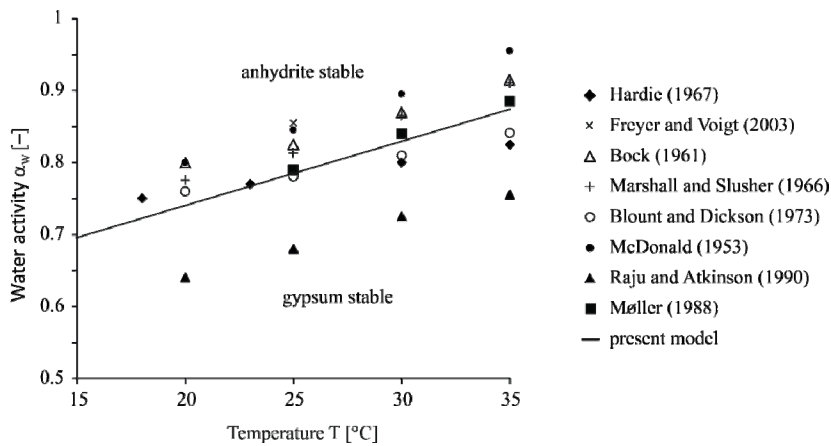


Figure 3.6 Relationship between temperature and water activity at anhydrite – gypsum equilibrium.

3.7 General equilibrium diagram

Under certain simplifying assumptions (same pressure acting on anhydrite and gypsum, negligible interfacial effects for anhydrite, radius of gypsum particles equal to pore radius), the interaction between the parameters that govern anhydrite-gypsum equilibrium can be visualized by means of one single equilibrium diagram (Fig. 3.7).

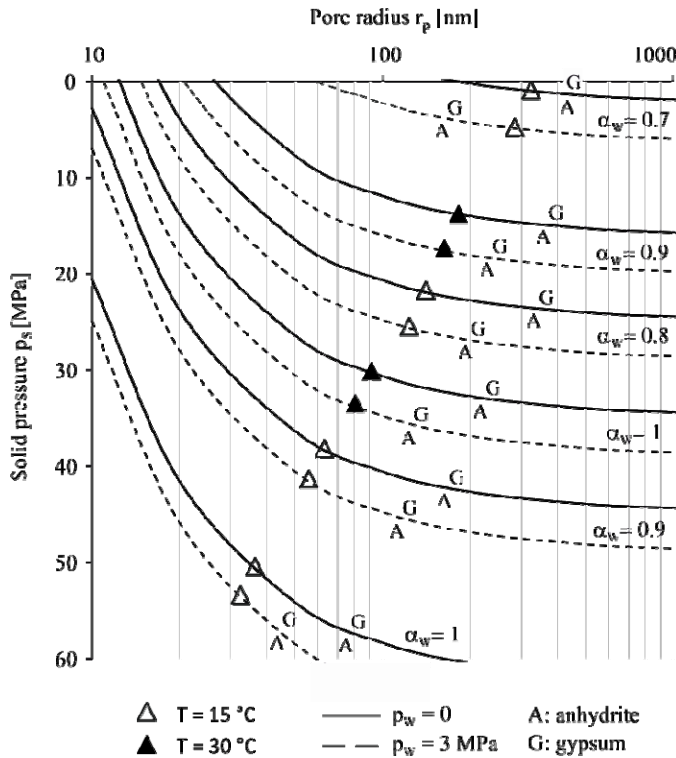


Figure 3.7 Anhydrite – gypsum equilibrium condition in terms of pore radius and solid pressure at different temperatures, water activities and pore pressures.

The diagram has been calculated assuming a value of $\gamma_G = 80$ mN/m and shows the anhydrite-gypsum equilibrium for the two boundaries of the relevant temperature range ($T = 15$ ° and 30 °C), for different values of the water activity a_w and for two assumptions concerning the pore water pressure: atmospheric pressure ($p_w = 0$) as well as a pore water pressure of $p_w = 3$ MPa, which corresponds to a cover depth of 300 m.

The stable phase above and below each curve is gypsum and anhydrite, respectively. According to Figure 3.7, the pore water pressure has a negligible effect on the equilibrium condition for the depths concerned. The effect of the other parameters is, however, significant. A high water activity a_w , low solid pressure p_s , low temperature T and big pore radius r_p favour gypsum as the stable phase.

3.8 Conclusions

A rigorous thermodynamic model was put forward for determining the equilibrium conditions between anhydrite, gypsum and water starting from the underlying dissolution and precipitation equations. The model predictions are close to the measured solubilities reported in the literature and agree with older theoretical predictions with respect to the gradient of the equilibrium temperature over depth.

In addition to the parameters usually considered, the model incorporates the effects of pore size and clay minerals, which are important particularly in the case of claystones with very small pores and finely distributed anhydrite. Both factors – a small pore size and the presence of clay minerals – increase the solubility of gypsum, thus shifting the thermodynamic equilibrium in favour of anhydrite.

4 Time development of sulphate hydration

4.1 Introduction

The swelling of anhydritic claystones is a markedly time-dependent process. It may take several decades to complete in nature. The present section aims to improve our understanding of the factors governing the time-dependency of swelling by investigating the kinetics of the underlying anhydrite dissolution and gypsum precipitation reactions.

The section begins with an overview of common formulations for dissolution and precipitation rates found in the literature (Section 4.2.1) and continues with an estimate of the kinetic parameters based on the published experimental data. Additional equations are subsequently presented in order to take the effect of the sealing of anhydrite by a layer of gypsum into account, which, according to existing investigations and observations, is decisive for the evolution of the swelling process under certain conditions (Section 4.2.2). Section 4.2.3 formulates the equations that govern the evolution of a closed system with simultaneous anhydrite dissolution and gypsum precipitation.

Section 4.3 checks the predictive capacity of the computational model on the basis of the existing experimental data from Kontrec *et al.* [76]. Section 4.4 investigates the effect of the initial composition of the system and of the surface areas of any minerals on the time-development of hydration in a closed system. It shows that anhydrite dissolution (rather than gypsum precipitation) is the governing factor for transformation durations in most cases and develops a simplified equation for estimating the hydration durations. The section finishes with parametric studies on the effect of anhydrite sealing (Section 4.5).

4.2 Kinetic model

4.2.1 Dissolution and precipitation rates

Generally, the dissolution and precipitation rates depend on the reactive surface area of the mineral, the temperature and the distance of the system from thermodynamic equilibrium. A general formulation for the mass change rate of a mineral in contact with water due to dissolution or precipitation is [82]:

$$dM/dt = k \cdot A \cdot f(c), \quad (4.1)$$

where dM/dt [kg/s] is the mass change rate of the mineral (positive for precipitation and negative for dissolution); A [m²] denotes the surface area of the mineral in contact with water (note that A may vary over time); k [kg/m²/s] is the reaction rate constant (increasing with temperature according to the equation of Arrhenius, *cf.*, e.g. [65]); and $f(c)$ is a function of the ion concentration c . It is given here as a function of the relative supersaturation [82]:

$$f(c) = \text{sgn}(c - c_{eq}) \cdot \left| (c - c_{eq}) / c_{eq} \right|^\delta. \quad (4.2)$$

where δ represents the order of the chemical reaction, c_{eq} is the equilibrium concentration of the mineral and, consequently, $(c - c_{eq})/c_{eq}$ expresses the degree of oversaturation, *i.e.* the driving force for dissolution and precipitation. For solutions that are supersaturated with respect to the mineral, *i.e.* $c > c_{eq}$, the mass change rate is positive and precipitation takes place, while in the case of undersaturated solutions ($c < c_{eq}$), the mass change rate is negative and the mineral dissolves.

Subsequently, the mass of constituent i per unit volume of the mixture will be denoted by:

$$m_i = M_i / V_{tot}, \quad (4.3)$$

where M_i [kg] denotes the mass of the i -th constituent at a given time and V_{tot} [m³] is the volume of the mixture which (for small volume changes) can be taken approximately equal to the initial mixture volume $V_{tot,0}$. Furthermore, the volume fractions of the mixture constituents are denoted by

$$\phi_i = V_i / V_{tot} = m_i / \rho_i, \quad (4.4)$$

where V_i and ρ_i are the volume and density of constituent i , respectively.

From Eqs. (4.1), (4.3) and (4.4) we obtain the following equation for the mass change of a mineral per unit volume of a mixture:

$$\frac{dm}{dt} = \rho \frac{d\phi}{dt} = k \phi F f(c), \quad (4.5)$$

where F [m⁻¹] is the specific surface area of the mineral, while the product of ϕ by F is equal to the surface area of the dissolving or precipitating mineral per unit volume of the mixture.

The rates of anhydrite dissolution and gypsum precipitation can then be expressed as follows:

$$\frac{dm_A}{dt} = -k_A \phi_A F_A \left(\frac{c_{eq,A} - c}{c_{eq,A}} \right)^{\delta_A} \quad (4.6)$$

and

$$\frac{dm_G}{dt} = k_G \phi_G F_G \left(\frac{c - c_{eq,G}}{c_{eq,G}} \right)^{\delta_G}, \quad (4.7)$$

where δ_A and δ_G denote the orders of reaction for anhydrite dissolution and gypsum precipitation, respectively, while F_A and F_G [m⁻¹] are the specific surface areas (particle surface per particle volume) of the anhydrite and gypsum particles, respectively.

According to available experimental data, a second order law applies both to the dissolution of anhydrite and to the precipitation of gypsum ($\delta_A = \delta_G = 2$). The analysis of the experimental results of Barton and Wilde [83] and James and Lupton [84] indicates an anhydrite dissolution rate constant k_A between 2.7 and 5.4·10⁻⁶ kg/m²/s, while the experiments of Kontrec *et al.* [76] indicate five to ten times lower values [8]. Furthermore, the experimental results of Liu and Nancollas [85], Smith and Sweett [86] and Kontrec *et al.* [76] indicate a gypsum precipitation rate constant k_G between 3.75·10⁻⁷ and 5.35·10⁻⁶ kg/m²/s [8].

For spherical or cubical particles, the specific surface area is equal to 3·(radius)⁻¹ or 6·(side length)⁻¹, respectively. As mentioned above, the terms $\phi_A F_A$ and $\phi_G F_G$ represent the area of the rock surface, which is in contact with the pore water per unit volume of mixture. It should be noted that the specific surfaces F_A and F_G generally change during the dissolution and precipitation process.

The anhydrite surface per unit volume ($\phi_A F_A$) can be expressed as a function of the anhydrite mass in the following way:

$$\frac{\phi_A F_A}{\phi_{A0} F_{A0}} = \left(\frac{m_A}{m_{A0}} \right)^\psi = \left(\frac{\phi_A}{\phi_{A0}} \right)^\psi, \quad (4.8)$$

where $\phi_{A0} F_{A0}$, ϕ_{A0} and m_{A0} are the initial anhydrite surface, volume and mass (per unit mixture volume), respectively, while the exponent ψ accounts for changes to reactive

surface sites caused by changes in crystal size or changes in the distribution of the crystal population during dissolution or precipitation [87]. It can readily be verified that $\psi = 2/3$ for uniformly dissolving, cubical or spherical anhydrite particles. This is because the volume of each particle is proportional to the cube of its radius (or of the edge length in the case of cubical particles), while its surface area is proportional to the square of the radius or side length. From Eqs. (4.6) and (4.8), we obtain the following expression for the mass rate of anhydrite in the case of spherical or cubical particles:

$$\frac{dm_A}{dt} = -k_A \phi_{A0} F_{A0} \left(\frac{m_A}{m_{A0}} \right)^{2/3} \left(\frac{c_{eq,A} - c}{c_{eq,A}} \right)^{\delta_A}, \quad (4.9)$$

where $F_{A0} = 3 \cdot (\text{radius})^{-1}$ for spherical particles and $F_{A0} = 6 \cdot (\text{side length})^{-1}$ for cubical particles.

For the case of growth on spherical or cubical gypsum particles a similar equation to Eq. (4.9) applies:

$$\frac{dm_G}{dt} = k_G \phi_{G0} F_{G0} \left(\frac{m_G}{m_{G0}} \right)^{2/3} \left(\frac{c - c_{eq,G}}{c_{eq,G}} \right)^{\delta_G}, \quad (4.10)$$

while for gypsum crystal growth on inert minerals of spherical or cubical particles Eq. (4.10) takes following form:

$$\frac{dm_G}{dt} = k_G \phi_s F_s \left(1 + \frac{\phi_G}{\phi_s} \right)^{2/3} \left(\frac{c - c_{eq,G}}{c_{eq,G}} \right)^{\delta_G}, \quad (4.11)$$

where F_s and ϕ_s denote the specific surface area and the volume fraction, respectively, of the inert mineral on which gypsum growth takes place.

An alternative way to express the dissolution and precipitation rates is in terms of the distance s of the surface of a mineral at time t from the initial mineral surface (see Fig. 4.1 for the definition and the sign of s). Equation (4.1) is equivalent to the following equation for the rate of s :

$$\frac{ds}{dt} = \frac{k}{\rho} f(c), \quad (4.12)$$

where $f(c)$ is given by Eq. (4.2). For mineral dissolution, $f(c) < 0$ and consequently s decreases, while for mineral precipitation $f(c) > 0$ and s increases.

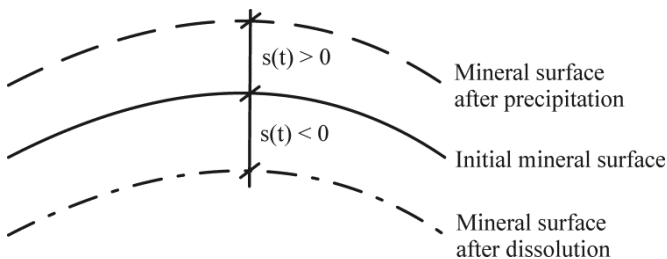


Figure 4.1 Movement of mineral surface due to dissolution or precipitation.

The anhydrite surface in contact with water (which, according to Eq. 4.1, is decisive for the mass change rate) depends on the anhydrite content ϕ_A and on the specific surface F_A of the particles, *i.e.* on their size and shape. Langbein *et al.* [88] presented a qualitative classification of anhydrite with respect to these two factors (Fig. 4.2). Despite the lack of values concerning size, the classification of Figure 4.2 provides an overview of the possible occurrence of anhydrite in natural rocks. The typical examples in Figure 4.3

give an impression of the particle size. Anhydrite appears either in the form of layers of different thicknesses and spacings (Fig. 4.3d, 4.3e) or as particles. The latter may have a form closer to a sphere (nodules, Fig. 4.3a, 4.3f) or a rather prismatic form (Fig. 4.3b, 4.3c). Their size lies within a wide range (a few μm to a few cm).

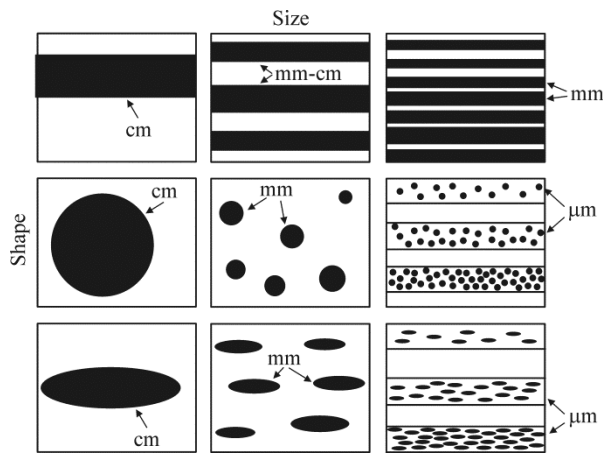


Figure 4.2 Classification of anhydrite in natural rocks (after Langbein *et al.* [88]) and order of particle size (left to right decreasing size, top to down different shapes).

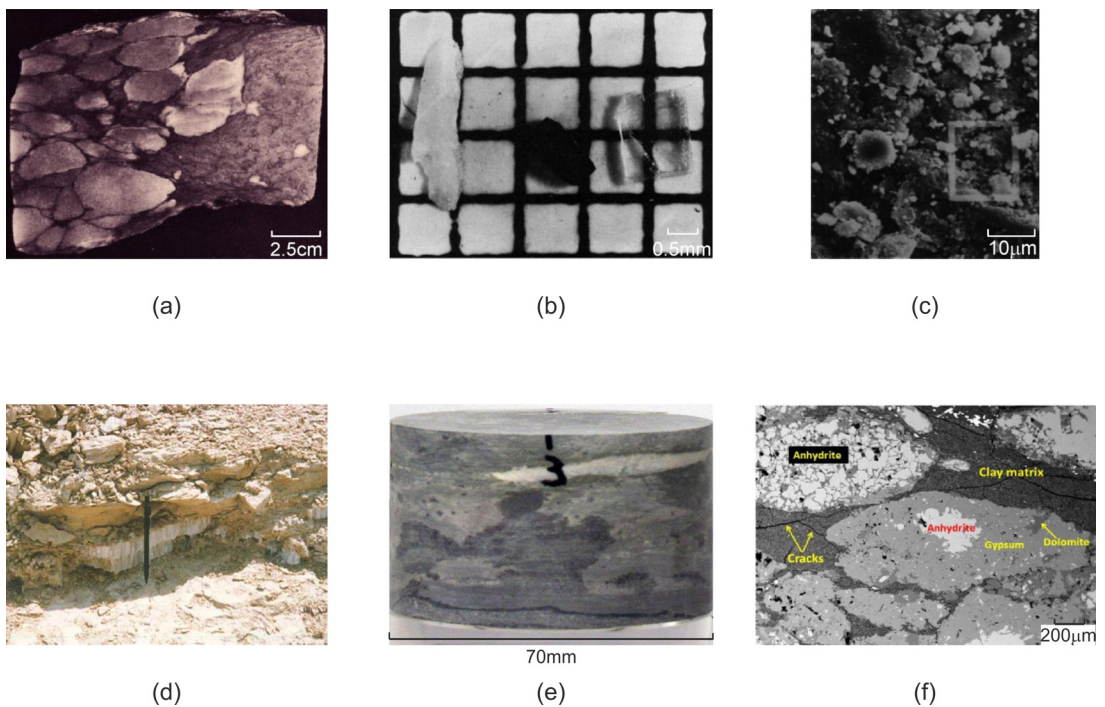


Figure 4.3 (a) Bed of nodular anhydrite [89]; (b) Anhydrite types in reflected light [89]; (c) SEM micrograph of anhydrite [90]; (d) Layered anhydrite near Dammam [91]; (e) Claystone with a remarkable anhydrite vein (sample 935/3/1/1 from Chienberg tunnel [92]); (f) SEM image of anhydritic claystone (sample 2040 (12) from Chienberg tunnel).

4.2.2 Sealing of anhydrite by the formed gypsum

Gypsum growth may also take place on an anhydrite surface, forming a layer of gradually increasing thickness. According to Böhringer *et al.* [93], this happens within a few months. The gypsum layer can be up to a few millimetres thick and may, depending on its thickness and porosity, slow down or even stop anhydrite dissolution, due to the fact that the dissolving ions must diffuse through this layer in order to reach the macropores. At

the same time, the gypsum seals the anhydrite by clogging communicating pores and fissures, which also leads to a significant deceleration or even a halt in anhydrite dissolution and thus also in the hydration process [94]. This is why massive anhydrite, *i.e.* compact rock consisting mainly of anhydrite, does not swell. Amstad and Kovári [95] concluded on the basis of a synthesis of various observations that anhydrite layers do not swell within the usual service life of tunnels (100 years) if they are thicker than 20 mm.

The sealing effect of gypsum was noticed by Wiesmann [96] during the construction of Hauenstein Base Tunnel in Switzerland. Similar observations were made in the Simplon Tunnel, where massive anhydrite with some insignificant dolomite inclusions was encountered in the bottom adit over a 100 m long section [95]. According to Andraea [97], this part of the adit (km 9.7 - 9.8 from the Northern portal) remained unlined for about 10 years. However, no swelling was observed although the relative humidity of the air was practically 100%, due to a nearby spring of natural steaming hot water. Gassmann *et al.* [98] mentioned that anhydrite sealing was also observed on the tunnel walls and in boreholes in the exploration gallery of Val Canaria. Existing fissures were sealed by a gypsum layer within 50 years. Additional evidence on the negligible swelling potential of massive anhydrite can be found in a number of tunnels in Southern Germany crossing Gypsum Keuper ([22], [99], [100]).

Similar observations were made by Sahores [101] who investigated masonry built with anhydrite quarry stones. The masonry remained in very good condition despite being exposed to temperature changes and rainwater for more than 50 years. Sahores [101] attributed this to a thin gypsum layer formed on the surface of the anhydrite blocks, and confirmed this hypothesis in laboratory tests.

Madsen and Nüesch [102] experimentally investigated the behaviour of massive anhydrite from the Weiach borehole. After almost two years of testing, rock samples consisting of 99 weight-% anhydrite and 1 weight-% clay and carbonate, developed swelling pressures of up to 0.05 MPa and swelling strains of up to 1% only. These figures are negligible relative to those of claystones with finely distributed anhydrite, which exhibit swelling pressures and strains of up to 7 - 8 MPa and up to 30 - 40%, respectively.

Sievert *et al.* [103] studied the hydration of anhydrite in a ball mill as a function of time and temperature. Based on the experimental results, they proposed the following mechanism for the sealing of anhydrite by the formed gypsum: Anhydrite starts to dissolve into its ions according to Eq. (3.2) and the solution becomes saturated with respect to these. The ions are rapidly absorbed at the surface of the anhydrite and form a layer around it, the thickness of which increases with time. The adsorbed layer hinders both the circulation of the ions towards the solution and the tendency of water to interact with the surface of the anhydrite. As the layer increases in thickness, cracks are formed after a certain limit. Although this is a slow process, the ball mill accelerates it considerably. The molecules of water enter through the cracks and come into contact with particles of anhydrite. Nuclei of gypsum start to form when enough sulphate and calcium ions are present, along with water molecules. If the nucleus has a radius greater than the critical length (*cf.* [82]), gypsum starts to crystallise. Once a sufficient amount of gypsum has precipitated on the anhydrite particle, the further hydration of the latter becomes effectively impossible.

We model here the sealing effect of the gypsum layer in a similar way to Bezjak and Jelenic [104], Pignat *et al.* [105] and Bishnoi and Scrivener [106], who investigated the transformation of tricalcium silicate (C_3S) to calcium silicate hydrate ($C-S-H$) in the context of cement technology. The similarity to the sealing effect of gypsum is due to the fact that diffusion through the $C-S-H$ layer (which covers the C_3S grains) represents – in addition to nucleation/growth and phase boundary reactions – one of the mechanisms governing the time evolution of the C_3S hydration.

In the absence of a gypsum sealing layer, anhydrite dissolution would occur according to Eqs. (4.2) and (4.12), *i.e.* the dissolution front would move at the following rate:

$$\left. \frac{ds_A}{dt} \right|_{DIS} = - \frac{k_A}{\rho_A} \left(\frac{c_{eq,A} - c}{c_{eq,A}} \right)^{\delta_A}. \quad (4.13)$$

The sealing effect of the gypsum layer on anhydrite dissolution can be taken into account by considering that the diffusive flow of the calcium and sulphate ions through the gypsum may be the limiting mechanism. According to Fick's law, the diffusive flux

$$J = -D n_G T_G \frac{c - c_{eq,A}}{s_G}, \quad (4.14)$$

where D [m²/s], T_G [-], n_G [-] and s_G [m] denote the molecular diffusion coefficient, the tortuosity through the gypsum layer, the porosity and the thickness of the gypsum layer, respectively. Since tortuosity is hard to measure, it is often assumed to be isotropic and is expressed by a single parameter [107]. With increasing thickness of the gypsum layer, the diffusive flow may become slower than the flow predicted by Eq. (4.13) and may become the decisive factor for the rate of the anhydrite dissolution. In this case, the anhydrite surface will retreat at the following rate:

$$\left. \frac{ds_A}{dt} \right|_{DIF} = - \frac{J}{\rho_A} = -n_G T_G \frac{D}{\rho_A} \frac{c_{eq,A} - c}{s_G}. \quad (4.15)$$

Equation (4.13) applies for the initial stage of the dissolution process, *i.e.* as long as it leads to lower values than Eq. (4.15). According to Eq. (4.15) the sealing effect of the gypsum layer depends essentially on how dense this layer is, *i.e.* on its porosity. Porosity probably decreases over time as more and more crystals grow, particularly if gypsum growth in the pore space is constrained (*cf.* [104], [108]). In the absence of experimental data, we make the simplifying assumption of a constant porosity n_G and investigate its effect quantitatively.

4.2.3 Governing equations for a closed system

From Eqs. (4.2), (4.12), (4.13) and (4.15), the following dimensionless relationships can be obtained for the movement rate of the dissolution and precipitation front s_A and s_G , respectively:

$$\frac{d\bar{s}_A}{d\bar{\tau}} = - \min \left[(1 - \tilde{c})^{\delta_A}; n_G T_G \frac{D}{k_A S_{A0} \bar{s}_G} (1 - \tilde{c}) \right], \quad (4.16)$$

$$\frac{d\bar{s}_G}{d\bar{\tau}} = \bar{\Lambda} \left(\frac{\tilde{c}}{\tilde{c}_{eq,G}} - 1 \right)^{\delta_G} \frac{1}{1 - n_G}, \quad (4.17)$$

where

$$\tilde{c} = c/c_{eq,A}, \quad \tilde{c}_{eq,G} = c_{eq,G}/c_{eq,A}, \quad (4.18)$$

$$\bar{\tau} = \frac{k_A}{S_{A0} \rho_A}, \quad \bar{\Lambda} = \frac{k_G \rho_A}{k_A \rho_G}, \quad \bar{s}_A = s_A/S_{A0}, \quad \bar{s}_G = s_G/S_{A0}. \quad (4.19)$$

The last term in Eq. (4.17) accounts for the porosity of the sealing layer (Section 4.2.2). The variable $\bar{\tau}$ denotes a dimensionless time, while S_{A0} is a characteristic length (*e.g.* the initial diameter of the anhydrite particles in the case of spherical anhydrite particles) used here for normalizing s_A and s_G .

Equation (4.16) applies only under the following conditions:

$$c < c_{eq,A}, \quad \phi_A > 0, \quad \phi_G < \frac{172}{36} \frac{\rho_W}{\rho_G} \phi_{W0} + \phi_{G0}. \quad (4.20)$$

The last inequality follows from the condition $\phi_W > 0$ and the mass balance equation for the water:

$$m_W = m_{W0} - 36(m_G - m_{G0})/172. \quad (4.21)$$

It must also be fulfilled (in addition to $c > c_{eq,G}$) due to Eq. (4.17).

Equations (4.16) and (4.17) are coupled via the dimensionless concentration \tilde{c} which is a function of the ion concentration c (Eq. 4.18). The ion concentration c can be expressed as a function of the ion and water masses per unit volume as follows:

$$c = M_I / V_W = \rho_W m_I / m_W. \quad (4.22)$$

From Eqs. (4.21) and (4.22) and the mass balance of ions (*cf.* Eq. 3.1) we obtain \tilde{c} as a function of the volume fractions of anhydrite and gypsum:

$$\tilde{c} = \tilde{c}_0 \frac{\phi_{W0}}{\phi_W} + \frac{\rho_A}{c_{eq,A}} \frac{\phi_{A0} - \phi_A - \frac{136}{172} \frac{\rho_G}{\rho_A} \phi_G}{\phi_W}, \quad (4.23)$$

where ϕ_W and ϕ_{W0} denote the porosity and the initial porosity, respectively,

$$\phi_W = \phi_{W0} - \frac{36}{172} \frac{\rho_G}{\rho_W} \phi_G, \quad \phi_{W0} = 1 - \phi_{A0} - \phi_{G0} - \phi_S \quad (4.24)$$

while

$$\tilde{c}_0 = c_0 / c_{eq,A}. \quad (4.25)$$

In order to calculate the concentration c in Eq. (4.23), the volume fractions of anhydrite and gypsum are needed. These depend on the shape and size of the anhydrite and gypsum particles and thus on the thicknesses s_A and s_G . Two shapes for the mineral particles will be considered here: parallelepipeds and spheres. The initial side lengths of the parallelepipeds are S_0 , aS_0 and bS_0 (Fig. 4.4a), while the spherical particles have an initial diameter S_0 (Fig. 4.4b). The characteristic length S_{A0} used for normalizing s_A and s_G is thus equal to the initial particle diameter (in the case of spherical anhydrite particles) or to the smallest side length if the anhydrite occurs in the form of parallelepipeds.

Gypsum may grow on pre-existing gypsum particles, on anhydrite particles or on other inert minerals. Therefore, the volume fraction of gypsum ϕ_G consists of the initial fraction ϕ_{G0} and three additional terms:

$$\phi_G = \phi_{G0} + \phi_{G,G} + \phi_{G,A} + \phi_{G,S}, \quad (4.26)$$

where $\phi_{G,G}$, $\phi_{G,A}$ and $\phi_{G,S}$ are the volume fractions of the gypsum that precipitates on gypsum, anhydrite and on other solids, respectively. For simplicity, we assume that gypsum growth occurs at the same rate on all particles in the system. Geometric relationships expressing the volume fractions ϕ_A , $\phi_{G,G}$, $\phi_{G,S}$ and $\phi_{G,A}$ in terms of the primary variables s_A and s_G can be found in [8].

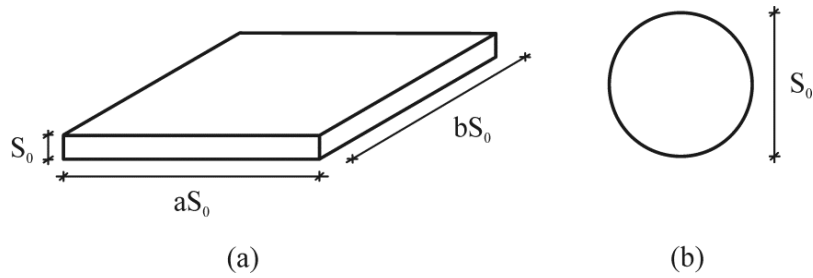


Figure 4.4 (a) Parallelepipedic and (b) spherical particle.

4.3 Comparison of predictions with tests involving simultaneous anhydrite dissolution and gypsum precipitation

The model in Section 4.2 was tested by comparing its predictions with the experimental results of Kontrec *et al.* [76]. Spherical particles are assumed for the calculations with a corresponding surface area ($3.78 \text{ m}^2/\text{g}$). Gypsum particles are elongated platelets with approximate proportions of 21:8:2 and a specific surface area of $0.3 \text{ m}^2/\text{g}$. Table 4.1 shows the orders of reactions used, as well as the rate constants for anhydrite dissolution and gypsum precipitation.

The first test used to check the model involves the dissolution of anhydrite for three different initial masses of anhydrite in the solution ($m_{A0} = 1.60, 2.28, 4.00 \text{ kg/m}^3$). The initial ion concentration was 15.5 mol/m^3 , *i.e.* equal to the gypsum equilibrium concentration at $T = 20 \text{ }^\circ\text{C}$ (Table 4.1). Figure 4.5a shows the computed ion concentration (solid line) over time and the measured values. The computational results generally agree with the experimental results.

The second test concerns the precipitation of gypsum with an initial mass of $m_{G0} = 2.28 \text{ kg/m}^3$ and initial ion concentration $c_0 = 33 \text{ mol/m}^3$. Figure 4.5b depicts the computed ion concentration (solid line) as a function of time. It agrees well with the measured values (dots).

Table 4.1 Assumed parameters

Parameter	Anhydrite	Gypsum
Densities ρ_A, ρ_G [kg/m^3]	2960	2320
Equilibrium concentrations $c_{eq,A}, c_{eq,G}$ [mol/m^3]*	21.0	15.5
Orders of reactions δ_A, δ_G [-]	2	2
Reaction rate constants k_A, k_G [$\text{kg/m}^2/\text{s}$]	$3 \cdot 10^{-6}$	$5 \cdot 10^{-7}$
Diffusion coefficient D [m^2/s]		$8 \cdot 10^{-10}$
Tortuosity T_G [-]		0.66
Porosity of sealing gypsum layer n_G [-]		1.00

*After [76]

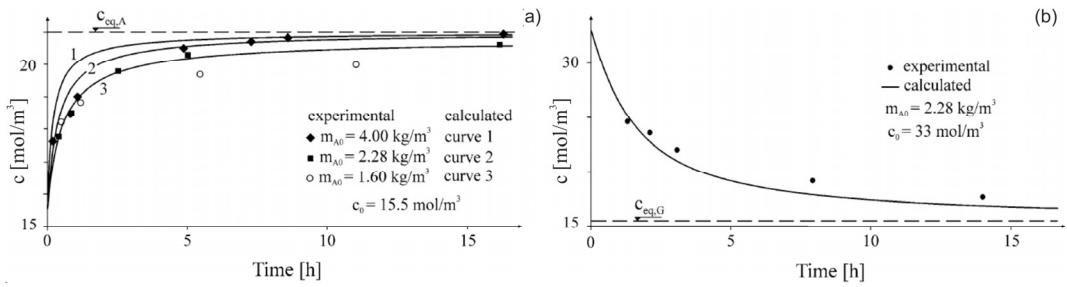


Figure 4.5 Predicted and measured ion concentration over time during, (a), anhydrite dissolution and, (b), gypsum precipitation

Finally, the model in Section 4.2 was tested in relation to the experimental results for simultaneous anhydrite dissolution and gypsum precipitation. The initial anhydrite and gypsum masses in the solution were equal in the test ($m_{A0} = m_{G0} = 2.312$ kg/m³). The initial ion concentration c_0 was 16 mol/m³, *i.e.* slightly higher than the gypsum equilibrium concentration (*cf.* Table 4.1).

Figure 4.6a shows the computed ion concentration over time (solid line) and the measured values (dots). The computational results agree to a great extent with experimental results from Kontrec *et al.* [76]. At the very initial stage of the process, the concentration is close to the gypsum equilibrium concentration and therefore only anhydrite dissolution takes place. Consequently, a steep increase in the concentration is observed. The effect of the increasing concentration is twofold: On the one hand, anhydrite dissolution slows down due to the fact that the difference between the actual concentration and the anhydrite equilibrium concentration decreases. On the other hand, as the solution becomes more and more oversaturated with gypsum, crystal growth starts to occur and consumes ions. Therefore, the concentration reaches a maximum and decreases thereafter. The second characteristic feature of the curve of concentration over time is the turning point at approximately $t = 33$ h. The turning point marks the termination of the anhydrite dissolution process (Fig. 4.6b).

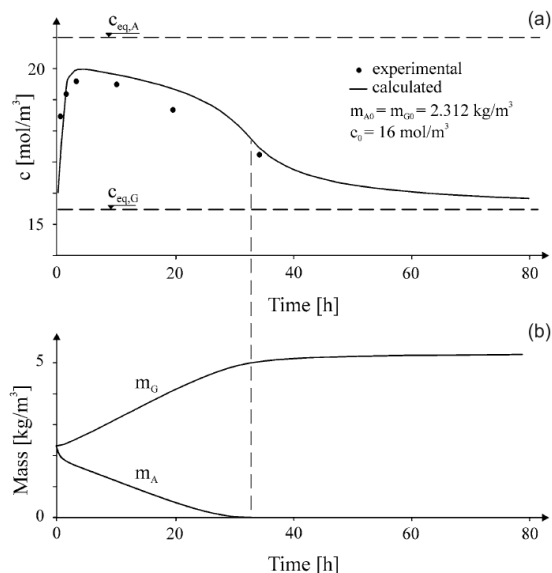


Figure 4.6 Predicted and measured time-development of, (a), ion concentration and, (b) anhydrite and gypsum mass during simultaneous anhydrite dissolution and gypsum.

4.4 Factors governing the time development of hydration

4.4.1 Introduction

The present Section investigates whether and under which conditions the transformation of anhydrite into gypsum is dissolution- or precipitation-controlled.

In tackling these questions, it is advantageous to formulate the governing equations in terms of the volume fractions of anhydrite and gypsum, instead of s_A and s_G . From Eqs. (4.4), (4.6) and (4.7) we obtain:

$$\frac{d\phi_A}{d\tau} = -\frac{\phi_A F_A}{\phi_{A0} F_{A0}} (1-\tilde{c})^{\delta_A}, \quad \frac{d\phi_G}{d\tau} = \Lambda \frac{\phi_P F_P}{\phi_S F_S} \left(\frac{\tilde{c}}{\tilde{c}_{eq,G}} - 1 \right)^{\delta_G}, \quad (4.27)$$

where the dimensionless parameter

$$\Lambda = \frac{k_G F_S \phi_S \rho_A}{k_A F_{A0} \phi_{A0} \rho_G} \quad (4.28)$$

expresses how quickly gypsum precipitation occurs relative to anhydrite dissolution (*i.e.* it provides a measure of the relative speed of the two processes), while the dimensionless time is:

$$\tau = t \frac{k_A F_{A0}}{\rho_A} \phi_{A0}. \quad (4.29)$$

The symbols ϕ_P and F_P denote the volume fraction and the specific surface area of the particles that are available for gypsum precipitation (an inert mineral on which gypsum may form). At $t = 0$, ϕ_P and F_P are equal to the volume fraction ϕ_S and to the specific surface F_S of the inert particles, respectively. In general, F_A and F_P change with time and are related to ϕ_A and ϕ_P in a more or less complex way, depending on the shape of the particles. For spherical particles Eqs. (4.27) become:

$$\frac{d\phi_A}{d\tau} = -\left(\frac{\phi_A}{\phi_{A0}} \right)^{2/3} (1-\tilde{c})^{\delta_A}, \quad \frac{d\phi_G}{d\tau} = \Lambda \left(1 + \frac{\phi_G}{\phi_S} \right)^{2/3} \left(\frac{\tilde{c}}{\tilde{c}_{eq,G}} - 1 \right)^{\delta_G}. \quad (4.30)$$

Equations (4.30), with the concentration \tilde{c} according to Eq. (4.23), represent a system of two non-linear ordinary differential equations for the evolution of the volume fractions of anhydrite and gypsum over time. The solution of this system can be expressed as follows:

$$\phi_A, \phi_G, \phi_W, \frac{c}{c_{eq,A}} = f \left(\tau, \Lambda, \phi_{A0}, \phi_{W0}, \frac{c_0}{c_{eq,A}}, \frac{c_{eq,G}}{c_{eq,A}}, \frac{c_{eq,A}}{\rho_A}, \frac{\rho_G}{\rho_A}, \frac{\rho_G}{\rho_W} \right). \quad (4.31)$$

The equations of this section also apply to the case where gypsum growth occurs on gypsum particles that pre-exist in the system (the only difference being that ϕ_P , F_P , ϕ_S and F_S should be replaced by ϕ_G , F_G , ϕ_{G0} and F_{G0} , respectively).

4.4.2 Evolution over time

We consider mixtures consisting initially of anhydrite, inert minerals and distilled water ($c_0 = 0 \text{ mol/m}^3$). For simplicity, all particles are assumed to be spherical and therefore Eqs. (4.30) can be used. The last five parameters on the right side of Eq. (4.31) are material constants. The initial water content ϕ_{W0} is kept equal to 0.15. Therefore, the evolution of the hydration process over time (represented by the dimensionless time τ) is

governed only by the dimensionless parameter Λ and by the initial anhydrite fraction ϕ_{A0} (cf. Eq. 4.31).

During the hydration process, pore water may be consumed while anhydrite is still present in the system. Hydration of the entire anhydrite presupposes the presence of sufficient water or, for given water content, that the anhydrite content does not exceed a critical value. The following relationship gives the critical volume fraction of anhydrite:

$$\phi_{A0,crit} = \frac{136}{36} \frac{\rho_W}{\rho_A} \phi_{W0} \cong 1.276 \phi_{W0}. \quad (4.32)$$

For the assumed initial water content $\phi_{W0} = 0.15$, hydration will end prematurely if the anhydrite content exceeds $\phi_{A0,crit} = 0.19$.

Figures 4.7a and 4.7b show the ion concentration and the anhydrite volume fraction, respectively, over the dimensionless time τ , for $\Lambda = 1$ and an initial anhydrite content ϕ_{A0} of 7.7%, 14.2%, 28.3% or 42.5%. In the last two cases, hydration remains incomplete due to consumption of the whole amount of water. It is interesting that the maximum concentration attained during the process does not depend on the initial anhydrite fraction (all curves in Fig. 4.7a reach the same maximum). As all ϕ_{A0} over τ curves exhibit about the same gradient (Fig. 4.7b), the initial anhydrite content ϕ_{A0} determines the time needed for the system to reach equilibrium: The duration of the process increases practically linearly with ϕ_{A0} .

The diagrams in Figs. 4.7c and 4.7d show the time development of the concentration c and the volume fraction of anhydrite ϕ_A , respectively, for a fixed initial mixture composition. Every curve corresponds to another value of the dimensionless parameter Λ . This parameter expresses the speed of gypsum formation relative to anhydrite dissolution. At high values of Λ , gypsum crystals grow much quicker than anhydrite dissolves and, consequently, ion consumption (which is associated with gypsum formation) occurs rapidly relative to ion production by anhydrite dissolution. Therefore, the concentration cannot increase very much and remains slightly above the gypsum equilibrium concentration (see curve for $\Lambda = 10$ in Fig. 4.7c). On the other hand, for low values of Λ , the precipitation of gypsum and the consumption of ions occur relatively slowly. In this case, anhydrite dissolution causes a pronounced oversaturation with respect to gypsum (Fig. 4.7c). Therefore, it is evident that the value of the dimensionless parameter Λ determines the maximum value of the concentration c_{max} : The higher the parameter Λ , the lower the maximum oversaturation with respect to gypsum will be.

In conclusion, the anhydrite content determines the duration of the hydration process for a given value of Λ , while Λ determines whether the process is dissolution- or precipitation-controlled. Further investigations have shown that these results also remain valid for other mixtures, including dilute aqueous solutions (cf. [109]).

4.4.3 Limiting mechanism

As mentioned earlier, the maximum concentration c_{max} shows whether anhydrite dissolution or gypsum precipitation will determine the duration of the hydration process. If anhydrite dissolution represents the limiting mechanism, the concentration will be close to the gypsum equilibrium concentration. If, however, the process is governed by gypsum precipitation, the concentration will reach values closer to the anhydrite equilibrium concentration. As explained in Section 4.3, a steep increase in the concentration can be observed at the beginning of the process, where anhydrite dissolution alone takes place (Fig. 4.7a and 4.7c). The increasing concentration slows down the anhydrite dissolution and accelerates the gypsum growth with the consequence that the curve of concentration over time exhibits a maximum. Figure 4.7c indicates that the maximum concentration c_{max} depends solely on the dimensionless parameter Λ . This can also be shown in the governing equations. Considering the fact that the quantity of anhydrite that has to be dissolved in order for c_{max} to be reached is so low that $\phi_A = \phi_{A0}$, $F_A = F_{A0}$ and $\phi_G = 0$ can be

assumed in Eqs. (4.27), the condition $dc/dt = 0$ (which applies when $c = c_{max}$) leads to an equation for c_{max} , whose solution reads as follows:

$$c_{max} = c_{eq,G} \frac{\Lambda^* + 1}{\Lambda^* + c_{eq,G}/c_{eq,A}}, \text{ with } \Lambda^* = \sqrt{\frac{136 k_G F_S \phi_S}{172 k_A F_{A0} \phi_{A0}}}. \quad (4.33)$$

This equation confirms that the maximum concentration c_{max} that develops during the hydration process depends only on the dimensionless parameter Λ . Figure 4.8 shows the maximum concentration c_{max} as a function of Λ (the abscissa also contains the term $F_S \phi_S / F_{A0} \phi_{A0}$). It can be seen that for high Λ -values, *i.e.* for rapid gypsum precipitation, the c_{max} -values are only slightly higher than the gypsum equilibrium concentration $c_{eq,G}$. In this case, anhydrite dissolution constitutes the limiting mechanism. On the other hand, for very low values of Λ , the maximum concentration c_{max} approaches the anhydrite equilibrium concentration $c_{eq,A}$. In this case, gypsum precipitation is considerably slower than anhydrite dissolution, and it governs the time-development of the hydration process.

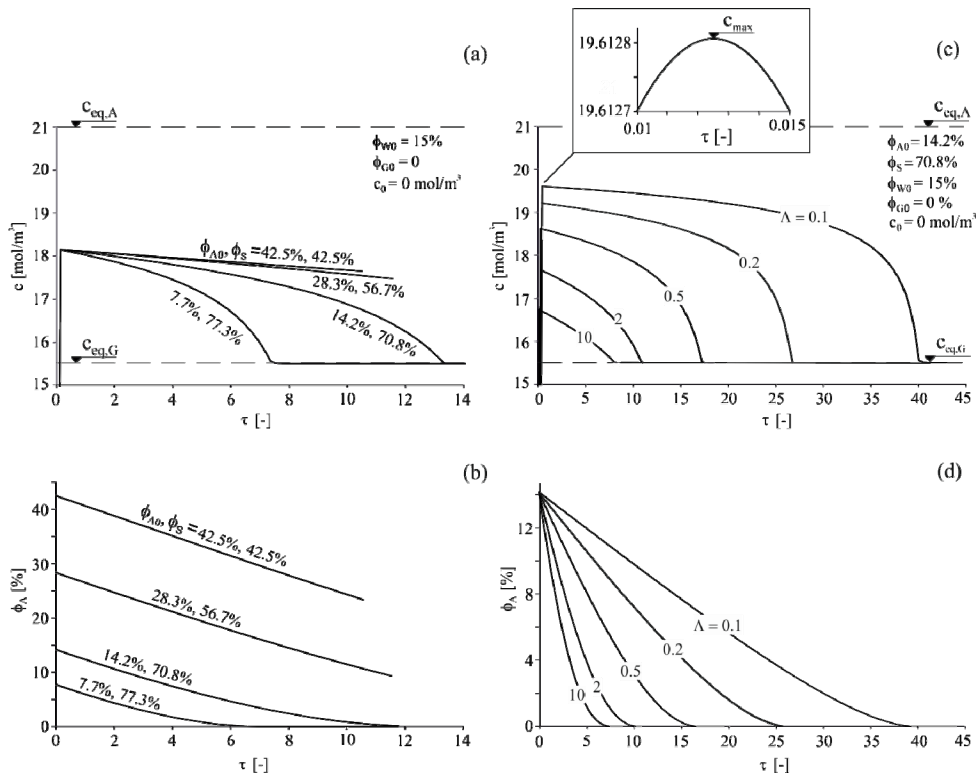


Figure 4.7 (a) Ion concentration c and, (b), volume fraction of anhydrite ϕ_A over dimensionless time τ for different initial anhydrite fractions ϕ_{A0} . (c) Ion concentration c and, (d), volume fraction of anhydrite ϕ_A over dimensionless time τ for different values of the dimensionless parameter Λ .

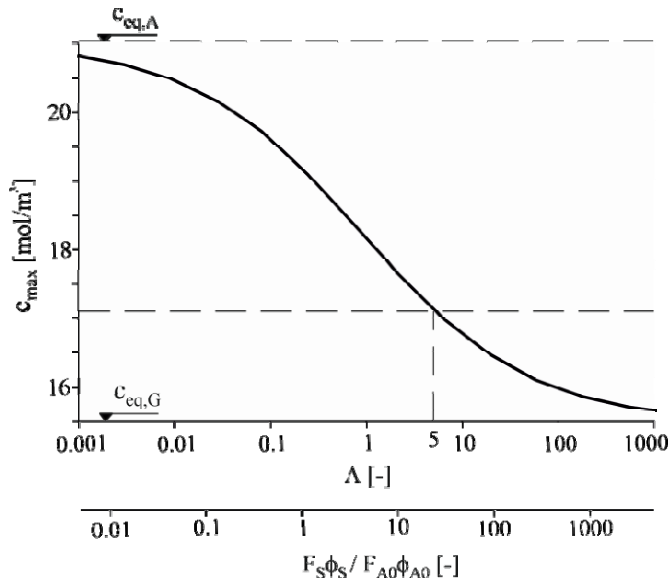


Figure 4.8 Maximum concentration c_{max} over dimensionless parameter Λ .

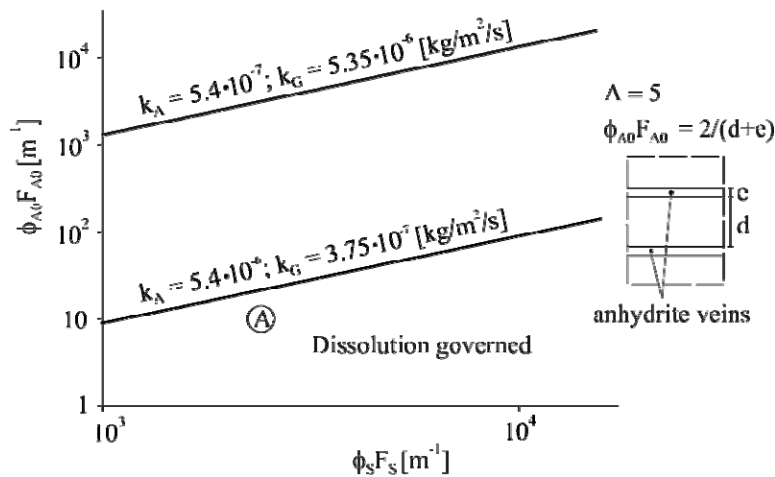


Figure 4.9 Surface area of anhydrite over surface area available for gypsum growth per unit volume of rock.

We assume that the process occurs close to gypsum equilibrium (*i.e.* its time development is controlled by the dissolution of anhydrite) when Λ is higher than about 5, where $c_{max} \approx 17 \text{ mol/m}^3$ (*cf.* Fig. 4.8). Taking the definition of Λ (Eq. 4.28) into account, this criterion leads to the following inequality:

$$F_{A0} \phi_{A0} < \frac{k_G \rho_A}{5 k_A \rho_G} F_S \phi_S. \tag{4.34}$$

Figure 4.9 illustrates this condition graphically. The two lines correspond to extreme combinations of the reaction rate constants for anhydrite dissolution and gypsum precipitation found in the literature (*cf.* Section 4.2.1). Points below the lower line clearly satisfy inequality (4.34), thus indicating conditions under which the dissolution of anhydrite constitutes the limiting mechanism. For points lying between the upper and the lower line, it is not possible to make a clear statement about the limiting mechanism due to the uncertainty related to the rate constants. According to Figure 4.9, anhydrite dissolution governs the overall process if the anhydrite surface area $\phi_{A0} F_{A0}$ amounts to a maximum of 10 – 100 m^2/m^3 of rock. This will be the case where anhydrite is in the form

of veins at least 10 mm thick, spaced about 200 mm apart, with the gypsum crystals growing on spherical particles with a maximum radius of 1 mm (point A in Fig. 4.9).

4.4.4 Duration of the hydration process

According to Figure 4.7b, after the very short initial period of rapidly increasing concentration, the volume fraction of anhydrite decreases at an approximately constant rate that does not depend on ϕ_S/ϕ_{A0} over a long period of time. This rate can be derived from Eq. (4.27), by substituting $\phi_A \approx \phi_{A0}$, $F_A = F_{A0}$ and $c \approx c_{max}$. Assuming the presence of a sufficient quantity of water (i.e. that $\phi_{A0} < \phi_{A0,crit}$), we obtain the following approximation for the hydration time:

$$t_h \cong \frac{\rho_A}{k_A F_{A0}} \left(\frac{c_{eq,A}}{c_{eq,A} - c_{eq,G}} \right)^2 \left(1 + \frac{c_{eq,G}/c_{eq,A}}{\Lambda^*} \right)^2. \quad (4.35)$$

Due to the slight curvature of the ϕ_A over τ curve, this equation gives the lower bound for hydration time. Figure 4.10 is based on Eq. (4.35) and shows the hydration time t_h as a function of the initial specific surface area F_{A0} of the anhydritic particles for different ratios of the initial surfaces areas $\phi_{A0}F_{A0}/\phi_S F_S$. Depending on the initial specific surface area of the anhydrite F_{A0} and on the available surface area for gypsum precipitation $\phi_S F_S$, hydration takes from a few hours to several years.

If the process is dissolution-controlled (i.e. for large Λ values), the last right side term of Eq. (4.35) becomes equal to 1. The hydration time is then inversely proportional to the specific surface of anhydrite F_{A0} and does not depend on its volume fraction ϕ_{A0} . This result emphasizes the importance of anhydrite distribution for the intensity of swelling. For the cases of practical interest where $\Lambda > 5$, the parameter values of Table 4.1 and anhydrite particle radii of 0.1 to 10 mm, Eq. (4.35) gives hydration times between 5 days and 18 months. This result does not take the sealing effect into account.

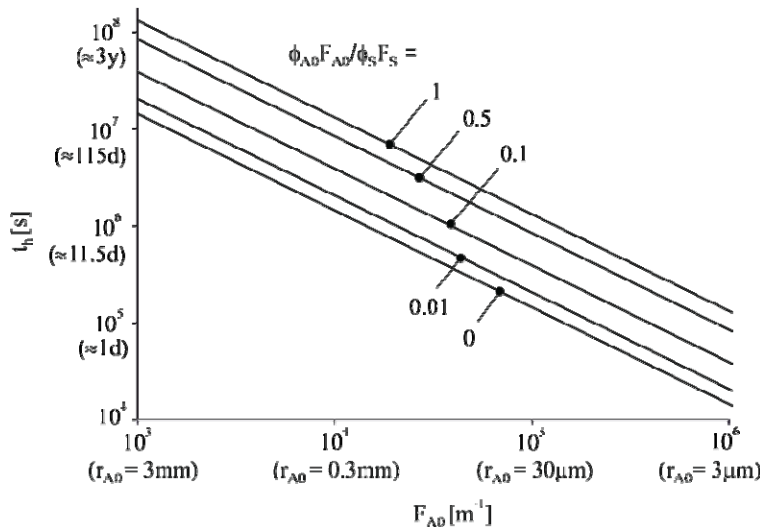


Figure 4.10 Hydration time t_h over initial specific surface area of anhydrite

4.5 The effect of sealing

As explained in Section 4.2.2, the kinetics of anhydrite dissolution in the presence of a gypsum coating will be governed by the slowest mechanisms of dissolution and diffusion under Eqs. (4.13) and (4.15), respectively. Figure 4.11 shows the retreat rate of the dissolution front as a function of the ion concentration c . Curve 5 is the second order dissolution equation (Eq. 4.13) for the values of Table 4.1. The straight lines 1 to 4 were calculated according to the diffusion equation (Eq. 4.15) for different porosities n_G and thicknesses s_G of the gypsum layer. The tortuosity and the diffusion coefficient for sulphate ions through a gypsum layer (Table 4.1) were taken from Böhm *et al.* [110] and Li and Gregory [111], respectively. Li and Gregory [111] give a range of $6 - 10 \cdot 10^{-10} \text{ m}^2/\text{s}$ for the diffusion coefficient at $T = 20 \text{ }^\circ\text{C}$.

The behaviour of the model can be explained by considering the example of a 2 mm thick gypsum layer with 10% porosity (line 2 of Fig. 4.11). For concentrations to the right of the intersection of line 2 with curve 5 (point A), dissolution (curve 5) constitutes the slowest mechanism and therefore governs the process. The transition from one mechanism to the other occurs when the two rates become equal (point A). For lower concentrations (to the left of point A), diffusion through the gypsum layer limits the dissolution rate (line 2).

The porosity n_G of the gypsum layer has a major effect as can be seen by comparing line 1 with line 4. The two lines apply to a 5 mm thick gypsum layer with a porosity n_G of 0.5 or 0.01. The denser gypsum layer controls dissolution over practically the entire concentration range (line 4). The porosity n_G is considered here as an independent parameter, but must depend essentially on the pressure conditions prevailing during growth. It will be larger or smaller depending on whether gypsum growth occurs freely or is constrained by the surrounding rock matrix. We do not investigate this aspect in detail, but note that the porosity n_G could be measured with the experimental technique of Neveux *et al.* [112], who investigated dissolution and precipitation processes in the deep burial diagenesis of carbonate reservoirs.

At the beginning of the dissolution process, the gypsum layer is still thin and its porosity is probably high, so that diffusion is not relevant in relation to the kinetics of anhydrite dissolution. Over time, the gypsum thickness s_G increases, with the result that the diffusion rate decreases and becomes the governing mechanism, particularly in the region of low supersaturation, *i.e.* at concentrations close to the gypsum equilibrium concentration $c_{\text{eq},G}$ which are characteristic for dissolution-controlled hydration.

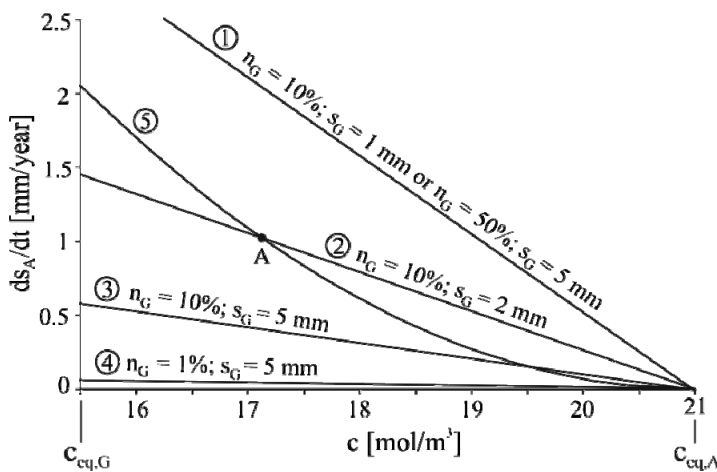


Figure 4.11 Retreat rate of the anhydrite dissolution front over concentration according to second order reaction kinetics (curve 5) and the diffusion equation (lines 1 to 4.).

Figure 4.12a shows how the hydration of an anhydrite layer that is initially 100 mm thick proceeds over time, assuming that gypsum crystals grow only on anhydrite and form a layer of thickness s_G . The two solid curves show the location of the gypsum – anhydrite interface (curve " $S_{A'}/2$ ") and the gypsum surface (curve " $S_{G,A'}/2$ ") according to the standard second order anhydrite dissolution and gypsum precipitation equations, *i.e.* disregarding the sealing effect of the gypsum layer on anhydrite dissolution. The distance of the two curves corresponds to the thickness s_G of the gypsum layer. It can be seen that the anhydrite core shrinks, but the total thickness of the layer increases by about 60% due to the higher molar volume of gypsum.

The dashed curves incorporate the effect of sealing, *i.e.* they assume that the retreat rate of the dissolution front is given by Eq. (4.15) if it yields a lower value than Eq. (4.13). It can be seen that sealing delays hydration by more than one order of magnitude. However, this result is true only for thick anhydrite layers. Figure 4.12b is obtained for a 1 mm thick anhydrite vein and shows that sealing is irrelevant for this particular case. For thick anhydrite layers, sealing plays a prominent role, because only a very small percentage of the anhydrite will have hydrated by the time the gypsum thickness reaches the critical value above which diffusion retards dissolution. This actually happens so rapidly that diffusion can be regarded as the governing mechanism for almost the entire hydration process. On the other hand, for finely distributed anhydrite (Fig. 4.12b), most of the anhydrite will already have dissolved before the gypsum layer reaches the critical thickness (time t_d). Therefore, the effect of sealing is almost negligible.

Figure 4.13 shows the reduction in the volume fraction of layered anhydrite over time for different gypsum porosities n_G and anhydrite layer thicknesses S_{A0} , assuming that gypsum growth takes place both on the anhydrite layers and on other spherical particles of inert minerals. The initial volume fractions of anhydrite and inert minerals are $\phi_{A0} = 0.2$ and $\phi_S = 0.5$, respectively. Under these conditions, the quantity of water available is sufficient for hydration of the entire quantity of anhydrite (*cf.* Eq. 4.32). Lines 3 to 6 apply to a 100 mm thick anhydrite layer. Line 3 disregards the effect of sealing, while lines 4, 5 and 6 take sealing into account and apply to layer porosities of 0.5, 0.1 and 0.01, respectively. In the absence of sealing, total hydration of the anhydrite would take approximately 38 years. Sealing increases the hydration time to 57 years if the gypsum layer has a porosity of $n_G = 0.5$, and to 147 years for a porosity of $n_G = 0.1$. At lower porosities, hydration would be practically irrelevant for tunnelling because it would take several centuries.

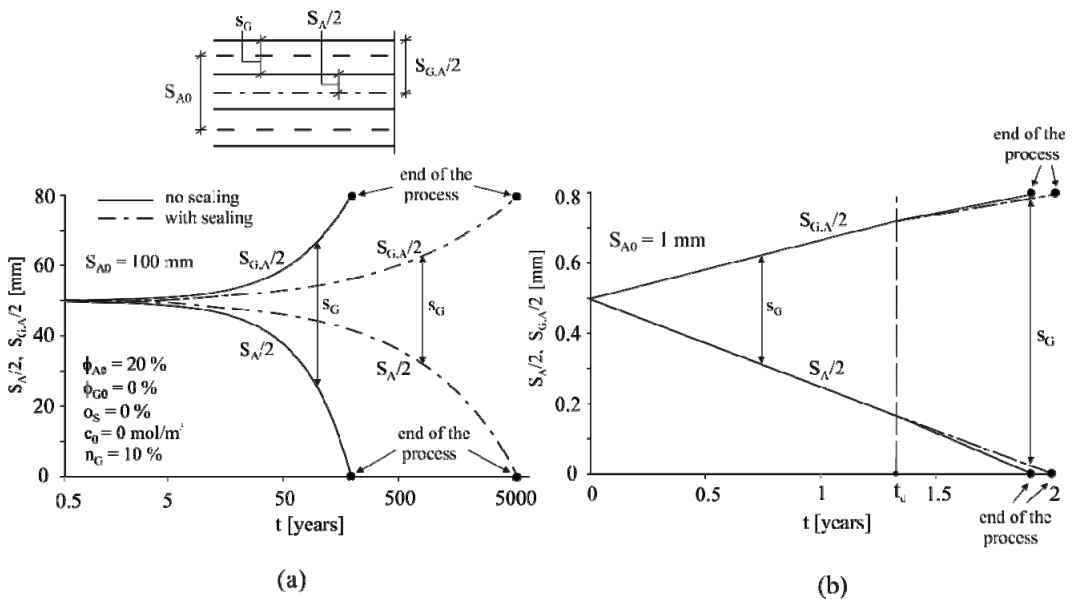


Figure 4.12 Thickness of anhydrite and gypsum layer over time t , (a), for a $S_{A0} = 100$ mm thick anhydrite layer and, (b), for a $S_{A0} = 1$ mm thick layer with sealing taken into account (dashed lines) and not taken into account (solid curves).

Line 1 in Figure 4.13 corresponds to the case of finely distributed anhydrite ($S_{A0} = 1$ mm). For gypsum layer porosities n_G of 0.1 or more, sealing does not affect the hydration duration. However, for a very low porosity ($n_G = 0.01$, line 2), the hydration time amounts to more than 5 years, *i.e.* three times more than without sealing (line 1). To summarise, sealing is important for thick anhydrite layers. In the case of finely distributed anhydrite, sealing plays a role only if the formed gypsum is very dense.

Finally, Figure 4.14 shows the total hydration time t_h as a function of the initial anhydrite layer thickness for different gypsum porosities n_G , with and without anhydrite sealing being taken into account. In this case as well, gypsum grows both on the layers of anhydrite and on spherical particles of inert minerals. Figure 4.14 once more illustrates the importance of gypsum porosity and particle size for the sealing effect and thus for the time evolution of the hydration process.

The modelling results agree with (and provide an explanation for) the general observation made in tunnelling that thicker anhydrite veins and layers do not swell (*cf.* Section 4.2.2).

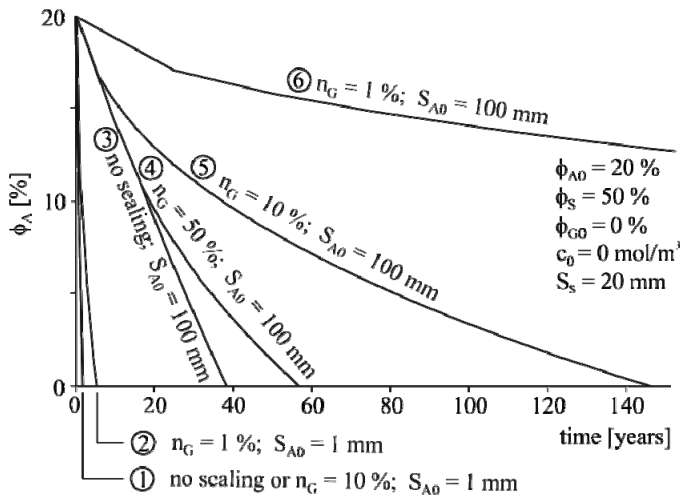


Figure 4.13 Volume fraction of anhydrite over time for different anhydrite layer thicknesses and gypsum layer porosities.

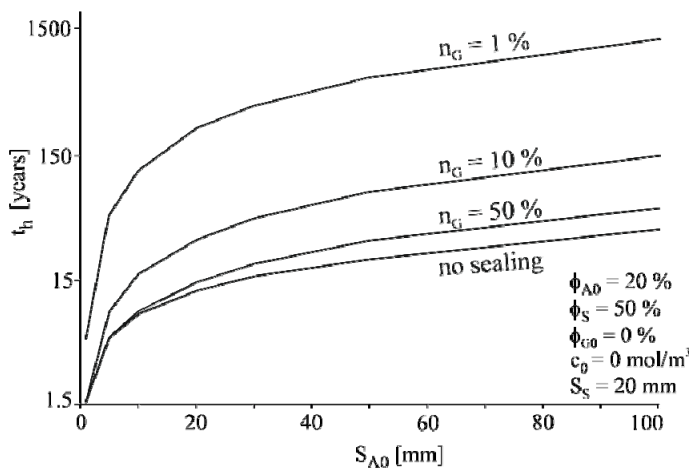


Figure 4.14 Hydration time of an anhydrite layer as a function of its initial thickness.

4.6 Conclusions

A model has been developed for the simultaneous dissolution of anhydrite and precipitation of gypsum in a closed system. The model accounts for the sealing effect caused by the precipitation of gypsum onto the anhydrite mineral. The model predictions agree well with experimental results. According to the computational results anhydrite dissolution (rather than gypsum precipitation) is the limiting mechanism if anhydrite occurs in the form of larger particles or thicker veins (> 1 mm) and there are sufficient nuclei for gypsum growth (e.g. precipitation takes place on the surfaces of inert minerals). It has also been shown that the time required for the whole amount of anhydrite to hydrate may vary by orders of magnitude. Moreover, for systems where dissolution is the governing mechanism, the initial volume fraction of anhydrite does not play any role in terms of the hydration time.

Sealing has been shown to be decisive for the time evolution of the hydration process where gypsum with low porosity precipitates on thick layers of anhydrite. Depending on the gypsum porosity and the thickness of the anhydrite layers, the hydration time of anhydrite may increase by many orders of magnitude and far exceed the usual service life of tunnels (100 years). The quantitative results provide a theoretical explanation for the well-known observation that anhydrite layers of at least a few cm thick hardly swell at all.

As flow of water to the anhydrite surface may be hindered (either by pores becoming clogged due to the precipitation of gypsum, or by the existence of a clay matrix that tends to absorb water), the actual hydration times may be considerably higher. Transport processes and interaction between the anhydrite and the clay matrix are probably important in this respect.

5 On the role of transport processes

5.1 Introduction

In a closed system, *i.e.* a system where water and ions cannot flow in or out, anhydrite is the only supplier of ions. In addition, anhydrite can only be consumed by the precipitation of gypsum. Consequently, the transformation of anhydrite into gypsum can be considered practically as a topochemical reaction (see Section 4). In an open system, however, the ions may circulate by advection (with the pore water) and, in the presence of ionic concentration gradients, also by diffusion. Anhydrite dissolution and gypsum precipitation are in general coupled with transport. This raises the question as to whether and under what conditions advection or diffusion are relevant in relation to the time-dependent processes of sulphate dissolution or precipitation. Identifying the conditions under which transport might play a role is valuable for the formulation of manageable continuum-mechanical models (*i.e.* models that are not unnecessarily overloaded with irrelevant coupled processes), for planning the respective validation experiments and for conducting meaningful laboratory tests and interpreting their results correctly.

For example, in an oedometer swelling test, the ions produced by the dissolution of anhydrite can move by diffusion out of the oedometer if the container contains distilled water. On the other hand, if a saturated sulphate solution is used in the swelling test, then ions would be supplied to the rock specimen by advection and possibly also by diffusion. It is therefore obvious that quantifying the role of transport is important for the interpretation of the test results.

As another practical example illustrating the potential role of advective transport, *in situ* conditions may be considered where seepage flow occurs either from the rock towards the tunnel or vice versa (*cf.* [113], [114]). Depending on the seepage flow velocity relative to the rate of the chemical dissolution and precipitation reactions, it is at least theoretically possible that the flowing water transports the anhydrite dissolution products away before gypsum precipitates. In this case, seepage flow would decrease the calcium and sulphate content in a zone of the rock mass and increase the ion concentration in another zone, thus leading to rock leaching in the first zone and gypsum formation in the second zone – even if the latter did not initially contain anhydrite. Such phenomena have in fact been observed in the field, *e.g.* in the Schanz Tunnel [115]. The invert of this tunnel experienced an average yearly heave of 1.6 cm in the period 1880 - 1972, *i.e.* a cumulative heave of 1.50 m [116]. Mineralogical investigations in 1990 (110 years after construction of the tunnel) showed, however, that the rock contained no sulphate up to a depth of 3 m beneath the tunnel floor. Beneath this zone, the rock contained both gypsum and anhydrite. The anhydrite percentage increased with depth; at depths greater than about 10 m beneath the tunnel the sulphate was present only as anhydrite. The fact that the zone with the largest swelling deformations was gypsum-free is surprising at first sight, but it shows that advective transport may indeed be important.

The velocity of the seepage flow depends on rock permeability as well as on the hydraulic boundary conditions at the far field and at the tunnel boundary. The hydraulic boundary conditions also determine the extent of the water table drawdown as well as the potential development of an unsaturated zone ([113], [114]). The latter may be important for the swelling process, since a reduction in the saturation degree may lead to local supersaturation and, therefore, to gypsum growth (*cf.* [36]).

The present section analyses simple one-dimensional systems in order to investigate the conditions under which the seepage flow rate or the diffusion rate are so high (relatively to the rate of the chemical reactions) that these transport processes must be taken into account in continuum-mechanical modelling and in the planning and interpretation of laboratory tests. The question under investigation can also be formulated inversely: What are the conditions under which it is possible to ignore transport and consider swelling as a purely chemo-mechanical process?

Other potentially relevant effects, such as the subsequent leaching of the formed gypsum (as in the Schanz Tunnel), evaporation of pore water and development of an unsaturated zone, will not be investigated. Furthermore, since a full chemo-mechanical coupling is not essential for the questions under investigation, only the simplified case of a constrained system is considered (*i.e.* zero volumetric strain, as under the conditions prevailing in oedometer swelling pressure tests).

Section 5.2 formulates the governing equations for the advection-diffusion problem in the presence of dissolution and precipitation (the “HC model”), taking account of the kinetic properties in accordance with Section 4 but without considering the effect of sealing. The latter is significant only for thicker anhydrite veins (Section 4.6).

Section 5.3 investigates whether diffusion may cause a significant loss of sulphate in oedometer swelling tests performed with distilled water. Section 5.3.2 describes the problem layout and presents the overall model behaviour. The effect of diffusion is quantified by introducing a so-called “*leaching coefficient*”, which is by definition equal to the fraction of the sulphate that moves out of the system (Section 5.3.3). The *LC* is obviously equal to 0 in the case of a closed system and constitutes a measure of the difference between the behaviour of an open system (with diffusion) and that of a closed system. A high *LC*-value means that the influence of diffusion is significant. The computations of Section 5.3 were carried-out without considering the seepage flow of the distilled water towards the specimen. They showed that diffusion is relevant only in very exceptional cases. As the effect of diffusion would be even smaller in the presence of advection, it was not necessary to perform a coupled advection-diffusion analysis.

Section 5.4 investigates the seepage flow rates for which advection significantly interferes with the anhydrite dissolution and gypsum precipitation process. Based on the results of Section 5.3, according to which diffusion is not significant, only advective flow is considered. Its effect is quantified, as in Section 5.3, by means of the *LC*.

5.2 Governing equations of the advection-diffusion model

5.2.1 Mass balance and geometric equations

We consider a system consisting of a solid phase and a liquid phase under isothermal conditions. In the most general case the constituents of the solid phase are anhydrite (subscript *A*), gypsum (subscript *G*), and inert minerals, *i.e.* minerals that do not participate in the chemical reactions (*e.g.* dolomite). The liquid phase contains water (subscript *W*), as well as calcium and sulphate ions (subscript *I*). The chemical reactions and the masses involved are given by Eqs. (3.2) and (3.1) for anhydrite and gypsum, respectively. In the forthcoming equations, these two chemical reactions will be denoted by the subscripts “*R1*” and “*R2*”.

In the most general case of an open system, mass changes in respect of the ions, water, anhydrite and gypsum may take place due to chemical reactions (dissolution and precipitation of anhydrite or gypsum), diffusion or advection (seepage flow). The general equation for the mass change rate of the *i*-th constituent reads as follows (the dot notation is applied hereinafter for time derivatives):

$$\dot{m}_i = \dot{m}_{i,R1} + \dot{m}_{i,R2} + \dot{m}_{i,dif} + \dot{m}_{i,adv}, \quad (5.1)$$

where the subscripts “*R1*”, “*R2*”, “*dif*” and “*adv*” denote the mass change rates due to anhydrite dissolution or precipitation, gypsum dissolution or precipitation, diffusion and advection, respectively. Subsequently, Eq. (5.1) will be applied to the different constituents of the system.

The mass change of the solid phase (anhydrite and gypsum) is due to dissolution and precipitation only. The anhydrite and gypsum mass change rates read as follows:

$$\dot{m}_A = \dot{m}_{A,R1} = -\dot{m}_{I,R1}, \quad (5.2)$$

$$\dot{m}_G = \dot{m}_{G,R2} = -\dot{m}_{I,R2} - \dot{m}_{W,R2}. \quad (5.3)$$

On account of the stoichiometry of gypsum precipitation (Eq. 3.1) the following equations apply:

$$\dot{m}_{I,R2} = -\frac{136.14}{172.14} \cdot \dot{m}_G \quad (5.4)$$

and

$$\dot{m}_{W,R2} = -\frac{36}{172.14} \cdot \dot{m}_G. \quad (5.5)$$

For the ion mass change rate all components of Eq. (5.1) must be taken into account:

$$\dot{m}_I = \dot{m}_{I,R1} + \dot{m}_{I,R2} + \dot{m}_{I,adv} + \dot{m}_{I,dif}. \quad (5.6)$$

Additionally, taking $c_{Ca^{2+}} = c_{SO_4^{2-}} = c$ and considering a saturated porous medium, the ion mass depends on the concentration c (defined as ion mass M_I per water volume V_W) according to:

$$m_I = \frac{M_I}{V_{tot,0}} = \frac{M_I}{V_W} \cdot \frac{V_W}{V_{tot,0}} = \frac{M_I}{V_W} \cdot \frac{V_P}{V_{tot,0}} = c \cdot \phi. \quad (5.7)$$

where ϕ is the porosity, defined as the pore volume V_P per unit of total volume.

The mass of water may change due to advection (seepage flow), gypsum growth or dissolution:

$$\dot{m}_W = \dot{m}_{W,R2} + \dot{m}_{W,adv}. \quad (5.8)$$

Moreover, the water mass per unit rock volume is related to the porosity ϕ according to:

$$m_W = \frac{M_W}{V_{tot,0}} = \frac{\rho_W \cdot V_W}{V_{tot,0}} = \frac{\rho_W \cdot V_P}{V_{tot,0}} = \rho_W \cdot \phi. \quad (5.9)$$

Differentiating Eq. (5.9) with respect to time gives:

$$\dot{m}_W = \rho_W \dot{\phi} + \phi \dot{\rho}_W. \quad (5.10)$$

Taking the water compressibility c_W into account leads to the following relationship for the water mass balance:

$$\frac{\dot{m}_W}{\rho_W} = \dot{\phi} + \gamma_W \cdot \phi \cdot c_W \cdot \dot{h}, \quad (5.11)$$

where γ_W is the unit weight of the water and h the hydraulic head.

Under the condition of zero volumetric strain, the porosity changes only due to the chemical reactions, *i.e.* at the following rate:

$$\dot{\phi} = -\frac{\dot{m}_A}{\rho_A} - \frac{\dot{m}_G}{\rho_G}. \quad (5.12)$$

5.2.2 Transport

Advection is described by Darcy's law

$$q_x = -K \frac{\partial h}{\partial x}, \quad (5.13)$$

where q_x is the seepage flow velocity, $h = z + p/(\rho_W g)$ denotes the hydraulic head, p the pore pressure, ρ_W the density of water, g the gravitational acceleration ($\approx 10 \text{ m/s}^2$), z the geodetic head and K the hydraulic conductivity. The latter depends in general on the porosity and on the pore structure, as well as on the occurrence of fractures, which either pre-exist in the rock or may be induced by swelling. Sulphate leaching increases porosity and thus also permeability, while gypsum growth may either increase permeability (by opening up fractures) or decrease it (by clogging up pores). These effects are not taken into account in the present report.

Due to advective flux (Eqs. 5.6 and 5.8), the masses of water and ions change at the following rates:

$$\dot{m}_{W,adv} = -\rho_W \partial_k q_k, \quad \dot{m}_{I,adv} = -\partial_k (c q_k). \quad (5.14)$$

The diffusive mass flux in a porous medium is given by Fick's law which reads, in its general form, as follows:

$$J_k^{dif} = -\phi \cdot T_k^* \cdot D \cdot \partial_k c, \quad (5.15)$$

where D is the molecular diffusion coefficient and T_k^* is the tortuosity of the porous medium. Typical tortuosity values for different media can be taken from Marsily [117] and Bear [118]. In the present case, we assume isotropic tortuosity and a value of $T^* = 0.1$. The mass change of the ions due to diffusive flux is then given in its general form by:

$$\dot{m}_{I,dif} = -\partial_k J_k^{dif}. \quad (5.16)$$

Equations (5.2), (5.4), (5.6) and (5.7) lead to the balance equation of the ions (advection-diffusion equation):

$$\frac{\partial(\phi c)}{\partial t} = -\frac{\partial}{\partial x} (c q_x) + \frac{\partial}{\partial x} \left(\phi T^* D \frac{\partial c}{\partial x} \right) - \dot{m}_A - \frac{136.14}{172.14} \dot{m}_G. \quad (5.17)$$

Furthermore, Eqs. (5.5), (5.8), (5.11), (5.12) and (5.14) result in the water balance equation:

$$\gamma_W \cdot \phi \cdot c_W \cdot \dot{h} = -\frac{36}{172.14} \frac{\dot{m}_G}{\rho_W} - \frac{\partial q_x}{\partial x} - \dot{\phi}. \quad (5.18)$$

The chemically-induced mass change rates of anhydrite and gypsum are given by Eqs. (4.9) and (4.11), neglecting the dependency of the dissolution rate on the flow velocity (*cf.* Section 4.2.1). This effect is irrelevant for the relatively slow flow velocities in natural rocks. As in Section 4, spherical mineral particles are considered. Furthermore, we assume that gypsum grows only on the surfaces of inert particles. As mentioned in Section 5.1, the sealing effect is not considered in the following investigation.

Equations (5.12), (5.13), (5.17), (5.18), (4.9) and (4.11) represent a system of 6 equations with 6 unknown parameters, which are functions of time and space: $m_G(x,t)$, $m_A(x,t)$, $\phi(x,t)$, $c(x,t)$, $q_x(x,t)$ and $h(x,t)$. For the solution of the system, a code has been developed in Mathematica 9 [119]. Depending on the specific findings in the following sections, some terms of the equations may vanish. Since we focus specifically on the effect of the

seepage flow rate (Section 5.1), the flow velocity q_x actually represents an independent input parameter for the questions under investigation.

The computational model presented above simplifies reality considerably since it does not consider a combination of effects such as variation of the hydraulic head and the seepage flow rate over time, the non-linearity imposed by porosity-dependent permeability, hydro-mechanical coupling (consolidation) or chemo-mechanical coupling (development of strains due to the dissolution or precipitation of the minerals). However, even this relatively simple model exhibits a highly complex and nonlinear behaviour; differences in the initial conditions result in completely different behavioural patterns regarding development over time and the spatial distribution of the field variables (*cf.* [8]). The inclusion of the above-mentioned effects (hydro-chemo-mechanical coupling, non-linearity of seepage flow *etc.*) in the mathematical model formulation and with arbitrary two- or three-dimensional systems is possible in principle, but would increase the complexity of the model behaviour even more. Therefore, it is valuable for future theoretical and experimental investigations to check the conditions under which diffusion and/or advection can be omitted. The next two sections deal with this question.

5.3 The role of diffusion in oedometer tests

5.3.1 Introduction

As mentioned in Section 5.1, it is at least theoretically possible that the ions produced by the dissolution of anhydrite within the rock specimen move out of the oedometer due to diffusion. The present section will show by means of numerical computations that the effect of ion diffusion out of the specimen can be neglected in most cases, even if the advective flow towards the specimen is slow. Taking the advective flow into account, the effect of diffusion would be even smaller, as the inflowing water would transport the ions towards the specimen, thus partially compensating for ion loss due to diffusive transport.

The ion concentration in the sample is governed by the combined effects of the anhydrite dissolution rate, the gypsum precipitation rate and the ion diffusion rate. If the diffusion is very slow relative to the chemical reactions, the anhydrite to gypsum transformation will proceed as a practically topochemical reaction (*i.e.* as in a closed system, Section 4). If, however, ion production and consumption by the chemical reactions is slow, the effect of diffusive transport may be significant. The lower the initial anhydrite content, the slower the ion production rate (Eq. 4.9) and the more pronounced the effect of diffusion will be. A small specific surface (or a large size) of the anhydrite particles will have the same effect, as it decelerates the dissolution process.

Section 5.3.2 outlines the model assumptions and discusses the general model behaviour. Section 5.3.3 investigates the conditions under which diffusion might play a role, based on the parametric study results.

5.3.2 Model description and behaviour

The computations are based upon the model in Section 5.2 without the advective terms. We consider a rock sample consisting of anhydrite, inert minerals and water which is immersed in a container with distilled water. The height of the rock sample is 30 mm while its diameter is not of interest, because ion diffusion occurs towards the filter plates of the oedometer, *i.e.* only in the axial direction. Taking the symmetry of the watering conditions into account (filter plates at both specimen ends), only a half of the specimen is modelled with the boundary conditions $\partial c / \partial t|_{x=0} = 0$ and $c(L, t) = 0$ at points A and B, respectively (Fig. 5.1). The boundaries A and B correspond to the mid-plane of the specimen and to its drained end, respectively. We assume, furthermore, that the pore water is initially ion-free ($c(x, 0) = 0$).

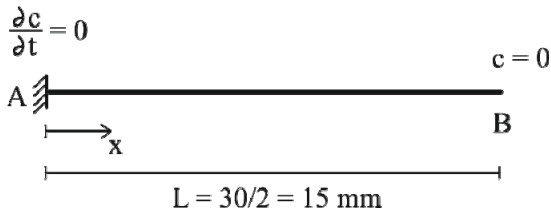


Figure 5.1 System and boundary conditions.

In order to get an idea of the evolution of the different field variables over time, a specific example is presented, addressing a mixture of low anhydrite content ($\phi_{A0} = 0.1$, $\phi_S = 0.8$ and $\phi_{W0} = 0.1$). Figure 5.2a shows the spatial distribution of the ion concentration at different times assuming rather large anhydrite particles ($r_{A0} = 1$ mm) and inert particles of radius $r_S = 0.1$ mm. (According to Section 4.2.1 the size of the anhydrite particles may generally vary from some μm to a few cm. The effect of this parameter will be investigated in the next section.) As anhydrite starts to dissolve, the concentration increases uniformly over the entire specimen, apart from the zone close to the drained boundary B, where diffusive transport occurs due to the prescribed boundary condition $c = 0$. Once the mixture reaches the gypsum equilibrium concentration $c_{eq,G}$, gypsum starts to precipitate almost everywhere, *i.e.* with the exception of the zone close to boundary B where the mixture cannot reach equilibrium concentration $c_{eq,G}$ (Fig. 5.2b). In order to facilitate the comparisons, Figure 5.2b also shows (as a straight line) the final mass of gypsum in the case of a closed system, *i.e.* without diffusive transport. The ions produced by the anhydrite dissolution close to the drained boundary B diffuse to the distilled water with the consequence that the gypsum quantity is less than in a closed system. The faster the diffusion and the slower the anhydrite dissolution, the more extended the zone will be where gypsum does not precipitate at all.

As expected, the ion concentration close to the mid-plane of the specimen (point A) drops more slowly than close to the drained boundary (point B). The reason is that the diffusive flux in the middle part of the specimen is slow due to the low concentration gradient. Close to the drained boundary the anhydrite dissolution occurs more quickly than elsewhere (Fig. 5.2c) due to the higher driving force $(c_{eq,A} - c)/c_{eq,A}$; in this zone, however, the effect of diffusion dominates due to contact with the distilled water.

The system reaches equilibrium when the concentration becomes zero everywhere. In the case of higher anhydrite content, the process would stop as soon as the pores are filled with gypsum.

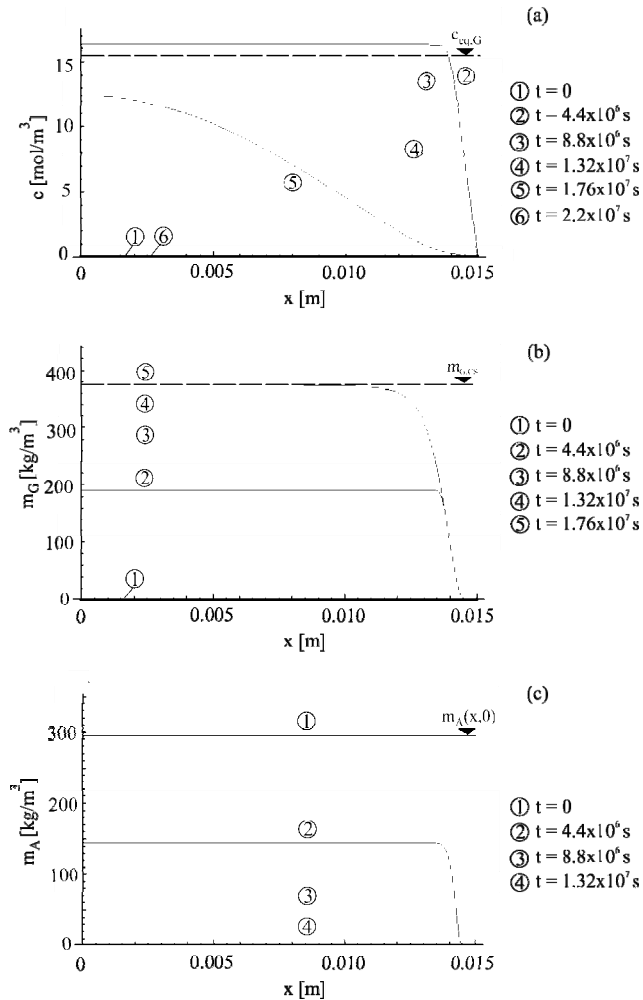


Figure 5.2 Spatial distribution of (a) ion concentration, (b) mass of gypsum and (c) mass of anhydrite, at different times.

5.3.3 Parametric study

The effect of diffusion (and of advection in Section 5.4) can be quantified by considering the leaching coefficient (LC), defined as follows:

$$LC = \frac{m_{A0} - \int_0^L \left[m_A(x) + m_l(x) + \frac{136}{172} m_G(x) \right] dx}{m_{A0}} \in [0,1], \quad (5.19)$$

where the integral denotes the mass of the calcium and sulphate within the system and m_{A0} is the initial mass of anhydrite. Figures 5.3a, b and c show the LC as a function of the anhydrite particle radius for different inert particle radii and initial anhydrite contents (volume fractions) ϕ_{A0} of 0.1, 0.2, and 0.4, respectively. The numerical simulations show that in the first case ($\phi_{A0} = 0.1$) the total amount of anhydrite dissolves, while in the other two cases ($\phi_{A0} = 0.2$ and 0.4) the process terminates sooner because the pores are filled with gypsum.

A high LC value means that the effect of diffusion is significant. Figures 5.3a-c show that this happens only under very specific conditions. The following conditions must be fulfilled cumulatively: low initial anhydrite content ($\phi_{A0} < 0.2$); large anhydrite particles ($r_{A0} > 1$ mm); small specific surface of the inert particles (which means that the surface area where gypsum precipitates is small).

In the interpretation of an oedometer swelling test, the possible effect of diffusion should be borne in mind. Significant diffusion (characterized by a high LC – value) would cause an underestimation of the swelling pressure or swelling strain by an amount which can be quantified either in comparative tests using sulphate-saturated water or computationally in a fully coupled HMC-model. The results of the present section indicate, however, that the diffusion effect can be neglected in most cases. The LC is less than 0.1, *i.e.* the error caused by neglecting the diffusive transport is less than 10 %, if the initial volume fraction of anhydrite is approximately greater than 0.2 and the anhydrite particles have a radius smaller than 1 mm. The error would be even smaller if advective transport towards the specimen was considered, as the inflow water would transport the ions to the specimen.

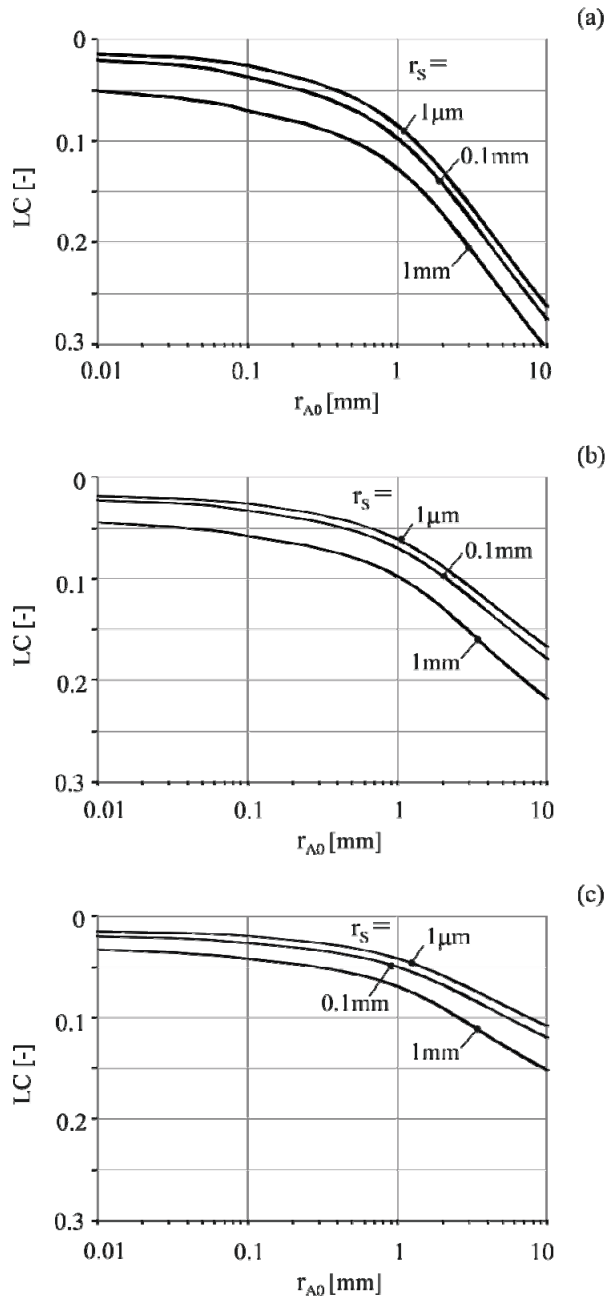


Figure 5.3 LC coefficient for (a) $\phi_{A0} = 0.1$, (b) $\phi_{A0} = 0.2$ and (c) $\phi_{A0} = 0.4$.

5.4 The role of advection

5.4.1 Problem layout

At the scale of a tunnel, it is at least theoretically possible that transport processes reduce the calcium and sulphate content in one mass region while increasing it in another region. In the first region, anhydrite leaching would take place, while in the second region gypsum would precipitate, even if this region was initially free of anhydrite (Fig. 5.4).

Figure 5.5 shows the considered one dimensional system and boundary conditions. More specifically, a zero ion concentration is prescribed at boundary A, while the ions can flow away at boundary B (Fig. 5.5). Furthermore, as the flow velocity is actually the independent input parameter and the process is steady with respect to seepage flow, a length of 1m and a hydraulic head gradient of unity are considered (*cf.* Section 5.2.2). The process of anhydrite dissolution and gypsum precipitation terminates either due to dissolution of all the anhydrite or due to the pores filling up with gypsum crystals in specific regions of the system. Since diffusive transport is relatively insignificant, the numerical examples in the present section are based upon the model in Section 5.2 without the diffusion terms.

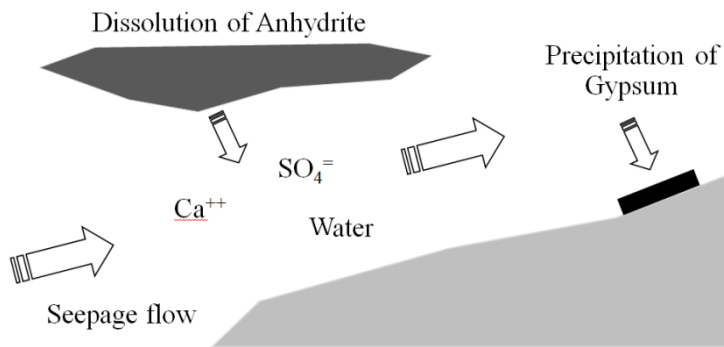


Figure 5.4 Anhydrite dissolution and gypsum precipitation in an anhydrite-free region.

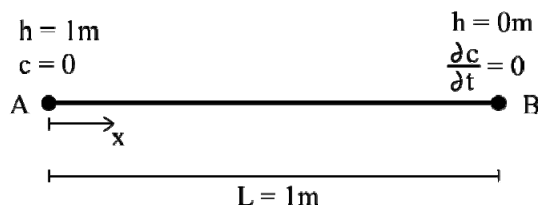


Figure 5.5 System and boundary conditions.

5.4.2 Parametric study

Figure 5.6 shows the LC as a function of the seepage flow velocity for different radii r_A of the anhydrite particles and $r_S = 1 \mu\text{m}$ for the inert minerals. This low value for the radius of the inert minerals indicates a high available specific surface area for the precipitation of gypsum and therefore a high precipitation rate. In the case of a low precipitation rate, the effect of advection would be more significant because the ions would stay longer in the solution and could thus be transported out of the system. Figures 5.6a, b and c have been calculated for initial anhydrite volume fractions of $\phi_{A0} = 0.1, 0.2$ and 0.4 , respectively. As expected, the leaching coefficient increases with increasing seepage flow velocity. Furthermore, the diagrams show that the larger the anhydrite particles are, the wider the range of seepage flow velocities where advection might play a role will be (LC is also less than 1 for lower velocities). The reason for this behaviour is the same as in Section 5.3: if the anhydrite particles are large (or if their specific surface is small), then

ion production will be slow and the mixture will take longer to reach gypsum equilibrium concentration (where precipitation would start to occur). Consequently, there is more time available for the flowing water to transport the ions out of the system. In the presence of larger particles, the effect of transport would be even more pronounced as they offer a smaller specific surface for precipitation.

In addition, according to Figure 5.6, the higher the initial anhydrite content, the lower the leaching coefficient and the smaller the effect of advection will be (other parameters being constant).

5.4.3 Discussion based on the results of Butscher *et al.* ([17], [18])

Finally, let us consider the actual seepage flow velocities in the Gypsum Keuper formation. Butscher *et al.* ([17], [18]) employed numerical simulations to investigate the hydrogeological conditions in the Gypsum Keuper formation before and after tunnel excavation. They found that tunnel excavation can increase flow rates by a factor of up to 30. Their study is very interesting for the question under investigation in the present section, particularly because it considered a series of hydrogeological models (homogeneous, hydrostratigraphic and aquifer-aquitard) with or without considering fault zones or a fractured zone around the tunnels. In the most extreme case (*i.e.* that of fractured zones), they determined high inflow rates of up to 623 l/m/d. For the diameter of the tunnel (11 m), the inflow rate of 623 l/m/d corresponds to a maximum seepage flow velocity of $q_x = 2 \cdot 10^{-7}$ m/s. This value is at the far left boundary of the diagrams in Figure 5.6, where advective transport has practically no effect on the dissolution and precipitation reactions. Therefore, even under the extreme assumptions behind an inflow value of 623 l/m/d, the effect of advective ionic transport can be neglected, which means that it is reasonable to consider the transformation of anhydrite to gypsum as a topochemical process. This result is very valuable for future research as it shows that continuum-mechanical formulations can be simplified.

5.5 Conclusions

A coupled HC model was formulated which takes account of anhydrite dissolution and gypsum crystal growth as well as advective and diffusive ion transport through a porous medium. We examined the role of diffusion in oedometer swelling tests and concluded that it is insignificant in most cases. Finally, the effect of advective transport was quantified in terms of the so-called leaching coefficient. The computational results indicate that for the low seepage flow velocities prevailing in the Gypsum Keuper formation, advective ion transport is rather insignificant. The leaching of anhydrite and precipitation of gypsum can occur in other locations only under the combination of a high flow velocity (greater than 10^{-5} m/s, *e.g.* in fracture zones), slowly dissolving large particles or veins of anhydrite and low initial anhydrite contents.

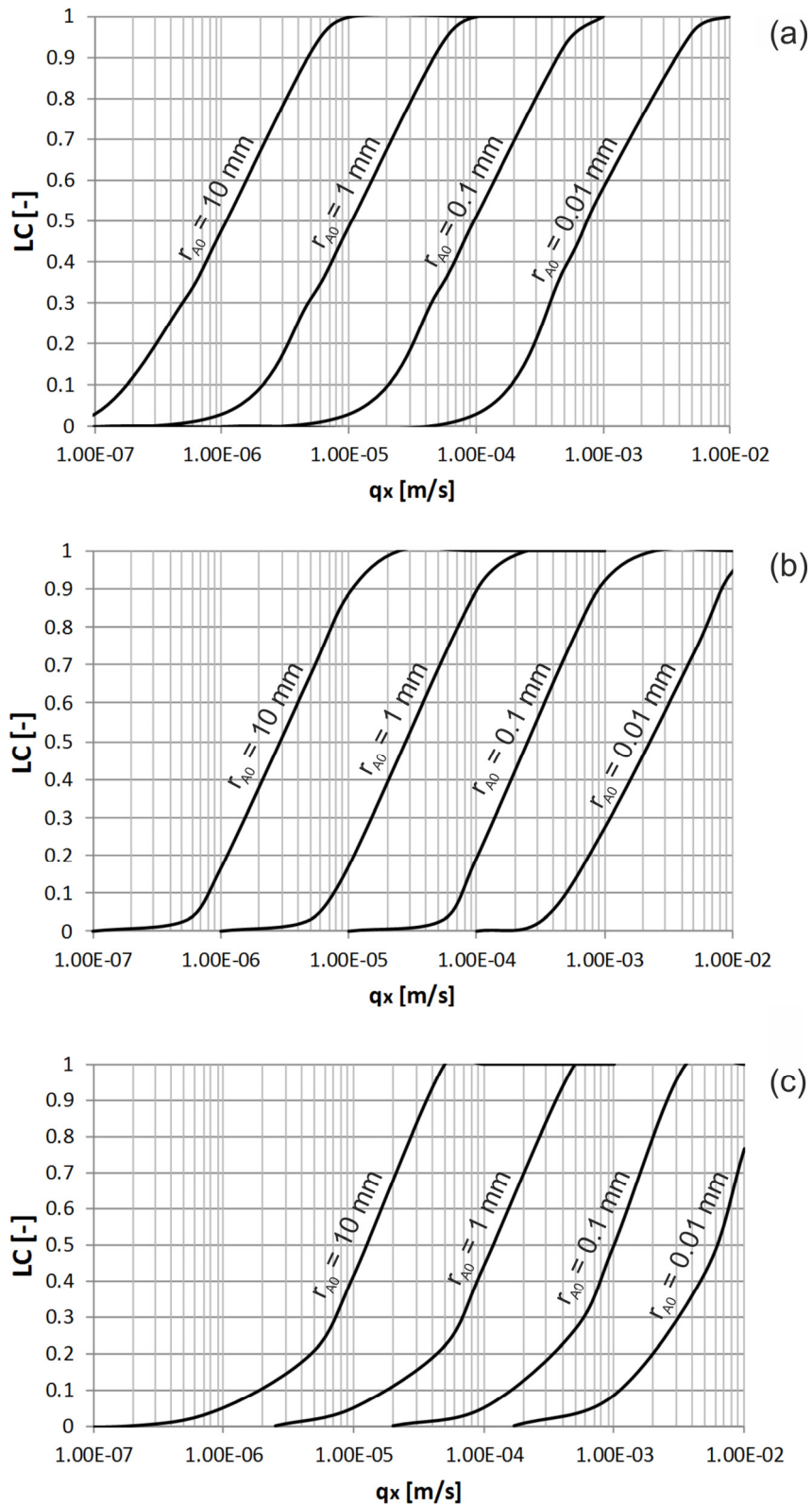


Figure 5.6 Leaching coefficient as a function of seepage flow velocity for (a) $\phi_{A0} = 0.1$, (b) $\phi_{A0} = 0.2$ and (c) $\phi_{A0} = 0.4$ ($r_s = 1 \mu m$).

6 Anhydrite in Gypsum Keuper at shallow depths

6.1 Introduction

The present section applies the fundamentals presented in Section 3 in order to analyse the initial conditions prevailing *in situ* in Gypsum Keuper before tunnelling. More specifically, the presence of calcium sulphate in the form of anhydrite is investigated, which, as will be shown, seems at first glance to be thermodynamically impossible. The following brief description of the geology of the Gypsum Keuper is based mainly on Amstad and Kovári [95].

The Gypsum Keuper consists of alternating sequences of sandstones, limestones, dolomites and claystones containing finely distributed anhydrite and gypsum. Swelling phenomena are observed only in the anhydritic claystones which are encountered in tunnelling at depths of mostly 50 – 150 m. The swelling is attributed to the combined effect of the anhydrite to gypsum transformation and to water uptake by expansive clay minerals such as corrensite, which are also present in Gypsum Keuper ([120], [121]).

The Gypsum Keuper in South-Western Germany (Baden-Württemberg) consists of three zones (Fig. 6.1a). In the leached Gypsum Keuper which lies above the so-called “*gypsum level*”, a large fraction of the sulphate has been dissolved and transported away. Therefore, the leached Gypsum Keuper consists of weathered rocks (marls and claystones) with gypsum residues, and these rocks are water-bearing and generally exhibit a high permeability. A transition zone separates the leached from the unleached Gypsum Keuper. Due to the low permeability of the transition zone, minor water flow is observed there ([122], [123], [124]). The “*anhydrite level*” represents the upper boundary of the zone, where the calcium sulphate is present in its anhydrous form. In this zone, the rock permeability is very low and the seepage flow practically non-existent. It is interesting to note that the gypsum level and the anhydrite level approximately follow the morphology of the surface (*cf. e.g.* the geological profile of the Wagenburg Tunnel in Figure 6.1b), exhibiting depressions beneath valleys or close to the tunnel portals (*cf., e.g.* [122], [123], [125], [126]).

In the Jura Mountains of Switzerland, the Gypsum Keuper is divided into the *Faltenjura* and the *Tafeljura* [121]. In the *Faltenjura*, the sedimentary gypsum had already been transformed into anhydrite before the beginning of the Jura folding [121]. However, in the course of this folding, anhydrite was partially able to transform into gypsum, as the anhydrite came into contact with water in the folded regions [121]. Gypsum is therefore expected to be present at greater depths in tectonically stressed rocks. In the *Tafeljura*, on the other hand, the structure of the rock mass is different due to the faults which created the so-called Gypsum Keuper blocks (Fig. 6.1c). At the boundaries of these blocks across the fault zones, the sulphatic rock was dissolved and subsequently transported away by the circulating water. Each Gypsum Keuper block in the *Tafeljura* is surrounded by a zone characterised by a variable degree of gypsification. Unlike the Gypsum Keuper formation of Baden Württemberg, the anhydrite- and gypsum-levels are not unique and do not follow the surface morphology very closely (Fig. 6.1d). These forms of Gypsum Keuper indicate the importance of water circulation for the gypsification process. The occurrence of anhydrite at the relatively small overburdens of Keuper tunnels is, however, surprising at first glance because one might expect gypsum rather than anhydrite to be the stable phase at the pressure and temperature conditions prevailing at these depths.

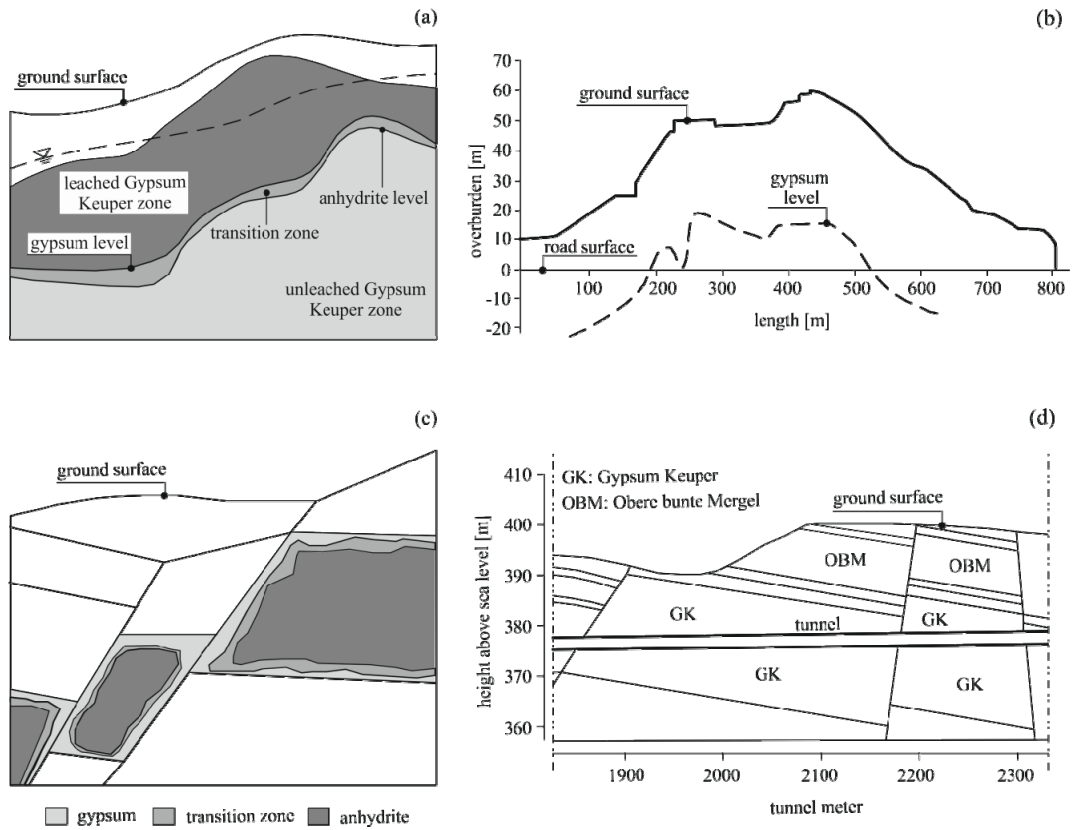


Figure 6.1 (a) Gypsum Keuper in Baden-Württemberg (after [95]) and, as an example, (b) geological profile of the Wagenburg Tunnel [122]; (c) typical rock mass model of the Gypsum Keuper in Tafeljura (after [95]) and, as an example, (d) geological profile of the Adler Tunnel [127].

More specifically, assuming that, (i) the solid-liquid interfacial effects are negligible (*cf.* Section 3.2.4), (ii) the pore water is thermodynamically free (*i.e.* the water activity $a_w = 1$), (iii) the solid pressures of anhydrite and gypsum are equal (*i.e.* $p_G = p_A$) and (iv) the solid pressures and the pore water pressure p_w increase linearly with the depth H (*cf.* Section 3.4.2), Eqs. (3.31) and (3.32) lead to the following linear relationship between the equilibrium temperature T_{eq} and the depth of cover H :

$$T_{eq} = T_0 + \frac{\Delta_{r,GA} G^0}{\Delta_{r,GA} S^0} + \frac{(V_G^0 - V_A^0) \gamma_r - 2V_W^0 \gamma_w}{\Delta_{r,GA} S^0} H, \quad (6.1)$$

where γ_r and γ_w denote the total unit weight of the rock and the unit weight of the water, respectively (taken as $\gamma_r = 25 \text{ kN/m}^3$ and $\gamma_w = 10 \text{ kN/m}^3$ in all following computations); T_0 is the standard temperature (25 °C); and the other symbols denote the common thermodynamic constants (see Table 3.1).

Figure 6.2 shows the anhydrite–gypsum equilibrium temperature as a function of the depth (solid straight line). By way of comparison, the diagram also shows the equilibrium temperature in the case of atmospheric pore pressure (dashed line, calculated by Eq. 6.1 without the γ_w - term). Gypsum represents the stable phase at temperatures below the equilibrium temperature (*i.e.* at points on the left side of the straight lines). Anhydrite is stable at higher temperatures, *i.e.* on the right side of the lines.

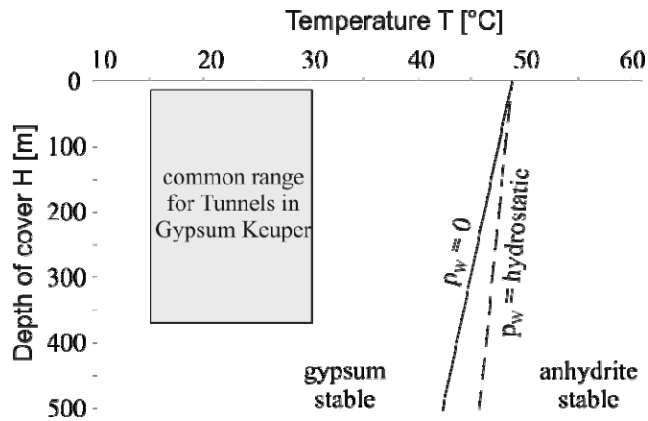


Figure 6.2 Anhydrite – gypsum equilibrium diagram (for $a_w = 1$, neglecting solid-liquid interfacial effects) and the range of values for tunnels in Gypsum Keuper.

Table 6.1 Depth of tunnels in Gypsum Keuper

Tunnel	minimum overburden in Gypsum Keuper [m]	maximum overburden in Gypsum Keuper [m]
Wagenburg Tunnel [126]	40	50
Schanz Tunnel [115]	20	90
Kappellesberg Tunnel [128]	30	80
Hauenstein Base-Tunnel [129]	270	300
Belchen Tunnel [22]	45	370
Chienberg Tunnel [17]	20	120
Engelberg Base-Tunnel [130]	40	85
Freudenstein Tunnel [131]	50	100
Adler Tunnel [127]	10	110
Bözberg Tunnel [132]	75	100
Mont Terri [133]	115	360
Lilla Tunnel [134]	20	115

The rectangle in Figure 6.2 indicates the relevant range for tunnels in Gypsum Keuper. The depth range is based on Table 6.1, which shows the minimum and maximum overburden of a number of tunnels crossing the Gypsum Keuper formation. The minimum overburden encountered is 10 m (Adler Tunnel), while the maximum overburden is 370 m in the case of the Belchen Tunnel. The data presented by Krause and Wurm [122] also show that Gypsum Keuper is encountered at a maximum depth of 280 m in tunnelling. The temperature range of 15 ° – 30 °C takes account of the relevant depth range and geothermal gradient in Switzerland, which is equal to about 30 ° – 40 °C/km [135].

The literature contains few works dealing with observations of anhydrite at shallow depths, and these mainly concern massive anhydrite beds. So, for example, Rolnick [136] discussed the findings from drill holes in evaporitic deposits in Nova Scotia and attributed the occurrence of anhydrite to chemical kinetics (extremely slow hydration of the anhydrite). In the following we focus on the literature dealing specifically with the case of finely distributed anhydrite. The latter is different from massive anhydrite considering that it offers a large specific surface to hydration.

Lippmann and Schüle [137] introduced the so-called “*corrensite-anhydrite theory*”, according to which the presence of anhydrite rather than gypsum in the rock provides an

indication as to the thermodynamic characteristics of corrensite (see also [120]). More specifically, corrensite cannot exist in its swollen, hydrated state, because this would imply the presence of free water, which would in turn lead to the gradual transformation of anhydrite into gypsum within a period of some years. The access of water (via the seepage flow which is triggered by tunnel excavation) has a twofold effect. It will cause both the swelling of corrensite and the transformation of anhydrite into gypsum. Since the latter is a rather slow process, the swelling of corrensite constitutes the main initial swelling mechanism and thus the main cause of heave of the tunnel invert in the early stages after tunnel excavation [137]. Fecker [138] provided support for the “*corrensite-anhydrite theory*” after performing *in situ* swelling tests in which the invert of an exploratory gallery (in the Wagenburg Tunnel near Stuttgart) was soaked with a saturated magnesium chloride solution. The dissolved magnesium chloride shifts the thermodynamic equilibrium in favour of anhydrite, *i.e.* it hinders the transformation of anhydrite to gypsum. Nevertheless, despite the suppression of the anhydrite transformation, considerable heave of the invert took place. According to Fecker [138] this can only be attributed to the swelling of corrensite, thus proving the validity of the theory.

An interesting alternative hypothesis was put forward by Wichter [139]. He proposed that gypsum growth starts from existing – and possibly very small – cavities, thereby compressing the surrounding rock and retarding or stopping the transformation process. The question therefore arises as to whether the stresses developing during growth might shift the equilibrium in favour of anhydrite, thus explaining the fact that anhydrite occurs at shallow depths.

Hauber *et al.* [140] also commented on the fact that anhydrite has been found at shallow depths during tunnel excavations in Gypsum Keuper. The point is made that, even assuming a high amount of dissolved salts in the circulating water (and thus low water activity, favouring thermodynamically stable anhydrite), the stability limit of anhydrite in terms of pressure and temperature is much higher than the actual values prevailing at the depths of the tunnels. Hauber *et al.* [140] concluded that anhydrite should therefore actually be unstable at shallow depths.

These studies, even though based upon qualitative considerations, provide useful indications as to the possible reasons for the occurrence of anhydrite at relatively shallow depths. The present section aims to close existing knowledge gaps by investigating a number of hypotheses on this phenomenon quantitatively.

One possible scenario is that gypsum is indeed the thermodynamically stable phase (as indicated by Fig. 6.2), but is not present *in situ* either because of a lack of water or because the hydration of anhydrite is an on-going process which proceeds extremely slowly in geological times. However, this scenario does not seem probable: On the one hand, anhydrite occurs in the form of veins or particles finely distributed in claystones, which may have a very low porosity (5-10%) but are nevertheless saturated. On the other hand, the hydration of finely distributed anhydrite (in contrast to that of massive anhydrite beds) occurs rapidly due to its large specific surface. It may take months or years (depending on the specific surface areas of the mineral particles) but certainly not geological times (*cf.* [22], [37], [141], [142], and also Section 5 of the present report).

For these reasons we focus here on the alternative scenario that anhydrite is the thermodynamically stable phase. This would mean that one or more of the simplifying assumptions behind the thermodynamic equilibrium diagram in Figure 6.2, which implies that gypsum rather than anhydrite is the stable form, cannot be true. Therefore, we examine which deviations from the assumptions of Figure 6.2 might explain why anhydrite is the stable phase. Specifically, we examine the assumptions concerning water activity, pore size and solid pressure, as a low water activity, small pore size and high solid pressure shift the thermodynamic equilibrium in favour of anhydrite (*cf.* Section 3). The underlying ideas are:

- The pore size may be extremely small (in the range of a few nm) with the consequence that solid-liquid interface effects become relevant, considerably increasing the chemical potential of gypsum.
- The growth of gypsum crystals may increase the stresses locally (in the close vicinity of the crystals) to values which are much higher than the ones corresponding to the overburden of the tunnels in Gypsum Keuper. (This hypothesis takes up Wichter's idea [139].)
- The activity of the pore water may be considerably lower than 1 due to its interactions with the clay minerals. (This hypothesis is very close to that of Lippmann and Schüle's [137], as it also focuses on the thermodynamic state of the water.)

These three hypotheses, herein referred to as the “*small pore hypothesis*”, the “*high pressure hypothesis*” and the “*low water activity hypothesis*”, will be examined in Sections 6.2, 6.3 and 6.4, respectively.

The investigations of the present section indicate that the third hypothesis is the most probable one. The results of this section, besides providing insight into an interesting observation, are also valuable for future research as they assist in the formulation of adequate initial conditions for continuum-mechanical models of the chemo-mechanical and transport processes in swelling anhydritic claystones.

6.2 The small pore hypothesis

6.2.1 Introduction

As explained in Section 3, small pores favour anhydrite as the stable phase, while large pores favour gypsum – all other conditions (pressure, temperature, water activity) being equal. This is due to the effect of surface energy, which is equivalent to that of a confining pressure. (The surface can be conceived of as a stretched membrane that encloses the crystal and exerts a confining pressure upon it.)

Consider, for instance, the solid line “a” in Figure 6.3 which has been calculated for the pressure and temperature conditions of the Belchen Tunnel (given in Section 6.2.3). It shows the gypsum equilibrium concentration as a function of the pore radius (computed from Eq. 3.19). With increasing pore radius, the surface energy and thus also the gypsum equilibrium concentration decrease. Additionally, the diagram shows the anhydrite equilibrium concentration for the same solid pressure and pore water pressure and temperature (line “b”, computed with Eq. 3.22). In pores with small radii r_p (hereafter referred to as “*subcritical pores*”), anhydrite exhibits a lower equilibrium concentration than gypsum and therefore represents the thermodynamically stable phase. In the pores with great radii r_p (hereafter referred to as “*supercritical pores*”), the opposite applies. The threshold pore size, *i.e.* the pore size where anhydrite and gypsum exhibit the same equilibrium concentration (intersection point “O” of the two lines), will be denoted from now on as the critical pore radius r_{cr} . It can be calculated according to Eq. (3.27), *i.e.* by setting the equilibrium concentrations of anhydrite and gypsum equal. Taking the radius of the gypsum particles equal to the pore radius ($r_G = r_p$) and considering that the solid-liquid interfacial effects are practically negligible for anhydrite and that anhydrite and gypsum are subject to the same stress ($p_G = p_A = p_{S,0}$), we obtain:

$$r_{cr} = \frac{2 \gamma_G V_G^0}{2RT \ln a_w + (T - T_0) \Delta_{r,GA} S^0 - \Delta_{r,GA} G^0 + 2p_W V_W^0 - p_{S,0} (V_G^0 - V_A^0)}, \quad (6.2)$$

where $p_{S,0}$ denotes the lithostatic pressure and the other parameters are already introduced in Section 3.

In the following sections we investigate whether the actual pore sizes of the anhydritic claystones of Gypsum Keuper are bigger or smaller than the critical pore radius.

6.2.2 Porosity and pore size distribution of anhydritic claystones

The porosity and the pore size distribution of natural rock samples were determined by means of mercury intrusion porosimetry (MIP) in the Clay Lab of our Institute [143] and in the EMPA [144].

The Gypsum Keuper samples were taken from the Belchen Tunnel and from the Chienberg Tunnel at depths of 200 m and 50-55 m, respectively. These tunnels are located in the Gypsum Keuper formation and have experienced serious damage due to swelling since or even during their excavation ([22], [145]). In total, four tests were conducted on samples from the Chienberg Tunnel (one by EMPA and three by the Clay Lab) and three tests on samples from the Belchen Tunnel (one by EMPA and two by the Clay Lab). Anhydritic claystones consist of different constituents and may be very heterogeneous in the scale of a specimen. In order to determine the pore size distribution of the claystone matrix, samples with a macroscopically high content of clay were selected. The mass of the samples was 1.6 to 5.1 gr.

Figure 6.4 shows the results of the seven MIP-tests. The abscissa depicts the pore radius r_p and the ordinate describes the pore percentage \bar{n} . (For example, a percentage of $\bar{n} = 20\%$ for a pore radius of 100 nm means that 20% of the total pore volume consists of pores with radius greater than 100 nm). According to Figure 6.4, the samples of the Belchen Tunnel (solid lines) have smaller pores than the samples from the Chienberg Tunnel (dashed lines). This can be attributed to the greater overburden of the Belchen Tunnel (200 vs. 50 m). Furthermore, the Chienberg Tunnel crosses the so-called Tafeljura, while the rock in the Belchen Tunnel belongs to the intensively folded part of the Jura Mountains (the so-called Faltenjura), where high tectonic stresses may have caused additional compaction [146].

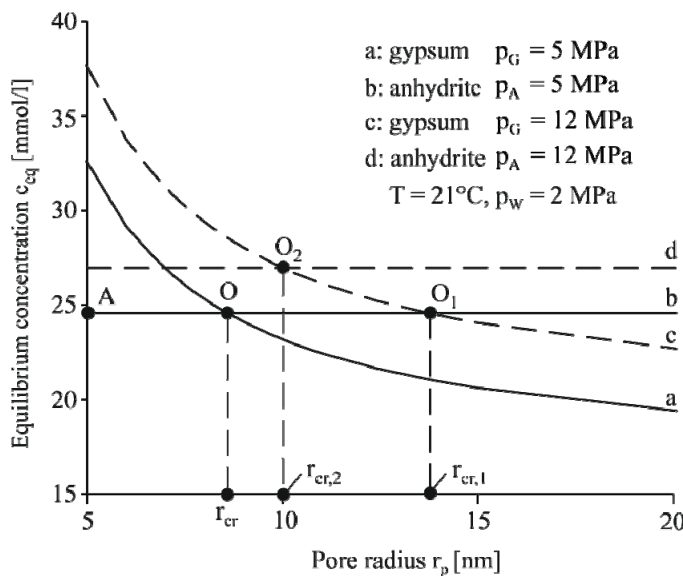


Figure 6.3 Equilibrium concentrations of anhydrite and gypsum as a function of pore radius for the temperature and pore pressure conditions of the Belchen Tunnel, $a_w = 1$ and different stress values on the anhydrite and gypsum.

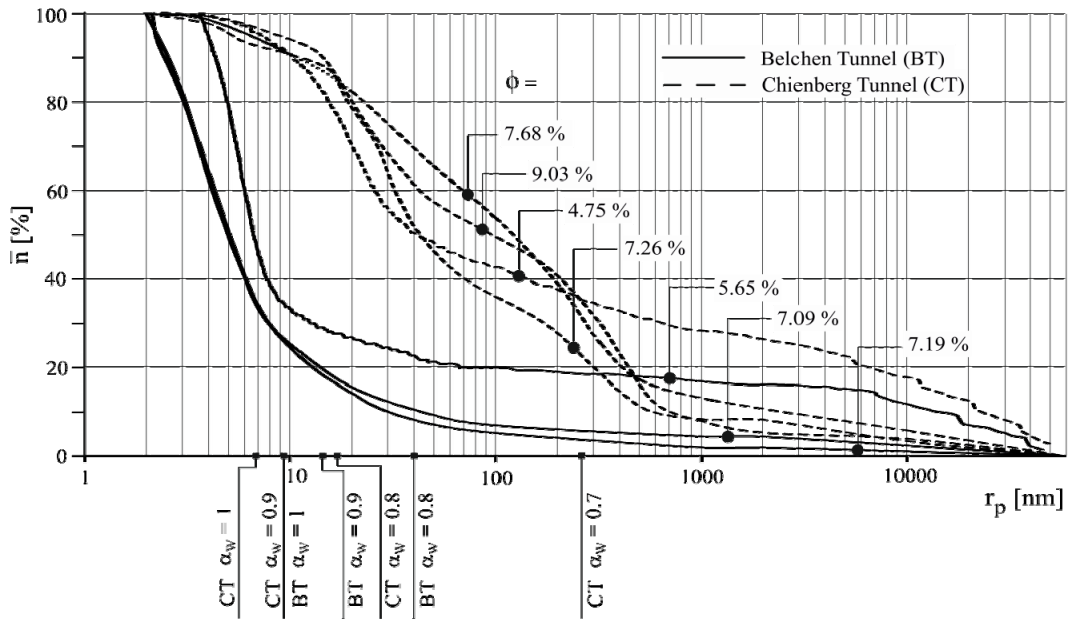


Figure 6.4 Pore size distributions and porosities ϕ of samples from the Chienberg and the Belchen Tunnel with critical radii r_{cr} calculated for different water activities.

6.2.3 Discussion

Taking the sampling depth into account and assuming hydrostatic pore pressure distribution and a unit total weight of 25 kN/m^3 for the rock mass, we get $p_w = 2 \text{ MPa}$ and $p_{s,0} = 5 \text{ MPa}$ for the Belchen Tunnel, while for the Chienberg Tunnel the corresponding values read $p_w = 0.5 \text{ MPa}$, $p_{s,0} = 1.25 \text{ MPa}$. Furthermore, with regard to the geothermal gradient in Northern Switzerland (cf. Section 6.1), $T = 21^\circ$ and 15°C for the Belchen and the Chienberg Tunnel, respectively. Under these considerations, Eq. (6.2) leads to critical radii r_{cr} between 7 and 250 nm, depending on the pore water activity a_w . These critical radii are shown also in Figure 6.4 beneath the abscissa. One can readily verify that all samples contain a larger (Chienberg Tunnel) or smaller (Belchen Tunnel) quantity of supercritical pores.

As explained in the following, the presence of even a few supercritical pores is sufficient for the entire anhydrite to transform into gypsum – including the anhydrite in regions with small pores, where it represents the thermodynamically stable phase. The consequence would be a completely anhydrite-free rock.

Assume that the rock contains both subcritical and supercritical pores. In the subcritical pores, where anhydrite represents the thermodynamically stable phase, the concentration c in the pore water would be equal to the equilibrium concentration $c_{eq,A}$ of the anhydrite (given by the line AO in Figure 6.3). Analogously, in the supercritical pores, the concentration would be equal to the equilibrium concentration $c_{eq,G}$ of gypsum (given by the line Oa in Fig. 6.3). Such a non-uniform concentration field would be unstable: As the porosity of the claystones is interconnected, ions will migrate by diffusion from the subcritical pores to the supercritical pores, thus reducing the concentration in the former and increasing the concentration in the latter. This will trigger dissolution of anhydrite in the subcritical pores and gypsum growth in the supercritical pores. This process – mineral dissolution in the small pores, diffusion of the dissolved ions to the larger pores and crystal growth in the latter – will continue until the entire anhydrite is transformed. Such processes are well known from the literature ([147], [148], [149]).

In conclusion, the small pore hypothesis must be abandoned even in the case of the extremely fine porous claystones from the Belchen Tunnel and even under the favourable assumptions of spherical pore shape and of negligible “ink-bottle” effect. The “ink-bottle” effect is a drawback of the MIP method which leads to an overestimation of the

percentage of small pores and thus to an underestimation of the supercritical porosity ([150], [151], [152], [153]). The effect of surface energy is more pronounced in the case of spherical pores than with other shapes, for example, cylindrical pores. This is because the effect of the surface energy in the case of cylindrical pores is γ/r_i (one radius of curvature tends to infinity, *cf.*, *e.g.*, Scherer [51]), while as already mentioned in Section 3.2.4, it equals $2\gamma/r_i$ for spherical pores.

6.3 The high pressure hypothesis

6.3.1 Introduction

The present section investigates whether the pressures which develop locally during the growth of gypsum in the supercritical pores are able to explain the occurrence of anhydrite (rather than gypsum) at shallow depths in Gypsum Keuper. In order to answer this question we must estimate: (i) the pressure which is required for the hydration to cease according to the thermodynamic equilibrium condition (this pressure will be hereafter referred to as the “*required solid pressure*”); (ii) the expansion-induced counterpressure of the matrix, *i.e.* the pressure that develops due to the confinement of gypsum by the surrounding claystone (this pressure will be hereafter referred to as the “*mechanically possible pressure*”). In order for the high stress hypothesis to be valid, the sum of the mechanically possible counterpressure and the pore water pressure must be higher than the required solid pressure.

An additional necessary condition is that the formation of only a small amount of gypsum is sufficient to mobilize the required counterpressure of the surrounding matrix. Otherwise, a considerable quantity of gypsum would also be present *in situ*. Thus, the validity of the high pressure hypothesis presupposes not only that the mechanically possible counterpressure reaches the required stress, but also that this happens with the formation of a small amount of gypsum. Obviously, the stiffer the matrix and the greater the pore expansion, the higher the mechanically possible counterpressure will be. Small quantities of gypsum can cause a considerable increase in pressure only if the surrounding matrix is sufficiently hard.

A third necessary condition is that the radial stress that must develop at the pore wall in order for gypsum growth to stop may involve some cracking, but is not so high that tensile failure of an extended zone of the rock matrix occurs between the supercritical pores; if this were not the case, the rock at the scale of a specimen would appear completely disintegrated, resembling granular soil, which does not agree with the observed high quality of anhydritic claystones.

Section 6.3.2 determines the *required solid pressure* by means of thermodynamic computations. Subsequently, we estimate the *mechanically possible counterpressure* in Section 6.3.3 based on a simplified cavity expansion model. In Section 6.3.4 we apply this model to the pressure and temperature conditions of the Belchen Tunnel and the Chienberg Tunnel in order to investigate the validity of the high pressure hypothesis. Finally, Section 6.3.5 discusses some important limitations of the simplified cavity expansion model by means of numerical calculations, which consider rock models with arbitrary pore sizes and arrangements.

6.3.2 Required pressure

During gypsum growth towards the pore walls, the gypsum pressure p_G increases, leading to an increase in the gypsum equilibrium concentration until the latter becomes equal to the anhydrite equilibrium concentration. The anhydrite equilibrium concentration depends, however, on the anhydrite pressure p_A , which may be variable: before growth, the anhydrite pressure is equal to the initial solid pressure $p_{S,0}$, but it may increase due to the pressure exerted by the growing gypsum. The anhydrite pressure obviously depends on the proximity of the anhydrite particles to the constrained gypsum growth. In this respect, two *borderline* cases can be considered which bound the range of possible

anhydrite pressures. As explained below, the two borderline cases correspond to extreme rates of diffusive ion transport.

The calcium and sulphate ions that are necessary for the formation of gypsum crystals are supplied by the dissolution of the anhydrite. The dissolving anhydrite particles cause an increase in the ion concentration in adjacent pores. Should the ions stay in the adjacent pores (slow diffusion), then the concentration in these pores would rise above the gypsum equilibrium concentration with the consequence that gypsum would start to precipitate close to the anhydrite particles.

However, the ions may also move by diffusion away from the anhydrite particles due to the fact that the ion concentration in the vicinity of the latter is higher than the concentration in the pores further away from them. Should the diffusion occur rapidly relative to the dissolution of anhydrite and the precipitation of gypsum, the concentration would then increase uniformly in the pores and gypsum growth would occur in all supercritical pores, as well as in pores further away from the anhydrite particles. In conclusion, the location where the crystals grow depends on whether diffusion occurs slowly or rapidly with regard to anhydrite dissolution and gypsum precipitation. The two limiting cases are the following: (1) gypsum growth in all supercritical pores (Fig. 6.5a) and (2) gypsum growth only in the supercritical pores very close to the anhydrite particles (Fig. 6.5b).

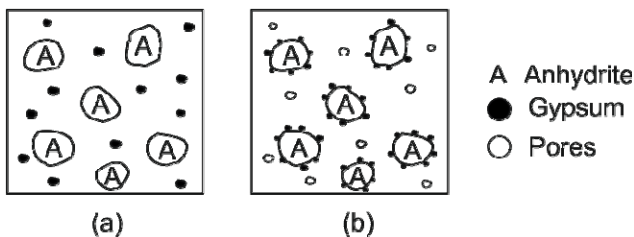


Figure 6.5 (a) Gypsum growth in all pores (case 1); (b) gypsum growth only in pores close to the anhydrite particles (case 2).

Let us consider the first case where gypsum crystals grow in all supercritical pores. In this case the pressure induced only affects the gypsum particles, while the anhydrite particles remain under the initial solid pressure, *i.e.* $p_A = p_{S,0}$ (lower bound). As mentioned above, the gypsum equilibrium concentration also increases with increasing pressure p_G . Therefore, in the diagram of Figure 6.3, the equilibrium concentration – pore radius curve of gypsum will move upwards (dashed line “c” instead of line “a”), while the anhydrite equilibrium concentration will remain the same as before (solid line “b”), because we made the assumption that confined gypsum growth causes a higher pressure only on the gypsum particles. (Line “c” of Fig. 6.3 was calculated from Eq. 3.19, assuming that the solid pressure increases locally from $p_G = p_{S,0} = 5$ MPa to, *e.g.*, $p_G = 12$ MPa, due to the growth of gypsum crystals.) As can be seen from Figure 6.3, the intersection point of the two equilibrium concentration – pore radius curves moves to the right (from point “O” to point “O₁”), which means that the critical radius becomes larger ($r_{cr,1}$ instead of r_{cr}) and the range of pore sizes where anhydrite is the stable mineral becomes larger. The process of gypsification will continue as long as supercritical pores exist, *i.e.* as long as the critical pore radius (which, as mentioned above, increases with the solid pressure p_G that develops during gypsum crystal growth) is smaller than the largest pore in the rock. The process will stop when the critical pore radius becomes equal to the radius r_{max} of the largest pore, which will happen at a certain solid pressure p_G (the “required pressure”).

Where gypsum crystals grow close to anhydrite particles (case 2), the latter may also experience a certain pressure increase (*i.e.* $p_G > p_A > p_{S,0}$). The anhydrite solid pressure p_A depends on the distance between the supercritical pores and the anhydrite particles (or, more generally, on the spatial distribution of anhydrite and gypsum) as well as on the stiffness of the rock around the expanding gypsum crystals. In the *borderline* case (upper bound) both minerals will be subject to the same stress. Then, the required solid pressure would be higher, because the increase in the anhydrite solid pressure would cause an

increase in its equilibrium concentration. Therefore, line “b” in Figure 6.3 would move upwards (to line “d” for the example of $p_A = 12$ MPa, calculated with Eq. 3.22) and the intersection point with the gypsum curve would move to the left (point “O₂” instead of point “O₁”). This means that the increase of the critical radius is less pronounced here (from r_{cr} to $r_{cr,2}$ rather than to $r_{cr,1}$) or, in other words, that a higher stress must develop in order for the critical radius to reach the radius r_{max} of the largest pore.

The required solid pressure for equilibrium to be reached can be determined by setting the gypsum equilibrium concentration (Eq. 3.19) equal to that of anhydrite (Eq. 3.22) with $\gamma_A/r_A = 0$ and $r_G = r_{max}$. Taking the lower bound for the pressure exerted on anhydrite, (i.e. $p_A = p_{S,0}$, $p_G = p_{req}$), the lower bound of the required pressure can be calculated as

$$p_{req, LB} = \frac{2RT \ln a_w + (T - T_0) \Delta_{r,GA} S^0 - \Delta_{r,GA} G^0 + 2p_W V_W^0 - 2 \frac{\gamma_G}{r_{max}} V_G^0 + p_{S,0} V_A^0}{V_G^0}, \quad (6.3a)$$

while in the case that $p_A = p_G = p_{req}$, i.e. upper bound

$$p_{req, UB} = \frac{2RT \ln a_w + (T - T_0) \Delta_{r,GA} S^0 - \Delta_{r,GA} G^0 + 2p_W V_W^0 - 2 \frac{\gamma_G}{r_{max}} V_G^0}{V_G^0 - V_A^0}. \quad (6.3b)$$

Figure 6.6 shows the required pressure as a function of temperature and water activity, while neglecting liquid-solid interface effects (i.e. for $\gamma_G/r_{max} = 0$). The solid lines correspond to the lower bound and the dashed lines to the upper bound of the required pressure. The higher the temperature and the lower the water activity, the lower the required pressure will be. The diagram applies to specific values of initial solid and pore pressure. However, parametric studies have shown that the influence of these parameters is small within the relevant range of values for initial solid and pore pressure.

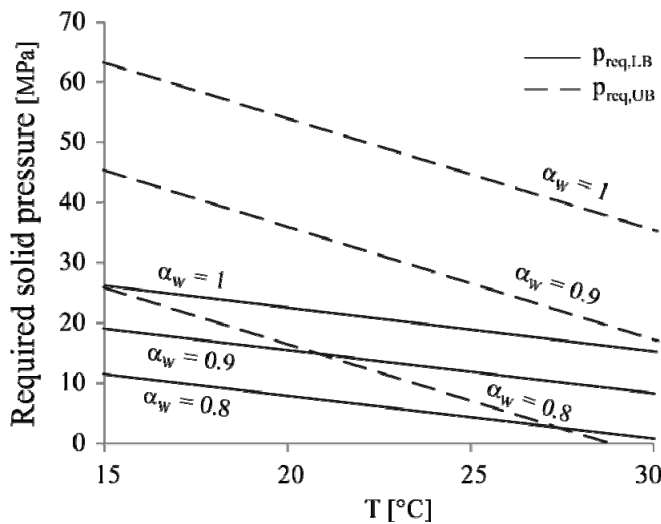


Figure 6.6 Required solid pressure ($p_G = p_{req}$) for the termination of the gypsum growth as a function of temperature and water activity ($\phi \approx 0$, $p_{S,0} = 5$ MPa, $p_W = 2$ MPa)

6.3.3 Mechanically possible pressure

In general, the mechanically possible pressure, which could be developed during crystal growth, depends on the stiffness of the surrounding medium and on the spatial distribution of the supercritical pores. In order to illustrate the effect of the spatial distribution, let us consider a claystone layer at depth H below the ground surface (Fig. 6.7a) which contains sparsely distributed supercritical pores (Fig. 6.7b). The expansion of each pore changes the stresses in the surrounding matrix. More specifically, it mobilizes a counterpressure in the radial direction (the radial compressive stress increases), while the tangential stress decreases. With further pore expansion, the tangential stress becomes zero and then negative (tension). When it reaches the tensile strength of the claystone, cracks develop in the radial direction and the tangential stress drops to zero. (Figure 6.7c shows only the horizontal cracks.) Assume for the sake of simplicity that the tensile strength is equal to zero and consider the distribution of the vertical stress in a horizontal cross section through the rock (Fig. 6.7d). For the reasons explained above, the vertical stress will be higher at the locations of the expanding pores and lower (or even zero) in the spaces between the pores. Note that the vertical stress must fulfil equilibrium, *i.e.* counterbalance the weight of the overburden, which means that the average vertical stress over the considered section must be equal to the initial stress σ'_0 at the depth of the layer ($\sigma'_0 = \gamma'_r \cdot H$). Pore expansion can only result in a high vertical stress locally if there is a space between the expanding pores where the vertical stress decreases to below the initial stress. This is only possible if the expanding pores are sparsely distributed: For simple equilibrium reasons, gypsum growth in densely spaced pores would occur under a practically constant vertical stress (the initial stress σ'_0).

The importance of the pore distribution becomes clearly evident when considering the extreme state of Figure 6.7e, where the entire area between the expanded pores fails in tension and its vertical stress is equal to zero. In this case, the material in the expanded pores would bear the full weight of the overburden and, consequently, the local stress would reach its highest possible value σ'_{max} . (Figure 6.7f shows the corresponding stress distribution.) Due to the equilibrium condition in the vertical direction, the average vertical stress over the area of the supercritical pores reads as follows:

$$\sigma'_{max} = \frac{F_{tot}}{F_p} \sigma'_0 = \frac{F_{tot}}{N_p \bar{F}_p} \sigma'_0, \quad (6.4)$$

where σ'_0 is the initial stress; F_{tot} is the total area of the horizontal cross section (Fig. 6.7g); F_p is the sum of the areas of the cross sections of the pores; N_p is the number of pores; and \bar{F}_p is the average cross section area of the pores. According to Eq. (6.4), for a given pore size distribution (*i.e.* for a fixed average area \bar{F}_p), the maximum stress increases with a decreasing number of pores or with increasing distances between the pores. Crystal growth in a few sparsely distributed large pores results in the same maximum local stress as crystal growth in many densely distributed small pores: The ratio of the pore distance to the pore size governs the maximum local stress.

Note that in the state of Figure 6.7e, the rock in the scale of a specimen would be completely fractured, thus resembling granular soil. This does not agree with the actual quality of rock cores from tunnels in Gypsum Keuper. It is reasonable to assume that the stress developing due to crystal growth may involve some cracking, but this should happen only in a limited zone around the expanding pores. The high local stress according to Eq. (6.4) is thus only theoretically possible. The actual stress must be lower than the stress according to Eq. (6.4)

The mechanically possible expansion-induced pressure can be estimated by means of a simple spherical cavity expansion model. Considering a rock element with regularly distributed spherical pores of uniform radius (Fig. 6.8) results to the spherically symmetric model of a hollow thick-walled sphere with internal and external radii equal to r_p and b_p , respectively (Fig. 6.9). The hollow sphere is subjected to a uniform radial pressure at its outer boundary (corresponding to the *in situ* pressure) and to a gradually increasing,

uniform radial displacement of its inner boundary (caused by the gypsum growth). The rock around the expanding cavity is considered as a linearly elastic no-tension material.

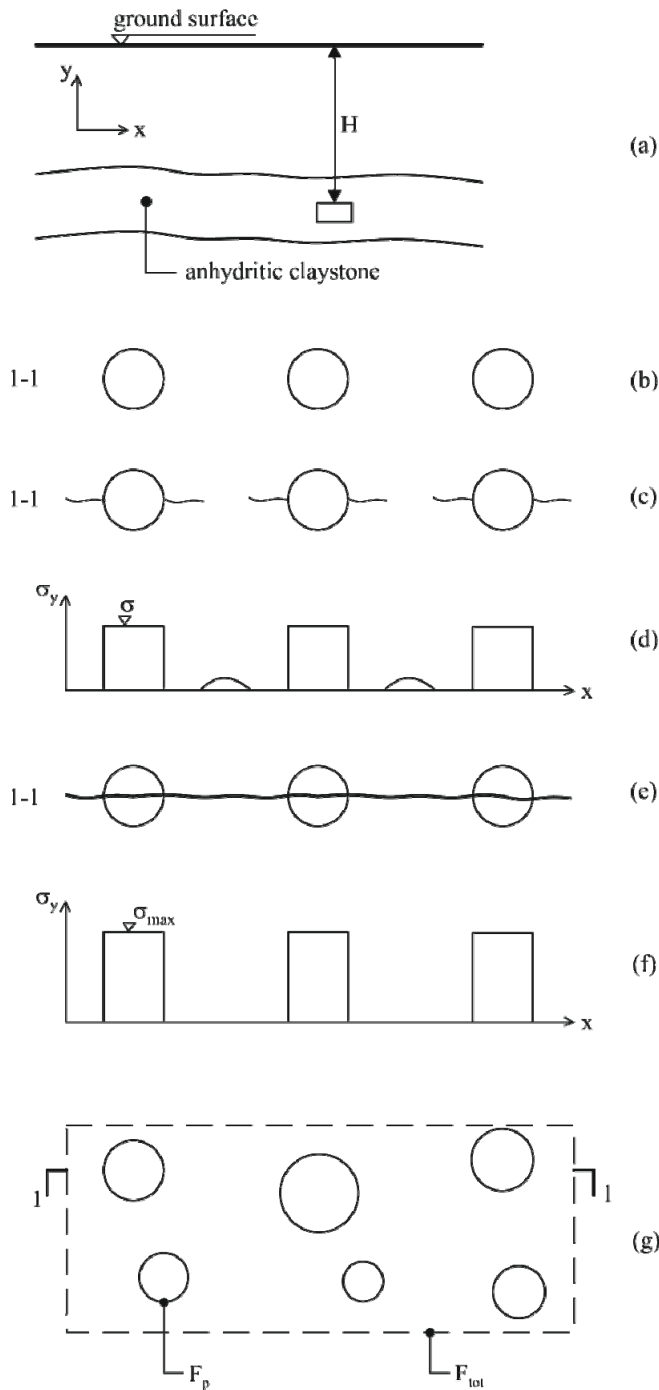


Figure 6.7 (a) In situ situation; (b) detail A with indicative distribution of the supercritical pores; (c) detail A with radial cracks due to pore expansion and, (d) corresponding distribution of the vertical stress σ_y ; (e) detail A with tensile failure of the entire matrix between the expanding pores and, (f) corresponding distribution of the vertical stress σ_y ; (g) horizontal cross section.

The inner pressure at the limit state (*i.e.* when the entire rock around the expanding cavity fails in tension) is given by the equation

$$P_{p,max} = \left(\frac{b_p}{r_p} \right)^2 (P_{S,0} - P_W) + P_W, \tag{6.5}$$

while the expansion associated with the development of this pressure reads as follows [8]:

$$\frac{u_p}{r_p} = \frac{P_{S,0} - P_W}{E} \left[b_p / r_p (b_p / r_p - 1 + \nu) + 1 - 2\nu \right]. \tag{6.6}$$

It should be noted that Eq. (6.5) represents an *upper* bound of the mechanically possible pressure $p_{p,max}$, because the underlying model presupposes tensile failure of the entire rock between the expanding pores, which does not agree with the observations. The mechanically possible pressure developing in the more realistic case of partial rock failure between the pores is lower and can also be estimated analytically [8]. For the purpose of the present section, however, it is sufficient to consider the upper limit (Eq. 6.5), because we will see that the "high pressure"-hypothesis fails to explain the occurrence of anhydrite even if considering this upper limit.

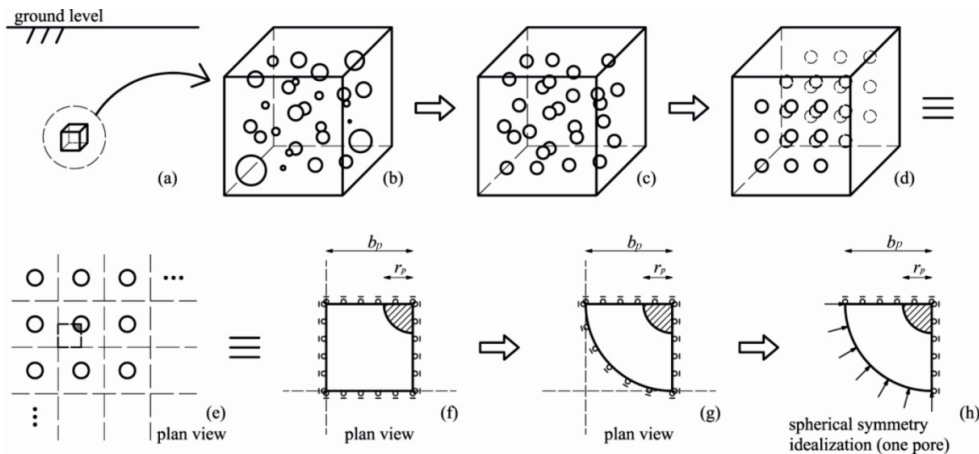


Figure 6.8 Successive assumptions for defining the spherical cavity expansion model.

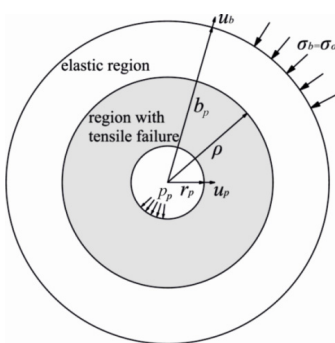


Figure 6.9 Cavity expansion model.

The outer radius b_p appearing in Eqs. (6.5) and (6.6) represents a measure of the distance between the pores (Fig. 6.8f) and is important with respect to the stress, which is mobilized by the rock as a reaction to the expansion of the growing gypsum crystals in the pores. It can be determined from the results of the porosimetry and simple geometric factors. More specifically, for a given porosity ϕ , the volume of the supercritical pores per unit volume of rock (hereafter referred to as “*supercritical porosity*”) is equal to $\phi_{cr} = \phi \cdot \bar{n}_{cr}$. Thus, under the assumptions of uniform pore size (radius r_p), the number N_p of these pores per unit volume is given by the following equation:

$$N_p = \frac{3\phi_{cr}}{4\pi r_p^3}. \quad (6.7)$$

On the other hand, for a regular arrangement of spherical pores on a cubic grid, the number of pores per unit volume is equal to

$$N_p = \frac{1}{(2b_p)^3}. \quad (6.8)$$

From these two equations we obtain:

$$\frac{b_p}{r_p} = \left(\frac{\pi}{6\phi_{cr}} \right)^{\frac{1}{3}}, \quad (6.9)$$

which means that the ratio between the outer radius b_p and the pore radius r_p depends only on the supercritical porosity ϕ_{cr} . As mentioned above, this equation presupposes that the pores are arranged on a regular cubic grid. This assumption is not essential. For other arrangements, e.g. the densest packing, one obtains similar results [8]. Introducing b_p/r_p from Eq. (6.9) to Eqs. (6.5) and (6.6) leads to the following relationships for the maximum mechanically possible pressure and the expansion that causes this pressure:

$$p_{p,max} = \left(\frac{\pi}{6\phi_{cr}} \right)^{\frac{2}{3}} (p_{S,0} - p_W) + p_W, \quad (6.10)$$

$$\frac{u_p}{r_p} = \frac{p_{S,0} - p_W}{E} \left[\left(\frac{\pi}{6\phi_{cr}} \right)^{\frac{2}{3}} - (1-\nu) \left(\frac{\pi}{6\phi_{cr}} \right)^{\frac{1}{3}} + 1 - 2\nu \right]. \quad (6.11)$$

According to these equations, the mechanically possible pressure and the normalized expansion depend linearly on the initial pressure and on the pore water pressure, and non-linearly on the supercritical porosity. They are independent from the radius r_p of the supercritical pores. Figure 6.10 shows these two entities as a function of the supercritical porosity, assuming atmospheric pore water pressure. The lower the supercritical porosity, the higher the mechanically possible pressure will be. At supercritical porosities lower than 5%, the mechanically possible pressure may be higher than the far field stress by a factor of 5 – 15.

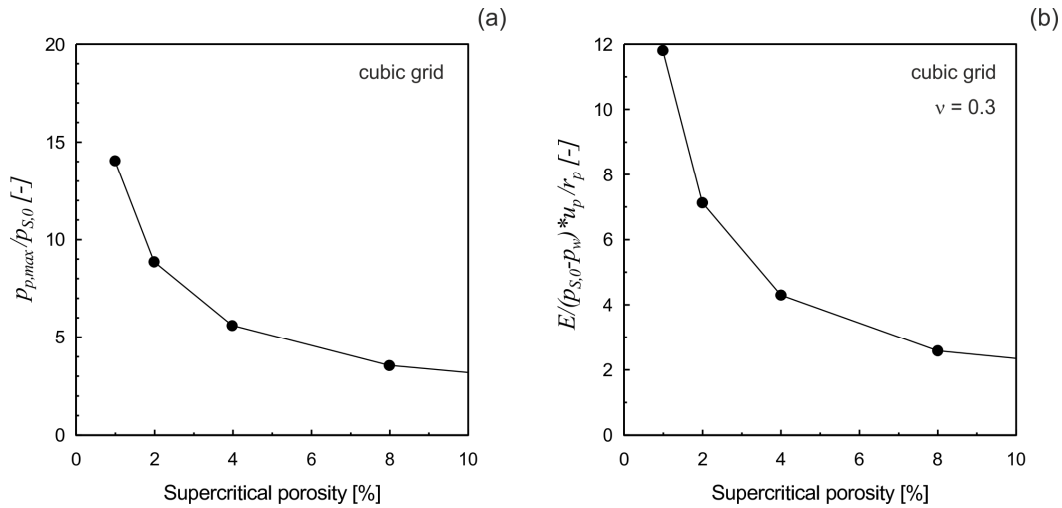


Figure 6.10 (a) Normalized mechanically possible pressure and, (b), pore expansion at mechanically possible pressure as a function of the supercritical porosity (atmospheric pore water pressure).

6.3.4 Application to the Belchen and the Chienberg Tunnel

The models presented above will be applied in relation to the data from the Belchen Tunnel and the Chienberg Tunnel in order to investigate whether the high pressure hypothesis might explain the presence of anhydrite at shallow depths of cover.

Necessary pore expansion

As explained in Section 6.3.1, an initial condition for the validity of the high pressure hypothesis is that a minor pore expansion will be sufficient for mobilising expansion-induced pressure. We will see here that this condition is fulfilled in the present case. According to Eq. (6.6) the expansion which is needed in order to mobilize the mechanically possible pressure increases with an increasing *in situ* initial solid pressure $p_{S,0}$ and with a decreasing Young's modulus E of the rock. Consequently, an upper boundary for the necessary expansion can be obtained by assuming a high *in situ* solid pressure $p_{S,0}$ in combination with a low pore pressure and a low Young's modulus E . The latter will be taken equal to 2 MPa considering tests on rock specimens from Belchen, Adler and Chienberg Tunnels.

This value of E leads in combination with a normalized pore expansion ($E u_p / [(p_{S,0} - p_w) r_p]$) of about 10 (Fig. 6.10b) and a high *in situ* stress of 7.5 MPa (corresponding to a depth of cover of about 300 m, cf. Table 6.1, and to the lowest possible pore pressure, i.e. atmospheric) to an expansion u_p / r_p of about 4%. In conclusion, even under the extreme assumptions made, the expansion which must occur in order to mobilize the mechanically possible pressure is in the range of only a few percent.

In the following we will focus on the second condition: Do the mechanically possible pressure and the pore water pressure reach the solid pressure that is required in order for anhydrite to represent the thermodynamically stable phase? The required solid pressure will be estimated according to Section 6.3.2 by neglecting solid-liquid interfacial effects (i.e. $\gamma_G / r_G = 0$), which is reasonable in view of the size of the supercritical pores (several 100s nm, Fig. 6.4). The mechanically possible pressure will be determined from the simplified spherical cavity expansion model in Section 6.3.3.

Chienberg Tunnel

Let us consider the pore size distribution of the Chienberg sample with porosity $\phi = 4.75\%$ (Fig. 6.4). For a water activity $a_W = 1$ the critical pore radius r_{cr} is equal to 9 nm (Eq. 6.2), which corresponds to a critical pore percentage $\bar{n}_{cr} = 96\%$. With a cubic lattice arrangement of the pores, the mechanically possible pressure becomes $p_{p,max} = p_p = 4.3$ MPa (cf. Eq. 6.10). Repeating this process for several water activity values, we obtain the pressure p_p as a function of the water activity (Fig. 6.11a). This calculation is performed up to a water activity of 0.69. As will be shown in Section 6.4, this value corresponds to the equilibrium water activity $a_{W,eq,0}$, i.e. the water activity at which anhydrite and gypsum co-exist in the system. Below this value, anhydrite will be the stable mineral.

According to Figure 6.11a, the mechanically possible pressure increases with decreasing water activity, because the lower the water activity, the greater the critical pore radius, the lower the supercritical porosity and the greater the distances between the supercritical pores will be.

Figure 6.11a additionally shows the lower bound of the required pressure $p_{req,LB}$ according to Eq. (6.3a) as a function of the water activity. Anhydrite will be stable if the mechanically possible pressure and the pore water pressure are higher than $p_{req,LB}$. It is evident that this is only true at water activities below 0.755, which is only slightly higher than the equilibrium water activity of $a_{W,eq,0} = 0.69$. This means that the pressures developing locally due to gypsum growth have a minor effect and in any case are not sufficiently high to prevent gypsum growth. The high pressure hypothesis fails to explain the presence of anhydrite under the small depth of cover of the Chienberg project area. If we had considered an upper bound for the required pressure $p_{req,UB}$, Eq. (6.3b) would apply, leading to even lower water activities, as in this case the required pressure is even higher (cf. Fig. 6.6).

Belchen Tunnel

We follow the same approach for the anhydritic claystones of the Belchen Tunnel, with a pore size distribution according to the upper Belchen curve of Figure 6.4, which corresponds to a porosity $\phi = 5.65\%$. Figure 6.11b shows both of the required pressures $p_{req,LB}$ and $p_{req,UB}$ as well as the mechanically possible pressure p_p .

According to this diagram, the maximum mechanically possible pressure exceeds the lower bound of the required pressure, even when assuming a water activity of unity. This means that the high pressure hypothesis would explain the presence of anhydrite in this case. The reason for this is the very large percentage of small pores in the Belchen claystones, a consequence of which is a low supercritical porosity and rather high distances between the supercritical pores, thus allowing development of local pressures which are considerably higher than in the case of Chienberg (compare the two diagrams of Fig. 6.11). On the other hand, however, where gypsum and anhydrite particles experience the same pressure, anhydrite is stable for water activities below 0.885 (Fig. 6.11b). This means that the high pressure hypothesis is not sufficient to explain the presence of anhydrite by itself. Nonetheless, one should bear in mind that as the two cases (lower and upper bound) constitute *borderlines*, the most likely situation in reality will be somewhere between these two.

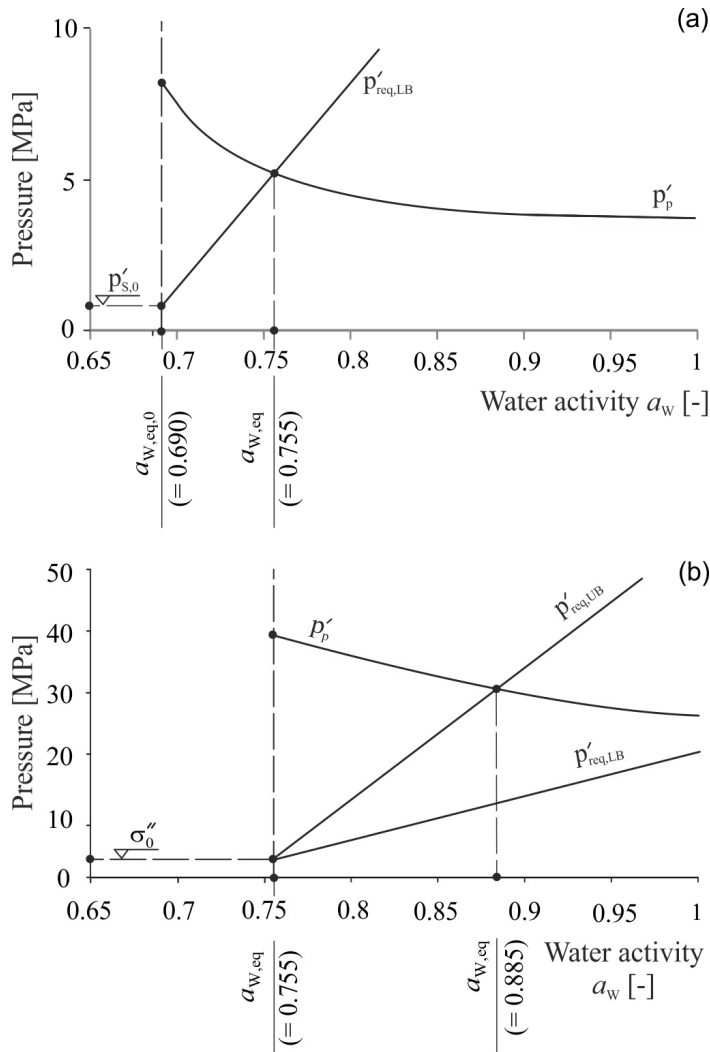


Figure 6.11 Mechanically possible pressure (according to the simplified cavity expansion model) and required pressure as a function of water activity, (a), for the Chienberg Tunnel and, (b), for the Belchen Tunnel.

6.3.5 Major draw-back of the high pressure hypothesis

The simplified, spherically symmetric cavity expansion model of Section 6.3.3 considers regularly distributed pores of uniform radius. The adequacy of this model was checked by means of comparative numerical computations, which were carried-out for rocks with irregularly distributed pores of different sizes [8].

Figure 6.12 concerns the example of a rock element containing 118 irregularly distributed pores of equal radius. The diagram shows the results of a numerical simulation. Each thin curve corresponds to another pore and shows its numerically computed minimum principal stress as a function of expansion. Curves “s” and “t” in Figure 6.12 apply to regularly distributed pores (on a square or on a triangular grid, respectively) and were obtained by means of the simplified rotationally symmetric cavity expansion model. It is interesting that the simplified rotationally symmetric model predicts the average of all pores well (curve “a” in Fig. 6.12). On the other hand, the numerically computed stresses exhibit a large scatter, meaning that the stress will be considerably low at some pores. The scatter can be explained by considering two specific pores (denoted by “A” and “B” in Fig. 6.12): The expansion of pore A generates a high stress locally, because this pore is far away from other pores; on the other hand, the stress is low in the case of pore B, because this pore forms a cluster with other pores.

Particularly low stresses develop in some pores if one considers the variability in the pore size additionally (Fig. 6.13). Pore expansion results to very low or even zero (due to cracking) stresses tangentially to the pore circumference (Fig. 6.13c). Therefore, small pores that are located close to large pores cannot develop a high stress and may not reach the required pressure.

As ion concentration increases with stress, concentration in the higher stress pores will be higher than in the lower stress pores. Therefore ions would move by diffusion from the pores that reach the required pressure towards the pores with lower local stresses. This would increase concentration and keep precipitation ongoing in the lower stress pores. Consequently, all of the anhydrite would transform into gypsum. The high pressure hypothesis would explain the presence of anhydrite at shallow depths only for extremely fine-porous anhydritic rocks, and only under the unrealistic assumption of poorly graded and uniformly distributed pores.

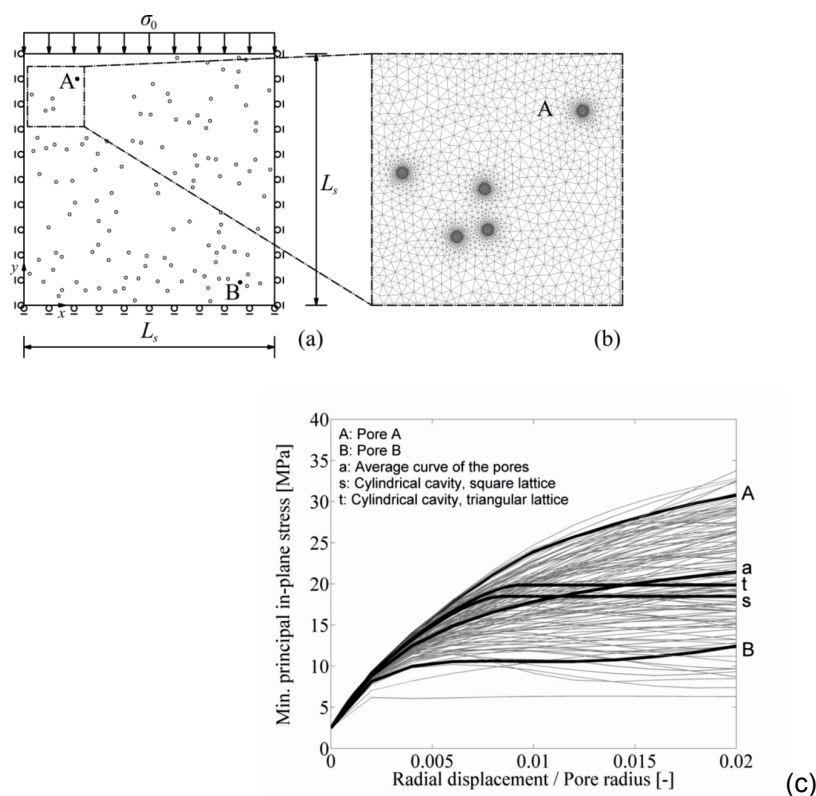


Figure 6.12 (a) 2D computational model for a rock element containing 118 cylindrical pores of uniform size; (b) detail of the finite element mesh; (c) minimum principal in-plane stress as a function of the normalized cavity expansion.

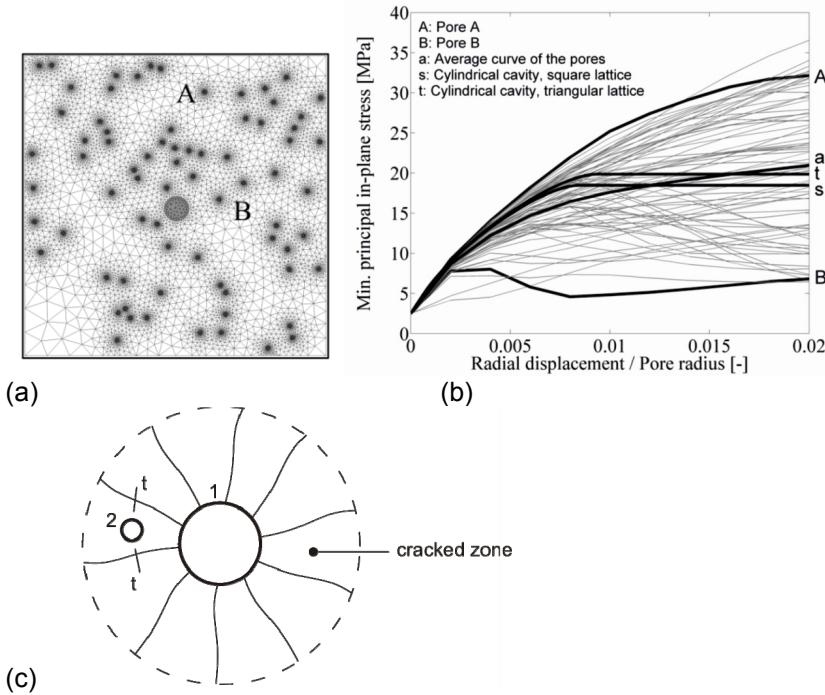


Figure 6.13 (a) 2D computational model for a rock element containing one big pore and 74 smaller pores of uniform size; (b) minimum principal in-plane stress as a function of the normalized cavity expansion; (c) small supercritical pore "2" within the cracked zone that is formed around a larger pore "1" during its expansion.

6.4 The low water activity hypothesis

As shown in Section 3, a low water activity favours anhydrite as the stable phase. In order to estimate the water activity values at which anhydrite would represent the stable mineral at the concerned depths and temperatures we apply the thermodynamic model of Section 3 and in particular Eq. (3.27). The underlying assumptions of these equations are that porosity is very low, the solid pressures of anhydrite and gypsum are equal to the lithostatic pressure $p_{S,0}$ (i.e. $p_G = p_A = p_{S,0}$) and the solid-liquid interfacial effects are neglected. The water activity at which anhydrite and gypsum co-exist in a system reads as follows:

$$a_{W,eq} = \exp\left(\frac{\Delta_{r,GA}G^0 + (T_0 - T)\Delta_{r,GA}S^0 + (V_G^0 - V_A^0)p_{S,0} - 2V_W^0p_W}{2RT}\right). \quad (6.12)$$

Anhydrite is stable if the water activity is lower than the one given by Eq. (6.12). Figure 6.14 shows the equilibrium water activity as a function of the temperature for two depths of cover ($H = 50$ m and 300 m), assuming that total stress and pore pressure increase linearly with the depth H . In the relevant temperature range, the equilibrium water activity varies between $a_{W,eq} = 0.69 - 0.84$. Such low water activities might occur either due to high levels of dissolved ions in the pore water or due to interaction between the pore water and the clay minerals. Mineralogical analyses of water from the Gypsum Keuper show, however, that the actual ionic concentration is far too low to explain water activities as low as 0.70 – 0.80. The remainder of the present Section therefore deals with the other possibility, i.e. with the interaction between the pore water and the clay minerals. As discussed below, this scenario is entirely possible.

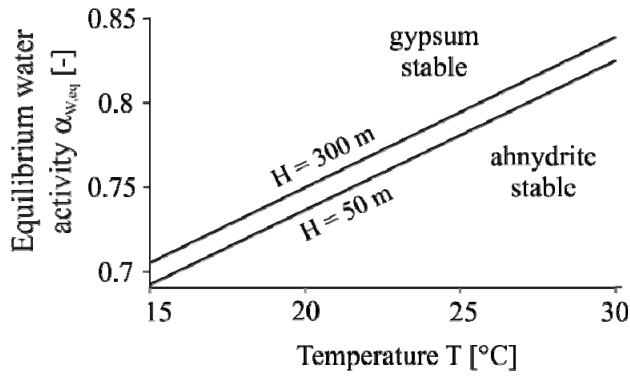


Figure 6.14 Equilibrium activity of water as a function of temperature at depths of 50 and 300 m.

An assumption that the activity of the pore water is associated with its potential Ψ according to Eq. (3.13) and Eq. (6.12) leads to the following expression for the potential at the anhydrite-gypsum equilibrium:

$$\Psi_{eq} = \frac{\Delta_{r,G}G^0 + (T_0 - T) \Delta_{r,G}S^0 + (V_G^0 - V_A^0) P_{S,0}}{2V_W^0} - p_w. \quad (6.13)$$

According to this equation, the equilibrium potential Ψ varies between -50 MPa and -25 MPa in the relevant depth and temperature range. Anhydrite would be stable under the conditions prevailing before tunnel excavation, provided the *in situ* pore water potential Ψ_0 is lower than the equilibrium potential, *i.e.* -50 to -25 MPa. It is well known from the literature that pore water in claystones often exhibits potentials as low as these, or very low activity values. Alonso and Olivella [36], for example, measured potential values as low as -40 to -20 MPa by means of a transistor psychrometer (*cf.* [154]). Other studies supporting the hypothesis of very low water potential or activity values include those of Mitaritonna *et al.* [155], Mohajerani *et al.* [156] and Zhang *et al.* [157].

6.5 Conclusions

Based on the thermodynamic model developed in Section 3, an attempt was made to quantitatively explain the occurrence of anhydrite in Gypsum Keuper at low depths prior to tunnel excavation. Three effects were quantitatively investigated: the size of the pores; the local stresses generated due to gypsum growth in the pores; the thermodynamic state of water in the presence of the clay phase.

In order to determine the role of the pore size of anhydritic claystones, MIP experiments were performed on samples from the Gypsum Keuper. Natural anhydritic rocks were found to contain not only extremely small pores, where anhydrite would be stable and gypsum growth thermodynamically impossible, but also larger pores, where gypsum would precipitate, thus sustaining a process of anhydrite dissolution and ionic diffusion from the small pores to the large pores. The consequence would be a complete transformation of anhydrite into gypsum. The so called “small pore hypothesis” must therefore be abandoned as it does not provide a general and robust explanation for the occurrence of anhydrite under the *in situ* conditions.

The hypothesis of high local stresses, initially proposed in relation to the Gypsum Keuper formation by Wichter [139], has also proved deficient, except for the unusual combination of extremely fine-porous rocks with uniform, regularly distributed pores. In general, the stress developing locally does not reach the level thermodynamically required for anhydrite to be stable in all pores, which would cause a complete transformation of anhydrite to gypsum via dissolution and diffusion.

The low activity hypothesis, which, following Lippmann and Schüle [137], emphasises the role of clay minerals with respect to the thermodynamic state of the pore water, provides the most convincing explanation for the occurrence of anhydrite at shallow depths. Although no experimental confirmation has yet been made specifically for the anhydritic claystones of the Gypsum Keuper, the low water activity hypothesis does not make any unrealistic assumptions.

In addition, it provides a consistent explanation of the processes taking place when anhydritic claystones come into contact with water: Swelling starts with water uptake by the clay minerals. During this first phase, the pore water activity gradually increases, eventually reaching the gypsum – anhydrite equilibrium activity. From this point on, anhydrite to gypsum transformation takes place, consuming water and thus maintaining the water deficiency of the clay and sustaining the water uptake until all of the anhydrite is transformed into gypsum. At the end of the swelling process the water activity reaches unity (the fully swollen state of the clay).

7 Maximum swelling pressure of anhydritic claystones

7.1 Introduction

The microscopic mechanism behind the development of the swelling pressure *in situ* is the growth of gypsum crystals inside the rock matrix: If a crystal is in equilibrium with an oversaturated solution and its growth is completely prevented by the surrounding matrix, then it exerts so-called crystallisation pressure [158]. However, the pressure, which is necessary in order to keep the overall volume of the rock constant, must be lower than the crystallisation pressure. The reason is that the latter acts only locally within the rock matrix and, in addition, the matrix may, depending on its stiffness, allow a certain amount of crystal growth. Obviously, swelling pressure as well as the notion of “complete volume constraint” depends on scale. Therefore, a distinction between the micro-, the macro- and the megascale is indispensable (Fig. 7.1).

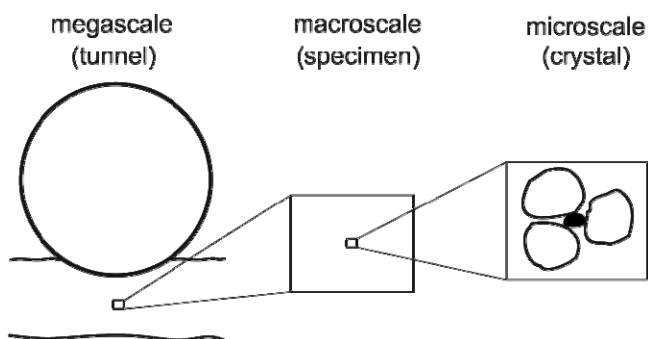


Figure 7.1 Scales examined in the swelling process.

The microscale refers to the scale of the individual gypsum crystal. Complete volume constraint at this scale means that the matrix does not allow the gypsum to grow. (The pressurized crystal is in thermodynamic equilibrium with the pore solution.) The swelling pressure at the microscale comprises the above-mentioned crystallisation pressure.

The term “macroscale” refers to the scale of a rock specimen containing gypsum crystals. Complete volume constraint at this scale means that the volume of the rock specimen is kept constant. This is the condition applied in the standardized oedometer test for determining axial swelling stress [44].

The megascale refers to the scale of a tunnel. Complete volume constraint at this scale means that the heave of the tunnel floor is completely constrained. The swelling pressure at the megascale is the pressure developing *in situ* upon a stiff invert arch. The distinction between macro- and megascale is necessary for the following reasons: (i) The boundary conditions *in situ* are different from those in laboratory test (a stiff invert arch does not completely prevent an increase in rock volume). (ii) The rock mass generally contains non-swelling layers as well, which, depending on their stiffness, may allow some increase in the volume of the swelling layers. (iii) The water circulation conditions *in situ* are in general less favourable than under laboratory conditions, where the specimens are constantly supplied with water [1].

The structure of the present section takes account of these three scales.

7.2 Microscale

A critical review of previous theoretical estimates of crystallisation pressure can be found in [8]. Winkler and Singer [159] and Winkler [160] estimated the crystallisation pressure of gypsum by applying Correns and Steinborn's (1939) theory. However, they erroneously considered a molar volume of gypsum of $V_G^0 = 54.8 \text{ cm}^3/\text{mol}$ instead of the correct value ($74.3 \text{ cm}^3/\text{mol}$). In addition, they did not take into account the activities of the reacting substances.

The results of Winkler [160] were later adopted by Wichter [139]. Assuming that supersaturation in Gypsum Keuper rarely exceeds 2, he concluded that the crystallisation pressure amounts to about 30 MPa at $T = 25 \text{ °C}$. Nevertheless, Wichter [139] did not substantiate the assumption concerning supersaturation, either empirically or theoretically. Another theoretical estimate can be found in Flückiger [161] and Flückiger *et al.* [162], who used thermodynamic calculations to determine a value of 3.7 MPa for the crystallisation pressure of gypsum at room temperature ($T = 20 \text{ °C}$). This value was later used by Steiner *et al.* [163], who investigated the role of brittle fractures on the swelling of anhydritic claystones. The value of 3.7 MPa is lower than all previous thermodynamic estimates and also lower than the swelling pressures that are frequently measured in swelling pressure tests under volume constraint (see [141], and Section 7.3.1). The value is based, however, upon erroneous thermodynamic considerations and questionable assumptions [8].

In the following a rigorous thermodynamic model for the crystallisation pressure will be presented and the influencing factors will be discussed, with an emphasis on the ion concentration in closed or open systems.

7.2.1 Crystallisation pressure

The crystallisation pressure p_c depends on the concentration c of calcium and sulphate ions in the solution, the quantity of foreign ions, the presence of clay minerals, the pore water pressure p_w , the temperature T and the geometry and size of the pores and crystal grains ([51], [147], [50]). Based on Eqs. (3.18) and (3.19) these dependencies can be written in the following form:

$$p_c = \frac{2RT \ln a_w}{V_G^0} - \frac{2\gamma_G}{r_G} + \frac{RT \ln \left(\gamma_{Ca^{2+}} \gamma_{SO_4^{2-}} \frac{c_{Ca^{2+}}}{c_0} \frac{c_{SO_4^{2-}}}{c_0} \right) + \Delta_{r,G} G^0 - (T - T_0) \Delta_{r,G} S^0}{V_G^0} \quad (7.1)$$

Based on Eq. (7.1) and taking atmospheric pore pressure into account ($p_w = 0$), the factors that affect crystallisation pressure are as follows: the concentration of the ions, the radius of the gypsum r_G (which coincides with the pore radius r_p), the water activity a_w , the presence of foreign ions and the temperature T . The effect of these factors is investigated in the following sections. More specifically, in the parametric analyses of Section 7.2.2, the concentration of the sulphate and calcium is taken as an independent, given parameter. The actual concentration in a closed system is a result of anhydrite dissolution and gypsum precipitation, while an open system also involves transport processes (advection and diffusion). Sections 7.2.3 and 7.2.4 deal with the value of the ion concentration in closed and open systems, respectively.

7.2.2 Relationship between crystallisation pressure and concentration

Figure 7.2 shows the relationship between crystallisation pressure and concentration c (assuming equal calcium and sulphate concentrations, *i.e.* $c_{Ca^{2+}} = c_{SO_4^{2-}} = c$) for different values of the other parameters.

Effect of the radius of the gypsum particles

Figure 4.2a shows the effect of the solid-liquid interface, which is expressed by the term $2\gamma_G/r_G$ in Eq. (7.1). It decreases with increasing r_G and can be totally neglected for radii greater than $1\mu\text{m}$. For small radii r_G , however, it is relevant: The surface of the crystal can be conceived of as a stretched membrane which exerts a pressure upon the crystal, thus taking over some of the crystallisation pressure; crystallisation pressure therefore decreases with decreasing radius r_G ([51], [72]). This can also be seen from Eq. (7.1), according to which the surface energy effect reduces crystallisation pressure by $2\gamma_G/r_G$.

Effect of water activity

Clay minerals or a high ionic concentration may substantially reduce the ability of water to take part in chemical reactions. This is taken into account by the activity coefficient a_w (*cf.* Section 3.2.3). Figure 7.2b shows the effect of the water activity a_w . The lower its value, the lower the crystallisation pressure will be. As can be verified from Eq. (7.1), a water activity less than 1 decreases crystallisation pressure by $|2RT \ln a_w / V_G^0|$.

Effect of the presence of foreign ions

Foreign ions (*e.g.* sodium or chloride) decrease the activities of all reactants (water, calcium and sulphate ions) that participate in the growth of gypsum and thus also in its crystallisation pressure. This is taken into account in Eq. (7.1) via the water activity a_w and the ion activity coefficients $\gamma_{Ca^{2+}}$ and $\gamma_{SO_4^{2-}}$ (*cf.* Section 3.2.3). Figure 7.2c compares the crystallisation pressure in the case of a $NaCl$ solution of $0.2\text{ mol/l } H_2O$ with the crystallisation pressure without foreign ions. For the sake of simplicity, the activity of the water, which is slightly lower than 1 at this $NaCl$ concentration [164], was taken equal to 1. The presence of foreign ions clearly decreases crystallisation pressure.

Effect of temperature

As the temperature affects several terms of Eq. (7.1), its effect cannot be seen immediately. According to Figure 7.2d, temperature has a minor effect on crystallisation pressure. It should be noted that this conclusion is true only for given concentration c , *i.e.* under the assumption that the actual concentration itself does not depend on the temperature. However, as we will see in Section 7.2.3, in a closed system containing gypsum, anhydrite and water, the concentration c is equal to the equilibrium concentration $c_{eq,A}$ of anhydrite, which is sensitive to temperature ([74], [165]). In this particular case, the crystallisation pressure of the gypsum also depends to a considerable extent on the temperature (see end of Section 7.2.3).

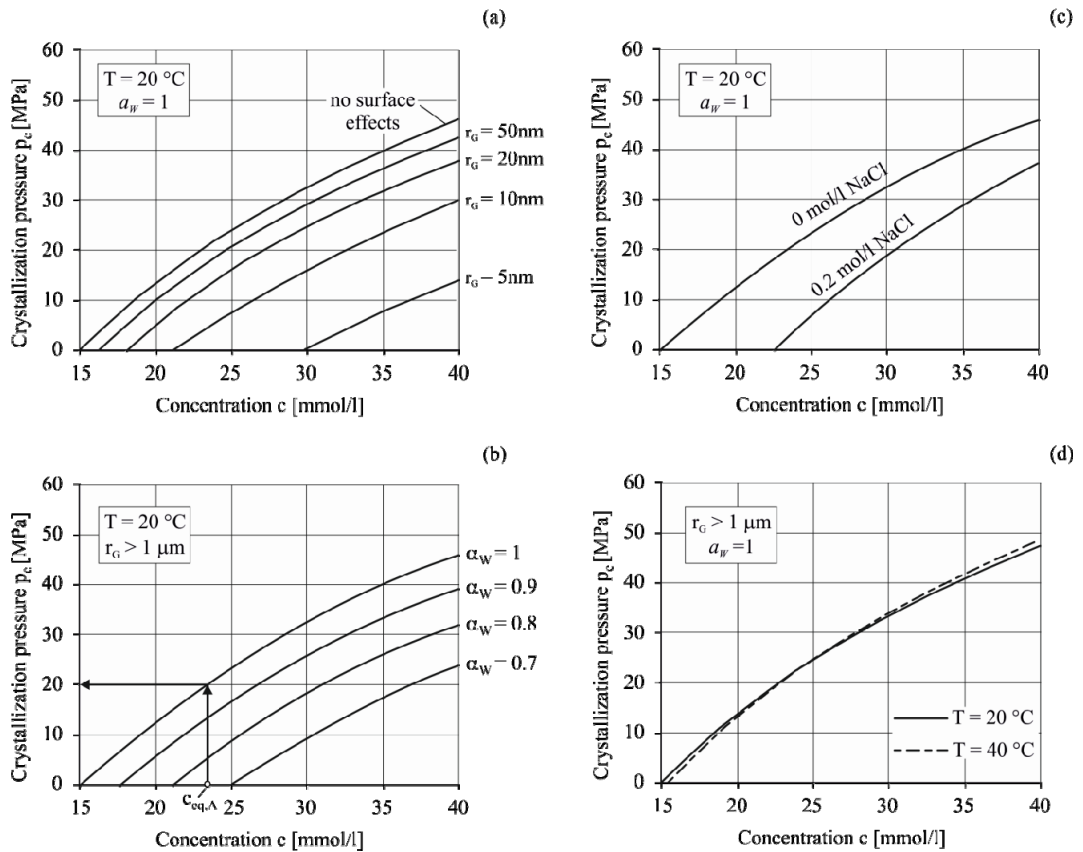


Figure 7.2 Crystallisation pressure p_c of gypsum as a function of the ion concentration c : (a) effect of the pore radius; (b) effect of the water activity; (c) effect of foreign ions; (d) effect of temperature.

7.2.3 Ion concentration in a closed system containing anhydrite and gypsum

Let us first consider a system where water and ions cannot flow in or out. In this case, anhydrite is the only supplier of ions. Anhydrite dissolution increases the concentration of ions in the pore water until it reaches the equilibrium concentration $c_{eq,A}$ of anhydrite. The latter can be determined by means of Eqs. (3.22) and (3.26). Under atmospheric pressure ($p_A = 0$) and $T = 20\text{ °C}$, it is equal to 23.4 mmol/l. As this concentration is higher than the gypsum equilibrium concentration under the same conditions (15 mmol/l, determined from Eqs. (3.19) and (3.20) with $p_G = 0$, neglecting the effects of water activity and surface energy), gypsum will develop a crystallisation pressure of about 20 MPa (see, e.g., Fig. 7.2b for $c = c_{eq,A} = 23.4\text{ mmol/l}$ and $a_W = 1$). The development of this pressure will also cause a certain increase in the pressure p_A acting on the anhydrite particles. The increase in pressure depends on the spatial distribution of the anhydrite and the gypsum particles, whose growth is constrained by the surrounding medium. In the *borderline* case where the constrained gypsum crystals are very closely spaced and located close to the anhydrite grains (cf. Fig. 6.5b), the pressure developing upon the latter can be taken approximately equal to the crystallisation pressure of the gypsum.

The increased anhydrite pressure will cause an increase in the anhydrite equilibrium concentration to a value that is higher than the equilibrium concentration under atmospheric pressure (23.4 mmol/l). This in turn will further increase the crystallisation pressure of gypsum to more than 20 MPa, which will again further increase the anhydrite equilibrium concentration. The process of a successive pressure-induced increase in the equilibrium concentration of the dissolving mineral is well known from petrography (cf. [166]). It can be illustrated graphically by plotting in one and the same diagram the following two curves (Fig. 7.3): (i) the crystallisation pressure p_c of the gypsum as a

function of the actual concentration c (determined by Eq. 7.1 with $c_{Ca^{2+}} = c_{SO_4^{2-}} = c$) and (ii) the relationship between the pressure p_A acting upon the anhydrite particles and the anhydrite equilibrium concentration, determined according to Eq. (3.22) and taking atmospheric pressure into account, *i.e.* $p_W = 0$, by:

$$p_A = \frac{1}{V_A^0} \left[RT \ln \left(\gamma_{Ca^{2+}} \gamma_{SO_4^{2-}} \frac{c_{Ca^{2+}} c_{SO_4^{2-}}}{c_0^2} \right) + \Delta_{r,A} G^0 - (T - T_0) \Delta_{r,A} S^0 \right], \quad (7.2)$$

where the general equation $K_A = \gamma_{Ca^{2+}} \gamma_{SO_4^{2-}} c_{Ca^{2+}} c_{SO_4^{2-}} / c_0^2$ (similar to Eq. 3.18 which applies for gypsum) has been used for the ion activity product of anhydrite.

Points 1 and 2 in Figure 7.3 show the anhydrite equilibrium concentration under atmospheric pressure and the corresponding crystallisation pressure of gypsum, respectively. Point 3 shows the increased anhydrite equilibrium concentration assuming that the crystallisation pressure of 20 MPa also acts upon the anhydrite particles. At this higher concentration, the crystallisation pressure of gypsum would also be higher (about 30 - 35 MPa, point 4), which would in turn increase the anhydrite equilibrium concentration (point 5) and so on. The system reaches equilibrium only at the intersection point of the two curves. At this point, the anhydrite equilibrium concentration amounts to about 46 mmol/l (about twice the equilibrium concentration under atmospheric pressure) and the crystallisation pressure of gypsum to 53 MPa.

By solving Eq. (3.27) for the crystallisation pressure (taking into account that $p_c = p_G$), we obtain:

$$p_c = \frac{p_A V_A^0 + 2RT \ln a_w + (T - T_0) \Delta_{r,GA} S^0 - \Delta_{r,GA} G^0 - \frac{2\gamma_G V_G^0}{r_G}}{V_G^0}, \quad (7.3)$$

In general, the crystallisation pressure at equilibrium can be obtained by setting $p_A = p_c$ solving with respect to p_c

$$p_c = \frac{2RT \ln a_w + (T - T_0) \Delta_{r,GA} S^0 - \Delta_{r,GA} G^0 - \frac{2\gamma_G V_G^0}{r_G}}{V_G^0 - V_A^0}, \quad (7.4)$$

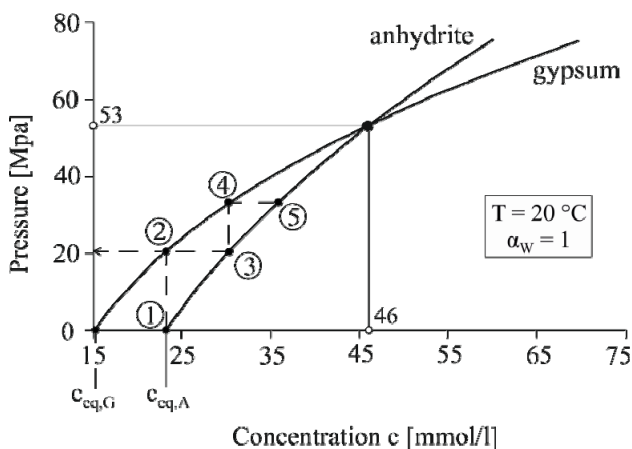


Figure 7.3 Relationship between gypsum crystallisation pressure and the ion concentration, and between pressure and the anhydrite equilibrium concentration.

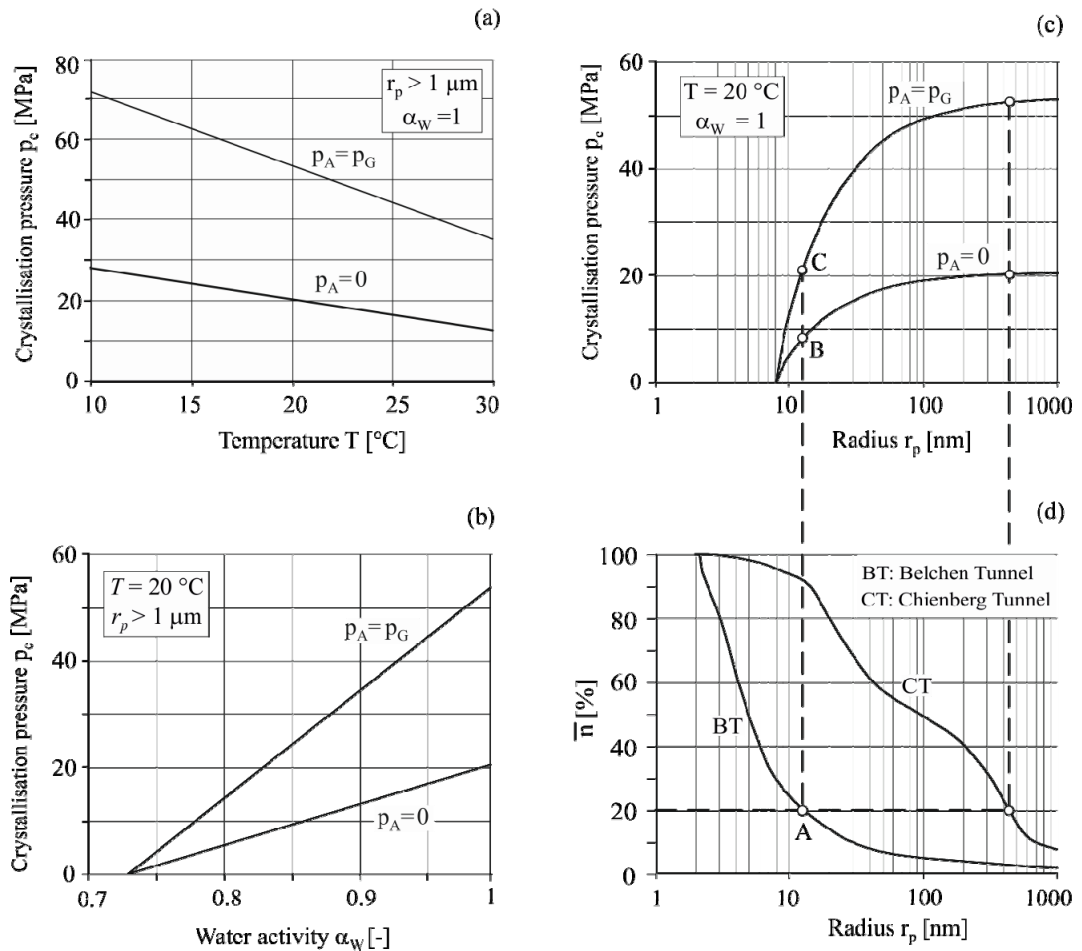


Figure 7.4 Crystallisation pressure p_c of gypsum as a function of (a) temperature T ; (b) water activity a_w (c) gypsum particle radius r_G .

As mentioned above, Eq. (7.4) assumes that the anhydrite pressure is equal to the pressure developed by the gypsum crystals. If the latter are sparsely distributed within the rock matrix and located at greater distances from the anhydrite grains, the anhydrite will experience a smaller pressure increase than the walls of the pores constraining the gypsum growth. In the *borderline* case, where the anhydrite pressure remains equal to atmospheric pressure, the crystallisation pressure of gypsum can be determined by setting $p_A = 0$ in Eq. (3.27) resulting in

$$p_c = \frac{2RT \ln a_w + (T - T_0) \Delta_{r,GA} S^0 - \Delta_{r,GA} G^0 - \frac{2\gamma_G}{r_G} V_G^0}{V_G^0} \quad (7.5)$$

Let us revisit now the question of Section 7.2.2, *i.e.* study the effect of temperature, water activity and pore size, taking into account the specific conditions prevailing in a closed system. Figure 7.4a, 7.4b and 7.4c show the crystallisation pressure as a function of these parameters for the two bounds of anhydrite pressure ($p_A = 0$ or $p_A = p_c$). It is evident that in a system where anhydrite is the only ion supplier, the anhydrite pressure significantly influences the crystallisation pressure of gypsum.

As the anhydrite equilibrium concentration depends on the temperature, both the supersaturation with respect to gypsum and the crystallisation pressure of gypsum also depend on the temperature (Fig. 7.4a). More specifically, with increasing temperature, the crystallisation pressure decreases by 1 – 2 MPa/°C depending on the anhydrite pressure.

According to Figure 7.4c, the surface energy effect is relevant only for pore radii of up to 100 nm. Figure 7.4d gives an idea of the pore sizes of sulphatic claystones. More

specifically, the diagram indicatively shows the two curves of the MIP results presented in Fig. 6.4, one on a sample from the Chienberg Tunnel and one from the Belchen Tunnel. The diagram can be read in combination with the overlying diagram (Fig. 7.4c). Consider, for example, the curve for the sample from the Belchen Tunnel and a percentage of $\bar{n} = 20\%$. The corresponding pore radius and crystallisation pressure amount to about 12 nm (point A in Fig. 7.4d) and 8 – 21 MPa (points B and C in Fig. 7.4c), respectively. This means that in 80% of the total pore space (which consists of pores smaller than 12 nm) the crystallisation pressure amounts to 8 – 21 MPa, which is significantly lower than the pressure in the remaining larger pores (20 – 52 MPa, Fig. 7.4c). The effect of the surface energy is thus significant in the case of the Belchen Tunnel. By the same line of argument, it can easily be seen from Figures 7.4c and 7.4d that this effect is less important in the case of Chienberg Tunnel. The sample from this tunnel has considerably larger pores, probably due to the smaller depth of sampling (*cf.* Section 6.2.2). Furthermore, the Chienberg Tunnel crosses the so-called Tafeljura, while the rock in the Belchen Tunnel belongs to the intensively folded part of the Jura mountains, the Faltenjura (*cf.* Section 6.1), where high tectonic stresses may have caused additional compaction [146].

In conclusion, the thermodynamically possible range for the crystallisation pressure of gypsum is very wide even under the relatively simple conditions of a closed system. In the absence of surface energy effects or of interactions with clay minerals, the crystallisation pressure is equal to 20 – 50 MPa (Fig. 7.4a for $T = 20\text{ °C}$), depending on how much the pressure on the anhydrite particles increases due to the pressure exerted by the gypsum crystals upon the pore walls.

7.2.4 Ion concentration in open systems

In an open system, additional uncertainties exist with respect to the actual ion concentration. Consider, for example, the relatively simple conditions of a rock sample that is placed in an oedometer device and immersed in a container filled with distilled water. Under the conditions of a swelling pressure test, the volume of the specimen is kept constant and consequently water uptake by and seepage flow towards the specimen is negligible. However, even in the absence of advection, it is possible under certain conditions (*cf.* Section 5.3) that the ions produced by the dissolution of anhydrite can move by diffusion out of the oedometer, towards the water of the container. The ion concentration in the sample is governed by the combined effect of the anhydrite dissolution rate and the ion diffusion rate. If the diffusion rate is very high compared to the rate of anhydrite dissolution, then the actual ion concentration and thus the crystallisation pressure of gypsum will be very low or even zero. On the other hand, if the diffusion is very slow, then the situation will be close to that of the closed system discussed above.

In general, ion transport may also occur by advection (*cf.* Section 5.4). This is particularly true *in situ* due to seepage flow around the tunnel. Seepage flow introduces an additional source of uncertainty making a theoretical determination of the ion concentration and thus also of the crystallisation pressure *in situ* extremely difficult. The ion concentration in a rock element might vary from practically zero to values even higher than the anhydrite equilibrium concentration. Theoretically, anhydrite should then also start to precipitate or – if crystal growth is constrained – exert a crystallisation pressure. However, according to Klepetsanis and Koutsoukos [167], who investigated the precipitation of calcium sulphate within the temperature range $T = 20\text{ °} - 60\text{ °C}$, the only phase forming under these conditions is gypsum. The reason is that anhydrite precipitates much more slowly than gypsum. According to Fletcher and Merino [168], who evaluated the experimental results of Liu and Nancollas [85], the kinetic rate constant of anhydrite precipitation is lower than that of gypsum precipitation by a factor of about 200.

In view of the practical difficulties of producing a reliable estimate of ion concentrations *in situ*, we will estimate the crystallisation pressure based upon the concentrations measured in the three Swiss tunnels crossing the Gypsum Keuper formation mentioned in Section 6. Table 7.1 focuses only on the most common ions identified in water chemical analyses, *i.e.* calcium- (Ca^{2+}), sulphate- (SO_4^{2-}), sodium- (Na^+) and chloride-

(Cl) ions. Data from a number of chemical analyses were available for the present study. However, in order to get meaningful results we considered only measurements that included data for all of the aforementioned ions (not just for some of them). As mentioned above, crystallisation pressure increases with the concentration of calcium and sulphate ions and decreases with the concentration of foreign ions (*i.e.* mainly sodium and chloride in the present case). Based on the concentrations (columns 4 to 7 of Table 7.1) and assuming, for all three tunnels, that the temperature $T = 20$ °C, water activity is equal to 1, pore water pressure is atmospheric and the interfacial effects are negligible, Eq. (7.1) leads to crystallisation pressures up to 7.25 MPa for the Belchen Tunnel, 14.5 MPa for the Chienberg Tunnel and 4.73 MPa for the Adler Tunnel (column 8 of Table 7.1). For comparison, the results from the last section showed crystallisation pressures in a closed system amounting to 20 – 50 MPa.

Table 7.1 Measured ion concentrations and calculated crystallisation pressures for three Swiss tunnels in the Gypsum Keuper formation

Tunnel	Sample	Sulphate SO_4^{2-} [mg/l]	Calcium Ca^{2+} [mg/l]	Sodium Na^+ [mg/l]	Chlorine Cl^- [mg/l]	p_c [MPa]
Belchen [169]	Collecting box 1 (19.6.02)	2174.4	566.1	638	335.6	3.27
	Collecting box 1 (21.8.02)	2774.2	553.8	808	484.1	7.25
	Collecting box 3 (24.7.01)	2565	752.9	2628	2319	6.16
Adler [170]	Sample No. 9505819	1864	602	42	196	4.73
	Sample No. 95002582	1686	577	64	103	1.61
Chienberg [171]	Field No. O1 (Tm 1003)	2000	620	16	20	7.83
	Field No. O2 (Tm 1059)	1800	580	15	34	3.79
	Field No. O10 (Tm 1160)	1600	610	14	18	2.41
	Field No. O12 (Tm 1196)	3500	550	420	84	14.50
	Field No. 15 (Tm 862)	1750	860	200	41	10.80
	Field No. 16 (Tm 862)	2050	750	244	71	11.74

The circulation of ions by advection and/or diffusion may clearly be significant for the crystallisation pressure, as it appears to reduce ion concentrations to values lower than the anhydrite equilibrium concentration (which prevails in closed systems), thereby also reducing the driving force for gypsum precipitation (*cf.* Section 4.2.1).

7.3 Macroscale

7.3.1 Measured swelling pressures in laboratory tests

The macroscopic swelling pressure is the pressure developing at the scale of a rock specimen. Table 7.2 provides an overview of measured values reported in the literature. All the tests have been performed in oedometer devices under volume constraint, except for the early laboratory investigations by Sahores [101], who used dilatometers.

According to Table 7.2, swelling pressures of up to 10 MPa were measured in laboratory tests, with the mean value being less than 6 MPa. The clay and anhydrite content seem to be significant for the pressure. In spite of the optimum watering conditions prevailing in the laboratory, the testing times were usually very long. For example, the tests on samples from the Freudenstein Tunnel took more than 20 years [141]. As a consequence of the long testing times, relatively few tests have been performed, thereby raising doubts as to how representative the results are for an entire rock mass. In addition, tests were

often terminated before reaching a steady state, which means that the measured pressures may not be the maximum ones.

Table 7.2 Measured swelling pressures at the scale of a specimen

Sample place	Test duration [months]	Swelling pressure [MPa]	Remarks
Belchen Tunnel, Switzerland [22]	8-9	< 3.8	
Belchen Tunnel, Switzerland [172]	≈ 24	> 5	
Hauenstein Tunnel, Switzerland (30-70% anhydrite, 5-20% clay and < 25% quartz, dolomite, magnesite) [173]	> 24	4.7	Maximum swelling pressure developed perpendicular to the foliation plane in a sample with clay content 5%
Adler Tunnel, Switzerland [174]	≈ 60	7.1	
Belchen, Adler and Chienberg Tunnel, Switzerland [21]		< 4.6	Maximum swelling pressure developed for clay content of 10-15%
Nagra-borehole Weiach, Switzerland [102], [13]	≈ 24	< 4.5	Maximum swelling pressure developed for 10-15% clay and 70-75% anhydrite
Exploration gallery of the B-14 Heslach Tunnel, Germany [175]	48	6.8	
Freudenstein Tunnel, Germany [176]	48	> 7	Tests not completed
Freudenstein Tunnel, Germany [141]		7 – 10	Swelling pressure could not be determined explicitly
Freudenstein Tunnel, Germany [177]	240	9.6	
Artificial sulphatic claystones (15% clay, 85% anhydrite) [21]		< 7.9	
Artificial anhydrite-montigel (a swelling clay) and anhydrite-gypsum mixtures [162]		5	Maximum swelling pressure developed for 15% montigel - 85% anhydrite
Massive anhydritic rock with sulphates as accelerators [101]		1.6	Swelling pressure determined by extrapolation of the results of dilatometer tests

7.3.2 Model for the theoretical estimation of macroscopic swelling pressure

Even with the above-mentioned experimental uncertainties, it is remarkable that the measured macroscopic swelling pressures σ_s are in general significantly lower than the crystallisation pressure p_c of gypsum (a few MPa versus tens of MPa in a closed system). This can be attributed either to the presence of foreign ions (*cf.* Section 7.2.4) or to the interaction between the growing crystals and the surrounding matrix. We will examine here the second effect by means of a computational model for macroscopic swelling pressure. The model accounts in a simplified way (similar to that of the model in Section 6) for the interaction between the growing gypsum crystals and the surrounding matrix.

In a specimen whose expansion is prevented by the oedometer apparatus, the gypsum exerts a pressure upon the pore walls because the rock matrix provides a resistance to gypsum growth. The counterpressure of the matrix may be higher or lower depending on its stiffness. Gypsum growth will continue as long as this counterpressure is lower than the pressure required for equilibrium, *i.e.* than the crystallisation pressure p_c according to Eq. (7.3). During this process, the swelling pressure of the rock specimen (*i.e.* the pressure developing along its constrained boundary) will also increase. This will happen more or less rapidly depending on the stiffness of the matrix and on the spatial distribution and quantity of growing crystals. The swelling pressure at the end of this

process will generally be lower than the pressure p_C , because the latter acts locally at the walls of the pores with gypsum growth. The difference will be significant if the growing gypsum crystals are sparsely distributed in the rock matrix.

The interaction between the growing gypsum and the surrounding rock matrix is studied with the aid of a cavity expansion model, where the expanding cavity and the solid material represent the growing gypsum and the matrix, respectively. A spherically symmetric model will be considered (Fig. 7.5). The underlying simplifying assumptions are: the expanding cavities are regularly distributed on a grid in a densest packing lattice; they are spherical and have a uniform initial radius a ; they expand uniformly (*i.e.* their boundaries experience the same radial displacement u_a).

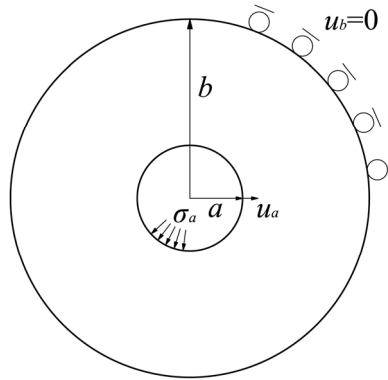


Figure 7.5 Spherical cavity expansion model.

The spherical computational domain of radius b represents the matrix around each expanding cavity. Obviously, the radius b is related to the volume fraction δ of the expanding cavities. For the ideal spatial arrangement of expanding cavities of uniform size the following relationship applies [8]:

$$b/a = \left[\pi / (3\sqrt{2}\delta) \right]^{1/3}. \quad (7.6)$$

A zero radial displacement is prescribed at the outer surface of the sphere as a boundary condition. The stress at the outer boundary of the model corresponds to σ_s , while the stress σ_a at the cavity boundary is equal to the pressure exerted by the growing gypsum upon the surrounding matrix. The rock is considered as a linearly elastic material with zero tensile strength.

Assuming that the entire ground has failed in tension in the circumferential direction, the following relation applies (in order to satisfy equilibrium in the radial direction):

$$\sigma_s = (b/a)^{-2} \sigma_a. \quad (7.7)$$

This condition expresses the static equilibrium between the gypsum and the matrix. It must be addressed simultaneously with the condition of thermodynamic equilibrium between anhydrite and gypsum (Eq. 7.3). In order to solve the system of Eqs. (7.3), (7.6) and (7.7), additional relationships linking p_G and p_A with σ_s and σ_a are required. The missing relationships depend on the locations of gypsum growth. In this respect, two borderline cases can be distinguished, depending on how rapidly the diffusive ionic transport takes place inside the specimen.

If diffusion occurs rapidly relative to the dissolution and precipitation reactions (1st borderline case), then the ions produced by anhydrite dissolution will increase the concentration uniformly everywhere in the pore space and gypsum will grow in all pores. In this case the expanding cavities are identical with the pores. Consequently, the fraction of the expanding cavities corresponds to the porosity ($\delta = \phi$), the pore wall stress is equal to the crystallisation pressure ($\sigma_a = p_G$) and the anhydrite particles will experience the

overall swelling pressure ($p_A = \sigma_s$). The condition of thermodynamic equilibrium (Eq. 7.3 with $a_w = 1$ and $\gamma_G/r_G = 0$, *i.e.* neglecting the effects of clay-water interactions and surface energy) in combination with Eqs. (7.6) and (7.7) leads to the following expression for the macroscopic swelling pressure:

$$\sigma_s = \frac{(T - T_0) \Delta_{r,GA} S^0 - \Delta_{r,GA} G^0}{V_G^0 (3\sqrt{2}\phi/\pi)^{-2/3} - V_A^0} \quad (7.8)$$

On the other hand, if diffusion occurs very slowly (2nd borderline case), then the gypsum will grow only in the pores next to the dissolving anhydrite particles. In order to simplify the geometry of the problem, we regard the expanding gypsum-filled pores as being 'smeared' over the surface of the anhydrite particles. The expanding cavities are then the spaces that are occupied by the anhydrite particles and their gypsum 'coat'. In this case δ is equal to the volume fraction ϕ_A of anhydrite particles. As the cavity expansion model smears the expanding pores over the entire surface of the anhydrite particles, the average pressure σ_a acting on them must be lower than p_G . The ratio of σ_a to p_G can be taken equal to the percentage of the anhydrite surface area that is in contact with the growing crystals. Assuming densest packing, $\sigma_a / p_G = (\pi\sqrt{3}/4)^{1/3} \phi^{2/3}$ [8]. This equation in combination with Eqs. (7.3), (7.6) and (7.7) leads to the following expression for the macroscopic swelling pressure:

$$\sigma_s = \left(3\sqrt{2}\phi_A/\pi\right)^{2/3} \frac{(T - T_0) \Delta_{r,GA} S^0 - \Delta_{r,GA} G^0}{V_G^0 (\pi\sqrt{3}/4)^{-1/3} \phi^{-2/3} - V_A^0} \quad (7.9)$$

Figure 7.6 shows the macroscopic swelling pressure σ_s as a function of the porosity ϕ for $T = 20$ °C and the two mentioned borderline cases, *i.e.* gypsum growth in all pores (solid line, Eq. 7.8) or only next to the anhydrite particles (dashed lines, Eq. 7.9). For the typical porosity range of anhydritic claystones (5-10% according to MIP test results, see Section 6.2), $\sigma_s \approx 1.5$ -6.5 MPa.

The macroscopic swelling pressures predicted by the simplified cavity expansion model are thus significantly lower than the microscopic crystallisation pressures (Section 7.2) and within the range of the experimental values for anhydritic claystones.

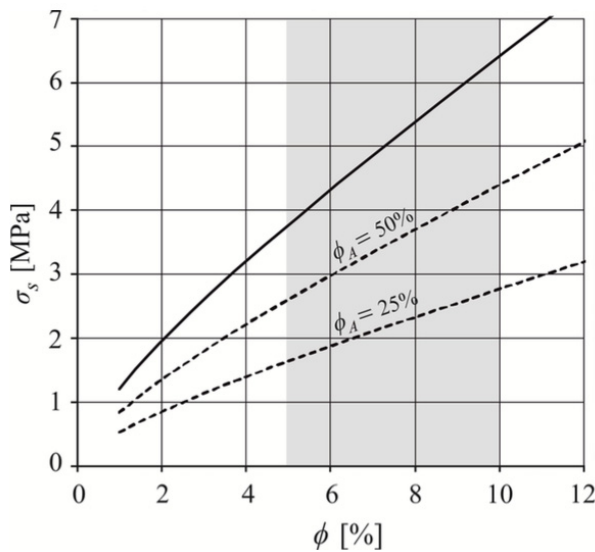


Figure 7.6 Macroscopic swelling pressure as a function of the porosity at $T = 20$ °C (solid line: gypsum growth in all pores, dashed lines: gypsum growth close to the anhydrite particles).

7.4 Megascale

Contrary to the conditions in swelling pressure oedometer tests, the development of swelling strains cannot be completely prevented *in situ*. Even a stiff lining may experience certain heave. In addition, intercalated non-swelling rock layers may accommodate some expansion of the swelling layers even if the overall volume of the rock mass remained practically constant. This can be seen, for instance, from the results of field measurements in the Belchen Tunnel, which showed that the development of swelling strains was accompanied by a heave of the invert arch and also by the partial compression of non-swelling layers (Fig. 7.7). For these reasons the swelling pressure *in situ* must be lower than the pressure developing under complete volume constraint in oedometer tests.

Large scale swelling tests, such as the one conducted in blocks XI to XIV of the Freudenstein exploratory gallery ([178], [95]), allow a straightforward determination to be made of the maximum swelling pressure *in situ*. In one Freudenstein field test, a constant support pressure was applied to the floor by means of prestressed anchors and the time development of the heave was monitored. Figure 7.8 shows the measured floor heave u as a function of the applied support pressure σ_s at different times from the start of the test. The extrapolations of the four lines tend to converge to a single point on the stress axis at about 1.2 MPa. This is the stress that would prevent floor heave completely, *i.e.* the swelling pressure *in situ*.

In general, an upper bound of the swelling pressure *in situ* can be determined from the bearing capacities of the linings of tunnels that cross heavily swelling rock but do not exhibit signs of overstressing [95]. Kovári [182] and Kovári and Vogelhuber [183] used this approach in order to analyse tunnels in Germany and Switzerland crossing the Gypsum Keuper formation and back-calculated *in situ* swelling pressures of 1 – 4 MPa. Serafeimidis [8] estimated (under the assumption of a unit safety factor) an upper bound for the *in situ* swelling pressure of about 5 MPa.

In conclusion, the existing observations seem to support the hypothesis that the swelling pressure *in situ* (megascale) is lower than the pressures developing in laboratory swelling tests (macroscale), although the difference is not as pronounced as the difference between the microscale and the macroscale.

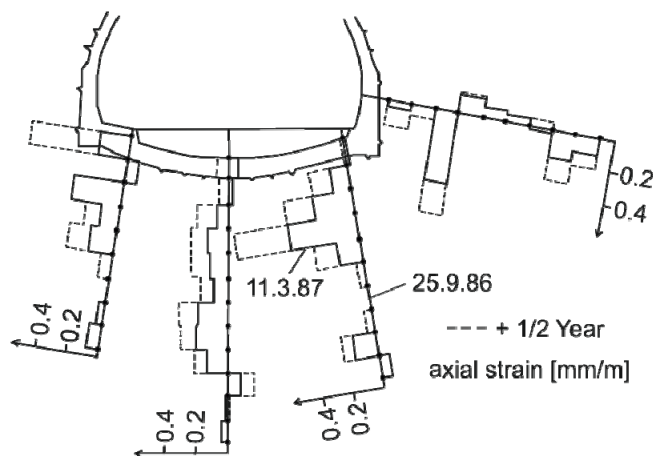


Figure 7.7 Strain profiles measured in the Belchen Tunnel (after [179]).

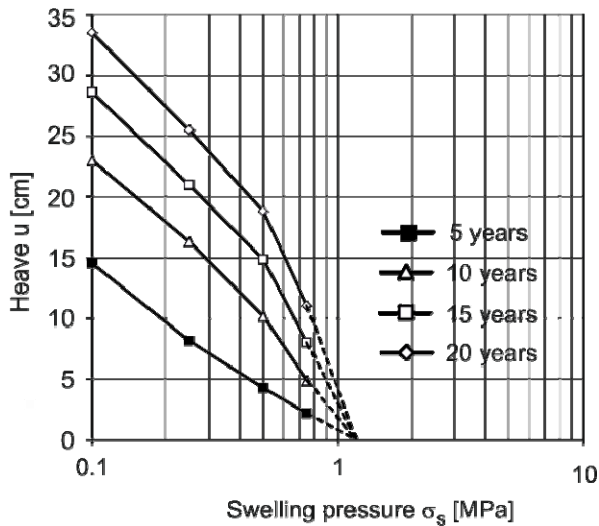


Figure 7.8 Floor heave as a function of the support pressure σ_s (5, 10, 15 and 20 years after test begin) in blocks XI to XIV of the exploratory gallery of the Freudenstein Tunnel ([180], [181] and [177]).

7.5 Conclusions

The swelling pressure depends on the scale considered. In this respect a distinction must be made between: (i), the pressure at the microscale (*i.e.* the crystallisation pressure of a single constrained crystal); (ii), the pressure at the macroscale (*i.e.* the pressure of a specimen in an oedometer test); and, (iii), the pressure at the megascale (*i.e.* the pressure developing upon a stiff invert lining *in situ*).

The factors affecting crystallisation pressure were investigated by means of thermodynamic computations. We considered different scenarios with respect to oversaturation for both closed and open systems and concluded that crystallisation pressure can vary across a very wide range.

In order to study the macroscopic pressure we used the cavity expansion model, which accounts in a simplified manner for the interaction between a growing crystal and the surrounding matrix. This model is able, in spite of its simplicity, to explain why the swelling pressures observed in laboratory tests are lower by one order of magnitude than the crystallisation pressure. The computations indicate, furthermore, that the development of swelling pressure in most cases does not cease until thermodynamic equilibrium is reached. The process may stop before reaching thermodynamic equilibrium (at a lower swelling pressure) only if the volume fraction of anhydrite is very low or if the rock matrix around the growing gypsum crystals is extremely soft. Finally, the data about the swelling pressure *in situ* are fraught with uncertainties, but seem to indicate that the *in situ* swelling pressures are in general lower than the pressures at the macroscale.

8 Overview of the experimental investigations

8.1 Introduction

The main aims of the experimental investigations were to determine the specific form of the constitutive equations, quantify some material constants appearing in them as well as to identify the basic mechanisms qualitatively (e.g. leaching, gypsum growth, clogging of pores, fracturing, and crystal growth in fragments). Some of these mechanisms concern coupled transport and chemical reaction processes. However, based on the findings of the theoretical investigations (Section 5), the role of transport was proven to be irrelevant for most practical situations. For this reason, the experimental investigations focused on the coupled chemo-mechanical processes, *i.e.* the development of stresses and strains during anhydrite to gypsum transformation (hereafter referred to as “AGT”), and on the investigations concerning the role of the clay matrix. Some preliminary experiments were performed to characterize the used materials (such as the determination of grain size distributions or porosity of the samples as well as mineralogical investigations). Additionally, experiments were carried out to determine kinetic constants, and investigate the effect of sealing of anhydrite due to gypsum growth on massive anhydrite.

In order to establish the constitutive equations, a large part of the experiments focused on elementary processes which needed to be studied isolated from other processes. These systematic investigations, however, could only be accomplished with artificial samples with clearly defined compositions. The artificial samples consist of mixtures of anhydrite and nearly non-reacting powders, which are herein referred to as “aggregates”. For the investigations concerning the role of the clay matrix, natural rock was used for the experiments.

The following section provides an overview of the performed experiments.

8.2 Description of the experiments

As described in Section 4, the *in situ* concentration of water containing calcium and sulphate ions is strongly dependent on various parameters, such as the temperature or the fraction of anhydrite and aggregates in contact with water. Furthermore, a thorough literature study was performed concerning the values of the reaction rate constants of anhydrite and gypsum (*cf.* Section 4). In order to check these parameters for the conditions prevailing in the laboratory, the electrical conductivity of water containing various mixtures of anhydrite and other materials was measured. This allows an estimation of the development of the *in situ* concentration over time. The influence of different types of aggregates and the amount of anhydrite in water on the development of the concentration is shown together with a description of the testing procedure in Section 10.

Pursuing Section 4.5, the formation of gypsum on massive anhydrite platelets in water is monitored with the aim of observing the effect of sealing of the anhydrite. These experiments are described in Section 11.

A central topic of the experimental investigations focuses on the relationship between AGT and the resulting swelling strains and stresses with the aim of understanding the involved coupled chemo-mechanical processes better. For this, multiple series of laboratory experiments under various boundary conditions (e.g. oedometric or completely constrained conditions) were performed with artificial samples (*cf.* Section 12).

A further important series of experiments concern the role of the clay matrix. It is being investigated, which amount of swelling of natural samples occurs due to swelling of clay and which amount is due to AGT (Section 13).

8.3 Description of standard analytical testing techniques used

8.3.1 Thermogravimetric analysis (TGA)

TGA is a thermal analysis method where the change of mass of a sample is recorded in dependency of temperature and time (*cf.*, *e.g.*, [184]). In cases where the qualitative mineralogical composition of a sample is known (such as artificial samples post swelling, which are known to contain anhydrite, gypsum and aggregates) TGA can be used to quantify the amount of gypsum in the sample. For this, a small representative specimen (17 - 20 mg) is heated (10°C per minute) and the change in weight is measured. At about 90° - 140°C a drop in the weight can be observed (see Appendix I), which is attributable to the reverse reaction of AGT: the gypsum dehydrates ($\text{CaSO}_4 \cdot 2\text{H}_2\text{O} \rightarrow \text{CaSO}_4 + 2\text{H}_2\text{O}$) and the now free water evaporates. By considering the molar masses of water and gypsum it is then possible to calculate the mass of gypsum in the sample post test and to determine (via back-calculation) the corresponding amount of dissolved anhydrite, as well as the mass of remaining anhydrite in the sample. TGA was performed by the authors on a Q50 Thermogravimetric Analyzer by TAInstruments [185] within the Institute for Building Materials at ETH, Zurich.

8.3.2 Microscopy

Some selected samples were investigated with scanning electron microscopy (SEM), where an electron beam scans the surface of a sample. From the interaction between the electrons and the sample, images of the topography of the samples (secondary electrons, SE) as well as images reflecting material contrast (back scattered electrons, BSE) can be collected (*cf.*, *e.g.*, [186]). SEM was mainly used to observe changes in structures or to identify the shape and form of gypsum within the samples after the experiments. Furthermore, SEM in combination with Energy-dispersive X-ray spectroscopy (EDX, with which the elements in a sample can be identified) was used *e.g.* to map out the distribution of calcium sulphates in the samples. The investigations were performed with Quanta 600 SEM and with a Quanta 200 3D with EDX by FEI.

Additionally, optical microscopes were used to study the surface of some samples (stereo microscope Leica M60) as well as to perform thin section analysis (transmitted light microscope Leica DM750 P in polarized light mode). The microscopic investigations were performed at the Institute for Building Materials at ETH, Zurich.

8.3.3 X-ray diffraction and Rietveld analysis (XRD analysis)

In the cases where it was necessary to determine the mineralogical composition of a sample, X-ray diffraction was executed and the composition was quantified via Rietveld analysis (*cf.*, *e.g.*, [187]). The investigations were performed in the Clay Lab of the Institute for Geotechnical Engineering at ETH, Zurich.

8.3.4 Mercury-Intrusion Porosimetry (MIP)

During MIP analysis mercury (as a non-wetting liquid) is pressed in a sample placed in the porosimeter. The required pressure for the mercury intrusion in a pore is a function of the contact angle and surface tension of the liquid and of the diameter of the pore. By recording the applied pressure and the volume of mercury intruded in the sample, the porosity, pore volume and pore size distribution can be determined [150]. MIP was performed on some selected samples in the Clay Lab of the Institute for Geotechnical Engineering at ETH, Zurich; *cf.* Section 6.2.

8.3.5 Laserdiffractometry

The particle size distribution of the used powders was determined via laserdiffractometry, where the intensity of light scattered when passing through a particle in suspension is

used to calculate the particle size (Laser Particle Size Analyzer LA-950 by Horiba [188]; *cf.*, *e.g.*, [189]). Depending on the type of powder, it was either in suspension in distilled water (*e.g.* kaolin, quartz flour) or in isopropanol (*e.g.* anhydrite). The investigations were performed in the Clay Lab of the Institute for Geotechnical Engineering at ETH, Zurich.

9 Characterization of sample materials

9.1 Anhydrite

Both commercial anhydrite powder and natural blocks of nearly pure anhydrite (95-99%) was used for the experiments. The commercial anhydrite was purchased from Sigma-Aldrich (abbr. "SA"). The natural anhydrite stems from the stone-quarries in Bex (canton of Vaud) and Leissigen (canton of Bern) and from bore-cores originating from the new Bözberg-Tunnel (canton of Aargau). Depending on the type of test, either intact samples were sawed from the natural blocks and bore-cores (Section 11), or they were crushed, milled and sieved to create a powder to use in artificially created samples (Section 12.5). Table 9.1 shows the mineralogical compositions of some of the used natural samples (results from XRD analysis). The particle size distributions of the commercial anhydrite (dotted line) and the milled natural anhydrite (solid lines) were measured with laserdiffractometry and are shown in Figure 9.1. The density of the anhydrite is assumed to be 2.96 g/cm^3 (cf., e.g. [190]).

Table 9.1 XRD results of the anhydrite samples collected from natural resources (weight%)

Sample name	An	Do	Il/ Mu	K-F	Qu
Bex1	96.5	3.2			0.3
Bözberg1	98.8			0.3	0.9
Bözberg3	94.5	3.0	1.3	0.8	0.4
Leissigen12	97.9	1.5			0.6

Key: An=Anhydrite, Do=Dolomite, Il=Illite, Mu=Muscovite, K-F=K-Feldspar, Qu=Quartz

9.2 Aggregates

For the artificial samples (Section 12), anhydrite powder was mixed with either kaolin (Polwhite E China Clay, a high quality medium particle size kaolin produced from deposits in the south west of England [191], [192]; abbr. "PW"), ground limestone (nekafill 15 from Kalkfabrik Netstal AG [193]; abbr. "KM") or quartz flour (sikron from Sibelco Benelux [194]; abbr. "QM"). The particle size distributions of these aggregates are shown in Figure 9.1 (dashed lines).

Kaolin has a very low swelling potential compared to other so-called swelling clays (e.g. montmorillonite, vermiculite etc.). On the one hand, kaolinite has no significant negative structural charge, so that little or no water is adsorbed in the lattice (the cation exchange capacity is 1 - 10 meq/100 g [195] as opposed to, e.g., 70 - 120 meq/100 g in the case of montmorillonite, a swelling clay [196]). On the other hand, kaolinite has a small specific surface in contact with the water compared to swelling clays, i.e. the adsorption of water molecules due to electric load concentration is negligible (the specific surface of kaolinite is 10 - 30 m^2/g while that of montmorillonite amounts to 750 - 820 m^2/g (cf., e.g. [197], [198]). It should be noted, however, that kaolin, like any fine powdered and compacted dry material, can swell upon saturation due to reduction of suction pressure (cf., e.g. [199]). However, this swelling mechanism is much faster than the swelling caused by AGT and thus the two swelling mechanisms can be distinguished from one another.

The average mineralogical composition of the kaolin (Table 9.2) was obtained with Rietveld analysis. The density of the kaolin is 2.6 g/cm^3 ([191], [192]).

Table 9.2 XRD results of the kaolin, Polwhite E Chinaclay (weight%)

Sample name	Il/ Mu	K-F	Ka	PI	Qu
Kaolin	10	16	69	2	3

Key: Il=Illite, Mu=Muscovite, K-F=K-Feldspar, Ka=Kaolinite, PI=Plagioclase, Qu=Quartz

9.3 Anhydritic claystones

For the investigations concerning the role of the clay, natural rock samples are being used. The samples originate from bore cores from the Belchen Tunnel (cantons of Basel Country and Solothurn) and consist mainly of clay, anhydrite, quartz and further inert minerals, as shown from the XRD results in Table 9.3. The core samples BH3 were collected within the framework of the ASTRA project 2011.006, where the boring campaign is described [200]. These cores were unprotected against drying when collected for this research project. The core SB6 stems from exploratory drillings in the Belchen tunnel in 2009 [201], after which the cores were stored in the Horburgtunnel until collected for this research project in November 2012; *i.e.*, the humidity and temperature did not change much and therefore the cores could be preserved with a higher degree of saturation compared to the previous ones. The cores are depicted in Section 13.2.

Table 9.3 XRD results of the Belchen bore cores, avg (min-max) (weight%)

Sample name	An	Ch	Gy	Il / Mu	K-F	Ma	PI	Qu	S/C
Belchen BH3 3.1-3.4	50.1 (38-67)	6.9 (4-9)		12.4 (7-18)	4.4 (2-6)	11.7 (9-15)	1.0	5.5 (3-9)	8.9 (5-15)
Belchen BH3 4.4-4.5	62.0 (46-81)	7.0 (2-13)		5.8 (2.2-10)	2.1 (0-4)	13.7 (6-22)	0.4	3.5 (2-5)	5.9 (3-12)
Belchen SB6 1.25-1.56	50.7 (31-73)	2.3 (0-5)	27.6 (11-40)	3.2 (1.2-5.8)	2.3 (1-4)			5.7 (3-8)	8 (3-12)

Key: An=Anhydrite, Ch=Chlorite, Gy=Gypsum, Il=Illite, Mu=Muscovite, K-F=K-Feldspar, Ma=Magnesite, PI=Plagioclase, Qu=Quartz, S=Smectite, C=Corrensite

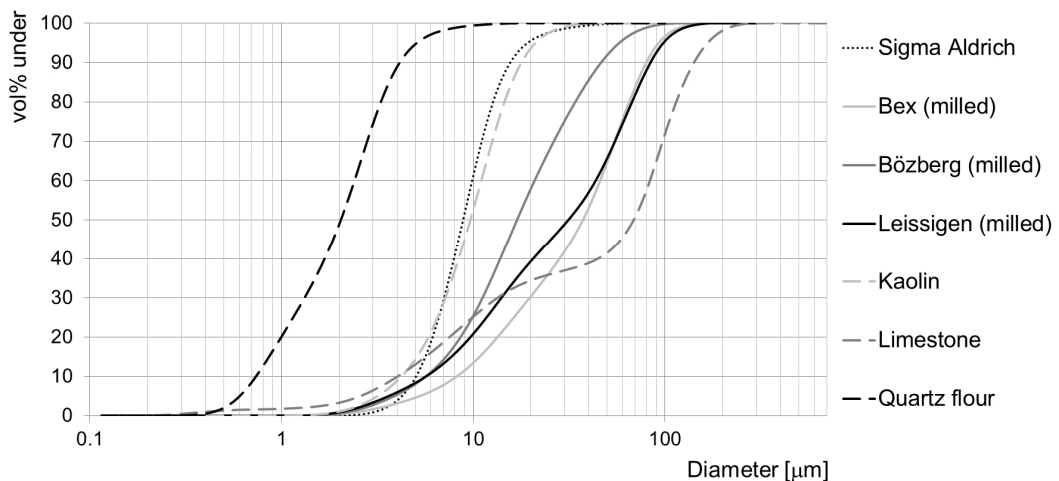


Figure 9.1 Particle size distribution of the used (granular) sample materials; results from laser diffractometry.

10 Solubilities

10.1 Introduction

In Section 3 the thermodynamic equations to calculate the equilibrium concentrations of anhydrite and gypsum under various boundary conditions were presented. Furthermore, simultaneous anhydrite dissolution and gypsum precipitation were discussed and the predictions based on the kinetic model (Section 4) were compared to literature values. In order to determine the kinetic parameters (particularly the reaction rate constants k_A and k_G in Eqs. 4.6 and 4.7) and verify the equilibrium concentrations for the conditions prevailing in the laboratory while considering the different kinds of sample materials used, the change of the ion concentration in water over time needed to be quantified.

The ion concentration in a solution can be determined in different ways, such as: via an ion-selective electrode (in this case calcium selective electrodes; *cf.*, *e.g.* [76]), titration with EDTA (*cf.*, *e.g.* [76], [202]), ICP-OES analysis (*cf.*, *e.g.* [203], [204]), gravimetry (*cf.*, *e.g.* [205]), or with quartz crystal microbalance (*cf.*, *e.g.* [206]). However, many of these methods require samples from the investigated solutions to be sacrificed and are arduous in their application. In this research, the main aim was to observe the change in concentration over time for various mixtures, which required a large amount of samples and the ability to measure the concentration within the same solution at various points in time. For this reason, the concentration was determined indirectly by repeatedly measuring the conductivity of each solution. The conductivity is a colligative property of the solutions, *i.e.* it is dependant only on the amount of dissolved ions in the water and not on the type of ions dissolved. Therefore, the change in concentration over time could be observed for varying conditions and the expected equilibrium concentrations could be verified with these experiments. For solutions with concentrations lower than $c_{eq,G}$ (2.05 g/l at room temperature), a linear relationship between the total dissolved solids and the conductivity is expected. This linear relationship was verified by dissolving clearly defined amounts of anhydrite up to 2 g/l in water and measuring the electrical conductivity of the solution. All other experiments are calibrated considering this relationship (shown in Section 10.3, Figure 10.2).

10.2 Experimental procedure

The powders mentioned in Sections 9.1 and 9.2 were mixed with either 100 ml or 250 ml of demineralized water. Immediately after adding water, the conductivity of each solution was measured with a SevenMulti pH meter from Mettler Toledo with a conductivity expansion unit [207]. The measurements were repeated at multiple points in time (up to several months). For every measurement the conductivity was noted before, immediately after and *ca.* ten minutes after shaking the bottles containing the mixtures. As will be seen in the next section, shaking the bottles affected the conductivity of each mixture to a different extent.

On the one hand, various amounts of commercial anhydrite SA (Section 9.1) were dissolved in distilled water, *i.e.* 0.5 / 1 / 2 / 2.5 / 3 / 4 / 8 / 32 g/l. On the other hand, the influence of the aggregates (Section 9.2) on the dissolution of anhydrite and precipitation of gypsum was investigated for the following mixtures: 4 g/l SA and 6 g/l PW / KM / QM; 4 g/l SA and 18 g/l PW / KM / QM; 32 g/l SA and 48 g/l PW / KM / QM.

At the temperatures prevailing in the laboratory, *i.e.* *ca.* 20°C, the expected equilibrium concentration of gypsum is 2.05 g/l (15.1 mol/m³), that of anhydrite 3.15 g/l (23.3 mol/m³). The latter value will not be reached during the tests, since gypsum precipitation occurs simultaneously and more rapidly than anhydrite dissolution (*cf.* Section 4.2).

In order to investigate the influence of the particle size of anhydrite, it was sieved through a 20 µm sieve using ethanol (the maximal grain size of SA is 40 µm). Two additional conductivity experiments were performed with the fractions larger and smaller than

20 μm . Additionally, a mixture was produced with 3 g/l anhydrite and 3 g/l gypsum as seed material (which was obtained from previous hydration of the same anhydrite).

10.3 Results

Figure 10.1 shows the results of the conductivity measurements made from the solutions where up to 2 g/l of anhydrite was dissolved, *i.e.* with a concentration lower than $c_{\text{eq,G}}$. The maximal values of these conductivity measurements are plotted against the amount of initial anhydrite mixed in water in Figure 10.2 (as well as the maximal values from all other conductivity tests where more anhydrite was dissolved, see Figure 10.3 to Figure 10.6). From the values below 2 g/l a clear linear relationship between conductivity and concentration can be seen. The established linear relationship can be used for the quantification of the *in situ* concentrations observed during the other tests with an initial amount of anhydrite greater than $c_{\text{eq,G}}$ in the cases where only anhydrite was used. It is assumed that this relationship remains also when one of the aggregates is added to the mixture, however for a definite quantification of the *in situ* concentration this needs to be verified with other measures (*e.g.* with a calcium selective electrode).

From the theoretical values of the equilibrium concentrations ($c_{\text{eq,A}}$, $c_{\text{eq,G}}$), the corresponding values for the conductivity can be obtained. Therefore, the conductivity corresponding to the equilibrium concentration of anhydrite is estimated to be at 3.1 mS/cm (this value is indicated also in Figure 10.2. to Figure 10.6).

Figure 10.3 shows the results of the conductivity experiments performed with varying amounts of anhydrite powder (no aggregates), whereas Figure 10.4 shows the conductivity over time for mixtures of anhydrite and one of the three aggregates. Note that in the diagram on the far right (anhydrite and quartz flour) the time axis is scaled to twice the duration of the other two.

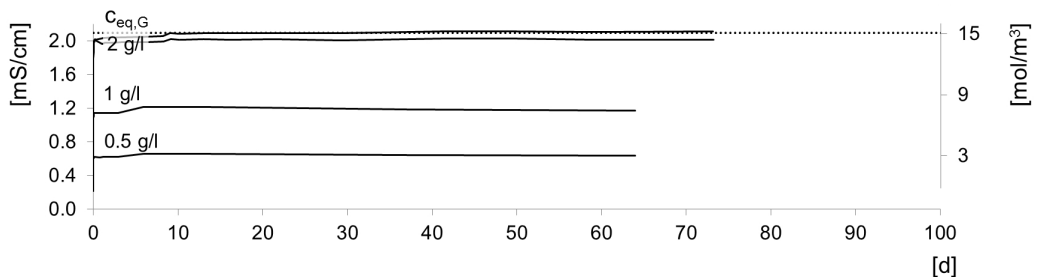


Figure 10.1 Results of conductivity measurements with only anhydrite up to 2 g/l. (The dotted line indicates the expected solubilities of gypsum.)

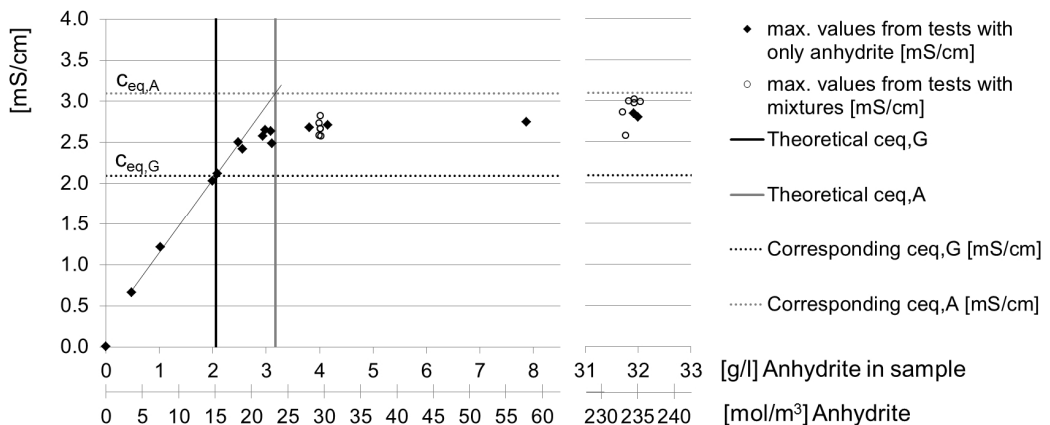


Figure 10.2 Maximal measured values for conductivity in [mS/cm] vs. amount of anhydrite used (in [g/l] and [mol/m³]) for each experiment.

Apart from the dashed curves in Figure 10.3 and Figure 10.4, all bottles were shaken as described in the previous section. The immediate influence of shaking varied among the samples, some not experiencing any change while others were acutely influenced. An example is given in Figure 10.5, where the left diagram shows a sample (4 g/l anhydrite and 6 g/l kaolin) which did not exhibit any change due to shaking, whereas the concentration of the sample in the diagram on the right (32 g/l anhydrite and 48 g/l kaolin) was affected immediately after shaking (these measurements are indicated by the circles). It can be seen that the conductivity resumes its value prior to shaking within a couple of minutes after shaking. This behaviour was strongest for the samples containing 32 g/l anhydrite and 48 g/l kaolin and 32 g/l anhydrite and 48 g/l quartz flour. However, the reason for which these samples were acutely affected stronger than the other samples was so far not investigated further. For sake of clarity, the data points after shaking were removed from the diagrams in the other figures in this section (*i.e.* for each session of measurements only the data point prior to shaking is plotted).

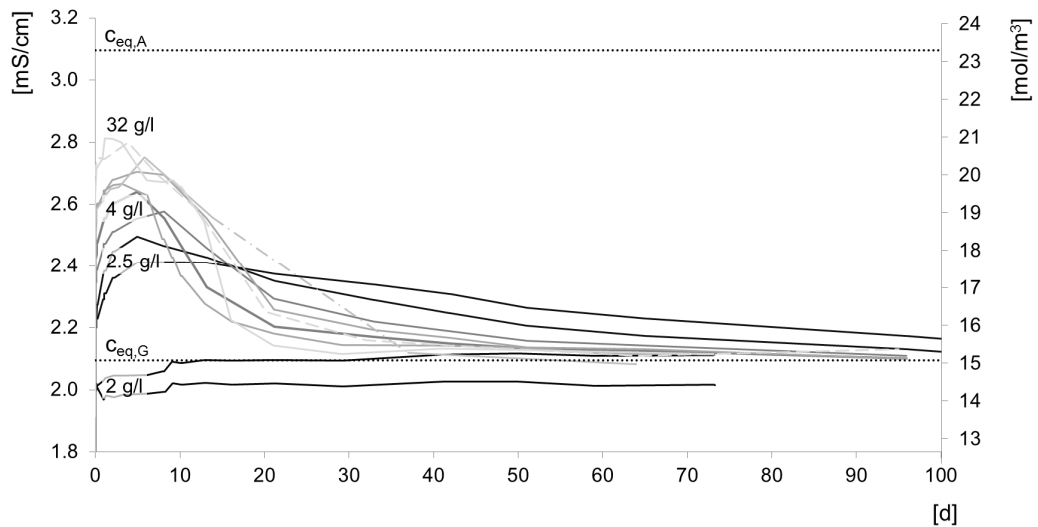


Figure 10.3 Results of conductivity measurements with only anhydrite. (Lighter lines indicate a higher anhydrite content compared to the darker lines. The dashed curve indicates a sample that was not shaken. The dot-dashed line indicates a longer period without measurement. The dotted lines indicate the expected solubilities of anhydrite and gypsum.)

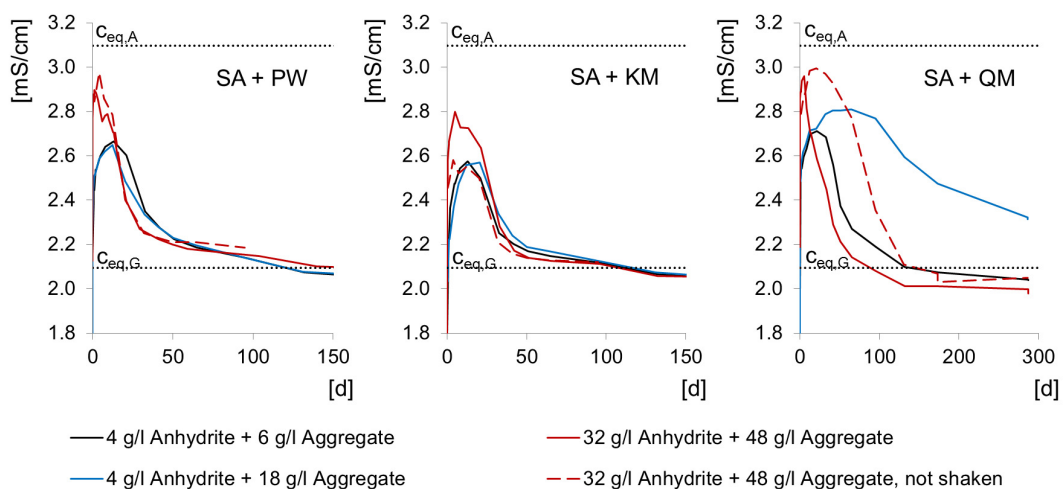


Figure 10.4 Results of conductivity measurements with mixtures of anhydrite and aggregates; from left to right: kaolin, limestone, quartz flour.

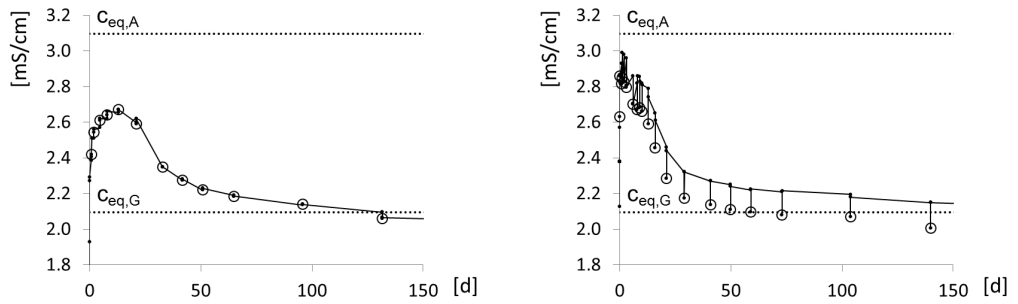


Figure 10.5 Acute influence of shaking: The circles correspond to the measurements taken immediately after shaking. Left: 4 g/l anhydrite and 6 g/l kaolin, right: 32 g/l anhydrite and 48 g/l kaolin.

It needs to be pointed out that the equilibrium concentrations indicated in Figure 10.4 and Figure 10.5 correspond to that obtained with the samples containing only anhydrite. They do not consider the influence of the aggregates on the conductivity, *i.e.* the values may differ from those indicated in Figure 10.4 and Figure 10.5.

The experiments containing 3 g/l anhydrite alone (of different grain sizes) and anhydrite mixed with 3 g/l gypsum are plotted in Figure 10.6. For a comparison with the results from Kontrec *et al.* [76], the results from one of her experimental data was added to the plot, where anhydrite (4 to 5 μm in size) and dihydrate (gypsum) with an initial mass ratio of 1:1 were added to deionized water.

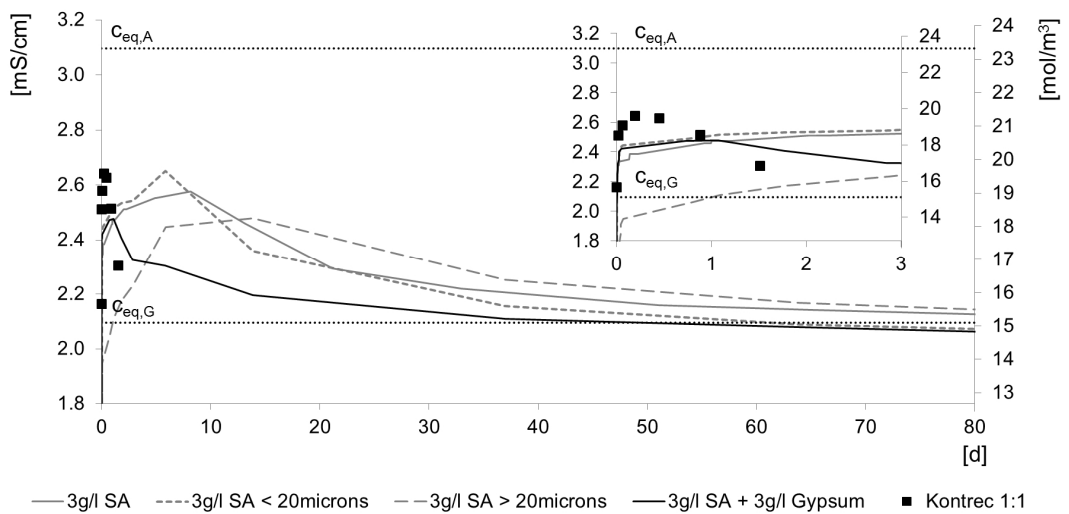


Figure 10.6 Results of conductivity measurements with 3 g/l of anhydrite under various conditions and comparison to the results from Kontrec *et al.* [76]. The image on the top right shows the same curves in greater detail for the first 3 days.

10.4 Discussion

As expected, a linear relationship between the maximally measured conductivity and the concentration of dissolved calcium and sulphate ions could be determined for solutions with low concentrations (Figure 10.2). It appears that this proportionality between conductivity and concentration even exceeds $c_{eq,G}$, *i.e.* up to 2.5 g/l anhydrite. For higher initial amounts of anhydrite the maximal measured value was 2.8 mS/cm (see Figure 10.2), which corresponds to 21.3 mol/m³, and in the case of mixtures with aggregates even 3.0 mS/cm was measured (*i.e.* 22.6 mol/m³).

In general, the experiments with more than 2 g/l of anhydrite (see results in Figure 10.3 to Figure 10.6) behaved as expected: at first the concentration increases rapidly, exceeds the equilibrium concentration of gypsum ($c_{eq,G}$), from which point on gypsum precipitation occurs parallel to anhydrite dissolution. Due to the decreasing difference between $c_{eq,A}$ and the concentration *in situ* as well as the consumption of ions due to gypsum precipitation, the rate at which the concentration increases slows down until it reaches a peak value (lower than $c_{eq,A}$). The *in situ* concentration then begins to decrease again due to further gypsum precipitation until it reaches its end value at $c_{eq,G}$.

It could further be observed that for samples with higher initial amounts of anhydrite not only the maximum values were reached faster (which corresponds to the findings in Section 4.4.3), but also the decrease in concentration over time occurred quicker (*cf.* Figure 10.3, grey lines vs. black lines).

From the experiments with mixtures (*i.e.* anhydrite and aggregates, Figure 10.4) it becomes evident that the type and amount of aggregate influences the anhydrite dissolution / gypsum precipitation process. The mixtures containing kaolin and limestone showed a fairly similar behaviour during the experiments. However, the maximally reached values were a bit higher in the case of kaolin and the concentration decreased quicker for higher initial anhydrite and kaolin-contents. Furthermore, the long-term behaviour of the concentrations of the anhydrite / kaolin mixtures seemed unaffected by shaking of the bottles (the red curves in the left diagram of Figure 10.4 are nearly identical), whereas the mixtures with limestone reached a much smaller peak value, when not shaken (dashed red curve in the middle diagram of Figure 10.4). It seems that the amount of kaolin or limestone barely changed the behaviour of the concentration in the water (comparison of black curves to blue curves in Figure 10.4, left and middle). However, in the case of quartz flour, it is clearly noticeable that a smaller ratio of initial anhydrite to quartz flour (*i.e.* 4 : 18 g/l vs. 4 : 6 g/l) slowed the gypsum precipitation process down by far. Furthermore, shaking the bottles containing quartz flour seemed to have increased the speed of the process (when comparing the dashed and the solid red lines in the right diagram of Figure 10.4).

As expected, Figure 10.6 indicates that the anhydrite dissolution / gypsum precipitation process occurs faster, if (a) smaller grain sizes of anhydrite are used and (b) gypsum is used as seed material.

However, it can be seen that the measurements performed by Kontrec *et al.* [76] (*cf.* Section 4.3) delivered a much faster change in concentration. On the one hand, this may be due to the far smaller grain size of anhydrite (4-5 μm , [76]), on the other hand, some parameters used in their research are unknown to us (*e.g.* the amount of anhydrite / gypsum used for this specific test or the size of the seed material).

The performed extensive, systematic investigation campaign did not reproduce the results for the reaction rate constants as given in Table 4.1, which were assumed from Kontrec *et al.* [76]. The duration of these experiments is far longer than those performed by Kontrec *et al.* [76]. The experiments are still ongoing, thus a concluding analysis of the results is outstanding.

11 Sealing

11.1 Introduction

As described in Section 5, gypsum precipitation occurs as a topochemical reaction in most cases, *i.e.* gypsum precipitates directly on the surface of dissolving anhydrite. The developing layer of gypsum slows further anhydrite dissolution down, since the dissolving ions must now diffuse through the layer of gypsum (*i.e.* the effect of sealing as described in Section 4.5).

In the interest of observing the effect of sealing experimentally, some platelets consisting only of natural anhydrite were inserted in water and the growing gypsum layer and gypsum needles were observed optically and the thickness of the gypsum layer was quantified with scanning electron microscopy. A prediction of the effect of sealing was made based on the kinetic model established for simultaneous anhydrite dissolution and gypsum precipitation (Section 4.5).

Two possible shapes of dissolving anhydrite particles were studied in Section 4.5: parallelepipeds and spherical particles. For these experiments anhydrite dissolution and gypsum precipitation on (large-scale) parallelepipeds of anhydrite is investigated (Figure 11.1). When totally immersed in water, the anhydrite will dissolve and since no inert material is considered, the gypsum is expected to precipitate directly on the surface of anhydrite. At any given time, the cross sections of the samples are expected to have changed according to Figure 11.1, right: a certain “thickness” of anhydrite has dissolved (s_A) and replaced by precipitated gypsum (s_G). The total thickness of the platelet (anhydrite and gypsum) is now $S_{G,A}$, whereas S_A is the thickness of the remaining anhydrite.

It was of interest to investigate the effect of sealing experimentally, while quantifying the thickness of the growing layer of gypsum on the anhydrite, and compare the results to the computational model.

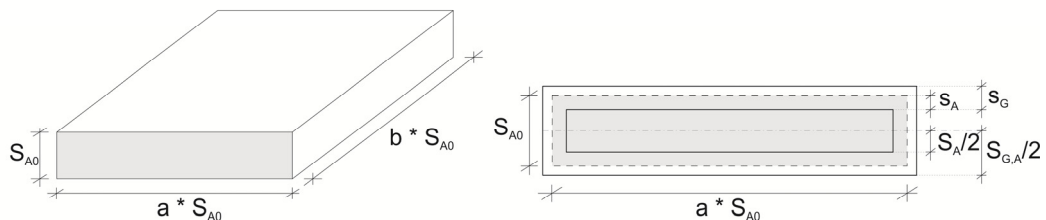


Figure 11.1 Left: Parallelepiped, right: Cross section area after anhydrite dissolution and gypsum precipitation.

11.2 Experimental procedure

The used samples are large-scale anhydrite platelets, which were cut from the natural rocks containing at least 95% of anhydrite as described in Section 9.1. The dimensions of the platelets were roughly $9 \times 22 \times 65 \text{ mm}^3$. The platelets were immersed in *ca.* $30 \cdot 10^3 \text{ mm}^3$ of water (saturated with respect to gypsum) in a container as shown in Figure 11.2.

Two series of experiments were performed, one at room temperature (20°C), one in a cooling box (5°C), at which the concentration gradient between $c_{eq,A}$ and $c_{eq,G}$ is higher, but the reaction rate constant will be smaller.

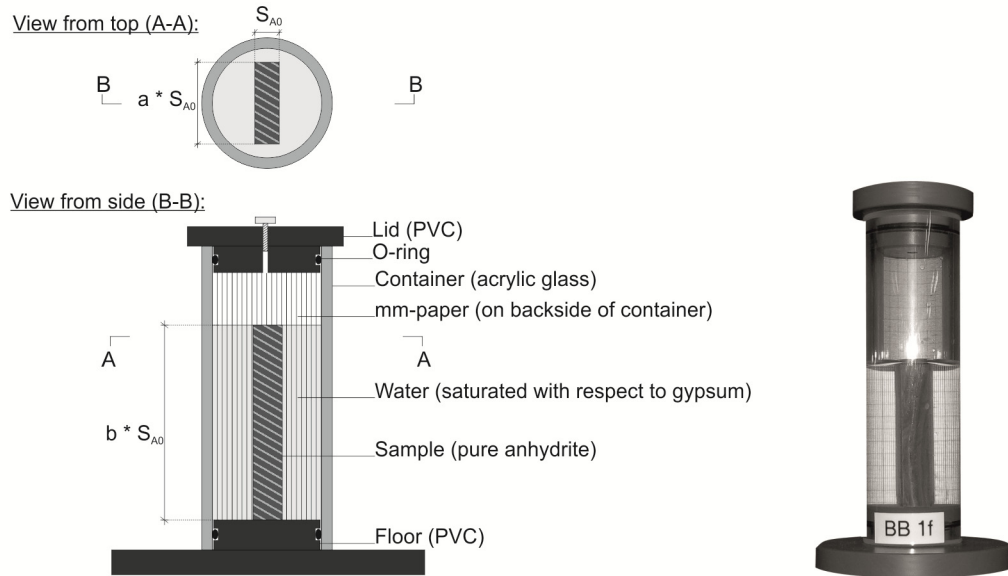


Figure 11.2 Test setup for the sealing experiments. (Left: conceptual sketch, right: example for an experiment, photograph). Typical dimensions were: $S_{A0} \approx 9 \text{ mm}$, $a \approx 2.4$, $b \approx 7.2$.

Every 1-2 months the samples are photographed and the change of the sample surfaces observed. One sample (from Bözberg, “BB 1f”) was extracted from a test at room temperature after 14 months and examined with a scanning electron microscope.

11.3 Results

11.3.1 Photography

Figure 11.3 shows the evolution of two exemplary samples, one at 20°C (Bözberg “BB 1f”) and one at 5°C (Bex 1b). Generally, all samples at 20°C produced clear clusters of (long) needles, as in the case of BB 1f. The samples at 5°C were however rather covered by a “fleece” of gypsum. At both temperatures, gypsum precipitation appeared to occur mainly in the lower area of the samples.

Unfortunately the cooling box malfunctioned after about 100 days and the water surrounding the 5°C -samples froze completely (the temperature was nearly at -40°C). They were then thawed and the experiments continued. No substantial change of the samples was observed.

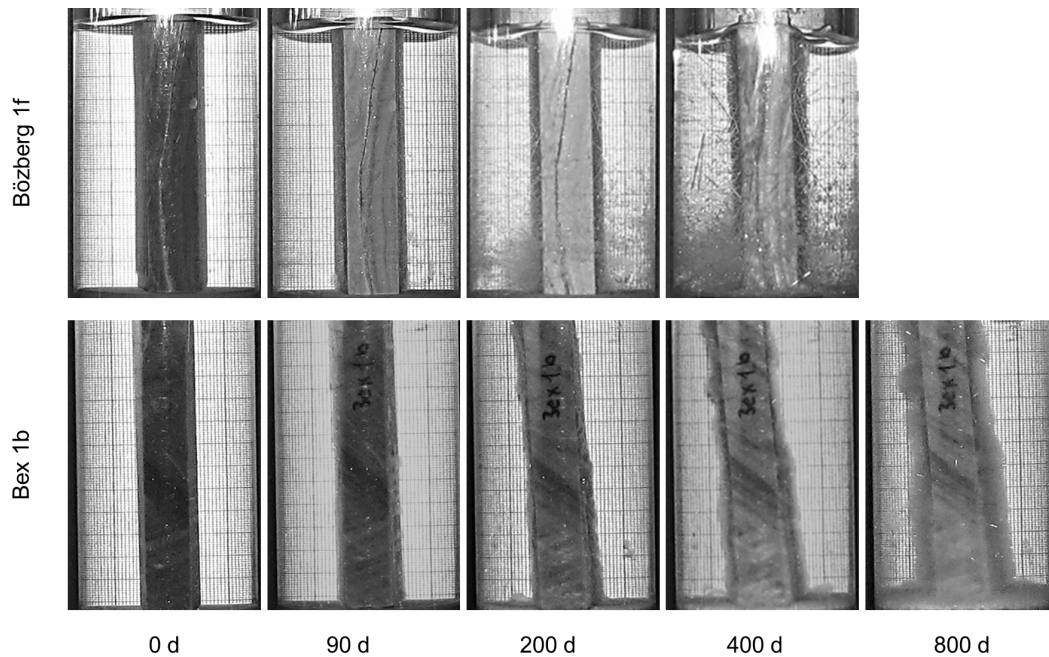


Figure 11.3 Photographs of two samples after various durations. Top row: BB 1f (Bözüberg) at 20°C, bottom row: Bex 1b at 5°C. (The distance between two vertical lines on the scale behind the samples is 0.5 mm.)

11.3.2 Microscopy

The last picture in the row of BB 1f was taken just before the sample was extracted for microscopic investigations. The sample was dried at 40°C and its lower half embedded in epoxy. From this, a specimen could be sawed off from the bottom for the investigations in the scanning electron microscope (see Figure 11.4).



Figure 11.4 Photographs of the sample BB 1f after embedding in epoxy (left) and after sawing (right).

A large scale “overview” image of a corner of the sample is shown in Figure 11.5, which gives a good impression of the overall structure along the edges. Due to the various densities of the minerals, the anhydrite (marked “A”) appears whiter than the gypsum (marked “G”) in the backscattered images while the pore space remains black. Therefore, one can distinguish between the rather compact inner core of anhydrite in the top area of Figure 11.5 and the outer layer of gypsum and cross sections of the gypsum needles. In certain regions a clearly defined border between anhydrite and gypsum can be identified (e.g. right edge in Figure 11.5 and in Figure 11.7), in others the border is more obscured

(e.g. bottom left edge in Figure 11.5, which is also shown closer in Figure 11.6, as well as the edge in Figure 11.8). In the latter case some anhydrite particles seem to appear in the “outer” gypsum layer. Therefore, the thicknesses of the “new” gypsum layer, s_G , and the receding anhydrite surface, s_A , cannot be clearly defined. This was attempted in Figure 11.6 to Figure 11.8, where some data concerning these thicknesses was gathered by measurements within the SEM images. s_{tot} indicates the difference between the new surface of the sample and the original (anhydrite) surface, and therefore corresponds to $s_G - s_A$.

The expected behaviour, with the receding anhydrite border and increasing gypsum layer, can be observed especially in Figure 11.8, where the precipitating gypsum filled the pores where anhydrite dissolved and also created a new outer layer consisting only of gypsum (no white anhydrite particles within the darker grey gypsum).

Figure 11.9 shows an area, where the anhydrite was clearly cracked (the cracks can also be seen in the SEM-specimen in Figure 11.4). The rather large cracks were originally hairline fissures, which seem to have been filled with gypsum. It appears that the gypsum crystals expanded the cracks further.

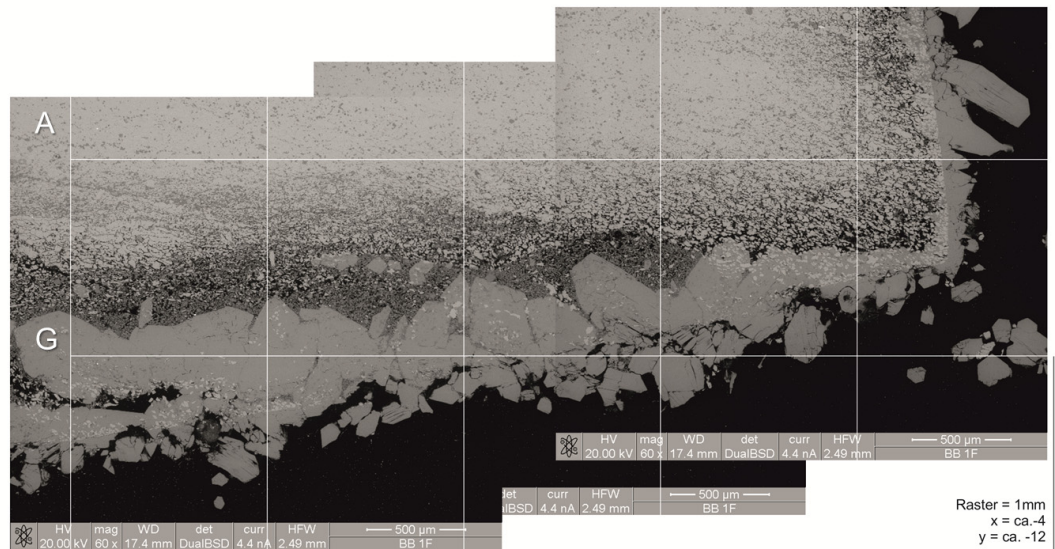


Figure 11.5 Large-scale SEM image (BSE) of a corner of the sample BB 1f (the grid indicates 1 mm).

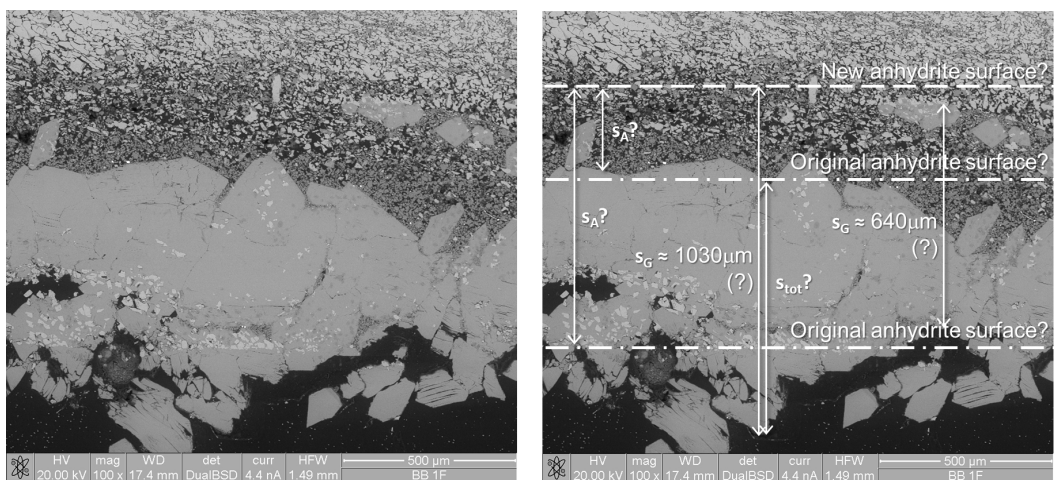


Figure 11.6 Small-scale SEM image (BSE) of the sample BB 1f. (The scale is indicated in the bottom right corner of each SEM image.)

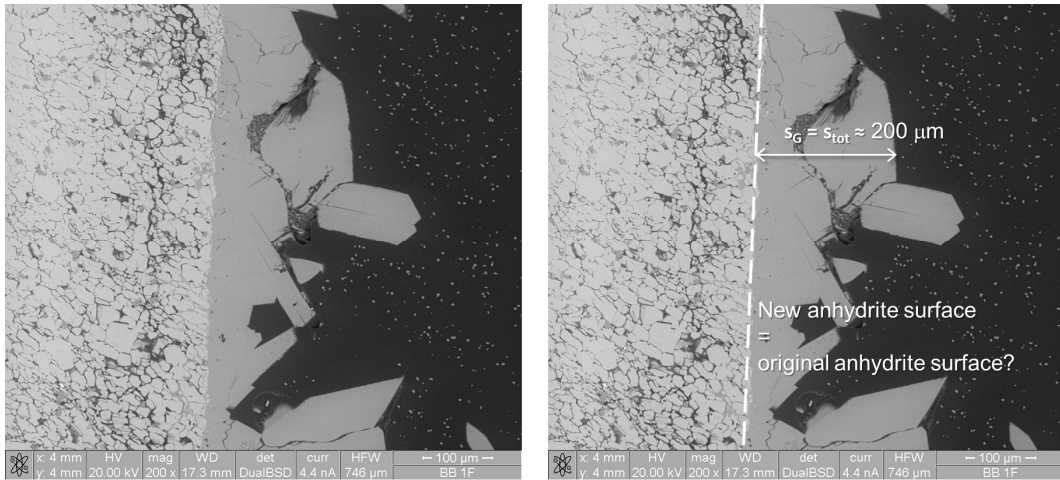


Figure 11.7 Small-scale SEM image of the sample BB 1f.

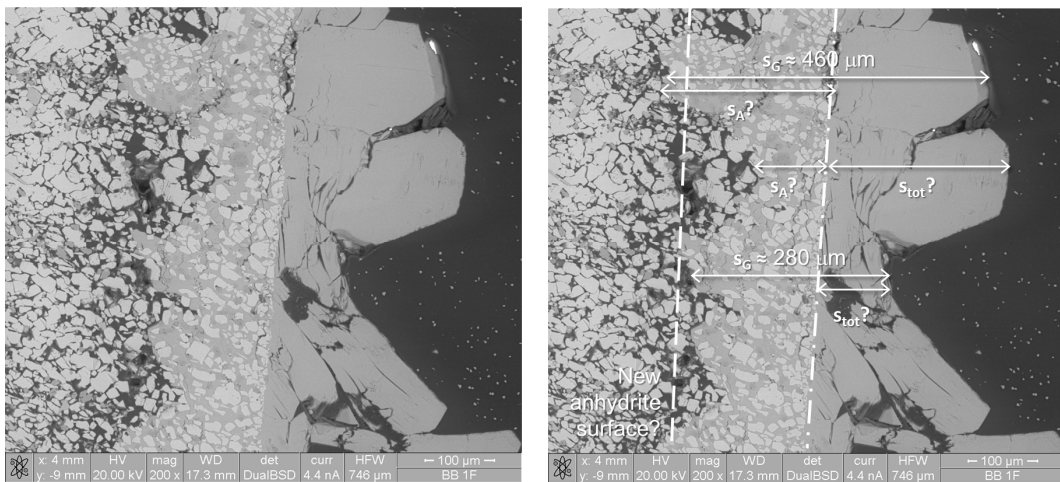


Figure 11.8 Small-scale SEM image of the sample BB 1f.

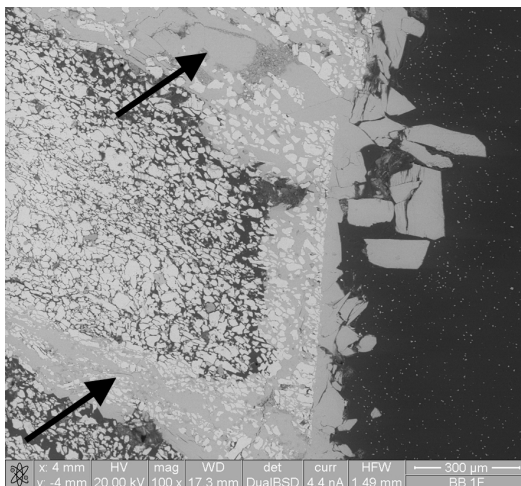


Figure 11.9 Small-scale SEM image of the sample BB 1f, gypsum precipitation in cracks (indicated by arrows).

11.3.3 Comparison to prediction

The theoretical change in anhydrite surface and gypsum coating was calculated by using the model from Section 4.5 and the geometries from these experiments. The main assumptions were taken from Section 4.5 with the following deviations: $c_{eq,A} = 23.3 \text{ mol/m}^3$, $c_{eq,G} = 15.1 \text{ mol/m}^3$ (which were calculated according to Section 3 for the prevailing conditions) and the porosity of the sealing gypsum layer is assumed to be $n_G = 0.1$. This value was chosen arbitrarily and its influence on the hydration time of anhydrite is discussed in Section 4.5.

The prediction, calculated based on the model and the assumptions above, as well as some measured values (indicated in the images on the right in Figure 11.6 to Figure 11.8) are shown in Figure 11.10.

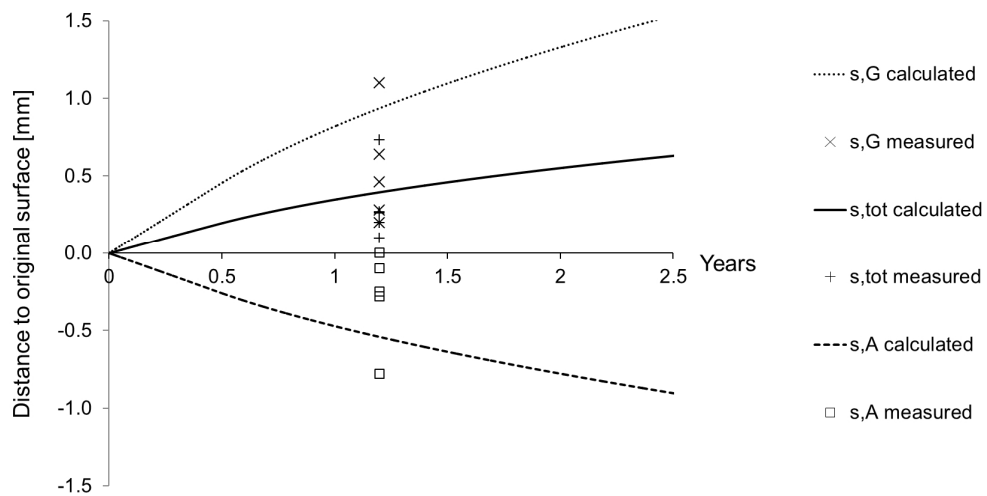


Figure 11.10 Thickness of anhydrite and gypsum layer over time (cf. Figure 11.1); prediction and measured values from SEM images.

11.4 Discussion

The experiments revealed an entirely different shape of gypsum precipitation at 5°C than at 20°C (“fleece” in the bottom row of Figure 11.3 vs. needles in the top row). This may be due to the fact that, for one, the diffusion rate is smaller at lower temperatures, and, that the concentration gradient ($c - c_{eq,G}$) is higher at lower temperatures (since $c_{eq,A}$ is higher at lower temperatures and may thus raise the value of c). The diffusion rate is dependent on the diffusion coefficient D , which can be described with the Stokes-Einstein equation:

$$D = \frac{k_B T}{6\pi\eta R_0} \quad (11.1)$$

where k_B , T , η , R_0 are the Boltzmann constant [J/K], the temperature [K], the dynamic viscosity of the solvent and the radius of the diffusing particle. Thus, the diffusion coefficient is 1.6 times smaller at 5 °C than at 20 °C and, consequently, the diffusion rate is slower at lower temperatures.

The dissolved ions also seem to sink slightly towards the bottom of the samples due to gravity and thus increase the ion concentration locally. Consequently, more gypsum is visible in the lower areas of the samples.

Furthermore, the SEM images of the cross section of BB 1f gave a first impression of the complexity of the sealing process: due to the receding anhydrite border a new pore space develops, which gets (at least) partly filled by gypsum. However, this border is usually not as clearly defined as anticipated. It proves to be difficult to quantify the effect of sealing in terms of thicknesses s_A , s_G , and s_{tot} . This becomes obvious when regarding the scatter of the measured values in Figure 11.10.

In order to quantify the thicknesses with less scatter, the samples would e.g. need to be embedded or subjected to some pressure so that the gypsum layer becomes more defined (less needles). Furthermore, more data needs to be collected in order to compare the behaviour of the samples better with the prediction. For example, cross sections at different levels of the samples would need to be investigated (as mentioned previously the gypsum seemed to precipitate mainly in the lower area of the samples) and multiple samples would need to be examined (for instance also those running at 5°C). Due to the fact that such a thorough, systematic SEM investigation programme of multiple samples at various points in time is extremely arduous, these questions were not pursued further within the scope of this research project.

12 Chemo-mechanical processes

12.1 Introduction

The establishment of a chemo-mechanical model which can take account of anhydrite dissolution, gypsum precipitation (*i.e.* the chemical reaction $\text{CaSO}_4 + 2\text{H}_2\text{O} \rightarrow \text{CaSO}_4 \cdot 2\text{H}_2\text{O}$) and also stresses and strains is necessary, *cf.* Section 1.

A general formulation for the chemo-mechanical model is given by Eq. (12.1), which connects the effective stress increments $\dot{\sigma}'_{ij}$ with the elastic strain increments $\dot{\epsilon}_{kl}^{EL}$. The latter is defined as the difference between the total strain increments and the strain increments due to plasticity and due to chemical reactions (see Eq. 12.2).

$$\dot{\sigma}'_{ij} = \mathbf{D}_{ijkl} \cdot \dot{\epsilon}_{kl}^{EL} \quad (12.1)$$

$$\dot{\epsilon}_{kl}^{EL} = \dot{\epsilon}_{kl} - \dot{\epsilon}_{kl}^{PL} - \dot{\epsilon}_{kl}^{CH} \quad (12.2)$$

The chemical strains due to AGT depend on changes of the volumes (and thus on the changes of the masses) of anhydrite and gypsum. For the sake of simplicity we assume that all dissolved calcium and sulphate ions from the anhydrite are used for gypsum precipitation (the rate of anhydrite dissolution is slower than that of gypsum precipitation, *cf.* Section 4) and that the ions are not transported by water (topochemical reaction). The chemically induced strains can therefore be expressed via the change in the mass of anhydrite and a single unknown material-specific tensor χ_{kl} :

$$\dot{\epsilon}_{kl}^{CH} = \frac{\chi_{kl}}{\rho_A} \cdot \dot{m}_A \quad (12.3)$$

The chosen strategy for establishing χ_{kl} is to perform multiple series of laboratory tests on samples containing anhydrite and that are subjected to water under various radial symmetric conditions, as shown in Figure 12.1. The set of boundary conditions on the left hand side of Figure 12.1 correspond to static oedometric conditions, where radial strains are prohibited and the axial deformation can be measured; in the middle sketch a sample is under complete constraint while the axial pressure is measured; the boundary conditions on the right hand side correspond to those of a “flexible” oedometer, where the axial and radial deformations are measured and the radial stress can be determined indirectly via the stiffness of the oedometer (see Section 12.8.2).

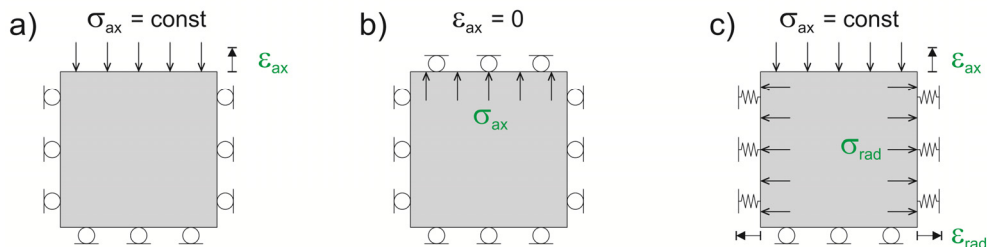


Figure 12.1 Investigated radial symmetric boundary conditions. a) Standard oedometric conditions, b) completely constrained conditions, c) “flexible oedometers”.

The elasticity tensor for the case of radial symmetric boundary conditions is determined by using Hooke’s linear elastic law and can be written as follows:

$$\mathbf{D}_{Triax} = \frac{E}{(1+\nu)(1-2\nu)} \begin{bmatrix} (1-\nu) & 2\nu \\ \nu & 1 \end{bmatrix} \quad (12.4)$$

The general formulation for the chemo-mechanical model as given in Eq. (12.1) can be formulated for radial symmetric boundary conditions, *i.e.* for stresses and strains in axial and radial directions, while inserting Eqs. (12.2)-(12.4) into Eq. (12.1). Hereby the principle of effective stresses is considered and it is assumed that no plastic strains occur:

$$\begin{bmatrix} \frac{\partial \sigma_{ax}}{\partial t} - \frac{\partial p}{\partial t} \\ \frac{\partial \sigma_{rad}}{\partial t} - \frac{\partial p}{\partial t} \end{bmatrix} = \frac{E}{(1+\nu)(1-2\nu)} \begin{bmatrix} (1-\nu) & 2\nu \\ \nu & 1 \end{bmatrix} \begin{bmatrix} \left(\frac{\partial \varepsilon_{ax}}{\partial t} - \chi_{ax} \frac{1}{\rho_A} \frac{\partial m_A}{\partial t} \right) \\ \left(\frac{\partial \varepsilon_{rad}}{\partial t} - \chi_{rad} \frac{1}{\rho_A} \frac{\partial m_A}{\partial t} \right) \end{bmatrix} \quad (12.5)$$

In the following, Eq. (12.5) is formulated for the boundary conditions shown in Figure 12.1, while assuming that the pore water pressure remains constant and equal to atmospheric pressure during each test.

For oedometric conditions (assuming the axial stress to be constant, the radial stress variable and – in the case of flexible oedometers, as in Figure 12.1c – the radial strain variable) Eqs. (12.6) and (12.7) are obtained for the rate of swelling strain in the axial direction and swelling stress in radial direction. These equations allow the factors χ_{ax} and χ_{rad} to be obtained separately based on the experimentally determined rates for axial strain, radial stress and anhydrite mass.

$$\frac{\partial \varepsilon_{ax}}{\partial t} = -\frac{2\nu}{(1-\nu)} \frac{\partial \varepsilon_{rad}}{\partial t} + \frac{1}{\rho_A} \frac{\partial m_A}{\partial t} \left(\chi_{ax} + \frac{2\nu}{(1-\nu)} \chi_{rad} \right) \quad (12.6)$$

$$\frac{\partial \sigma_{rad}}{\partial t} = \frac{E}{(1-\nu)} \left(\frac{\partial \varepsilon_{rad}}{\partial t} - \chi_{rad} \frac{1}{\rho_A} \frac{\partial m_A}{\partial t} \right) \quad (12.7)$$

However, in the case of standard oedometer cells (steel rings, as in Figure 12.1a), the radial strain $\varepsilon_{rad} = 0$, and it is not possible to measure the radial stresses. Therefore χ_{ax} and χ_{rad} are combined to a single unknown factor χ on the right-hand side of Eq. (12.8).

$$\frac{\partial \varepsilon_{ax}}{\partial t} = \frac{1}{\rho_A} \frac{\partial m_A}{\partial t} \left(\chi_{ax} + \frac{2\nu}{(1-\nu)} \chi_{rad} \right) = \chi \frac{1}{\rho_A} \frac{\partial m_A}{\partial t} \quad (12.8)$$

Under complete constraint (Figure 12.1b) the axial and radial strains are held constant while the axial stress is measured. Formulating Eq. (12.5) for these boundary conditions, again by combining χ_{ax} and χ_{rad} into the factor χ since the radial stress cannot be determined, the following relationship is obtained:

$$\begin{aligned} \frac{\partial \sigma_{ax}}{\partial t} &= -\frac{E(1-\nu)}{(1+\nu)(1-2\nu)} \left(\chi_{ax} + \frac{2\nu}{(1-\nu)} \chi_{rad} \right) \frac{1}{\rho_A} \frac{\partial m_A}{\partial t} \\ &= -\frac{E(1-\nu)}{(1+\nu)(1-2\nu)} \chi \frac{1}{\rho_A} \frac{\partial m_A}{\partial t} \end{aligned} \quad (12.9)$$

12.2 Overview of the experiments

First, the sample material and the sample preparation procedure needed to be determined. For this, simple free swelling tests were performed, where the swelling behaviour of various mixtures of anhydrite and aggregates was investigated (for reasons described in the next section, artificial samples were used for the experiments). These experiments are described in Section 12.4. Within the scope of preliminary tests for the definition of the sample material, these free swelling tests were complemented by tests under oedometric conditions where anhydrite powder from different origins was used and compared (*i.e.* commercial and natural anhydrite, see Section 12.5).

Following the preliminary tests, a series of oedometer tests were conducted (Section 12.6), where the axial deformation which develops during water uptake was measured. The influence of axial stress on the maximal strain was determined by measuring the swelling strain of samples under various constant axial stresses until they reached their final swelling strain, *i.e.* until a steady state was observed. The experimentally obtained relationship between the axial stress and the final swelling strain is presented in Section 12.6.2.

Two further series of oedometer tests were performed, where the samples were subjected to a specific axial stress and then extracted after different test durations, before the swelling reached a steady state (see Section 12.6.3). This enables to establish the relationship between the swelling strain and the mass of anhydrite in the samples over time (*i.e.* the unknown factor χ for standard oedometric conditions).

Parallel to the oedometer tests, a series of tests under nearly complete constraint were started, where the developing axial pressure is measured. Also, a new testing cell was established (the so-called “flexible” oedometers), where apart from the axial deformation also the radial deformations can be measured and thus via the stiffness of the oedometer the radial pressure can be determined. These experiments are currently still running at ETH. First results are presented in Sections 12.8.1 and 12.8.2.

Since the relationship between the deformation and the change in masses of anhydrite and gypsum is unknown (*e.g.* the gypsum can fill pores without causing any deformation at all, or it can expand the sample without filling the pores or cause cracking and thus generate new pores), the amount of gypsum and remaining anhydrite in the samples post test must be determined additionally. This information is necessary for the evaluation of the factor χ . This was accomplished via thermogravimetric analysis (TGA) and X-ray diffraction analysis (XRD), *cf.* Section 8.3 and Appendix I. These analysis techniques require the destruction of samples and thus the determination of mass changes can only be done after completion of a swelling test. Furthermore, the change in structure was investigated on a selection of samples with microscopy and porosimetry (Section 12.7).

12.3 Samples and sample preparation

Artificially created samples consisting of anhydrite and aggregates were used for the major part of the experiments concerning the investigation of the chemo-mechanical processes. This was decided in order to reduce uncertainties caused by the inhomogeneous compositions and structures of natural rock samples, to guarantee reproducibility (by adhering to the same sample preparation and testing procedures) and to isolate the swelling process due to AGT from that due to clay.

Unless stated otherwise, the samples consisted of 40% anhydrite powder (Section 9.1) and 60% of one of the aggregates (Section 9.2). The influence of the types and amounts of materials was investigated in a series of preliminary tests, so-called free swelling tests, which are described in Section 12.4.

During sample preparation, the two powders were weighed and mixed together while adding about 10% - 15% of pure ethanol in order to improve the compaction, reduce formation of dust during compaction and to bind the powder, thus ensuring that the

compacted samples did not crumble before they were used for testing. The mixed material was then inserted in a steel ring with a diameter of either 5.6 or 7 cm and compacted by cyclical loading with increasing axial pressure up to 100 MPa, thus creating cylindrical disks. In the case of the preliminary free swelling tests, the disks were pressed out of the steel rings. For the oedometer tests and complete constrained tests the disks remained in the steel rings they were compacted in. For the first series of flexible oedometer tests the samples remained in the cylinders they were compacted in, whereas for the later series the samples were compacted in separate cylinders (see Section 12.8.2). After compaction, the samples were air-dried so that nearly all of the ethanol evaporated. In order to achieve a more uniform and accelerated wetting of the samples during the following tests, a small hole with a diameter of 1.1 mm was bored through the centre of the samples. Figure 12.2 illustrates the described sample preparation procedure and shows examples for compacted samples.

The main properties of the samples (height, porosity, dry mass, density and anhydrite content) are summarised in Appendix II.

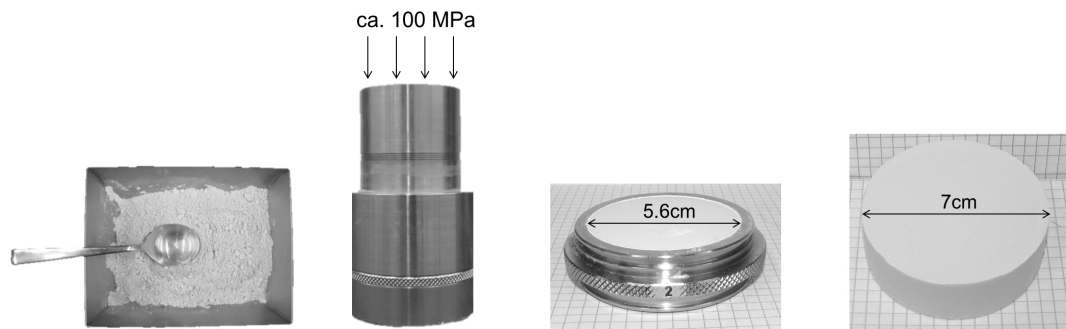


Figure 12.2 Sample preparation procedure. From left to right: mixture of powders; powders in steel cylinder under axial load (compaction); intact disk in 5.6 cm steel ring, after compaction (oedometer tests); intact disk after removing from 7 cm steel ring (free swelling tests).

12.4 Preliminary tests I: free axial swelling tests

12.4.1 Aim and procedure

Multiple free swelling tests (with no axial load) were performed with the aim of gaining experience with the sample preparation procedure, trying out various mixtures for the samples and comparing their swelling behaviour.

If not indicated otherwise, the samples were prepared as described in the previous section with anhydrite from Sigma Aldrich and either kaolin, limestone or quartz powder (see Appendix II).

The kaolin-samples could easily be extracted from the cylinder after compaction. The same accounts for the limestone samples, although they had the tendency to break slightly at the edges or perpendicular to the direction in which they were compacted. However, the quartz flour proved to generate problems when attempting to extract the samples from the apparatus after compacting. It was not possible to create intact, unconfined samples with the same procedure as described above. Therefore mixtures containing quartz flour could only be used for testing when the compacted sample was left within the steel ring and were not tested further in the preliminary free swelling tests, but for some of the oedometer tests described later (see Section 12.6).

During the tests, most samples were radially slightly confined by a rubber membrane (diameter of 7 cm) while some were radially completely confined by stiff steel cylinders

(diameter of 5.6 cm or 7 cm). The rubber membranes provided sufficient radial support in order to prevent the samples from crumbling during the test, but did not completely prohibit radial expansion. After sample preparation, the samples were inserted into demineralized or saturated water ($c_{eq,G} = 15 \text{ mol/l}$) and the occurring axial deformation was measured with a dial gauge.

12.4.2 Results

Eight samples were produced with varying mixtures of kaolin and anhydrite, five samples with only kaolin, four samples with mixtures of limestone and anhydrite, and two samples with only limestone.

The following table summarizes all samples containing kaolin and their testing conditions and results. The swelling strain curves over time are shown in Figure 12.3. Analogous, the information on the samples containing limestone is given in Table 12.2 and the results from the free swelling tests are presented in Figure 12.4.

Table 12.1 Overview of the preliminary tests with mixtures containing anhydrite (SA) and kaolin (PW)

Curve / Sample composition (SA...% / PW...%)	Sample preparation	Radial confinement	Fluid	Max. swelling strain ϵ [%]
—●— SA 60% PW 40%	mixed with ethanol, air-dried	rubber membrane	saturated water (Ca, SO ₄)	75.0
—○— SA 60% PW 40%				84.9
—●— SA 40% PW 60%				79.6
—○— SA 40% PW 60%				76.6
—●— SA 20% PW 80%				66.2
—○— SA 20% PW 80%				65.9
— — PW 100%				22.6
— — PW 100%	mixed with ethanol, test started immediately			28.3
— — PW 100%	mixed with 50% ethanol and 50% demineralized water, air-dried			22.4
— — PW 100%	mixed with ethanol, air-dried		demineralized water	32.7
····· PW 100%			ethanol	7.8
—○— SA 20% PW 80%		steel cylinder	saturated water (Ca, SO ₄)	71.1
—■— SA 20% PW 80%			saturated water (Ca, SO ₄), water supply via pipette	60.0

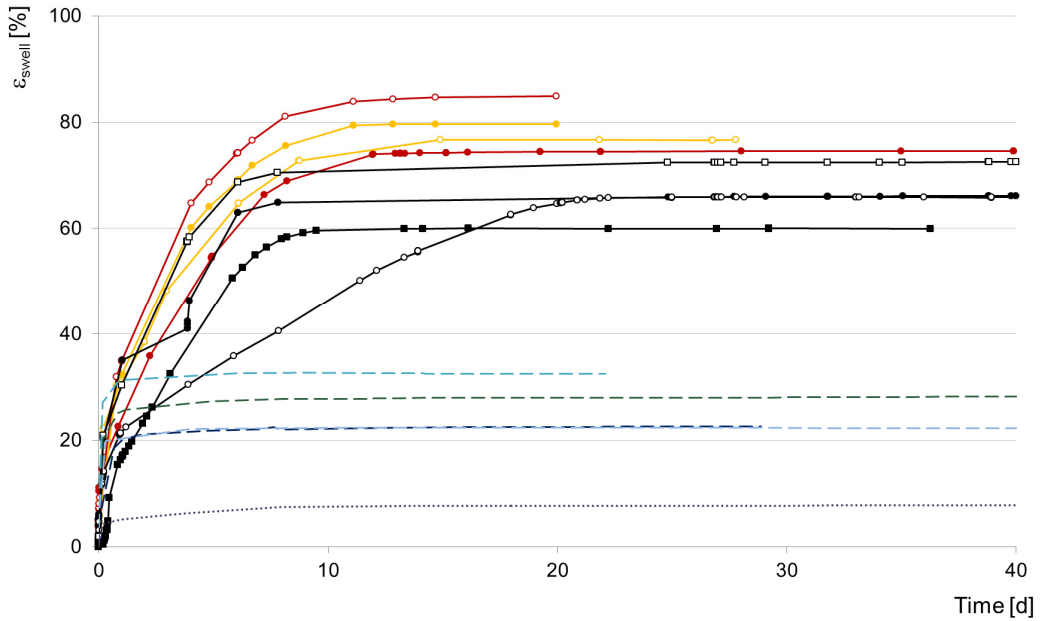


Figure 12.3 Swelling strain curves of preliminary tests (samples containing kaolin). The legend is given in Table 12.1.

Table 12.2 Overview of the preliminary tests with mixtures containing anhydrite (SA) and limestone (KM)

Curve / Sample composition (SA...% / KM...%)	Sample preparation	Radial confinement	Water	Max. swelling strain ϵ [%]
—●— SA 60% KM 40%	mixed with ethanol, air-dried	rubber membrane	saturated (Ca, SO ₄)	9.1
—●— SA 40% KM 60%				14.4
—●— SA 20% KM 80%				18.0
—■— SA 20% KM 80%		steel cylinder		1.0
— — KM 100%		rubber membrane		17.1
— — KM 100%			demineralized water	18.0

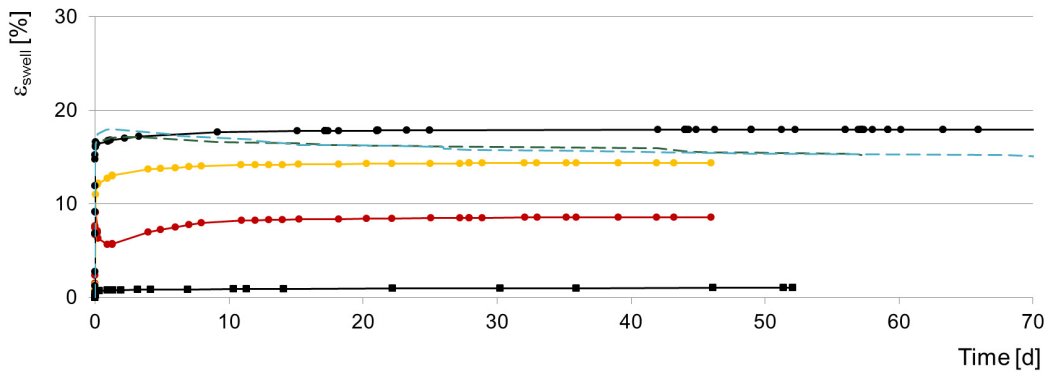


Figure 12.4 Swelling strain curves of preliminary tests (samples containing limestone). The legend is given in Table 12.2.

12.4.3 Discussion

In general, a first rapid heave directly after watering the samples can be observed. The strains then either increased almost linearly until reaching a maximal value or remained nearly constant after the initial heave (see Figure 12.3 and Figure 12.4).

The samples containing both kaolin (PW) and anhydrite (SA) all behaved similarly (Figure 12.3). At first, they exhibited a rapid increase in strain followed by a more or less linear increase over the first ca. 10 days, then slowing down and reaching a maximal value. The linear increase in strain occurs due to AGT. This becomes evident when comparing the strains of the samples with anhydrite to those without any anhydrite (which did not exhibit any further swelling strain after the initial heave).

The first rapid increase in strain occurred for all samples, independent of their composition, with the exception of one limestone sample. It is assumed that this first increase occurs due to water uptake and reduction of negative pore water pressure, which also leads to a reduction of the effective stress and thus to immediate strains of the samples containing no anhydrite. The only sample which did not exhibit any swelling due to hydration effects was the sample with 20% anhydrite and 80% pulverized limestone in a steel cylinder, where a slight axial load (<3 kPa) may have prohibited said strain. However, a slight axial load did not suppress the hydration strain in the case of the kaolin samples in a steel cylinder.

It was also investigated, whether the rapid initial strain changes by varying the testing conditions: one sample with 100% kaolin was tested with demineralized water instead of saturated water, another was inserted directly after compaction (no drying), a third was tested with ethanol instead of water, and a fourth was mixed with some water in addition to the ethanol before compaction (so the clay platelets may already bind some water before the test starts). The last did not change the results compared to the normal procedure (*i.e.* mixing the material with ethanol, air-drying the sample after compaction and using saturated water for the test). However, performing the test immediately after compaction or using demineralized water lead to even higher initial rapid strains, while performing the test with ethanol instead of water reduced the initial rapid strains significantly.

From Figure 12.4 it becomes apparent that a sample consisting of a matrix of crushed limestone does not produce the same strains due to AGT as a sample with kaolin does. With limestone, no swelling strain occurred after the first rapid strains. In order to find a possible explanation for this behaviour, the pore space of the samples was investigated more closely. The limestone samples were expected to have bigger pores compared to the kaolin samples, since the particle size of the crushed limestone is larger than that of the kaolin (*cf.* Figure 9.1). The larger pores could allow for gypsum to precipitate only within the pore space, thus leading to no additional swelling strain after the initial heave due to water uptake and reduction of negative pore water pressure. For this reason porosimetry and microscopic investigations (see Sections 12.7.1 and 12.7.2) were performed on a limestone sample prior to any wetting (*i.e.* initial state prior to swelling test) as well as on one of the samples presented in the results of this chapter. As will be shown later in Section 12.7.1, the limestone samples have only slightly larger pores in their initial state compared to the kaolin samples, while the total pore volume and the porosity are significantly smaller. After the swelling test, the smaller pores of the limestone samples seem to disappear, while at the same time the total pore volume increases and the porosity decreases (see Figure 12.15 and Figure 12.16 in Section 12.7.1). This leads to the assumption that many small pores have been filled with gypsum. However, optical analysis of the structure of a sample (see microscopic investigations, Section 12.7.2) also showed some clearly defined clusters of gypsum needles.

It is assumed that gypsum also precipitated within the pores in the case with the limestone sample in the steel ring, which did not exhibit any initial heave. In the case of the samples containing 100% limestone, the strains even begin to reduce again after the initial heave.

Figure 12.5 shows the reached swelling strain versus the initial anhydrite content of the sample. It becomes apparent that with only 20% anhydrite in the sample, already significant strains occur. Under these conditions, an increase in the amount of anhydrite in the sample to 60% only produces an additional heave of about 10%.

Following these preliminary tests it was decided to use samples of a mixture of 40% anhydrite (SA) and 60% kaolin (PW) for the main part of the following tests. Kaolin was chosen as aggregate because the sample preparation had a higher success rate compared to the quartz flour samples, which were more brittle. Limestone was discarded because of lack of swelling strains due to AGT. Since all variations of compositions (SA / PW) showed similar results, the ratio (40% SA, 60% PW) was chosen considering that natural samples containing anhydrite (e.g. cores from the Belchen Tunnel) showed typical values of 40%-60% anhydrite. Additionally, the choice of 40% anhydrite instead of 60% helps to spare the resources.

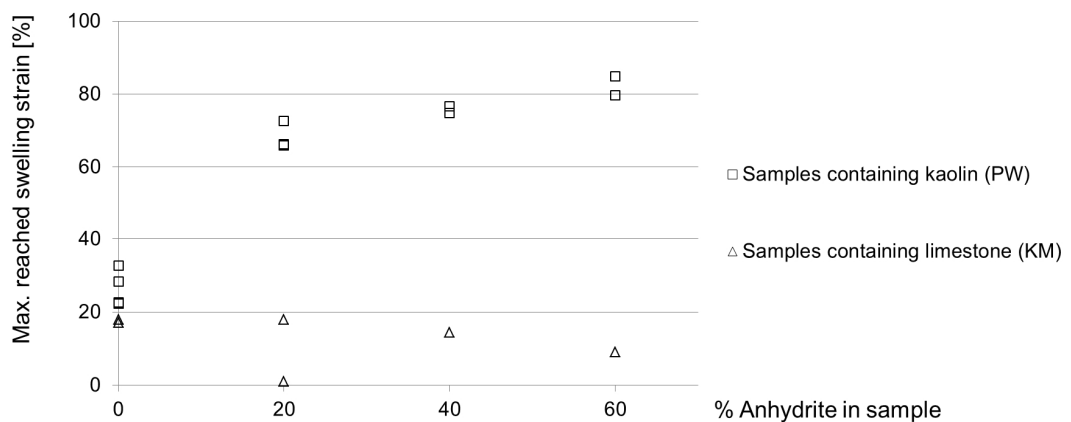


Figure 12.5 Max. swelling strain vs. anhydrite content.

12.5 Preliminary tests II: Comparison milled natural anhydrite – commercial anhydrite

12.5.1 Aim and procedure

In order to establish how well the commercial anhydrite represents natural anhydrite, a series of oedometer tests with an axial load of 3 kPa were performed with mixtures of 40% anhydrite (either from Sigma Aldrich, with a max. grain size of 40 μm , or from Bex, Bözberg or Leissigen, see Section 9.1, which were milled to powders with maximal grain sizes 50 μm resp. 80 μm) and 60% kaolin.

The sample preparation occurred as described in Section 12.3, whereas the samples remained in the oedometer rings after compaction, inserted into an oedometer cell (see conceptual sketch in Figure 12.6), loaded only with a piston (ca. 0.7 kg, i.e. 3 kPa) and connected to water supply, thus initiating the swelling process. The developing heave of the sample was measured with a dial gauge. Upon termination of a test, the sample was extracted from the oedometer ring, weighed before and after drying and its gypsum content measured via TGA, from which the change in mass of anhydrite could be calculated.

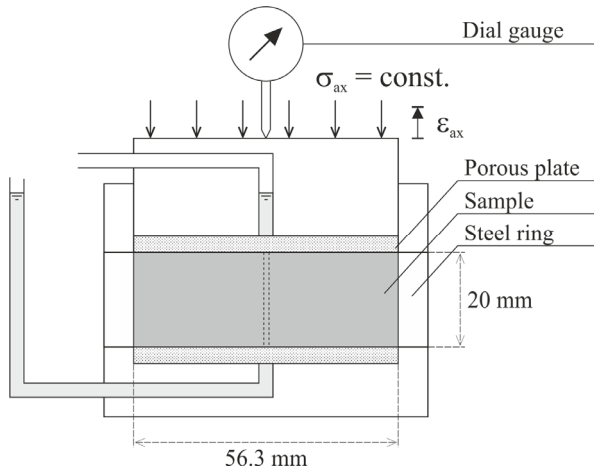


Figure 12.6 Basic setup of an oedometer cell (cross section).

12.5.2 Results

The results of the swelling strain tests are shown in the graph in Figure 12.7. The black curves show the results for the samples containing commercial anhydrite.

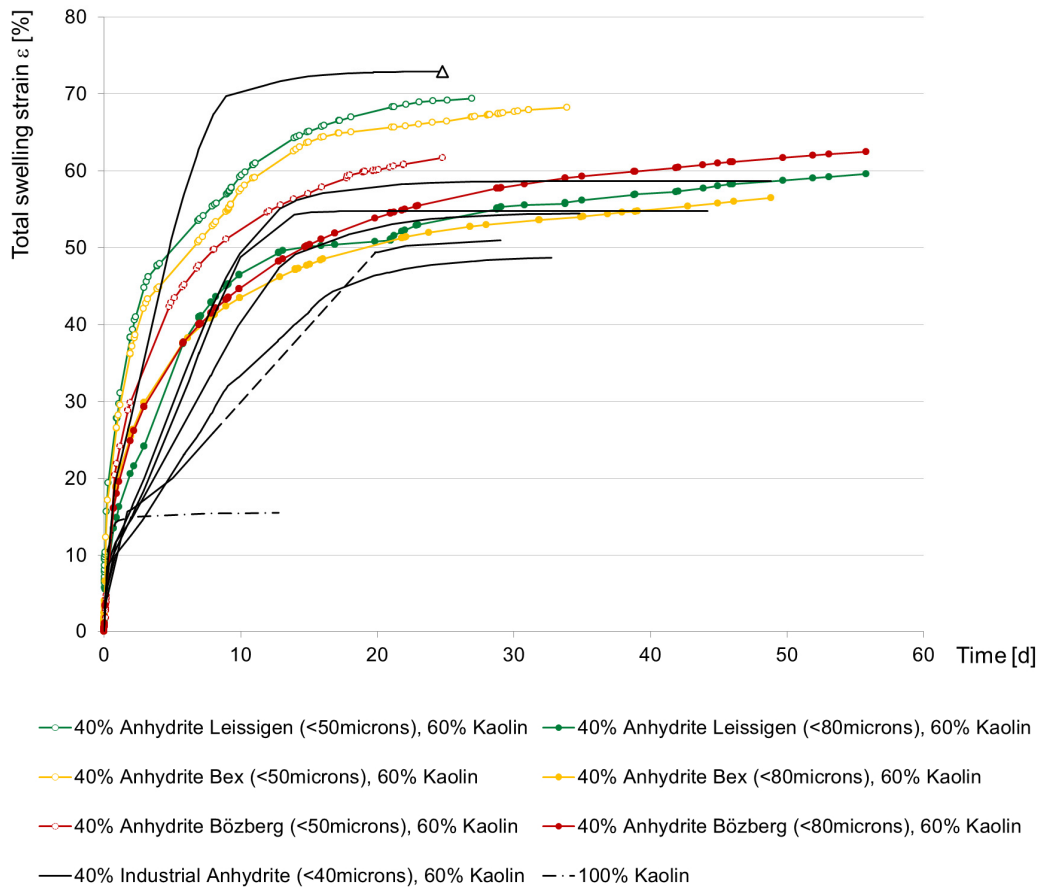


Figure 12.7 Swelling strain vs. time for $\sigma_{ax} = 3 \text{ kPa}$: comparison between mixtures containing natural and commercial anhydrite (note: the dashed line for one of the tests with SA indicates a longer period of time where the axial deformation was not measured).

12.5.3 Discussion

The graph in Figure 12.7 shows that the samples containing commercial anhydrite produce in general similar swelling strains as the samples containing natural anhydrite. However, the latter seem to not have reached the maximum swelling strain at the point of extraction (*i.e.* after 30 resp. 60 days, when the experiments were terminated) and it seems that they tend to produce higher strains than the commercial anhydrite does, with the one exception of the curve ending with a triangle. Furthermore, the shapes of the curves are slightly different. While the samples containing commercial anhydrite show a rather constant inclination and reach a plateau fairly abruptly, the samples containing natural anhydrite show more of a change in inclination and do not seem to have reached a steady state within the duration of the experiments.

One possible explanation for the different shapes of the curves is the different maximum grain size of the anhydrite in the samples. A larger grain size of the anhydrite particles slows the AGT process down and thus causes retardation in the swelling behaviour.

The scatter concerning the value of maximal swelling strain reached by the samples was seen to be dependent on their density (see Figure 12.8). Even though the same sample preparation procedure was strictly followed, the density of the samples still varied to some extent. The samples containing natural anhydrite had densities between 1.99 and 2.13 g/cm³, and the samples containing commercial anhydrite had densities between 1.86 and 1.94 g/cm³, with the one exception of a sample with 2.29 g/cm³, which showed the highest amount of swelling strain (corresponding to the black curve ending with a triangle in Figure 12.7).

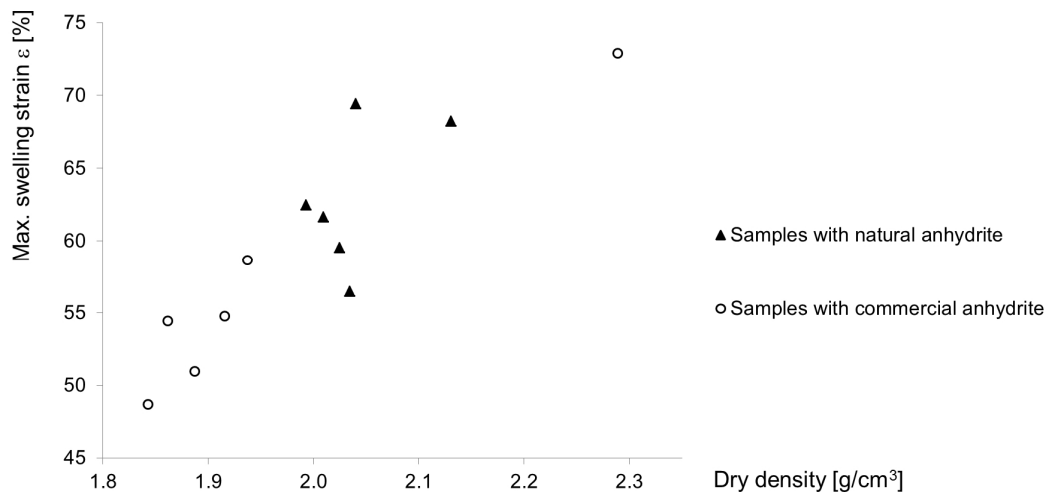


Figure 12.8 Maximal swelling strain vs. dry density prior to experiment.

12.6 Oedometer tests

12.6.1 Aim and procedure

The basic set up of the oedometer tests is the same as in Section 12.5, resp. Figure 12.6, whereas now higher loads are applied (up to 3.2 MPa). The loading of the samples occurred under dry conditions. The actual tests (time = 0) began as soon as the settlement of the samples in the dry state had steadied (the duration of which varied depending on the load and sample material), and at which point the samples were connected to the water supply. As in the previously described experiments, the heave of each sample was measured during the test and, when terminated, the mass of the sample was weighed before and after drying at 40°C in an oven for at least 24 hours. Afterwards the change in mass of anhydrite was determined indirectly via TGA. In

selected cases, microscopy, porosimetry or X-ray diffraction analysis was performed additionally.

In the first series of oedometer tests (Section 12.6.2) the aim was to determine the influence of axial stress on the maximal strain by measuring the swelling strain of samples under various constant axial stresses until they reach a steady state. These experiments were performed with samples consisting of anhydrite and kaolin as well as anhydrite and quartz flour.

With two further series of oedometer tests the relationship between the swelling strain and the change in mass of anhydrite in the samples over time was to be established (*i.e.* the unknown factor χ , *cf.* Eq. 12.8). For this purpose oedometer experiments were performed, where samples of anhydrite and kaolin were subjected to a specific axial stress and then extracted after different test durations, before the swelling strain reached a steady state (see Section 12.6.3).

12.6.2 Results of the first series (various axial loads – steady state)

In the first series of oedometer tests with anhydrite and kaolin axial stresses between 3 kPa and 3200 kPa were applied. For the series with anhydrite and quartz flour the axial stresses ranged from 3 kPa to 800 kPa. Two additional oedometer tests were performed at 3 kPa and 400 kPa on samples containing 100% kaolin. For each axial load at least one oedometer test was conducted until the swelling strain seemed to have reached a steady state and thus the final strain was measured.

The swelling strains obtained with an axial load of 3 kPa were taken from the experiments described in Section 12.5, *i.e.* the black curves shown in Figure 12.9 are the same as already shown in Figure 12.7 (with densities between 1.86 and 1.94 g/cm³).

The results from the oedometer tests are presented in Figure 12.9 and Figure 12.10, which show the measured swelling strain over time for the anhydrite/kaolin samples and the anhydrite/quartz flour samples, respectively, until the swelling strain reached a steady state for all the axial stresses investigated. At an axial stress of 3200 kPa no swelling strain could be observed over the entire duration of the test with a kaolin sample; for the samples containing quartz flour this was the case at an axial stress of 800 kPa. Note that the durations of both of these samples was *ca.* 80 days (*i.e.* also in the case of the 800 kPa sample in Figure 12.10).

At 3 kPa and at 800 kPa multiple tests were repeated with the anhydrite/kaolin samples and some scatter in the results was observed (*e.g.* the final swelling strain of the samples containing kaolin which were loaded with 800 kPa varied from 6% to 10%). The dot-dashed curves in Figure 12.9 indicate the swelling behaviour of the samples containing only kaolin, which also exhibited a rapid initial strain during the first couple of hours due to wetting of the sample and reduction of the negative pore pressure (similar to the other curves). It can be seen that this initial rapid strain is significant especially for low axial stresses and can lead to an overestimation of the chemical swelling strain.

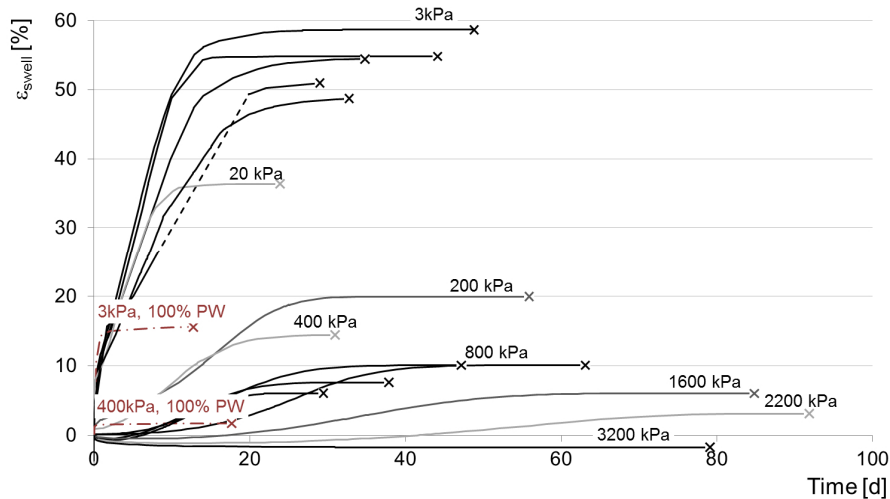


Figure 12.9 Results of oedometer tests up to a steady state for mixtures with kaolin (note: the dashed line for one of the tests with $\sigma_{ax} = 3$ kPa indicates a longer period of time where the axial deformation was not measured).

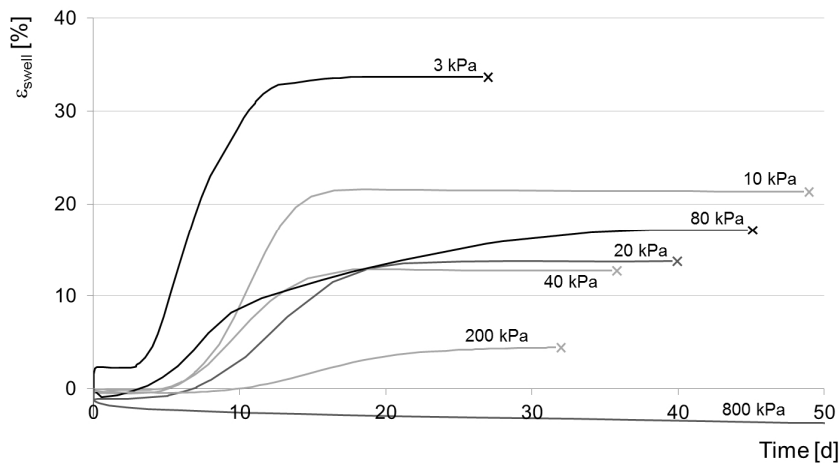


Figure 12.10 Results of oedometer tests up to a steady state for mixtures with quartz flour.

Figure 12.11 shows the final strain that was reached at each test versus the corresponding axial stress in a semi-logarithmic diagram. These results indicate a linear relationship between the final strains and the logarithm of the axial stress for both types of samples.

In all samples, the anhydrite appeared to have dissolved to a great extent with one exception: the anhydrite/kaolin sample that was loaded with 3200 kPa and did not swell at all (but even settled slightly) contained almost no gypsum according to the TGA results. This is shown in Figure 12.12, where the masses of anhydrite prior and post test, as well as the mass of gypsum post test (per unit volume), are mapped against the applied axial stresses for each sample. The values $m_{A,prior}$ are obtained directly from the initial measured geometry and mass of the sample, while $m_{A,End}$ was determined indirectly via TGA.

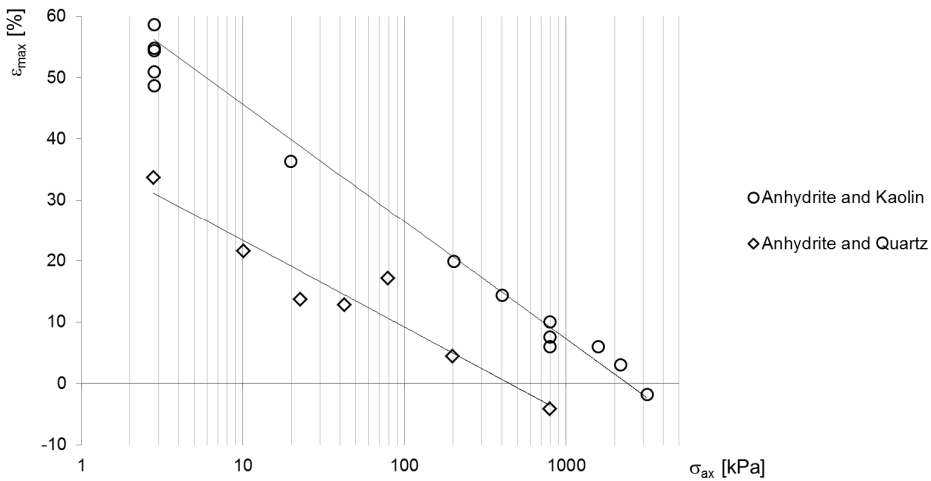


Figure 12.11 Final swelling strain vs. corresponding axially applied stress.

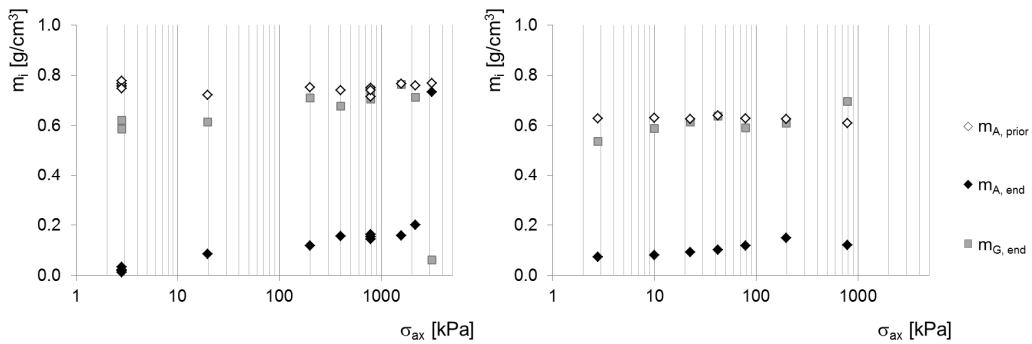


Figure 12.12 Masses per unit volume of anhydrite (prior and post test) as well as gypsum (post test) versus applied axial stress for the first series of oedometer tests. Left: anhydrite/kaolin samples, right: anhydrite/quartz powder samples.

12.6.3 Results: Various durations (only anhydrite/kaolin samples)

Figure 12.13 shows the swelling strain over time for additional oedometer tests performed with $\sigma_{ax} = 3$ kPa and 800 kPa, but where the samples were extracted prior to reaching a steady state. The points of extraction are indicated by an “x”. The amount of anhydrite in each sample post test, versus the reached swelling strain at the point of extraction, is shown in Figure 12.14. The values for m_A in Figure 12.14 are back-calculated based on the results from TGA (see Appendix I).

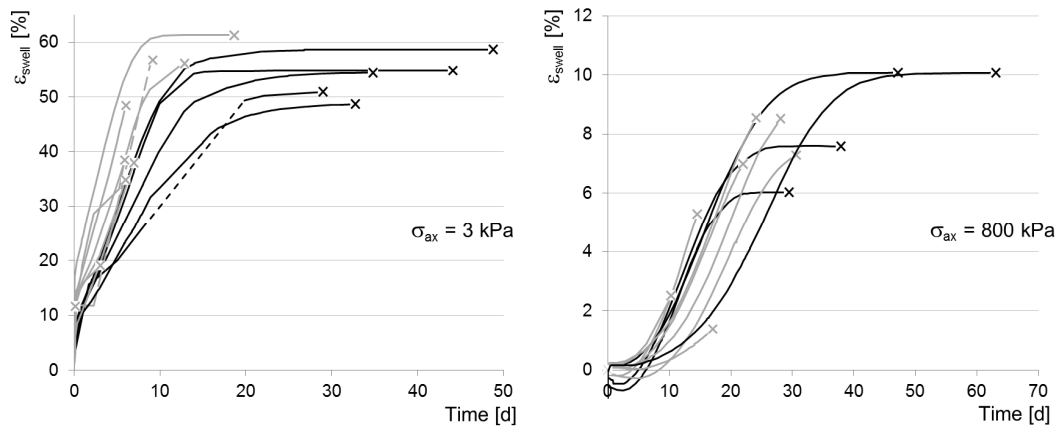


Figure 12.13 Results of oedometer tests up to various swelling strains. Left: results from tests with an axial stress of 3 kPa; right: 800 kPa. (Note: black lines indicate samples that reached steady state, while grey lines represent samples that were extracted prior to reaching the final swelling strain and dashed lines indicate a longer period of time where the axial deformation was not measured).

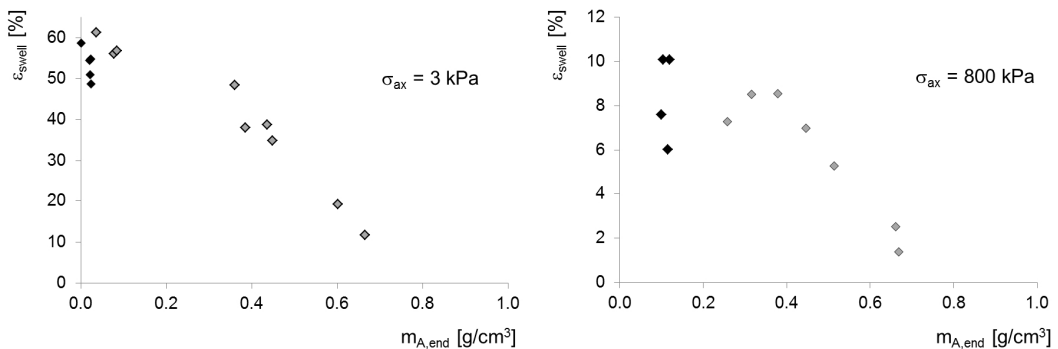


Figure 12.14 Swelling strain vs. anhydrite mass of the kaolin-samples. Left: 3 kPa axial stress, right: 800 kPa axial stress. (Note: black diamonds indicate samples that reached max. swelling strain, grey diamonds represent samples that were extracted prior to reaching the maximal swelling strain).

12.6.4 Discussion

By investigating the influence of axial stress on the swelling strain, Figure 12.9 to Figure 12.11 indicate for one that an upper boundary for the stress appears to exist, at which no swelling strain occurs (*i.e.* a confining pressure). In the case of anhydrite/kaolin this axial stress was 3200 kPa and in the case of anhydrite/quartz flour 800 kPa. In both cases the samples even settled. However, one major difference between the two samples was that AGT occurred in the quartz-sample but not in the kaolin-sample (this can be seen in Figure 12.12, where the mass of anhydrite in the sample prior and post test at 3200 kPa was nearly identical). It is unsure, whether the sample was in a state of equilibrium or whether AGT may have occurred further had the experiment gone longer. Also, based on the model for the determination of macroscopic swelling pressure (see Section 7.3.2), the confining pressure should be at least twice as high.

It can be seen from the first series of tests (Section 12.6.2) that a semi-logarithmic relationship seems to exist between the axial strains and the axial stresses for both types of samples. However, the extent of the swelling strains and the maximal pressure needed to suppress the strains differ from one mixture to the other. A reason for this is that the quartz samples had higher initial porosities compared to the kaolin samples (*ca.* 0.45 vs. *ca.* 0.30, see Appendix II) while the anhydrite volume fractions are lower (*i.e.* 0.2 vs. 0.25) and therefore most likely a proportionally larger amount of gypsum precipitated in the pores of the quartz samples. The differences in sample properties are due to the material

properties; the harder grains of the quartz powder allow for less compaction during sample preparation whereas the platelets of the kaolin and anhydrite may crush during compaction.

The results of the tests conducted up to various durations (Figure 12.14), reveal that a correlation exists between the change in the mass of anhydrite and the swelling strain. It seems that the relationship (denoted by χ in Eq. 12.8) is linear during the first stages of swelling, *i.e.* until about half the anhydrite is dissolved (*cf.* Figure 12.14). The swelling strain then stagnates while further anhydrite dissolves and gypsum precipitates. One possible explanation is that after a first expansion of the sample the gypsum precipitates mainly in its pores. However, further experiments are necessary to draw definite conclusions for the case when $m_{A,end} < 0.4 \text{ g/cm}^3$.

Further investigations concerning the structures of the samples were performed on selected anhydrite/kaolin samples. Microscopic analysis and porosimetry was done on the sample that did not swell (at 3200 kPa), one that did swell until steady state (at 800 kPa) and one where the swelling strain did not reach a steady state (at 800 kPa). The results are presented and discussed in the next section.

12.7 Investigations of sample structures

12.7.1 Porosimetry

In order to verify whether the porosities estimated via the geometries and masses of the samples are accurate, as well as to investigate the change in pore size distribution of a sample post swelling test compared to its initial state, some selected samples were analysed with MIP (*cf.* Section 8.3.4).

For this reason, a kaolin sample (40% SA and 60%PW) as well as a limestone sample (40% SA and 60%KM) was prepared for MIP as reference samples for the state prior to the swelling tests. MIP was performed on specimens from these samples as well as from three samples from oedometer tests after swelling (one loaded with 3200 kPa, where no swelling was observed; two loaded with 800 kPa after various stages of swelling), and from one sample of the preliminary free swelling tests performed with limestone. Of each sample, at least two specimens were taken and investigated with MIP. The main results from MIP are presented in Figure 12.15 (pore size distributions) and Figure 12.16 (porosity and total pore volume). The given AGT-values roughly indicate the completion of the AGT process (*i.e.* mass of anhydrite remaining in sample post test divided by original mass of anhydrite) and were obtained via TGA (see Appendix I).

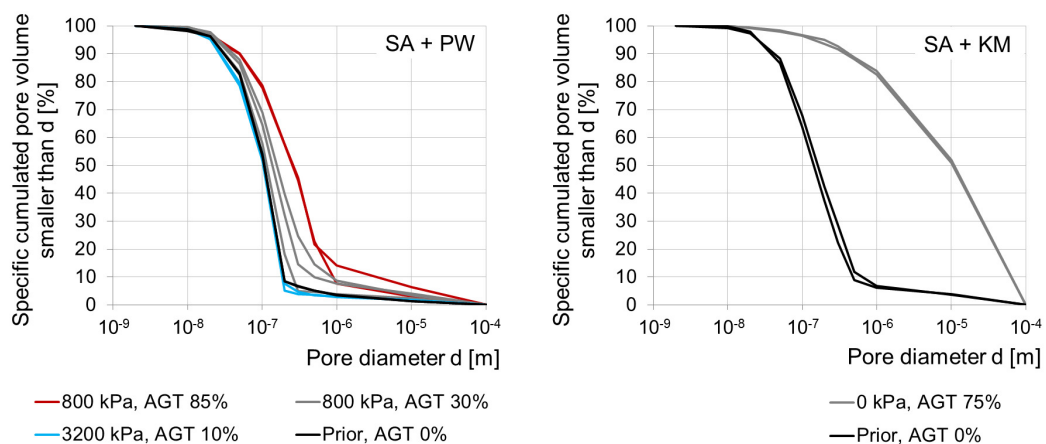


Figure 12.15 Pore size distributions for anhydrite / kaolin samples from oedometer tests (left) and anhydrite / limestone samples from preliminary free swelling tests.

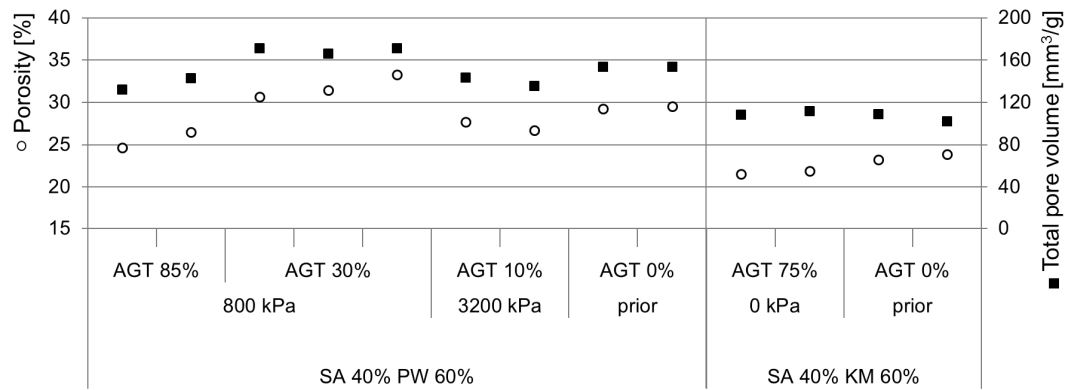


Figure 12.16 Porosity (white circles) and total pore volume (black squares) of anhydrite / kaolin samples from oedometer tests (left) and anhydrite / limestone samples from preliminary free swelling tests.

From Figure 12.15 it becomes apparent that the pore size distribution of the limestone sample changed significantly after the sample was subjected to water, while the oedometer samples containing kaolin did not change as much. With the latter, the sample loaded with 3200 kPa appeared not to have changed at all (the curves nearly overlap with those of a sample prior to swelling), while a sample loaded with 800 kPa tends to gain more larger pores during AGT (the pore size distribution shifts slightly to the right). In the case of the limestone sample, the initial state prior to swelling is very similar to that of a kaolin sample, however subjecting the sample to water seems to create a large amount of bigger pores (the pore size distribution changes its shape entirely and shifts to the right).

When looking at the porosities and total pore volumes (Figure 12.16), while keeping the swelling strain curves from Figure 12.9 and Figure 12.13 in mind, the following observations can be made: In the beginning, gypsum precipitation appears to increase the total pore volume and porosity of the kaolin samples. Then, when the swelling strain reaches a steady state, gypsum precipitates in the pores, thus decreasing the pore volume and the porosity (see Figure 12.16, at 800 kPa: at AGT 30% the values are higher than those of the sample prior to swelling, whereas at AGT 85% the values are lower). With the sample that was loaded with 3200 kPa a decrease in the total pore volume and porosity can be observed, which can be accounted to the settlement the sample experienced, since nearly no gypsum was found in the sample post test.

Though the total pore volume of the limestone samples increases from prior test to post test, the porosity decreases and – as mentioned above – the pore size distribution shifts drastically to the right. It is assumed that the initial heave created large pores, even cracks, however due to gypsum precipitation within the sample, the ratio of total pore volume to total volume (*i.e.* the porosity) decreased.

The sample properties obtained via porosimetry are compared to the estimations calculated from the measured dimensions of the samples and their masses in Appendix II. The estimated values prove to be within a satisfactory range of accuracy.

12.7.2 Microscopy

Additionally, the change in structure of the samples due to AGT (*e.g.* change of pore volume or aperture of cracks as well as the distribution and shape of the growing gypsum crystals) was investigated via microscopy on selected samples. In the following, these investigations are grouped by the types of tests the samples stem from. Table 12.3 gives an overview of all samples investigated.

Table 12.3 Overview of performed microscopic investigations

Original experiment	Description sample	Sample name	Sample type	Microscopic investigations
Free swelling tests (Section 12.4)	40% Anhydrite 60% Limestone AGT 75%	SA40 KM60	Fragment	Optical microscope, SEM & EDX
			Embedded (Epoxy) and polished	SEM & EDX
	40% Anhydrite 60% Limestone Prior, AGT 0%	SA40 KM60 prior	Embedded (Epoxy) and polished	SEM & EDX
Oedometer tests (Section 12.6)	40% Anhydrite 60% Kaolin 800 kPa, AGT 85%	Oe_5_2 (800kPa)	Fragment	SEM
			Polished	Optical microscope, thin sections, SEM & EDX
	40% Anhydrite 60% Kaolin 3200 kPa, AGT 10%	Oe_6_2 (3200kPa)	Fragment	SEM
			Polished	Optical microscope, thin sections, SEM & EDX
	40% Anhydrite 60% Kaolin 800 kPa, AGT 40%	Oe_5_4	Polished	SEM & EDX
40% Anhydrite 60% Kaolin 1600 kPa, AGT 85%	Oe_7_2 (800kPa)	Fragment	SEM	

Free swelling tests

Figure 12.17 shows close up images of two fragments broken off of the SA40 KM60 sample post test. In the plane perpendicular to loading, clear clusters of crystals are visible (such as the one marked with an arrow in the right image), while in the plane parallel to loading small cracks are visible (such as the one marked with an arrow in the left image). Figure 12.18 shows BSE images of one of these Fragments. The nodular crystals visible in these images are strongly assumed to be gypsum. The gypsum appears to have precipitated in clear “clusters” of needles, however the needles are also found evenly spread over the entire sample. A further section of this sample (Figure 12.19) was investigated with EDX by point analyses, to identify the elements occurring in the sample at different locations. From the EDX analyses (see Table 12.4) it is strongly assumed that the longer nodules (*i.e.* >100 μm) are gypsum crystals (point B), while there are still some remaining anhydrite crystals (*e.g.* point A) in the sample as well. Furthermore, spots were identified that were nearly free of sulphate, *i.e.* those are assumed to be mainly limestone (point C). These findings are in good accordance with the findings from TGA analysis, that about 75% of the anhydrite had been transformed to gypsum.

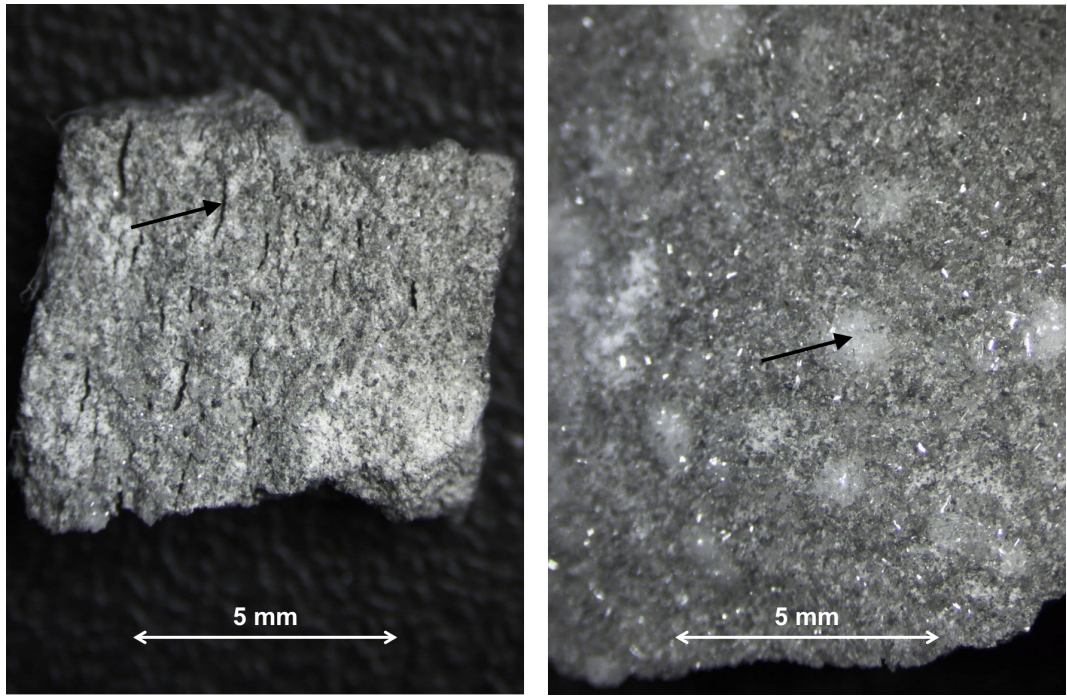


Figure 12.17 Images of SA40 KM60 fragment sample (post free swelling test) taken with an optical stereo microscope. Left: view perpendicular to direction of compaction, right: view parallel to direction of compaction.

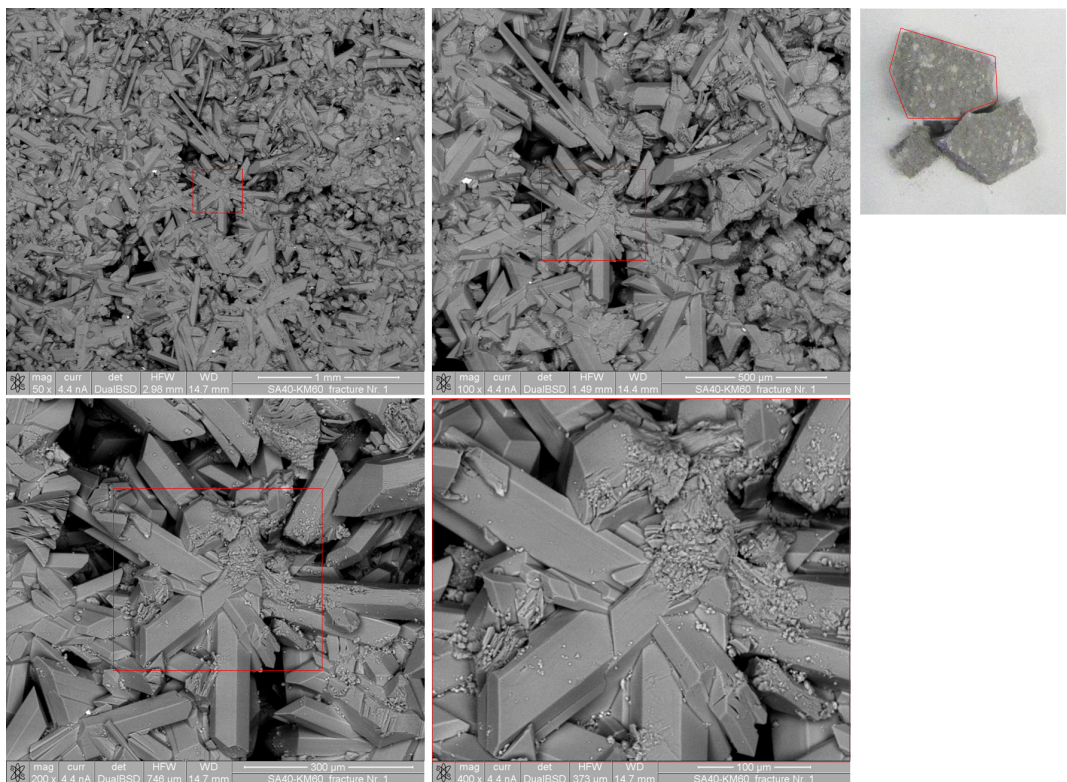


Figure 12.18 BSE images of SA40 KM60 fragment sample (post swelling test).

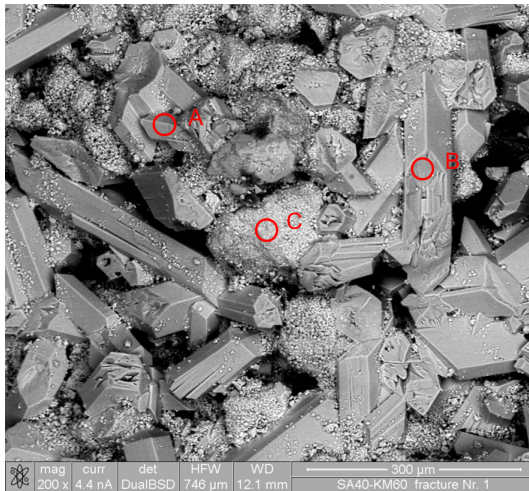


Figure 12.19 Point analyses of SA40 KM60 fragment (cf. Table 12.4).

Table 12.4 Point analyses of SA40 KM60 fragment (cf. Figure 12.19).

Point	S		Ca		C		O		Interpretation
	[wt%]	[At%]	[wt%]	[At%]	[wt%]	[At%]	[wt%]	[At%]	
A	23.41	19.24	48.14	31.65	4.11	9.02	24.34	40.09	CaSO ₄
B	19.42	13.74	35.31	19.99	4.43	8.38	40.84	57.90	CaSO ₄ ·2H ₂ O
C	2.75	2.29	67.64	45.04	5.94	13.19	23.67	39.48	CaCO ₃

[wt%] = weight percentage, [At%] = atomic percentage

In order to investigate the distribution of calcium sulphate in the sample more closely, a piece of the same sample was embedded in epoxy and its surface polished (see Figure 12.20, right). The sample was investigated with SEM (BSE images in Figure 12.20) in combination with EDX, where the main occurring elements on the surface of the specimen are mapped in Figure 12.22. Figure 12.23 shows another section of that same specimen at a closer scale.

The same was done for an SA40 KM60 sample prior to swelling. The SEM images are shown in Figure 12.21 and the EDX mapping is given in Figure 12.24 (same scale as Figure 12.23).

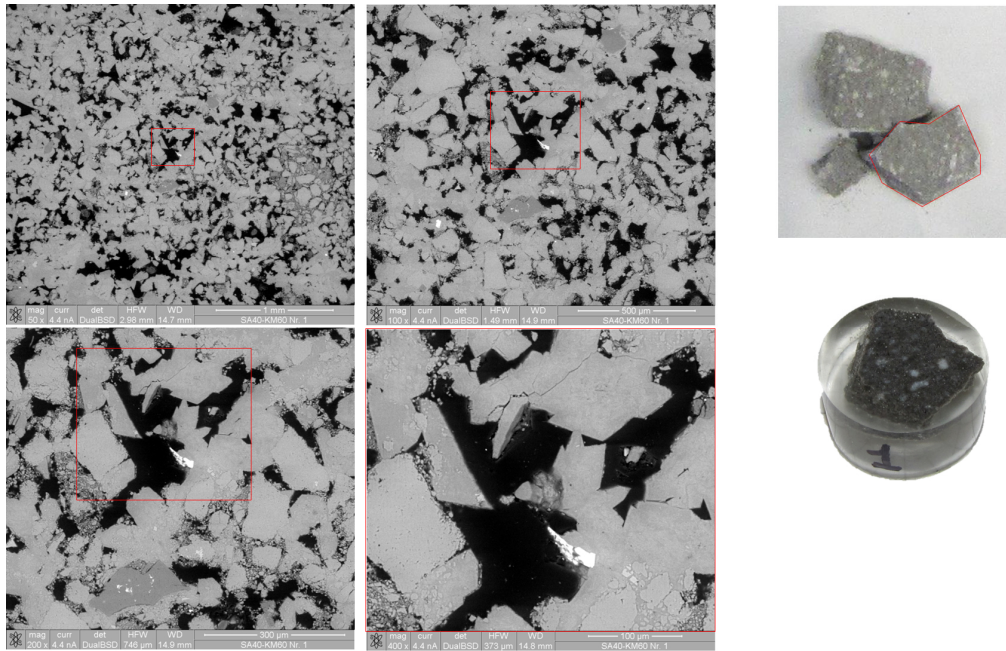


Figure 12.20 BSE images of SA40 KM60 polished sample (post swelling test).

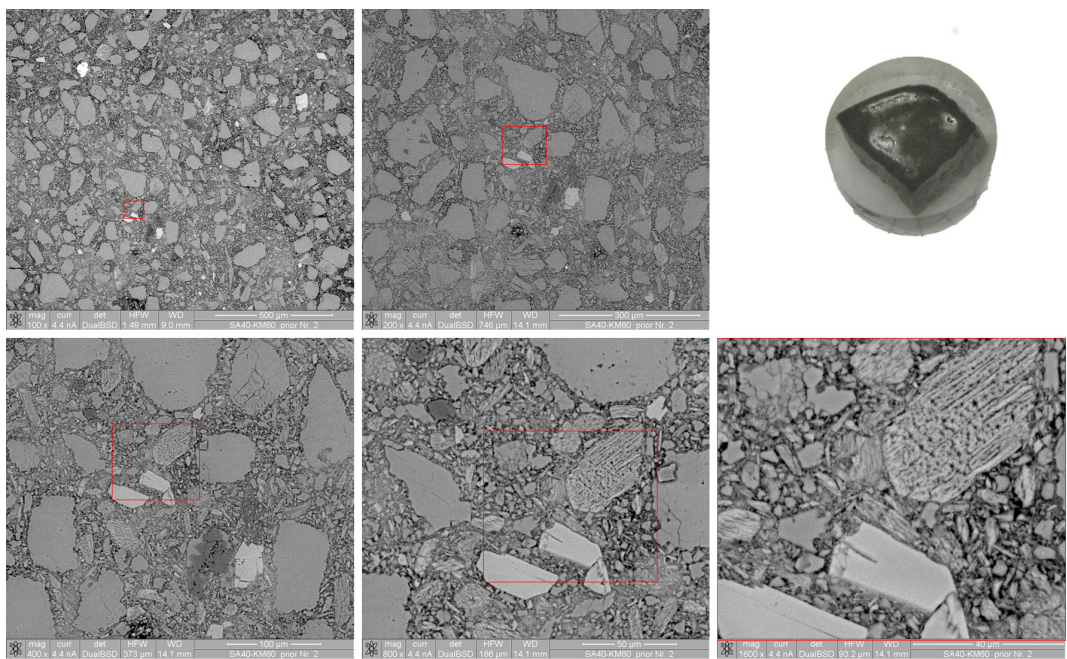


Figure 12.21 BSE images of SA40 KM60 polished sample (prior to swelling test).

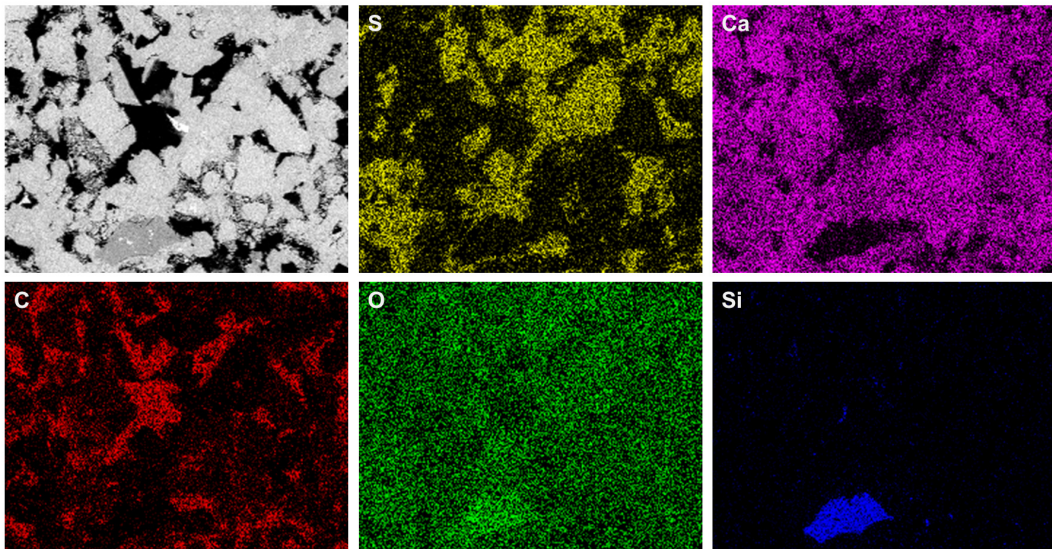


Figure 12.22 EDX mapping of the different elements of the SA40 KM60 polished sample (post swelling test). Note: the width of an image corresponds to ca. 800 μm (S = sulphur, Ca = calcium, C = carbon, O = oxygen and Si = silicon).

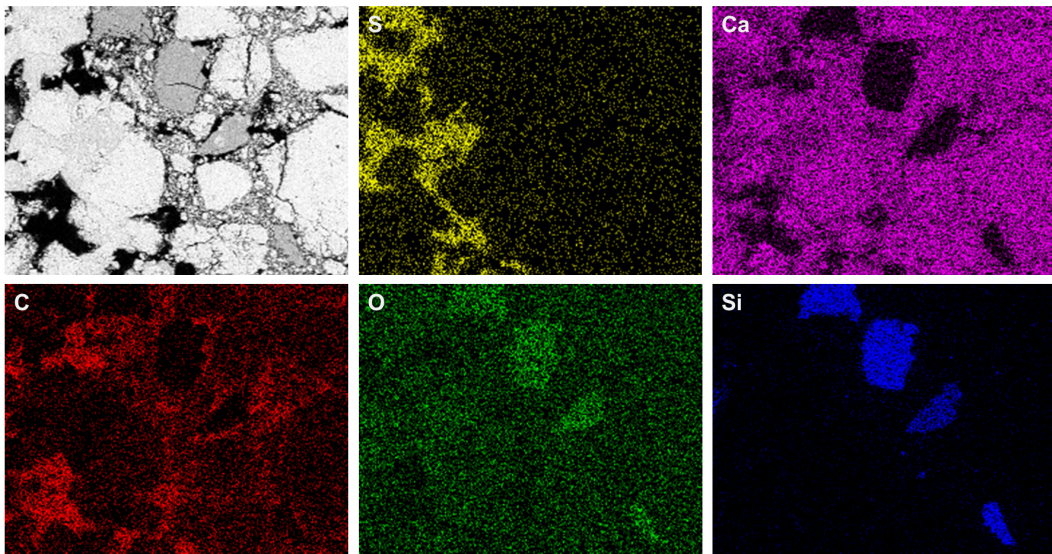


Figure 12.23 EDX mapping of the SA40 KM60 polished sample (post swelling test). Note: the width of an image corresponds to ca. 400 microns.

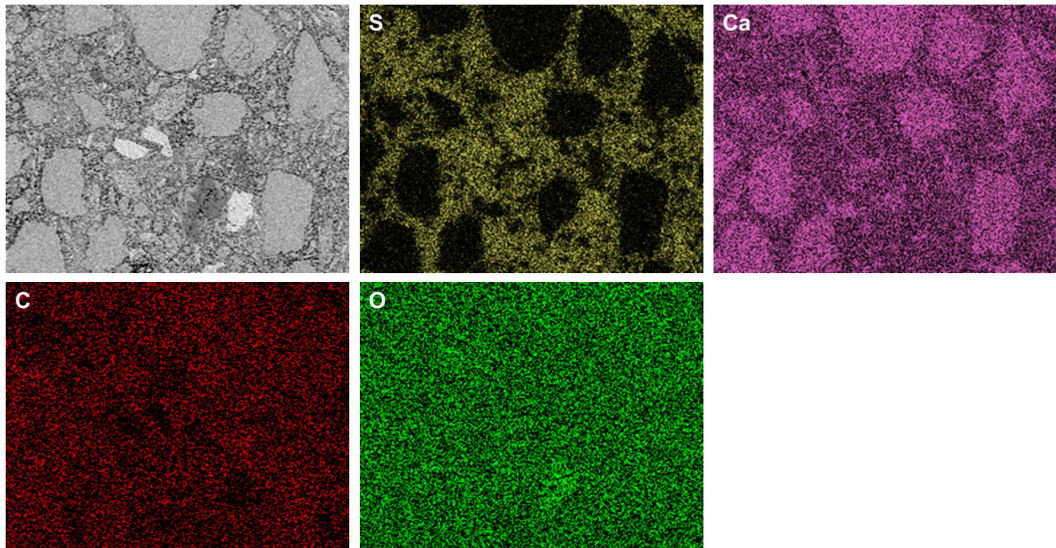


Figure 12.24 EDX mapping of the SA40 KM60 polished sample (prior to swelling test).
Note: the width of an image corresponds to ca. 400 microns.

The comparison of the sample prior to swelling to that post swelling leads to the following observations: prior to wetting, the sulphate seems to be finely distributed in the sample, while larger inclusions of limestone particles exist (“holes” in the sulphate mapping in Figure 12.24, which are however clearly displayed in the calcium mapping, indicating limestone). However, in the sample post test the appearance is reversed; here it seems that the sulphate (now mainly in the form of gypsum) is clustered and surrounded by the limestone (see the clearly defined main occurrence of sulphate in Figure 12.22 and Figure 12.23). This corresponds well to the expectations of a homogeneous sample (with the anhydrite finely distributed within the sample) after sample preparation and the tendency to formation of “clusters” of needles during gypsum precipitation due to the preferential precipitation on bigger gypsum crystals (Ostwald ripening phenomenon, *cf.* [208], according to which small crystals dissolve and redeposit onto larger crystals). The spaces where the anhydrite dissolved remain as pore spaces post test (black patches in Figure 12.22 and Figure 12.23).

Oedometer tests

In a first step, the surfaces of fragments of three samples post swelling under different loads (800 kPa, 1600 kPa and 3200 kPa) were investigated with SEM. The images (SE and BSE) are shown in Figure 12.25, Figure 12.26 and Figure 12.27. It needs to be noted that in the latter two cases the samples needed to be coated with gold and investigated under high vacuum, because no clear image could be obtained without coating.

In Oe_5_2 (800 kPa, Figure 12.25) one can clearly see clusters of precipitated gypsum (probably in a crack of the sample). In Oe_7_2 (1600 kPa, Figure 12.26) a single needle was found (which is assumed to be anhydrite, based on the orthorhombic shape of the needle and its size being smaller than 40 μm ; the needle is marked with an arrow in Figure 12.26). In Oe_6_2 (3200 kPa, Figure 12.27) anhydrite or gypsum was not distinguishable from the rest.

When comparing the images of these three samples, one can observe that there is a difference in the structure of the samples. It appears that a higher axial load during the test lead to a more homogeneous, compact matrix with less cracks.

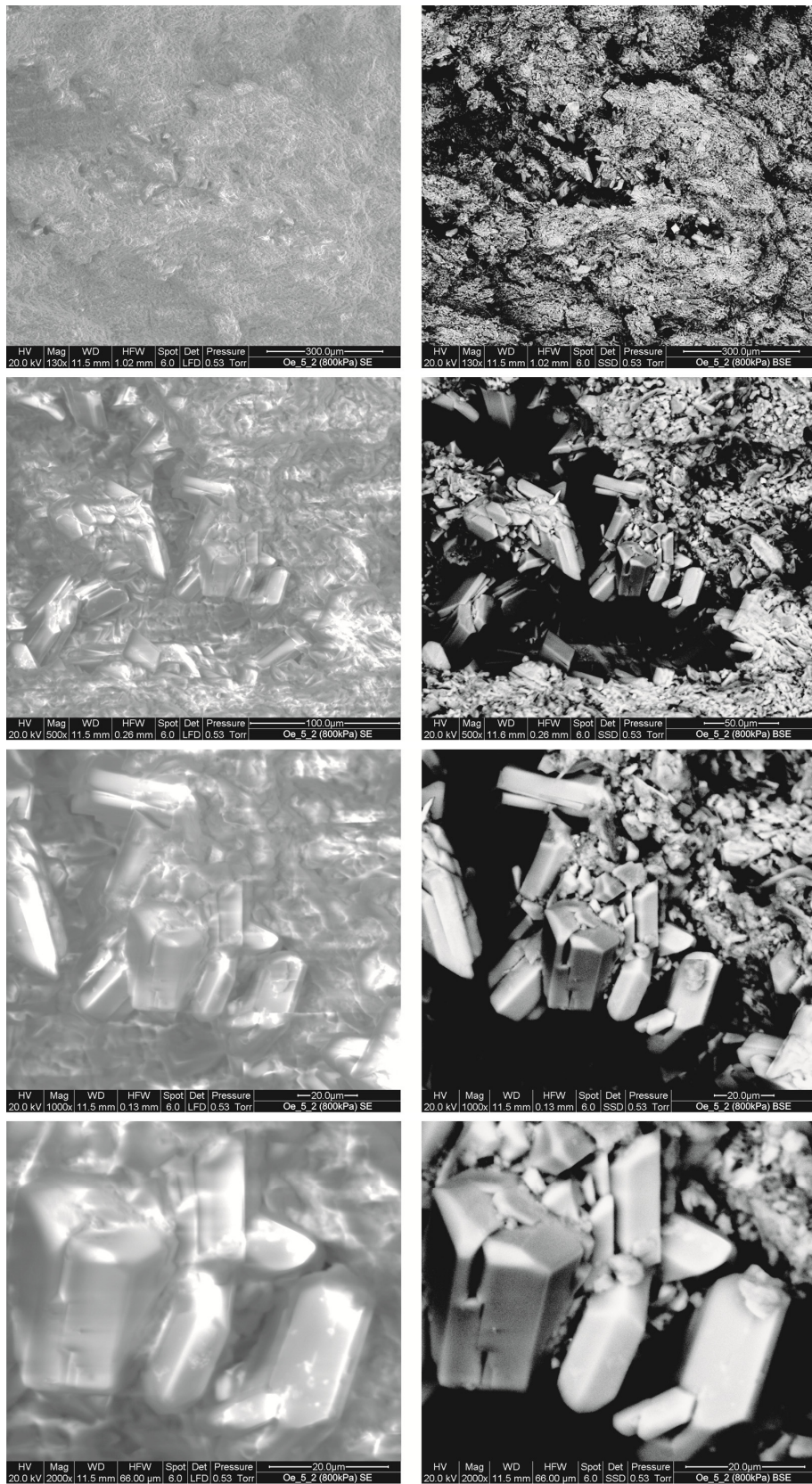


Figure 12.25 SE and BSE images of Oe_5_2 (800kPa).

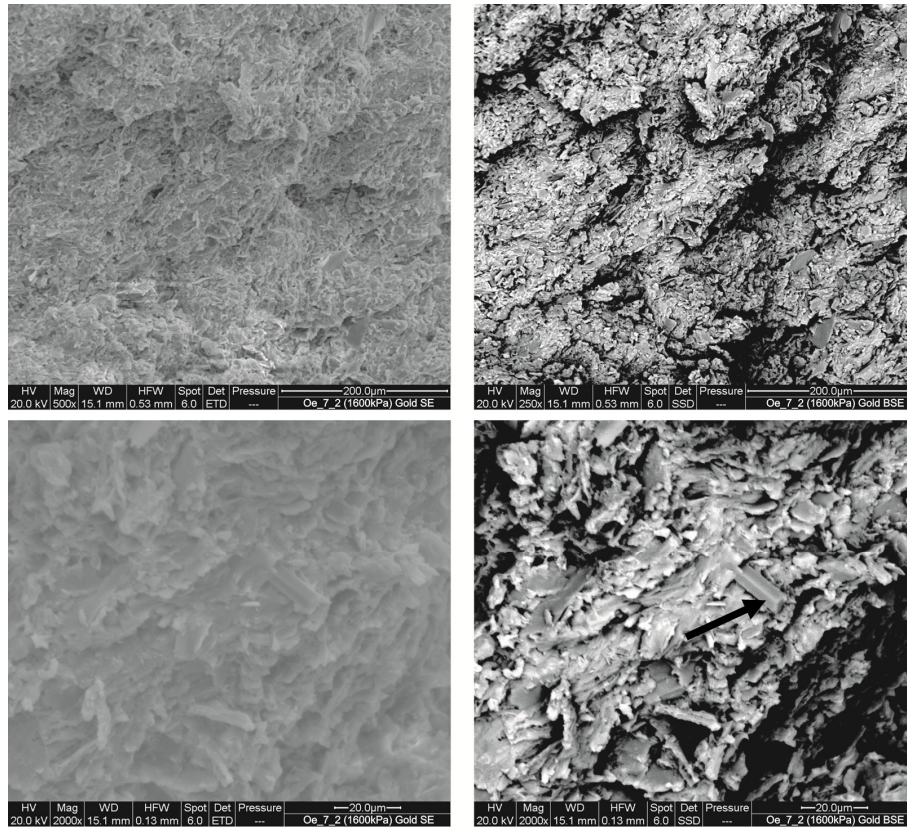


Figure 12.26 SE and BSE images of Oe_7_2 (1600kPa), coated with gold.

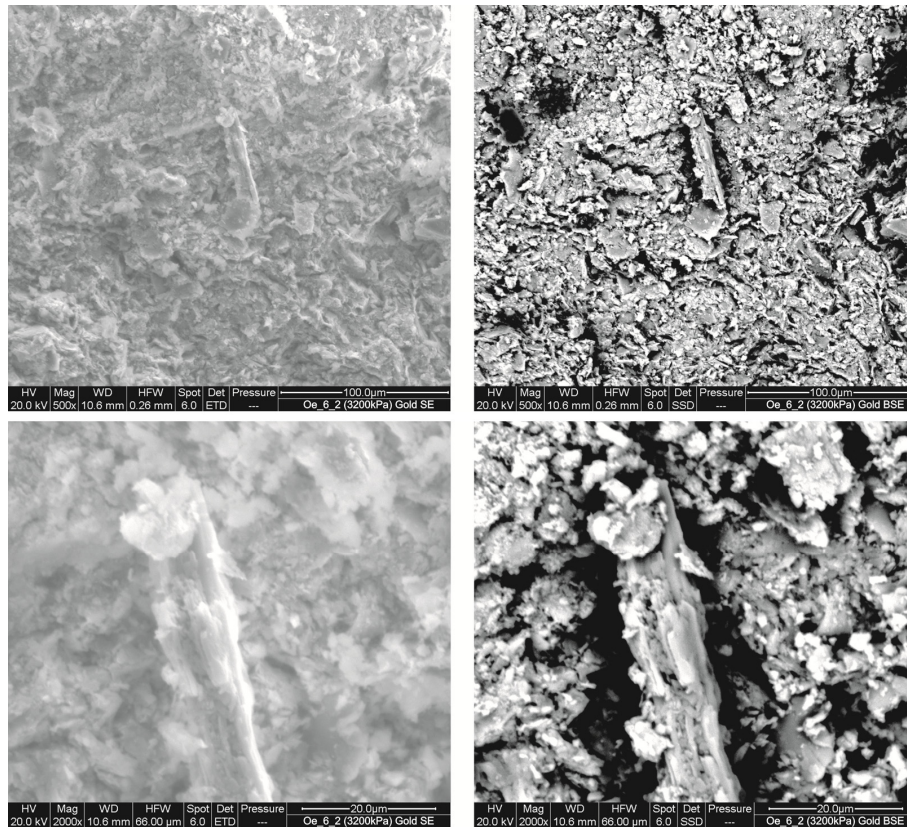


Figure 12.27 SE and BSE images of Oe_6_2 (3200kPa), coated with gold.

In order to investigate the difference between the sample Oe_5_2 (which was loaded with 800 kPa and swelled until steady state with roughly 85% AGT completed) and Oe_6_2 (which was loaded with 3200 kPa and did not swell at all within 80 days, during which ca. 10% AGT was completed), fragments of these samples were embedded in epoxy and polished (see Figure 12.28). These polished surfaces were then investigated with an optical stereo microscope (Figure 12.29) and with SEM and EDX, and ultimately thin sections were made from them and investigated with a transmitted light microscope in polarized light mode.

A close up investigation of the polished surfaces with an optical microscope shows a clear difference in structure as well. As already anticipated from the previous SEM investigations, the sample subjected to higher pressure during the test, Oe_6_2, seems more homogeneous with clearly “defined” pores and some white spots of (probably) anhydrite; Oe_5_2 seems more “weathered”, e.g. with gypsum crystals in pores.

SEM and EDX investigations of the polished surfaces lead to the images in Figure 12.30. It can be seen, that the sample Oe_6_2 shows more lighter components compared to Oe_5_2 which indicate a higher content of elements of higher atomic number (anhydrite, CaSO_4 , is therefore a lighter shade of grey in BSE images compared to gypsum, $\text{CaSO}_4 \cdot 2\text{H}_2\text{O}$), i.e. Oe_6_2 is assumed to have a higher content of anhydrite compared to gypsum, as was to be expected. The exact contents of anhydrite or gypsum cannot, however, be quantified with SEM and EDX, since they both contain the same elements (cf. sulphur mapping in Figure 12.30).

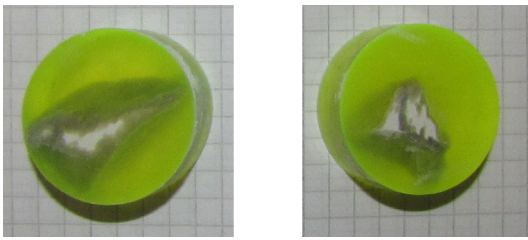


Figure 12.28 Embedded and polished samples Oe_5_2 (800 kPa, left) and Oe_6_2 (3200 kPa, right). The diameter of the specimens is 3 cm.

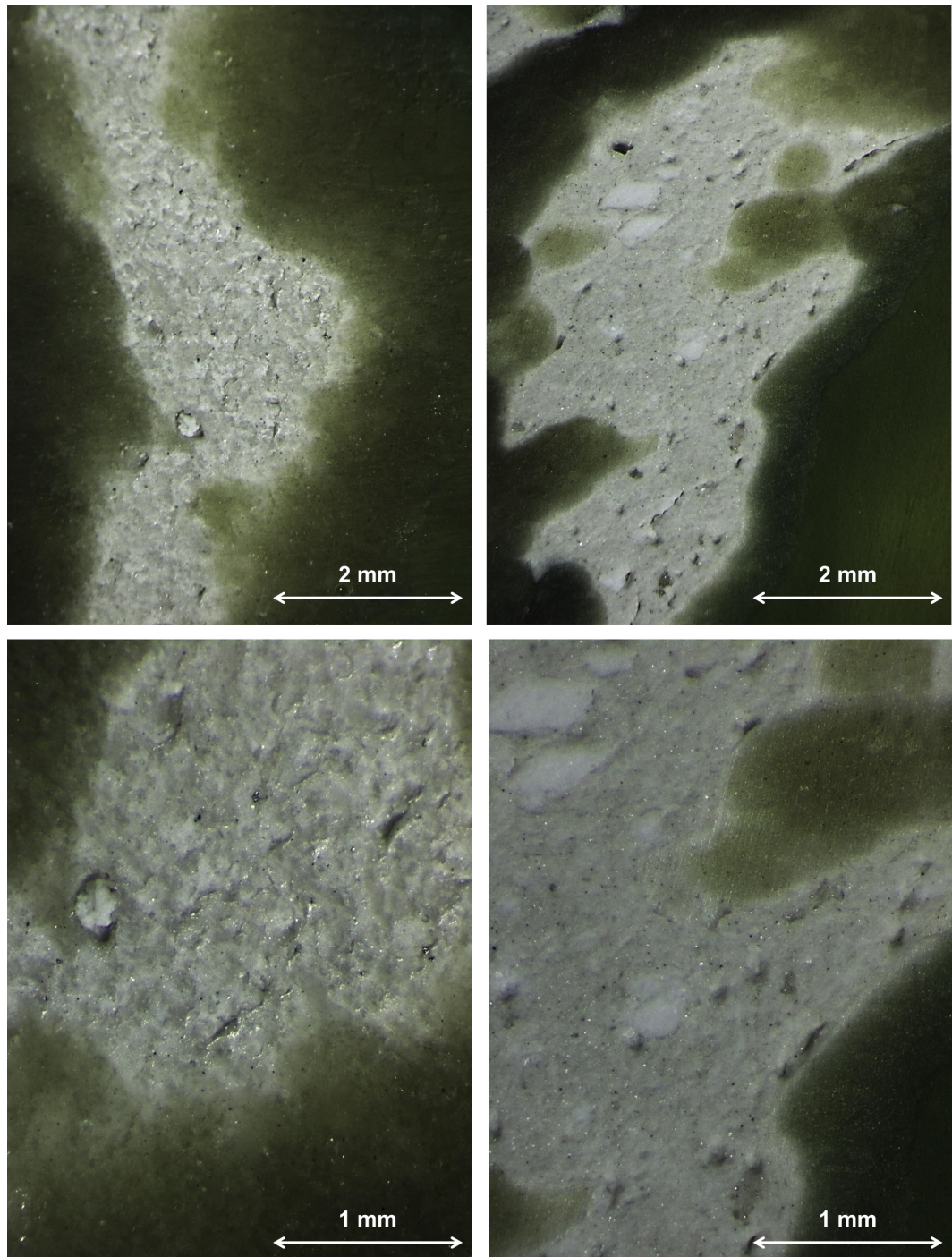


Figure 12.29 Embedded and polished samples Oe_5_2 (800 kPa, left) and Oe_6_2 (3200 kPa, right).

In order to investigate a sample where nearly the same amount of gypsum as anhydrite is supposed to be in the sample (*i.e.* an „intermediary“ sample between Oe_5_2 and Oe_6_2), a fragment from the oedometer sample Oe_5_4 (800kPa, AGT *ca.* 40% completed) was embedded and polished as well and observed with SEM and EDX. However, on a similar scale as used in Figure 12.30 (see Figure 12.31 bottom row), the distribution of sulphur within the sample appears very homogeneous, and no conclusions can be drawn regarding the distinction and distribution of anhydrite and gypsum within the sample.

The thin sections obtained from the samples Oe_5_2 and Oe_6_2 were analysed with a transmitted light microscope in polarized light mode. The comparison of two images in

Figure 12.32 shows that the right image (Oe_6_2) is composed of anhydrite crystals which can be distinguished by the higher birefringence. In the left image, gypsum crystals are observed as they have lower birefringence compared to anhydrite [209].

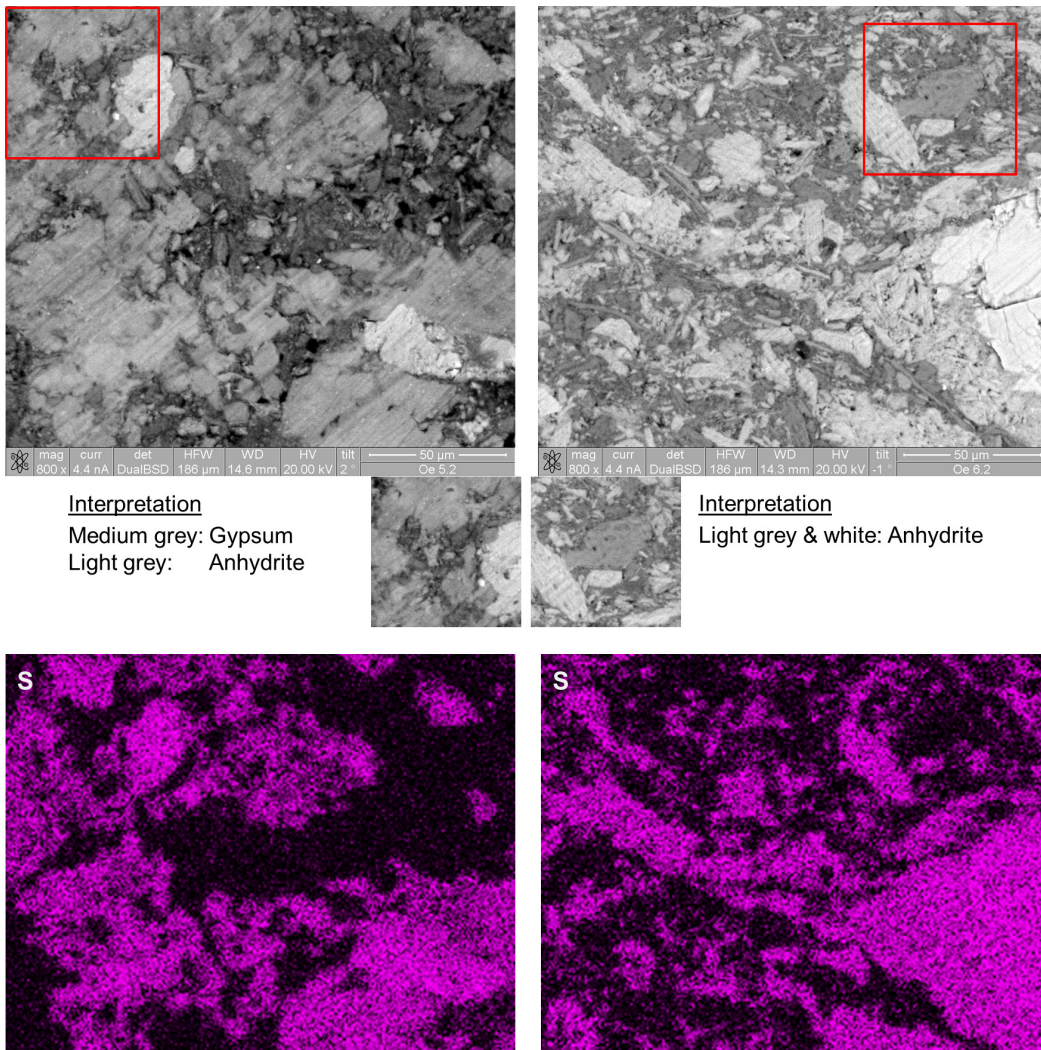


Figure 12.30 BSE images of embedded and polished samples Oe_5_2 (800 kPa, left) and Oe_6_2 (3200 kPa, right) and EDX mapping of sulphur.

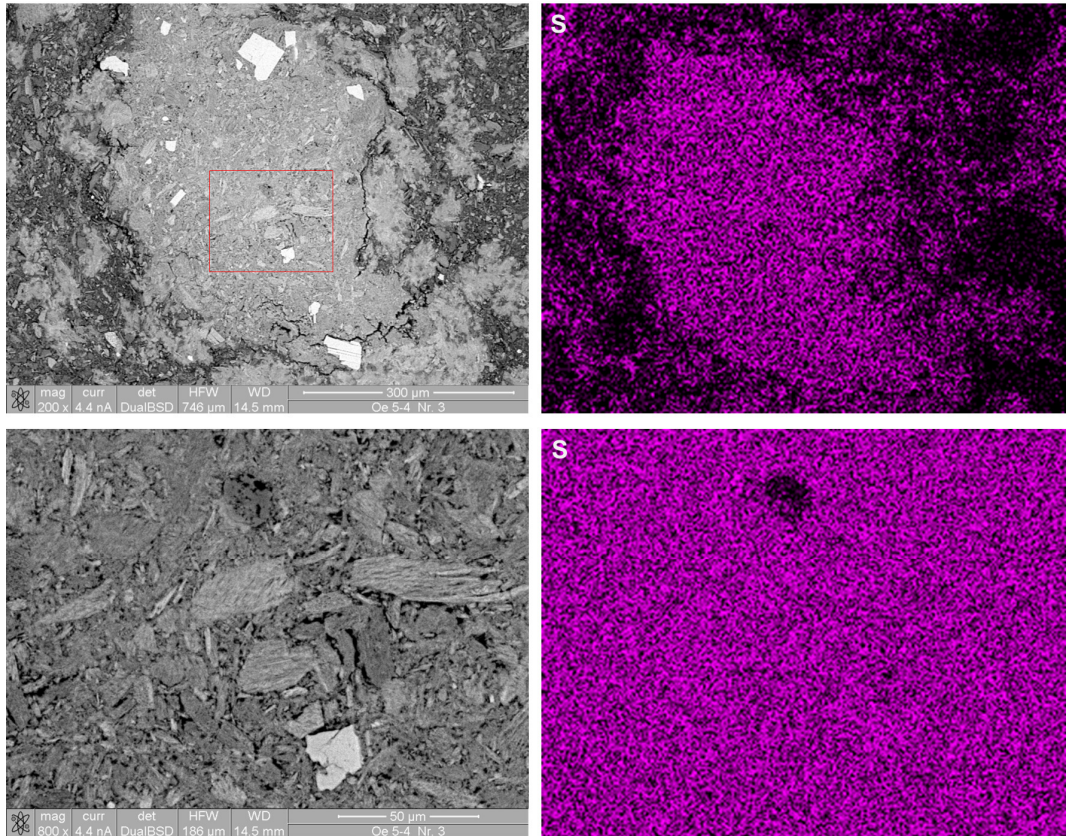


Figure 12.31 BSE images of embedded and polished samples Oe_5_4 (800 kPa, AGT ca 40%) and EDX mapping of sulphur.

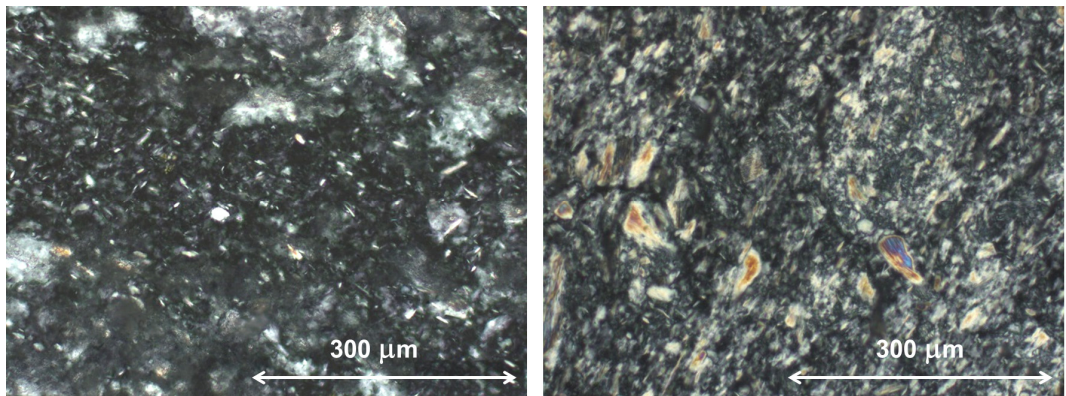


Figure 12.32 Images obtained from light microscopy in polarized light mode on thin sections of Oe_5_2 (800 kPa, left) and Oe_6_2 (3200 kPa, right).

Discussion

The applied microscopic techniques allow an insight into the structures of the samples and the distribution of anhydrite and gypsum within them. It could be seen that gypsum tends to form within pore spaces and creates clusters of needles. At lower axial stress (800 kPa) the structure of the sample appears more weathered compared to a sample that was loaded with a higher stress (3200 kPa). Due to the arduousness of the microscopic techniques, only the described selection of samples was investigated with microscopy. A more extensive and systematic series of microscopic investigations, where a large number of samples are observed and compared with one another, was not performed within the scope of this research project.

12.8 Ongoing experiments and outlook

The relationship between the chemical and mechanical processes needs to be established in greater detail, also by considering various boundary conditions (as indicated in Figure 12.1). For these investigations, new testing apparatuses needed to be designed and built. The testing equipment, procedure and first results are presented in the following sub-sections.

12.8.1 Complete constraint

Next to the relationship between axial swelling strain and change in mass of anhydrite, it is further of interest to obtain a relationship between the axial stress and change in mass of anhydrite. These investigations are being performed with samples as described in Section 12.3 under (nearly) completely constrained boundary conditions (as shown schematically in the middle image in Figure 12.1). For this, rigid frames were built (see Figure 12.33), in which the samples in steel rings (sample preparation similar as in the oedometers) are inserted and wetted. In axial direction the deformation is prohibited and the developing axial pressure is measured.

The used apparatuses are designed like the ones developed for the project FGU 2006/001 [92]. They consist of a stiff reaction frame with four columns. The vessel holding the water for the submersion of the specimen (1 in Figure 12.33) consists of a corrosion-resistant metallic plate and an acrylic cylinder (2). It is sealed hermetically with a cap containing a small opening with a removable plug (3), which enables water to be added at the beginning of a test and withdrawn during a test for analytical analysis. The sample is embedded between two filter plates (4), followed by perforated plates (5) for a more uniform watering of the specimen as well as spherical plates (6) in order to compensate for potentially eccentric swelling deformations. The deformation of the specimen is measured with two digital dial gauges (7). In axial direction the deformation is constrained with a jack (8) and the axial stress is obtained via measuring the oil pressure in the jack with a high precision digital manometer (9) which was calibrated with an electrical load cell.

The sample is inserted in a dry state and a small axial stress is applied ($\sigma_{ax} = 0.1$ MPa) via oil pressure. The valve (10) is then closed and the axial deformation is recorded. When the measured stresses and strains cease to change, the vessel is filled with water, thus completely immersing the sample and beginning the actual test.

For the evaluation of the tests, the boundary conditions are considered to be complete constraint, since the apparatus is very stiff and oil can be considered incompressible for the expected pressure ranges. Nevertheless, a slight deformation is still unavoidable but could, however, be compensated by externally increasing the oil pressure adequately.

Furthermore this apparatus offers the possibility of running not only deformation controlled tests but also load controlled tests by connecting an electronically controlled actuator to the jack.

The measured swelling stresses and minor strains (< 1.5%) of three experiments are shown in Figure 12.34 (the stresses are indicated by the solid lines while the strains are indicated by the dashed lines).

The results show that the stress which this type of artificial sample produces under constrained axial deformation can exceed the 3.2 MPa that were assumed to be a confining pressure based on the results from the oedometer tests (Section 12.6). Similar to the oedometer tests, the stress increases rapidly at first, then linearly for about 50 days at which point the stress rate begins to decrease. However, as can be seen from the sample CC_2_01, the swelling stress continues to increase even after more than one year. The fluctuations in the measurements were seen to correlate exactly with even the slightest temperature changes (note that with the exception of one incident, the temperature fluctuated between 20.3°C and 21.1°C for the entire duration of the tests).

These experiments are ongoing and will still be repeated, whereas the durations of the tests are to be varied and the change in mass of anhydrite determined for each sample in a similar way as described in Section 12.6.

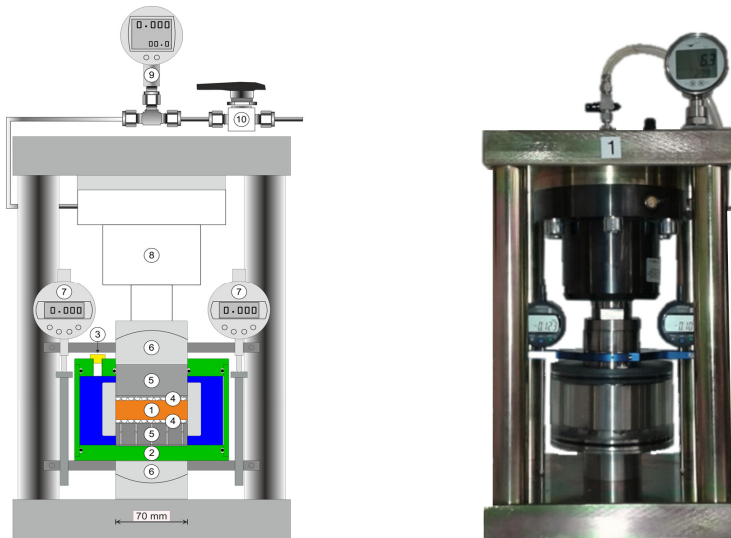


Figure 12.33 Apparatus for complete constraint tests.

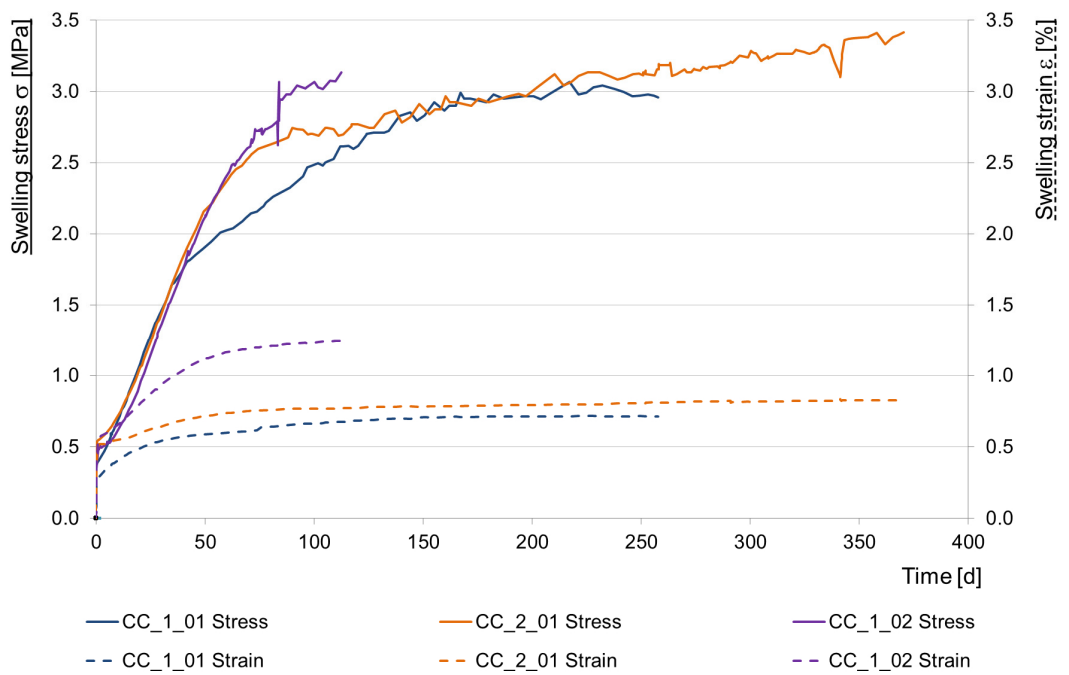


Figure 12.34 Completely constrained tests: results.

12.8.2 Flexible oedometers

In order to be able to distinguish χ_{ax} and χ_{rad} for the swelling behaviour in axial and radial behaviour (cf. Eqs. 12.6 and 12.7), so-called “flexible oedometer” experiments were designed (see Figure 12.35) to fulfil the boundary conditions shown on the right in Figure 12.1. Similar to the standard oedometers, the axial strain is measured via a dial gauge during swelling. However, in this case the samples are situated in a cylinder made of PVC rather than steel. The radial deformation of the PVC cylinder is measured during swelling with a digital high-precision measuring chain and via the stiffness of the cylinder it is possible to calculate the corresponding radial stress the sample exhibits on the inner wall of the cylinder.



Figure 12.35 Apparatus for flexible oedometer tests.

The correlation between the pressure on the inside of the cylinders and the measured radial deformation was obtained by applying water pressure on the inside of the cylinders and measuring the deformation. The dimensions of the PVC cylinder (inner diameter and wall thickness) were chosen so that the oedometer behaves elastically for the expected radial pressure range. The results from calibration tests on eight cylinders are shown in Figure 12.36. All cylinders deformed identically under inner radial pressure. It can be seen that a linear relationship exists between radial stress and deformation of the cylinders.

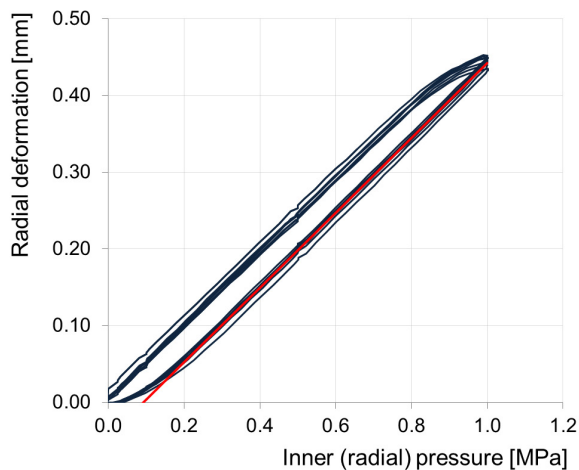


Figure 12.36 Calibration of PVC cylinders.

The diameter of the samples is equal to that of the standard oedometer samples. However, the height of the sample was chosen to be 4 cm instead of 2 cm, in order to guarantee homogeneous deformations in the region of the measuring chain and thus increase the accuracy of the measured radial deformation. The samples were compacted analogue to the sample preparation described in Section 12.3. Hereby, with eight samples the PVC cylinder was inserted into a steel cylinder for radial support during compaction of the samples directly inside the PVC cylinders. This however, led to a certain (unknown) initial radial stress acting on the samples (pre-stress). For this reason, four further samples were compacted outside the PVC cylinders and inserted only after compaction (curves ending with a triangle in Figure 12.37). The samples were loaded with 800 kPa or 1600 kPa in a dry state, then wetted with water saturated with respect to gypsum. Figure 12.37 shows the radial stress (left) and axial strain (right) measured after the samples were wetted, *i.e.* the mechanical reactions the samples exhibit due to swelling (the values in Figure 12.37 were set to zero after initial loading in the dry state).

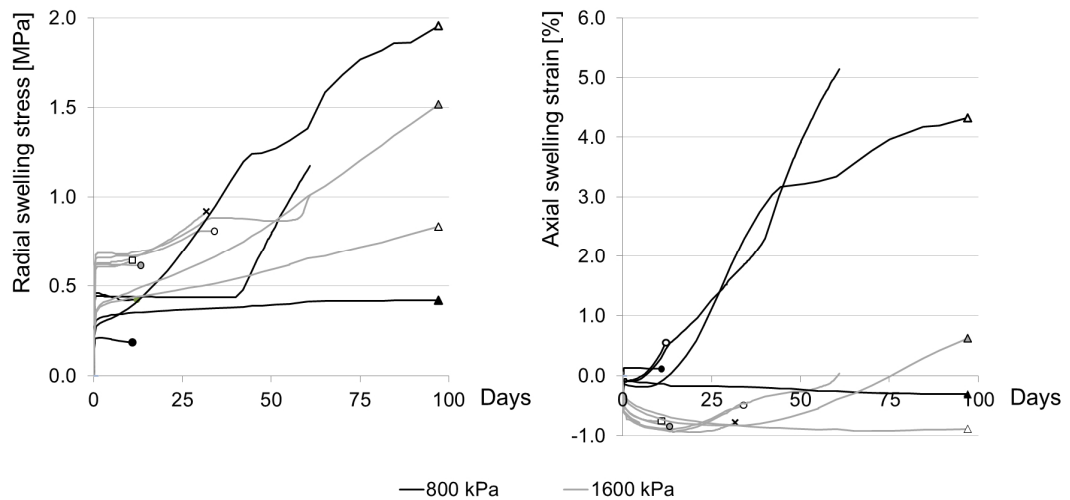


Figure 12.37 Results from the experiments with flexible oedometers.

It becomes apparent that – although the calibration of the PVC showed perfectly reproducible and explicit results – the actual “flexible oedometer”-experiments deliver a wide variety of results, both in radial and axial direction. Furthermore, no clear correlation can be seen between the axially applied load and the results. Therefore modifications and improvements are needed before further conclusions can be drawn.

13 Free swelling tests with natural samples

13.1 Introduction

In natural sulphatic claystones multiple swelling processes can occur simultaneously, *i.e.* due to osmotic swelling as well as due to AGT. However, while the clay matrix contributes to a rapid swelling strain, the hydration of anhydrite in the rock is a rather slow process. The quantification of the swelling due to the clay and due to the anhydrite in the rock is of interest (indicated figuratively in Figure 13.1). This is approached by performing free swelling tests on samples from bore cores originating from the Belchen Tunnel, see Section 9.3.

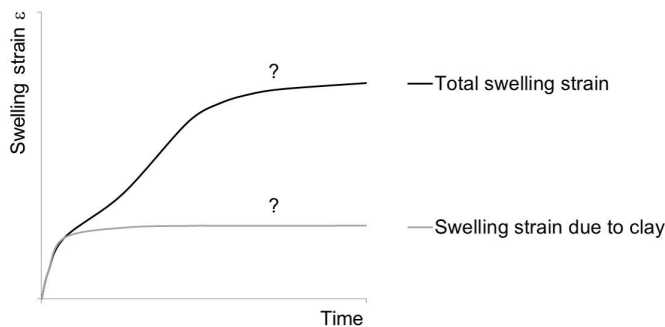


Figure 13.1 Conceptual graph of total swelling strain and possible corresponding amount of swelling strain due to clay alone.

In an undisturbed state, such as prior to excavation or – in the case of bore cores – after storage for a long period of time at constant temperature and humidity, the rock samples are in a state of thermodynamic equilibrium. Due to the fact that the clay particles are hydrophilic, the condition of a sample changes rapidly upon wetting or total immersion in water. For one, the degree of saturation increases which leads to a reduction of negative pore water pressure and thus (due to a decrease in effective strains) to a decompression of the sample, *i.e.* a rapid initial strain can be observed. Furthermore, an equilibration of negative electric charge of the clay platelets occurs, *i.e.* osmotic swelling. AGT cannot occur straight from the beginning on, since the activity of the pore water of the samples is considerably smaller than 1, due to the low water potential of partially saturated (or nearly completely dry) rocks, see Section 6. This is further fortified by the water bound in the sample via the Stern layer and the diffuse double layer.

The water activity a_w can be defined as the ratio between the partial evaporation pressure in the vicinity of the pore (p_D) to the saturated evaporation pressure over dilute water (p_S). This ratio corresponds to the definition of relative humidity RH , see Eq. (13.1):

$$a_w = \frac{p_D}{p_S} = \frac{RH}{100\%} \quad (13.1)$$

In order for AGT to occur, the activity of the pore water needs to increase, *i.e.* the clay matrix needs to absorb water (by mechanical swelling due to reduction of negative pore water pressure and by osmotic swelling) thus enabling so called free water (water with an activity a_w closer to 1) to come into contact with the anhydrite particles.

Therefore, the rapid initial swelling phenomenon can be attributed to swelling of clay whereas the clay matrix supplies the water used for AGT. However, a prediction of the amount of swelling due to the different phenomena is so far not possible. For this reason the experiments with natural rock focus on the quantification of the amount of swelling due to clay and due to AGT by means of simple free swelling tests.

13.2 Experimental procedure

13.2.1 Material and sample preparation

The sample material consists of remaining bore cores from the research project ASTRA project 2011.006 [200] (BH3) and from an exploratory boring campaign for the construction of the 3rd Belchen tunnel [201] (SB6), cf. Section 9.3.

In order to gain oriented bore cores (with a diameter of 34 mm), the bore cores from BH3 with a diameter of 84 mm were perforated in radial direction within the scope of the research performed by Amann et al. [200]. Figure 13.2 shows the bore core BH3 3.1-3.4 m, where the smaller radial boreholes with ca. 40 mm in diameter can be seen. In order to obtain samples for the swelling tests from the remaining material for the present project, the cores are first cut every 2 cm in radial direction, followed by individual cuts in axial direction – tangentially to the smaller boreholes. This leads to segmental samples, as shown in Figure 13.2 (hereafter referred to as “segments”).



Figure 13.2 Left: Bore core Belchen BH3 3.1-3.4m and example for one segmental sample. Right: typical dimensions of segmental samples.

From this bore core 15 segments were sawed for the free swelling tests (see white shaded boxes in Figure 13.3). Prior to the tests, the mineralogy was determined via X-ray diffraction on 10 XRD-samples (X11-X20 in Figure 13.3). The XRD results are shown in Figure 13.4.

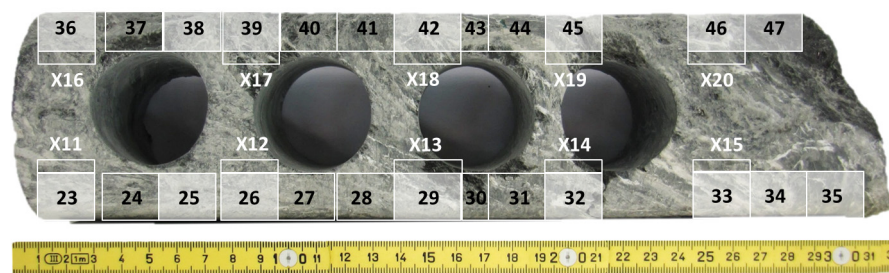


Figure 13.3 Bore core BH3, 3.1-3.4m: Selection of samples for free swelling tests (indicated by white shaded boxes).

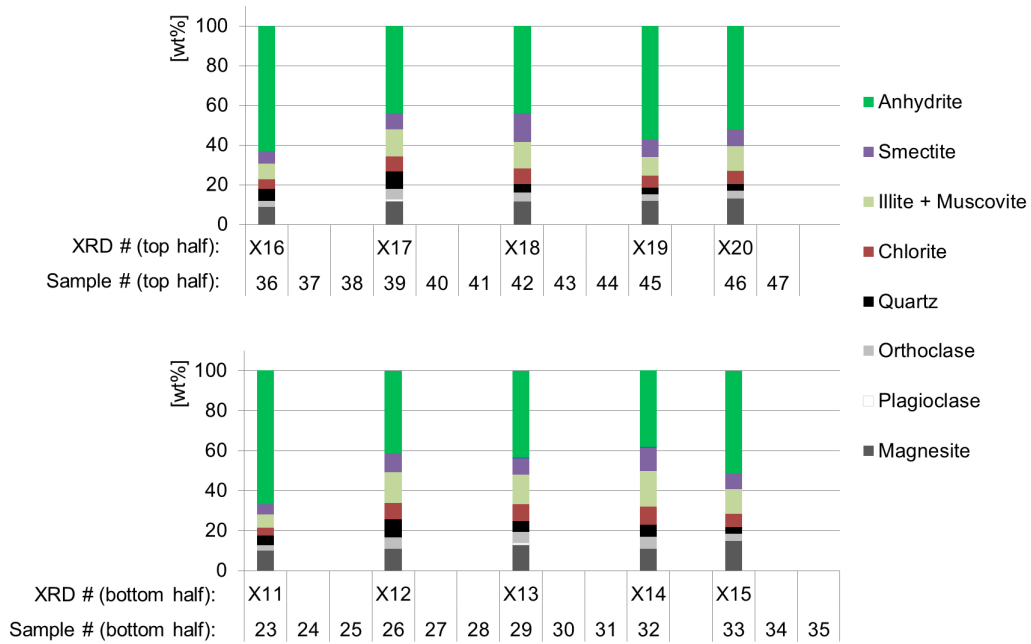


Figure 13.4 XRD results (X11-X20, Belchen BH3 3.1-3.4.). [wt%] = weight percentage.

The bore cores from SB6 (1.25-1.56 m) had a diameter of 72 mm and could be cut into “disks”, as opposed to the segments from the previous series. The compositions of the cores were established via XRD on samples adjacent to the disks (samples X21/ X22 and X25-X28, see Figure 13.6; however, these are not the exact results from the X-ray analysis but are corrected due to appearance of bassanite in the results as a consequence of faulty sample preparation, see Appendix I).



Figure 13.5 Belchen SB6, 1.25-1.38m and 1.4-1.56m.

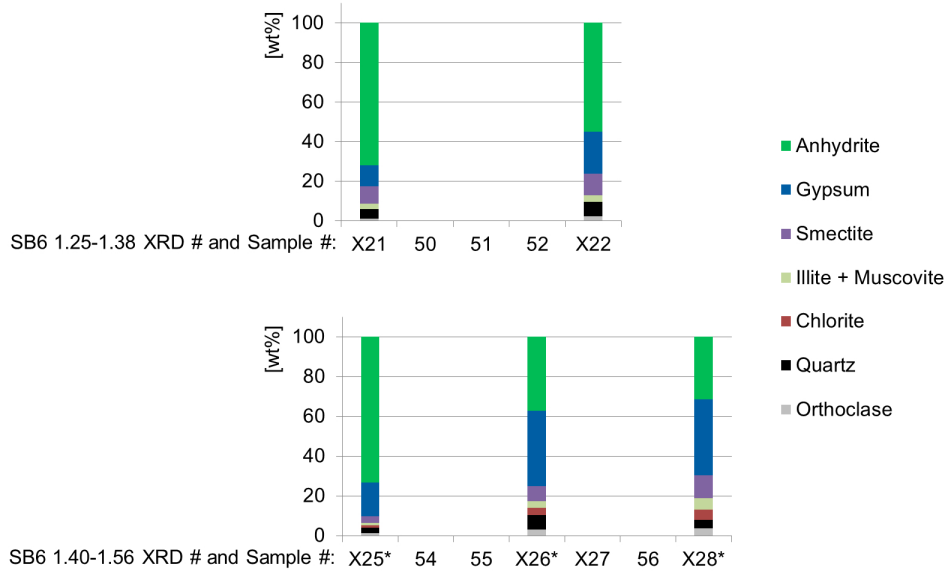


Figure 13.6 XRD results (X21-X28, Belchen SB6 1.25-1.56. The samples marked * were corrected according to Appendix I.)

All samples were obtained by cutting the above mentioned cores air-flushed with an electronically controlled diamond band saw, which allows a precise and smooth cut without inducing AGT.

13.2.2 Testing procedure

For the free swelling tests the samples were immersed in water and the axial swelling heave of each sample was measured regularly with a dial gauge.

First (preliminary) tests have shown that samples lying unsupported in water begin to decay radially (see Figure 13.8). For this reason the free swelling tests were performed with a slight radial support of the samples by a rigid foam (in the case of segments, cf. Figure 13.7 and Figure 13.8) or Teflon bands and rubber membranes (in the case of disks, Figure 13.9). This does not, however, prohibit radial strain completely.

The disks are embedded between two acrylic glass plates and a filter plate below the sample, which ensure a uniform watering of the sample.

The samples were extracted at various points in time, dried (at 65°C), and the mineralogical composition was determined via XRD.

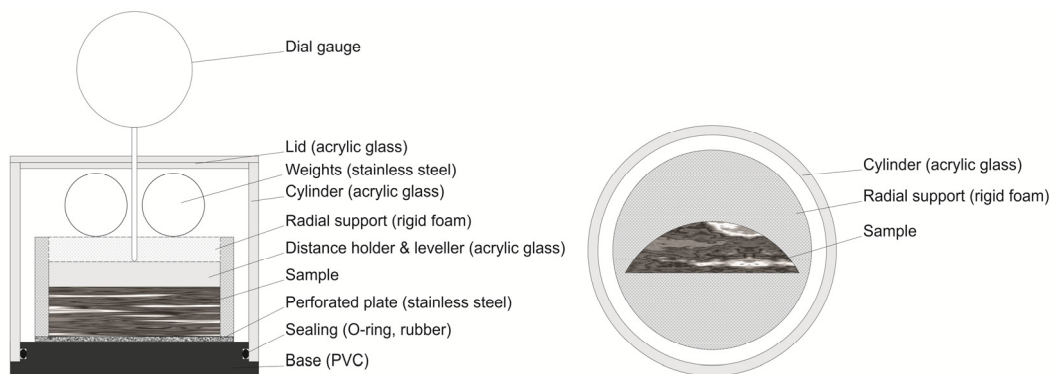


Figure 13.7 Testing apparatus. Left: Cross section. Right: View from top (without lid and distance holder).

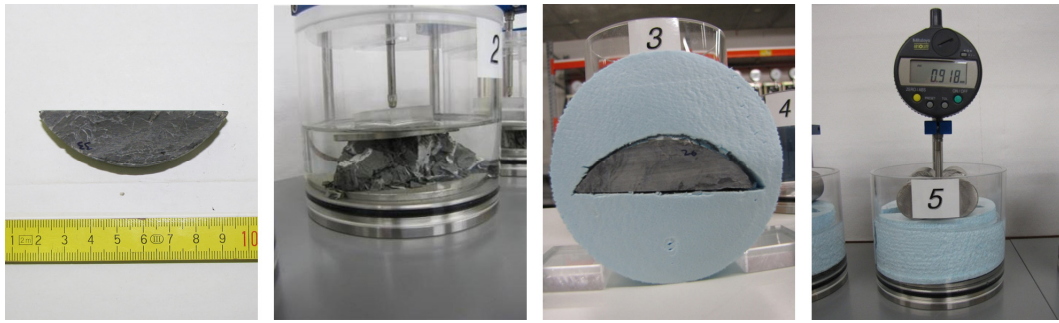


Figure 13.8 (From left to right) segmental sample, degradation of a trial sample, use of rigid foam as radial support, apparatus from the front.

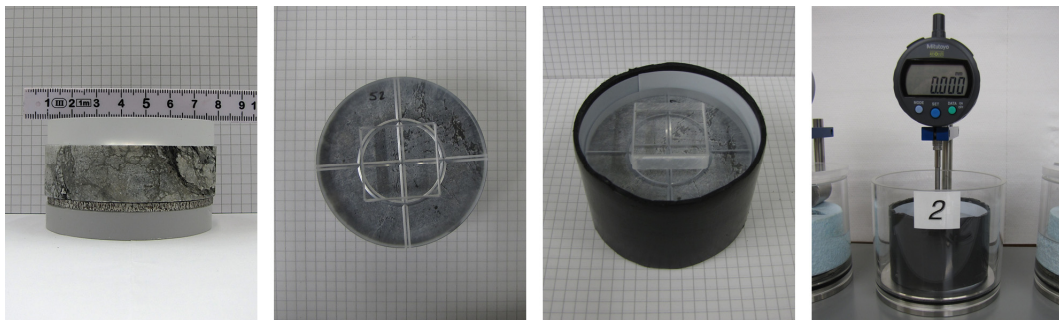


Figure 13.9 (From left to right) sample between acrylic glass plates and filter plate, then wrapped in a Teflon band and a rubber membrane and inserted in the apparatus.

13.3 Results

13.3.1 Segments

The diagram in Figure 13.10 shows the swelling strain over time for all tested samples. Five samples were extracted after 100 - 140 days, six samples after ca. one year and two samples after nearly 500 days. The points of extraction are indicated by the red crosses in the diagram.

Figure 13.10 shows that all samples swelled similarly, experiencing first a rapid heave due to water uptake, then the actual swelling due to clay and anhydrite in the samples began along a slightly S-shaped curve, some beginning with a slower rate, then accelerating and swelling nearly linearly for a while until the swelling rate begins slowing down again and even after three years appearing not to have reached an end value yet (samples 23 and 45 in Figure 13.10). However, the extent of swelling (*i.e.* the maximal measured value of swelling strain) scatters between ca. 22% and 42%.

The compositions of the samples post test were established via X-ray analysis and are shown in Figure 13.11. Here too, bassanite appeared in some of the results which was corrected in Figure 13.11 according to Appendix I.

From the mineralogical composition post test the amount of gypsum in each sample was determined from which the theoretical change in volume due to AGT can be back calculated (based on the knowledge that $\Delta V_G = 1.61 \cdot \Delta V_A$). This change in volume allows an estimation of the amount of swelling due to AGT (ε_{AGT}).

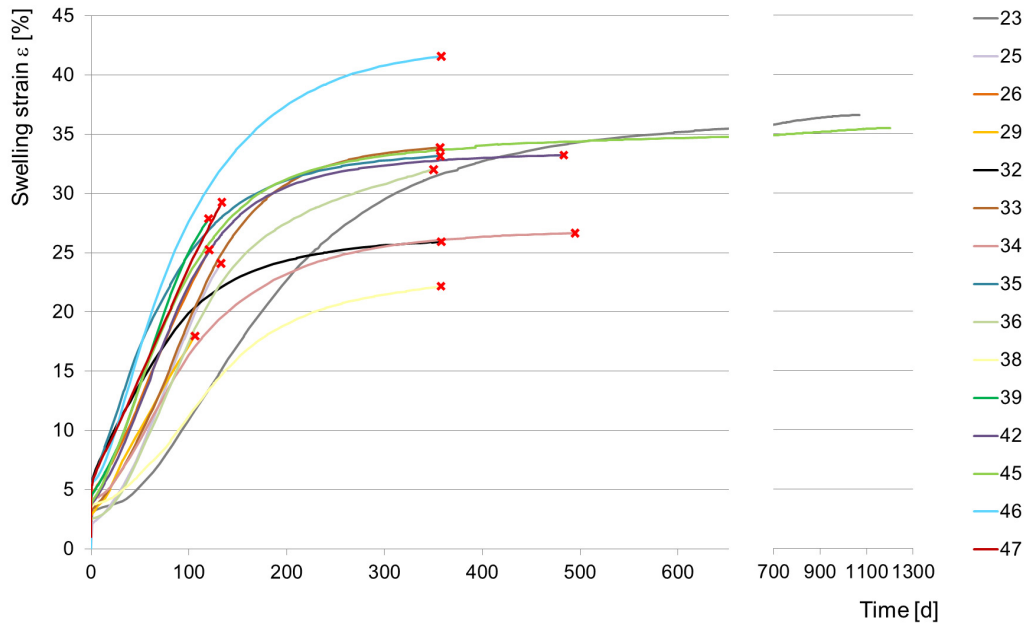


Figure 13.10 Swelling strain of segments over time. The red crosses indicate points of extraction.

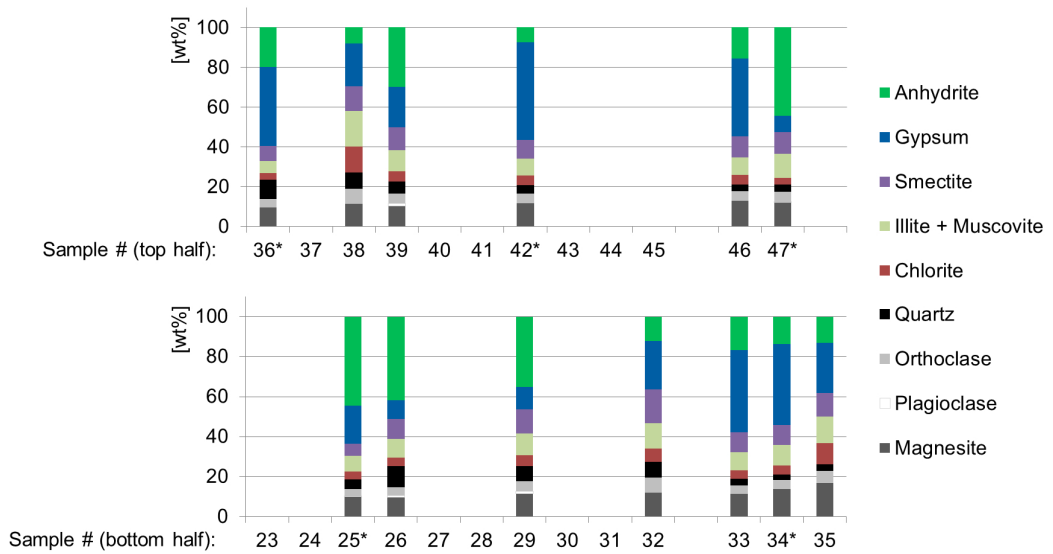


Figure 13.11 Sample compositions post test (the samples marked * were corrected according to Appendix I).

$\epsilon_{initial}$ (green) and ϵ_{AGT} (black) are indicated in the diagram in Figure 13.12 as fractions of the total strains of each segment. The grey pillars indicate the amount of swelling due to all other effects which could so far not be quantified, such as further cracking of the samples and swelling of clay (ϵ_{rest}). The columns are sorted by duration of the tests.

In general, the amount of strains due to AGT increases over time, however they vary strongly. This scatter can most likely be attributed to the heterogeneous compositions of the samples, since the XRD results showed initial values of anhydrite in the samples between 35% and 60%.

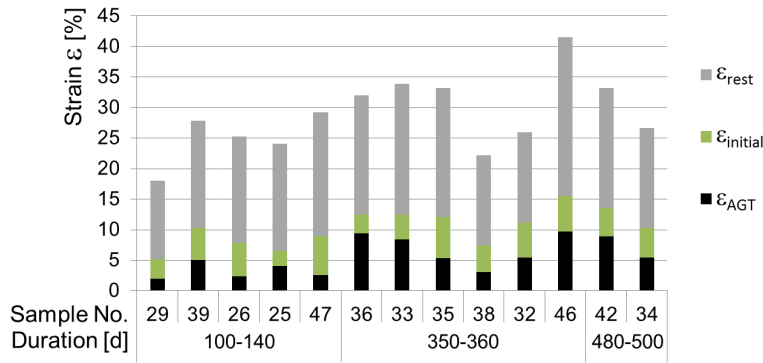


Figure 13.12 Swelling strains of segments divided into chemically induced and initial (immediate) strains and strains due to other processes.

Figure 13.13 shows the amount of transformed anhydrite for each extracted sample over time. Within the first 140 days maximally 35% of the anhydrite in the samples appears to have transformed to gypsum. After a year, 60 – 70% and after roughly 500 days 70 – 85% of the anhydrite has reacted. The rate with which the anhydrite transforms appears nearly constant for the entire duration of the observation period (100 - 500 days). Furthermore, the process was not completed with any of the terminated experiments, even after 500 days (as described previously, the swelling strain of the two ongoing samples is still increasing slightly, cf. Figure 13.10).

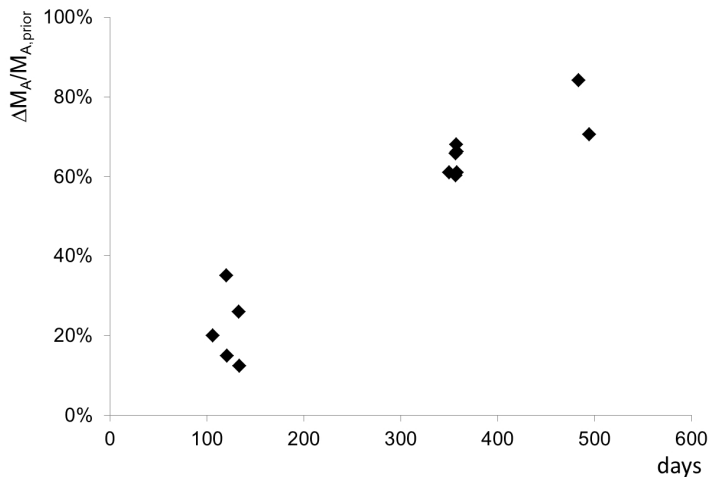


Figure 13.13 Transformed mass of anhydrite at the points of extraction vs. duration of each test.

13.3.2 Disks

Immersing the disks from the core SB6 in water and measuring the swelling heave delivered the swelling strain curves shown in Figure 13.14. These experiments are currently still running and were so far not yet extracted.

The behaviour of this series is very different from that of the segments: in general, a much smaller initial rapid swelling strain occurs, after which the samples swell slightly quicker at first, then steady to a linear increase in swelling strain. The constant rate of the swelling strain is much slower compared to the segments, the amount of swelling is much lower and the swelling strain rate did not begin to reduce considerably after about one year, which was the case with the segments.

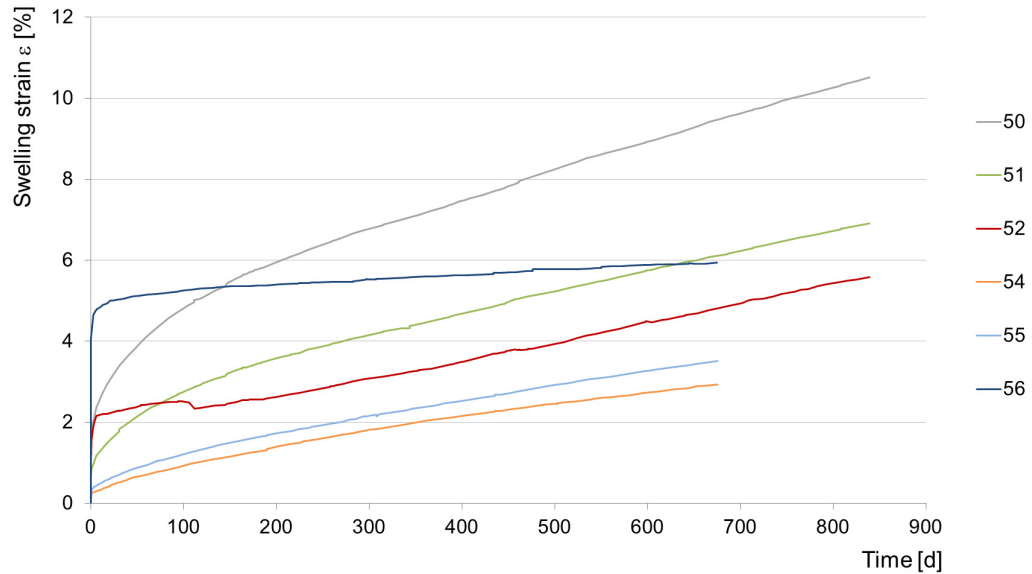


Figure 13.14 Swelling strain of disks over time.

13.4 Discussion

The rapid ascent occurring in the first hours of the tests (see Figure 13.10 and Figure 13.14) are most likely a result of the initially low degree of saturation of the samples, causing immediate water absorption and thus a rapid swelling, which was to be expected (*cf.* Section 13.1). This amount of swelling strain is assumed to appear independently of the osmotic swelling as well as the swelling due to AGT. The value for the rapid initial strains ($\varepsilon_{initial}$) can easily be estimated from the measurements, since each curve exhibited a distinguished change in the rate of swelling within the first 24h (most within one hour) of watering the samples. The initial heave of the disks was, however, smaller than that of the segments, which is most likely due to the fact that the initial degree of saturation of the disks was higher than that of the segments.

In the case of the segments, the anhydrite dissolution (and thus gypsum precipitation) seems to occur relatively linearly over time, whereas the total swelling strains (which developed in a curved „S“ shape) slowly reach an asymptotic value (even if AGT is not yet completed). Therefore, it appears that the osmotic swelling and change in structure (*e.g.* due to cracking of the samples) occurs faster than the swelling due to AGT. The gypsum precipitates probably mainly within the cracks (most likely expands them further), which explains why the total swelling strain remains nearly constant after a certain time, even though gypsum precipitates continuously.

In the case of the disks, the swelling strain develops far slower and is still increasing linearly even after 800 days. It is considered possible that this is caused by the gypsum in the samples (*cf.* effect of sealing of anhydrite, Section 4.5).

Due to the fact that the swelling strains scatter very strongly and the analysis is based on some uncertain assumptions (mainly due to the segmental shape and the appearance of bassanite in the samples post test, *cf.* Appendix I), a concluding interpretation of the results is so far not possible. The scatter in the results can furthermore be attributed to the heterogeneous composition of the samples.

In order to evaluate the amount of swelling due to clay, further free swelling tests will be performed in an oven at roughly 55°C at which temperature anhydrite dissolution does not occur (*i.e.* anhydrite is the stable phase).

Appendix

I	Analysis of sample composition (TGA, XRD)	169
II	Sample properties	173
III	Notation.....	176

I Analysis of sample composition (TGA, XRD)

Figure A.1 and Figure A.2 show the results of TGA analyses performed on the oedometer samples described in Sections 12.5 and 12.6. As described in Section 8.3.1, the drop in mass between 90°C and 140°C can be attributed solely to the dehydration of gypsum in the specimen. Note, that the drop at a temperature higher than 450°C occurs due to dihydroxylation of kaolin (*cf.* [210]) and is not of further interest in this work.

From the TGA measurements, the gypsum and anhydrite contents of the samples post oedometer test can be calculated based on the mass balances according to Eqs. (3.1) and (3.2) (since the samples did not contain any gypsum initially).

$$M_{G,end} = \Delta wt \cdot M_{tot,end} \cdot \frac{172[g/mol]}{36[g/mol]} \quad (A.1)$$

$$M_{A,end} = M_{A,prior} - \Delta wt \cdot M_{tot,end} \cdot \frac{136[g/mol]}{36[g/mol]} \quad (A.2)$$

where $M_{G,end}$, $M_{A,end}$ and $M_{tot,end}$ denote the masses of gypsum and anhydrite in the sample and total dry mass of the sample post test. Δwt corresponds to the measured change in mass in [wt%] according to the TGA analysis. From these total masses, the masses per unit volume can be derived (*cf.* Figure 12.12 and Figure 12.14):

$$m_{G,end} = \frac{M_{G,end}}{V_{tot,end}} \quad (A.3)$$

$$m_{A,end} = \frac{M_{A,end}}{V_{tot,end}} \quad (A.4)$$

whereas $V_{tot,end}$ corresponds to the total volume of the sample post test (calculated from measurements).

The completion of the AGT process within a sample can be estimated by the following ratio:

$$AGT[\%] = 1 - \frac{M_{A,end}}{M_{A,prior}} \quad (A.5)$$

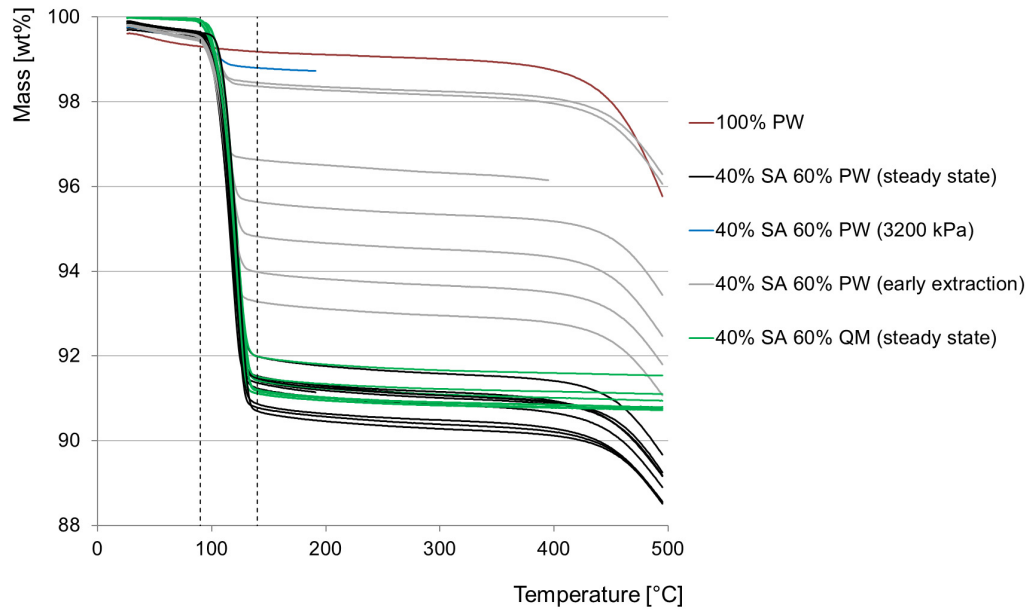


Figure A.1 TGA results of oedometer tests with $\sigma_{ax} > 3$ kPa.

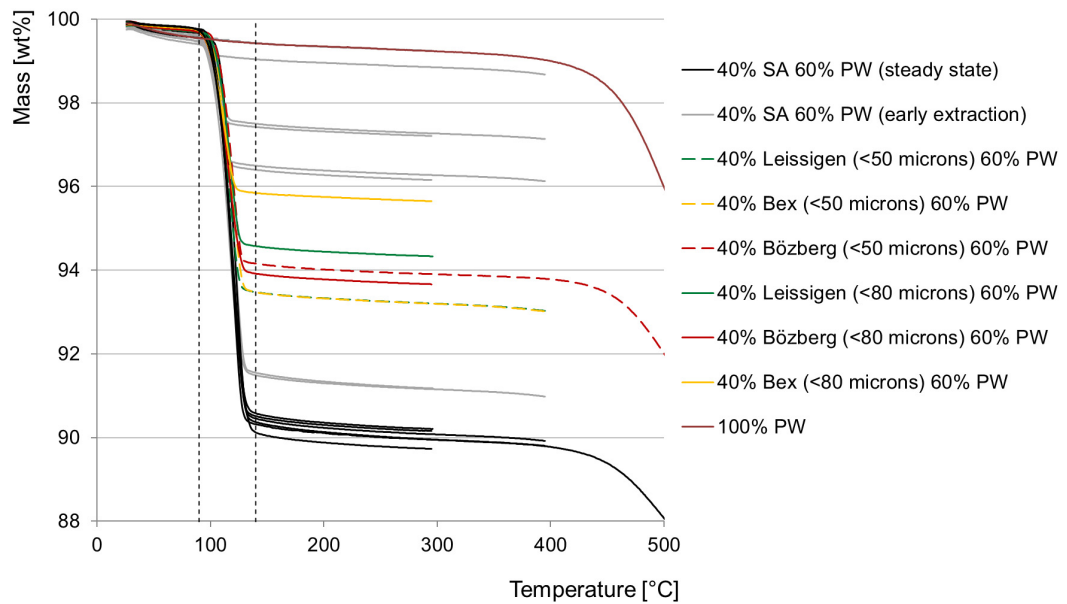


Figure A.2 TGA results of oedometer tests with $\sigma_{ax} = 3$ kPa.

In order to verify the reliability of the TGA results, XRD analysis was performed on three of the tested samples from Figure A.2 (*i.e.* 1_XRD, 2_XRD, 3a_XRD and 3d_XRD in Figure A.3) as well as on a reference specimen containing only the used kaolin (4_XRD). The results are shown in Figure A.3, where the mineralogical compositions of the specimens according to the XRD analysis are compared to the back-calculated results from TGA performed on specimens of the same oedometer-samples (e.g. comparison of “1_XRD” to “1_TGA”). Since the different minerals in the kaolin were not distinguished via TGA (as opposed to XRD, where each mineral is shown in a different colour in Figure A.3), the kaolin is shown as one component in the results from TGA (dark red pillars in Figure A.3).

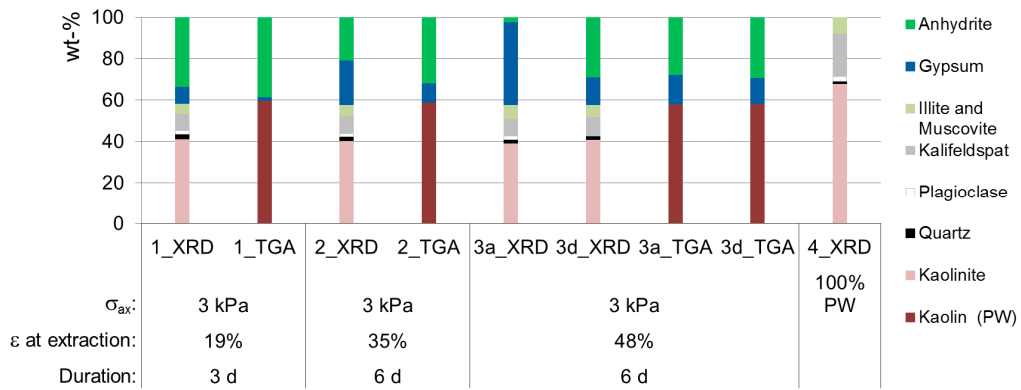


Figure A.3 Composition of three samples post oedometer test (comparison between results from X-ray diffraction analysis and thermogravimetric analysis) and mineralogical composition of the kaolin based on X-ray diffraction analysis (pillar on the far right).

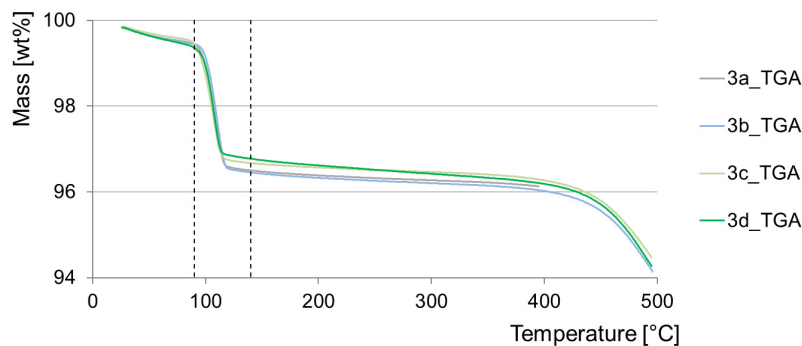


Figure A.4 TGA repetition of a sample.

One observation that can be made from Figure A.3 is that the analysis via TGA delivered generally higher anhydrite contents compared to the XRD analysis. This discrepancy was probably due to faulty specimen preparation (further gypsum may have precipitated during air-drying of specimens 1_XRD, 2_XRD and 3a_XRD at room temperature and humidity) because almost the same result was achieved as via TGA upon repetition of the X-ray analysis on one of the specimens (3d_XRD, which was dried in an oven at 40°C). Furthermore, repetition of TGA on that same sample (3a_TGA to 3d_TGA in Figure A.4) showed that the TGA results are very consistent concerning reproducibility. Therefore, the TGA results can be considered reliable and sufficiently accurate for the analysis of the oedometer tests.

The determination of the sample composition with XRD analysis was not always straight forward, which can be attributed to faulty specimen preparation, as was also the case in the example described above. Another example for this is the occurrence of a significant amount of bassanite (up to 30%) in the XRD results of some of the investigated samples described in Sections 12.5 and 13. Bassanite is a hemihydrate ($CaSO_4 \cdot 0.5H_2O$) and can be produced by heating the dihydrate (gypsum, $CaSO_4 \cdot 2H_2O$). It is strongly assumed to have been produced only after the tests during drying of the samples at too high temperatures (>60°C). The XRD results that showed bassanite were therefore corrected by assuming that all bassanite was gypsum prior to drying the samples. This was considered in the results given in Figure 13.11 and Figure 13.6 (samples marked with an asterisk).

This correction can be verified with the following example (sample X26 from Belchen SB6 1.40-1.56): The first results from the XRD analysis are shown in the pillar on the left in Figure A.5 (X26_1). Upon repetition of the X-ray analysis, where the specimen was air-dried at room temperature (as opposed to the oven at 65°) no bassanite was detected in the sample (right pillar in Figure A.5, X26_2). When using the results from X26_1 to calculate the amount of gypsum corresponding to the amount of bassanite, thus

correcting the results (with Eqs. A.6 and A.7), the pillar in the middle in Figure A.5 (X26_1*) is obtained. These corrected results correspond very well with the repeated XRD analysis (X26_2), thus the correction of the XRD results containing bassanite is acceptable. Therefore, the following equations were used for the corrections of the content of gypsum and other minerals of all results containing bassanite:

$$wt_G^* = \frac{wt_G + wt_B \frac{172 [g/mol]}{145 [g/mol]}}{1 + wt_B \left(\frac{172 [g/mol]}{145 [g/mol]} - 1 \right)} \quad (A.6)$$

$$wt_{Component}^* = \frac{wt_{Component}}{1 + wt_B \left(\frac{172 [g/mol]}{145 [g/mol]} - 1 \right)} \quad (A.7)$$

where wt_G , wt_B and $wt_{Component}$ are the contents (in wt%) of gypsum, bassanite and other components of the sample according to the XRD results while the asterisk indicates the corrected values.

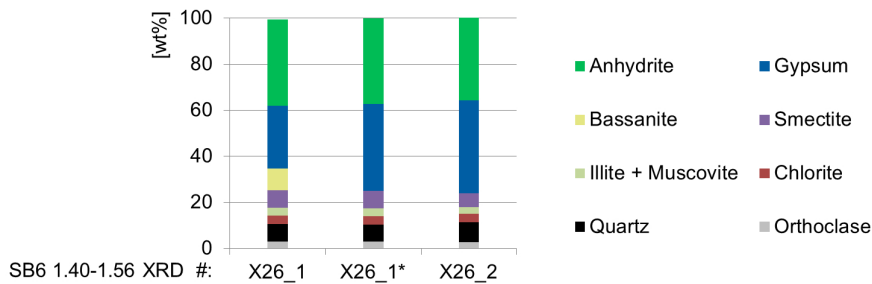


Figure A.5 XRD results of X26_1 (dried at 65° during sample preparation) and correction of bassanite (X26_1*) and XRD results of X26_2 (air-dried at room temperature during sample preparation).

The same procedure was used on some of the samples from Section 12.5, where different kinds of anhydrite were investigated in oedometer tests with $\sigma_{ax} = 3 \text{ kPa}$. One sample of each type of anhydrite was investigated with XRD in addition to the TGA analysis (of which the results are displayed in Figure A.2). The analysis of the sample composition is shown in Figure A.6, for the original and corrected XRD results as well as the results obtained via TGA. It can be seen that a very good correlation exists between the corrected XRD results and the TGA results, thus it is again confirmed that the bassanite was produced during the preparation of the XRD samples.

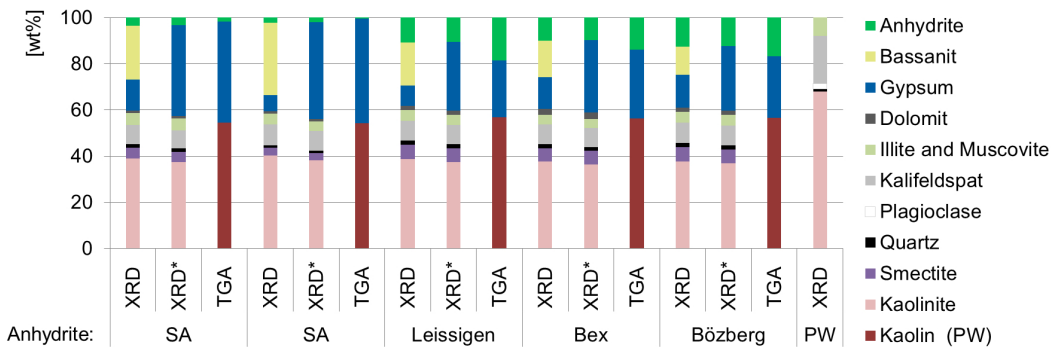


Figure A.6 Results from XRD and TGA analysis with correction of bassanite in the XRD results (marked *).

II Sample properties

The properties of all free swell and oedometer samples (from Sections 12.4, 12.5 and 12.6) are summarised in the following tables. The samples are sorted by their components, axially applied stress and duration of experiment. The samples marked with an asterisk * indicate reference samples that were not subjected to water.

Components	Sample properties prior to experiment							Experiment			Sample properties post experiment					
	Anhydrite [wt%]	Aggregate [wt%]	Height [mm]	Dry mass [g]	Porosity (back-calculated / grey = results from porosimetry) [-]	Bulk density (back-calculated / grey = results from porosimetry) [g/cm ³]	Mass of anhydrite per unit volume, $m_{a, \text{prior}}$ [g/cm ³]	Axial Stress [kPa]	Swelling strain ϵ_s [%]	Duration [d]	Height (via back-calculation) [mm]	Porosity (back-calculated / grey = results from porosimetry) [-]	Water content [%]	Bulk density (back-calculated / grey = results from porosimetry) [g/cm ³]	Mass of anhydrite per unit volume, $m_{a, \text{end}}$ (determined via TGA) [g/cm ³]	Mass of Gypsum per unit volume, $m_{g, \text{end}}$ (determined via TGA) [g/cm ³]
SA & Kaolin	60	40	22.3	169	0.31	1.9	1.16		75	97	39.0					
	60	40	22.4	169	0.31	1.9	1.16		85	20	41.4					
	40	60	23.5	175	0.31	1.9	0.76		77	28	41.6					
	40	60	22.9	167	0.32	1.9	0.74		80	20	41.1					
	20	80	22.6	163	0.31	1.8	0.37		66	124	37.6					
	20	80	16.6	160	0.34	2.5	0.35		73	124	28.7					
Kaolin	0	100	24.2	160	0.36	1.7	0.34		66	68	40.2					
	0	100	22.7	179	0.22	2.0	0.00		28	97	29.2					
	0	100	22.3	173	0.23	2.0	0.00		22	96	27.3					
	0	100	26.8	197	0.26	1.9	0.00	0	8	48	28.9					
	0	100	22.1	166	0.26	1.9	0.00		23	29	27.1					
	0	100	22.5	169	0.27	1.9	0.00		33	22	29.9					
SA * & Limestone	60	40	20.3	161	0.28	2.0	1.23		9	46	24.1	0.24	11	1.9	0.29	0.95
	40	60	21.0	169	0.26	2.1	0.83		14	46	24.6	0.25	12	1.9	0.18	0.68
	40	60	20.6	171	0.24	2.1	2.2									
	20	80	25.4	199	0.27	2.0	0.40									
Limestone	0	100	23.0	160	0.34	1.8	0.36		18	85	29.9					
	0	100	22.2	173	0.25	2.0	0.00		1	52	23.3					
	0	100	21.9	168	0.27	2.0	0.00		18	83	26.2					
	0	100	21.9	168	0.27	2.0	0.00		17	57	25.6					

Components	Sample properties prior to experiment							Experiment			Sample properties post experiment					
	Anhydrite [wt%]	Aggregate [wt%]	Height [mm]	Dry mass [g]	Porosity (back-calculated) [-]	Bulk density (back-calculated) [g/cm ³]	Mass of anhydrite per unit volume, $m_{a, prior}$ [g/cm ³]	Axial Stress [kPa]	Swelling strain ϵ_s [%]	Duration [h]	Height (via back-calculation) [mm]	Porosity (back-calculated) [-]	Water content [%]	Bulk density (back-calculated) [g/cm ³]	Mass of anhydrite per unit volume, $m_{a, end}$ (determined via TGA) [g/cm ³]	Mass of Gypsum per unit volume, $m_{g, end}$ (determined via TGA) [g/cm ³]
SA & Kaolin	40	60	20.8	97	0.31	1.9	0.75		12	0.2	23.2	0.38	20	1.7	0.66	0.01
	40	60	21.0	97	0.32	1.9	0.74		19	3	25.1	0.43	23	1.6	0.60	0.03
	40	60	20.6	98	0.30	1.9	0.76		39	6	28.6	0.47	32	1.4	0.44	0.15
	40	60	20.9	97	0.32	1.9	0.75		35	6	28.2	0.47	33	1.4	0.45	0.13
	40	60	20.7	96	0.31	1.9	0.75		48	6	30.7	0.51	35	1.3	0.36	0.18
	40	60	21.0	100	0.30	1.9	0.76		38	7	28.9	0.46	34	1.4	0.39	0.21
	40	60	20.6	98	0.30	1.9	0.76		57	9	32.3	0.47	35	1.3	0.08	0.51
	40	60	20.9	97	0.32	1.9	0.75		56	13	32.6	0.48	39	1.3	0.08	0.50
	40	60	20.8	98	0.30	1.9	0.76		61	19	33.5	0.48	36	1.3	0.04	0.55
	40	60	17.2	98	0.16	2.3	0.92		73	25	29.8	0.41	-	1.4	0.01	0.66
	40	60	20.9	98	0.31	1.9	0.76		51	29	31.5	0.44	32	1.4	0.02	0.61
	40	60	20.3	93	0.33	1.8	0.75		49	33	30.1	0.45	31	1.4	0.02	0.60
Leissigen & Kaolin	40	60	21.0	97	0.32	1.9	0.75	3	54	35	32.5	0.46	34	1.3	0.02	0.58
	40	60	20.5	98	0.30	1.9	0.77		55	44	31.7	0.45	33	1.4	0.02	0.60
	40	60	20.3	98	0.29	1.9	0.78		59	49	32.2	0.45	36	1.3	0.00	0.62
	40	60	18.6	94	0.25	2.0	0.84		69	27	31.5	0.49	37	1.3	0.18	0.38
	40	60	19.2	97	0.26	2.0	0.81		60	56	30.7	0.48	37	1.3	0.25	0.33
	40	60	19.2	96	0.26	2.0	0.81		62	25	31.1	0.49	-	1.3	0.22	0.35
	40	60	19.5	97	0.27	2.0	0.80		63	56	31.8	0.49	38	1.3	0.21	0.36
	40	60	17.9	95	0.22	2.1	0.87		68	34	30.1	0.47	35	1.4	0.19	0.40
	40	60	19.0	96	0.26	2.0	0.82		56	49	29.8	0.48	36	1.4	0.32	0.25
	0	100	22.0	97	0.32	1.8	0.00		16	13	25.5	0.41	-	-	0.00	0.00

Components	Sample properties prior to experiment										Experiment				Sample properties post experiment					
	Anhydrite [wt%]	Aggregate [wt%]	Height [mm]	Dry mass [g]	Porosity (back-calculated / grey = results from porosimetry) [-]	Bulk density (back-calculated / grey = results from porosimetry) [g/cm ³]	Mass of anhydrite per unit volume, $M_{a,prior}$ [g/cm ³]	Axial Stress [kPa]	Swelling strain ϵ [%]	Duration [d]	Height (via back-calculation) [mm]	Porosity (back-calculated / grey = results from porosimetry) [-]	Water content [%]	Bulk density (back-calculated / grey = results from porosimetry) [g/cm ³]	Mass of anhydrite per unit volume, $M_{a,post}$ [g/cm ³]	Mass of Gypsum per unit volume, $M_{g,post}$ [g/cm ³]				
SA & Kaolin	40	60	21.8	98	0.34	1.8	0.72	20	36	24	29.7	0.41	28	1.4	0.05	0.61				
	40	60	20.9	98	0.31	1.9	0.75	200	20	56	25.0	0.31	17	1.7	0.07	0.71				
	40	60	21.3	98	0.32	1.9	0.74	400	14	31	24.3	0.30	17	1.8	0.11	0.68				
	40	60	20.7	98	0.30	1.9	0.76	800	3	10	21.2	0.30	16	1.9	0.66	0.11				
	40	60	21.3	98	0.32	1.9	0.74	800	5	15	22.4	0.32	17	1.8	0.51	0.24				
	40	60	21.0	98	0.32	1.9	0.75	800	1	17	21.3	0.31	17	1.9	0.67	0.09				
	40	60	20.9	99	0.30	1.9	0.76	800	7	22	22.4	0.29	17	1.8	0.45	0.33				
	40	60	20.8	97	0.31	1.9	0.75	800	9	24	22.6	0.30	17	1.8	0.38	0.40				
	40	60	20.8	99	0.30	1.9	0.76	800	9	28	22.6	0.28	15	1.8	0.32	0.49				
	40	60	21.8	97	0.35	1.8	0.71	800	6	29	23.1	0.27	14	1.8	0.12	0.70				
Kaolin	40	60	21.3	97	0.33	1.8	0.74	800	7	31	22.8	0.28	15	1.8	0.26	0.54				
	40	60	20.3	93	0.32	1.9	0.74	800	8	38	21.8	0.25	14	1.9	0.10	0.74				
	40	60	20.7	97	0.31	1.9	0.75	800	10	47	22.8	0.26	13	1.9	0.10	0.73				
	40	60	20.6	98	0.30	1.9	0.77	800	10	63	22.7	0.24	13	1.9	0.12	0.73				
	40	60	20.7	98	0.30	1.9	0.77	1600	6	85	21.9	0.22	10	1.9	0.12	0.76				
	40	60	20.9	99	0.31	1.9	0.76	2200	3	92	21.6	0.21	11	1.9	0.17	0.71				
	40	60	20.8	99	0.30	1.9	0.77	3200	-2	79	20.4	0.27	13	2.0	0.19	0.06				
	*	40	60	20.9	97	0.32	1.9	0.75												
	Kaolin	0	100	21.8	97	0.31	1.8	0.00	400	2	18	22.1	0.33	21	1.8	0.00	0.00			
		0	100	21.2	99	0.28	1.9	0.00	3200	0	32	21.2	0.28	18	1.9	0.00	0.00			
40		60	20.2	79	0.43	1.6	0.63	3	34	27	27.0	0.49	37	1.3	0.05	0.54				
SA & Quartzpowder	40	60	20.2	79	0.43	1.6	0.63	10	22	49	24.6	0.44	30	1.4	0.05	0.59				
	40	60	20.4	79	0.43	1.6	0.63	20	14	40	23.2	0.40	27	1.5	0.06	0.61				
	40	60	20.0	79	0.42	1.6	0.64	40	13	36	22.5	0.38	25	1.5	0.06	0.64				
Quartzpowder	40	60	19.8	77	0.43	1.6	0.63	80	17	45	23.2	0.42	26	1.5	0.07	0.59				
	40	60	20.3	79	0.43	1.6	0.63	200	4	32	21.3	0.36	20	1.6	0.12	0.61				
	40	60	25.0	95	0.45	1.5	0.61	800	-4	82	24.0	0.31	17	1.7	0.08	0.70				

III Notation

A	mineral surface area in contact with water
A_i	total interfacial area of species i
a	radius of the expanding cavities
a_A	shape factor of parallelepipedic anhydrite particles
$a_{Ca^{2+}}$	activity of Ca^{2+}
a_i	radius of the i .th group of expanding cavities in the discretized numerical model
a_i	activity of constituent i
$a_{SO_4^{2-}}$	activity of SO_4^{2-}
a_W	water activity
$a_{W,eq,0}$	equilibrium water activity
b	radius of the spherical computational domain around the expanding cavity
b	shape factor of parallelepipedic particles
b_A	shape factor of parallelepipedic anhydrite particles
b_G	shape factor of parallelepipedic gypsum particles
b_p	half distance between the centres of pores
c	concentration
\tilde{c}	normalized concentration
$c_{Ca^{2+}}$	concentration of calcium ions
$c_{eq,A}$	anhydrite equilibrium concentration
$c_{eq,G}$	gypsum equilibrium concentration
$\tilde{c}_{eq,G}$	normalized gypsum equilibrium concentration
c_{max}	maximum concentration that develops during the hydration process
$c_{SO_4^{2-}}$	concentration of sulphate ions
c_0	concentration at standard state
c_0	initial concentration
\tilde{c}_0	normalized initial concentration
D	molecular diffusion coefficient
\mathbf{D}_{ijkl}	elasticity tensor
\mathbf{D}_{Triax}	elasticity tensor for radial symmetric boundary conditions
d	pore diameter
E	Young's modulus
F	specific surface area
F_A	anhydrite specific surface area
F_{A0}	initial anhydrite specific surface area
F_G	gypsum specific surface area
F_{G0}	initial gypsum specific surface area
F_S	inert solid specific surface area
F_p	pore area
\bar{F}_p	mean pore area

f	a function
F_{tot}	total area
G	Gibbs free energy
g	gravitational acceleration
H	depth of cover
h	hydraulic head
J	diffusive flux
$K_{eq,G}$	equilibrium solubility product of gypsum
K_G	ion activity product of gypsum
K_{ij}	hydraulic conductivity
k	reaction rate constant
k_A	reaction rate constant for anhydrite dissolution
k_B	Boltzmann constant
k_G	reaction rate constant for gypsum precipitation
M	mass
$M_{A,end}$	mass of anhydrite in sample post test
$M_{A,prior}$	initial mass of anhydrite in sample
$M_{G,end}$	mass of gypsum in sample post test
M_I	ion mass
$M_{tot,end}$	total dry mass of sample post test
m	mass per unit volume of mixture
m_A	anhydrite mass per unit volume of mixture
m_{A0}	initial anhydrite mass per unit volume of mixture
$m_{A,end}$	mass of anhydrite per unit volume of sample post test
m_G	gypsum mass per unit volume of mixture
m_{G0}	initial gypsum mass per unit volume of mixture
$m_{G,end}$	mass of gypsum per unit volume of sample post test
m_I	ion mass per unit volume of mixture
m_W	water mass per unit volume of mixture
m_{W0}	initial water mass per unit volume of mixture
N_p	number of pores
\bar{n}	pore percentage
$n_{Ca^{2+}}$	number of moles of Ca^{2+}
\bar{n}_{cr}	critical pore percentage
n_G	number of moles of gypsum
n_G	porosity of the gypsum layer
n_i	number of moles of constituent i
$n_{SO_4^{2-}}$	number of moles of SO_4^{2-}
n_W	number of moles of water
P_{atm}	atmospheric pressure
P_i	pressure of constituent i
p	pore water pressure
p_A	anhydrite pressure
p_c	crystallisation pressure

p_D	evaporation pressure in the vicinity of the pore
p_G	gypsum pressure
$p_{p,max}$	mechanically possible pressure exerted in the pore by crystal growth
p_{req}	required pressure
$p_{req,LB}$	lower bound of the required pressure
$p_{req,UB}$	upper bound of the required pressure
p_S	solid pressure
p_S	saturated evaporation pressure over dilute water
$p_{S,0}$	initial solid pressure
p_W	pore water pressure
Q	heat
q_x	seepage flow velocity
R	universal gas constant
R_0	Radius of diffusing particle
RH	relative humidity
r_{cr}	critical pore radius
r_G	radius of inert mineral particles
r_i	radius of particle i
r_{max}	largest pore radius
r_p	pore radius
\bar{s}_A	normalized characteristic length of anhydrite particles
S_A^0	molar entropy of anhydrite at standard state
S_{A0}	initial characteristic length of anhydrite particles
$S_{Ca^{2+}}^0$	molar entropy of Ca^{2+} at standard state
\bar{s}_G	normalized gypsum layer thickness
S_G^0	molar entropy of gypsum at standard state
S_i	molar entropy of constituent i
$S_{SO_4^{2-}}^0$	molar entropy of SO_4^{2-} at standard state
S_W^0	molar entropy of water at standard state
S_0	characteristic length (thickness and diameter for parallelepipedic and spherical particles, respectively)
s	distance of the mineral surface from its initial surface
s_A	thickness of dissolved anhydrite
\bar{s}_A	normalized thickness of dissolved anhydrite
s_G	gypsum layer thickness
s_{tot}	characteristic length (thickness and diameter for parallelepipedic and spherical particles, respectively)
T	temperature
T_{eq}	equilibrium temperature
T_{eq}^0	equilibrium temperature under atmospheric pressure
T_G	tortuosity of the gypsum layer
T_k^*	tortuosity of the porous medium
T_0	temperature at standard state

t	time
t_h	hydration time
U	internal energy
u	radial displacement or floor heave
u_α	radial displacement of the boundary of the expanding cavity
u_p^{cr}	critical radial displacement of the pore wall
V	volume
V_A^0	molar volume of anhydrite at standard state
$V_{Ca^{2+}}^0$	molar volume of Ca^{2+} at standard state
V_G^0	molar volume of gypsum at standard state
V_i	molar volume of constituent i
$V_{SO_4^{2-}}^0$	molar volume of SO_4^{2-} at standard state
V_{tot}	total volume of mixture
$V_{tot,0}$	initial total volume of mixture
$V_{tot,end}$	total volume of sample post test
V_W	molar volume of water
wt_B	content of bassanite in the sample in [wt%]
$wt_{Component}$	content of a certain mineral in the sample in [wt%]
wt_G	content of gypsum in the sample in [wt%]
z	geodetic head

Greek Symbols

γ_A	surface free energy of the anhydrite-water interface
$\gamma_{Ca^{2+}}$	activity coefficient of Ca^{2+}
γ_G	surface free energy of the gypsum-water interface
γ_i	activity coefficient of constituent i
γ_i	surface free energy of the interface of between constituent i and the water
γ_r	total unit weight of rock
$\gamma_{SO_4^{2-}}$	activity coefficient of SO_4^{2-}
γ_w	unit weight of water
γ_\pm	mean activity coefficient
δ	order of chemical reaction
δ	volume fraction order of the expanding cavity
δ_A	order of reaction for anhydrite dissolution
δ_G	order of reaction for gypsum precipitation
$\Delta_f G_{Ca^{2+}}^0$	standard Gibbs energy of formation of Ca^{2+}
$\Delta_f G_{SO_4^{2-}}^0$	standard Gibbs energy of formation of SO_4^{2-}
$\Delta_f G_A^0$	standard Gibbs energy of formation of anhydrite
$\Delta_f G_i^0$	standard Gibbs energy of formation of constituent i
$\Delta_f G_G^0$	standard Gibbs energy of formation of gypsum

$\Delta_f G_w^0$	standard Gibbs energy of formation of water
ΔM_A	mass of dissolved anhydrite
$\Delta_{r,A} G^0$	standard Gibbs energy of anhydrite dissolution
$\Delta_{r,A} V^0$	standard volume of anhydrite dissolution
$\Delta_{r,A} S^0$	standard entropy of anhydrite dissolution
$\Delta_{r,G} G^0$	standard Gibbs energy of gypsum dissolution
$\Delta_{r,G} V^0$	standard volume of gypsum dissolution
$\Delta_{r,G} S^0$	standard entropy of gypsum dissolution
$\Delta_{r,GA} G^0$	standard Gibbs energy of the transformation of anhydrite to gypsum
$\Delta_{r,GA} V^0$	standard volume of the transformation of anhydrite to gypsum
$\Delta_{r,GA} S^0$	standard entropy of anhydrite hydration
ΔV_A	volume of dissolved anhydrite
ΔV_G	volume of precipitated gypsum
Δwt	measured change in mass in [wt%]
ε_{AGT}	swelling strain due to increase in solid volume during AGT
ε_{ax}	axial swelling strain
$\varepsilon_{initial}$	immediate swelling strain due to reduction of negative pore water pressure
ε_{kl}	total strain tensor
ε_{kl}^{CH}	strain tensor due to chemical reactions
ε_{kl}^{EL}	strain tensor due to elasticity
ε_{kl}^{PL}	strain tensor due to plasticity
ε_{rad}	radial swelling strain
ε_{rest}	swelling strain due to processes other than AGT (e.g. clay swelling and change of sample structure)
ε_{swell}	swelling strain
η	dynamic viscosity of the solvent
Λ	dimensionless parameter
Λ^*	dimensionless parameter
$\bar{\Lambda}$	dimensionless parameter
μ_i	chemical potential of constituent i
μ_i^\ominus	chemical potential of constituent i under standard state conditions
ν	Poisson's ratio
ρ_A	anhydrite density
ρ_G	gypsum density
ρ_i	density of the constituent i
ρ_S	inert solid density
ρ_W	water density
σ_a	radial stress at the boundary of the expanding cavity
σ_{ax}	axial swelling stress
σ'_{ij}	effective stress tensor
σ'_{max}	highest possible effective stress
σ_p	radial stress at the outer boundary of the cracked zone

σ_p	radial stress at the pore wall
σ_r	radial stress
σ_{rad}	radial swelling stress
σ_s	macroscopic swelling pressure
σ_y	vertical stress
σ'_0	initial (<i>in situ</i>) effective stress
τ	dimensionless time
$\bar{\tau}$	dimensionless time
ϕ	porosity
ϕ_A	anhydrite volume fraction
ϕ_{A0}	initial anhydrite volume fraction
$\phi_{A0,crit}$	critical initial anhydrite volume fraction
ϕ_{cr}	volume fraction of pores with critical radius
ϕ_G	gypsum volume fraction
$\phi_{G,A}$	volume fraction of gypsum grown on anhydrite particles
$\phi_{G,G}$	volume fraction of gypsum grown on gypsum particles
$\phi_{G,S}$	volume fraction of gypsum grown on inert solid particles
ϕ_{G0}	initial gypsum volume fraction
ϕ_P	volume fraction of particles consisting of inert solid and gypsum
ϕ_S	inert solid volume fraction
ϕ_i	volume fraction of the constituent <i>i</i>
ϕ_W	water volume fraction
ϕ_{W0}	initial water volume fraction
χ	unknown material specific parameter
χ_{kl}	unknown material specific tensor
χ_{ax}	unknown material specific parameter
χ_{rad}	unknown material specific parameter
Ψ	potential
Ψ_{eq}	potential at anhydrite-gypsum equilibrium
Ψ_0	potential of pore water <i>in situ</i>

Literaturverzeichnis

- [1] Anagnostou, G. 2007. *Design Uncertainties in Tunnelling through Anhydritic Swelling Rocks*. Felsbau. p. 48-54.
- [2] Anagnostou, G., Pimentel, E., Serafeimidis, K. 2010. *Swelling of sulphatic claystones – some fundamental questions and their practical relevance / Quellen von sulfatführenden Tonsteinen – Themen der Grundlagenforschung und ihre praktische Bedeutung*. Geomechanics and Tunnelling, Vol. 3(5): p. 567-572.
- [3] Alonso, E. E., Berdugo, I. R., Ramon, A. 2013. *Extreme expansive phenomena in anhydritic-gypsiferous claystone: the case of Lilla tunnel*. Geotechnique, Vol. 63(7): p. 584-612.
- [4] Serafeimidis, K., Anagnostou, G. 2015. *The Solubilities and Thermodynamic Equilibrium of Anhydrite and Gypsum*. Rock Mechanics and Rock Engineering, Vol. 48(1): p. 15-31.
- [5] Anagnostou, G., Serafeimidis, K., Vrakas, A. 2015. *On the Occurrence of Anhydrite in the Sulphatic Claystones of the Gypsum Keuper*. Rock Mechanics and Rock Engineering, Vol. 48(1): p. 1-13.
- [6] Serafeimidis, K., Anagnostou, G. 2013. *On the Time-Development of Sulphate Hydration in Anhydritic Swelling Rocks*. Rock Mechanics and Rock Engineering, Vol. 46(3): p. 619-634.
- [7] Serafeimidis K., G., A. 2012. *On the kinetics of the chemical reactions underlying the swelling of anhydritic rocks*. Eurock. Stockholm.
- [8] Serafeimidis, K. 2014. *On the dissolution, precipitation and transport processes in sulphatic swelling rocks*. Zürich: vdf Hochschulverlag AG an der ETH Zürich.
- [9] Serafeimidis, K., Anagnostou, G. 2014. *On the crystallisation pressure of gypsum*. Environmental Earth Sciences, Vol. 72(12): p. 4985-4994.
- [10] Serafeimidis, K., Anagnostou, G., Vrakas, A. 2014. *Scale effects in relation to swelling pressure in anhydritic claystones*. Int Symp on Geomech from Micro to Macro, IS-Cambridge.
- [11] Huber, T., Pimentel, E., Anagnostou, G. 2015. *Experimental Investigations for the Modelling of Chemo-mechanical Processes in Anhydritic Rock*. Energy Procedia, Vol. 76(87-95).
- [12] Pimentel, E. 2015. *Existing Methods for Swelling Tests – A Critical Review*. European Geosciences Union General Assembly 2015, EGU, Wien, Österreich, Vol. 76: p. 96-105.
- [13] Madsen, F. T., Nuesch, R. 1991. *The Swelling Behaviour of Clay-sulfate Rocks*. International Society for Rock Mechanics.
- [14] Madsen, F. T., Vonmoos, M. *Das Quellen der Tone*: p. 39-50.
- [15] Huggenberger, P. 2008. *Influence of groundwater flow on swelling in the Gipskeuper formation of the Belchentunnel* Research Project ASTRA / FGU 2008-004.
- [16] Huggenberger, P. 2008. *Influence of groundwater flow on swelling in the Gipskeuper formation of the Chienbergtunnel*. Research Project ASTRA / FGU 2008-005.
- [17] Butscher, C., Huggenberger, P., Zechner, E., Einstein, H. H. 2011. *Relation between hydrogeological setting and swelling potential of clay-sulphate*. Engineering Geology, Vol. 122: p. 204–214.
- [18] Butscher, C., Huggenberger, P., Zechner, E. 2011. *Impact of tunneling on regional groundwater flow and implications for swelling of clay-sulfate rocks*. Engineering Geology, Vol. 117: p. 198–206.
- [19] Butscher, C., Einstein, H. H., Huggenberger, P. 2015. *Darcy flux as hydrological indicator for the swelling potential of clay-sulfate rocks in tunneling*. Engineering Geology, Vol. 197: p. 11-19.
- [20] Madsen, F. T., Ed. 1976. *Quelldruckmessung an Tongesteinen und Berechnung des Quelldrucks nach der DLVO - Theorie*. Mitteilungen des Institutes für Grundbau und Bodenmechanik ETH Zürich.

- [21] Ko, S. C., Nüesch, R., Madsen, F. T. 1997. *Tonminerale und Sulfatgesteine als Ursache für druckhaftes Verhalten von Gesteinen. Forschungsprojekt Quellverhalten der Juragesteine*. Interim Report Laboratory for Clay Mineralogy Institute of Geotechnical Engineering ETH-Zurich.
- [22] Grob, H. Year. *Schwelldruck im Belchentunnel - Swelling Pressure Illustrated with the Example of the Belchen Tunnel*. In *Internationales Symposium für Untertagebau*. 1972. Luzern.
- [23] Einstein, H. H., Bischoff, N., Hofmann, E. 1972. *Verhalten von Stollensohlen in quellendem Mergel*. Internationales Symposium für Untertagebau. Luzern. p. 296-319.
- [24] Gysel, M. 1977. *A Contribution to the Design of a Tunnel Lining in Swelling Rock*. Rock Mechanics, Vol. 10: p. 55-71.
- [25] Wittke, W., Rissler, P. 1976. *Bemessung der Auskleidung von Hohlräumen in quellendem Gebirge nach der Finite-Element-Methode*. Veröffentlichungen des Institutes für Grundbau, Bodenmechanik, Felsmechanik und Verkehrswasserbau der RWTH Aachen, Vol. 2: p. 7-46.
- [26] Fröhlich, B. 1986. *Anisotropes Quellverhalten diagenetisch verfestigter Tonsteine*. Veröffentlichungen des Institutes für Bodenmechanik und Felsmechanik der Universität Fridericiana in Karlsruhe Vol. Heft 99.
- [27] Bellwald, P., Einstein, H. H. 1987. *Elasto-plastic constitutive model*. Proc. 6th Int. Conf. of the ISRM, Aachen: p. 1489-1492.
- [28] Aristorenas, G. V. 1992. *Time-dependent behaviour of tunnels excavated in shale*. Doctoral thesis, Massachusetts Institute of Technology.
- [29] Barla, M. 1999. *Tunnels in swelling ground*. Doctoral thesis, Politecnico di Torino.
- [30] Barla, M., Ferrero, S., Barla, G. 2003. *A new approach for predicting the swelling behaviour of expansive clays in tunnelling*. IC on New Developments in Soil Mechanics and Geotechnical Engineering ZM2003, Lefkosa, Turkish Republic of Northern Cyprus.
- [31] Barla, M. 2008. *Numerical simulation of the swelling behaviour around tunnels based on special triaxial tests*. Tunnelling and Underground Space Technology, Vol. 23: p. 508-521.
- [32] Anagnostou, G. 1991. *Untersuchungen zur Statik des Tunnelbaus in quellfähigem Gebirge*(Diss. Techn. Wiss. ETH Zürich 9553).
- [33] Kiehl, J. R. 1990. *Ein dreidimensionales Quellgesetz und seine Anwendung auf den Felshohlraum*. Proc. 9. Nat. Felsmechanik Symposium Aachen 1990: p. 185-207.
- [34] Wittke-Gattermann, P. 1998. *Verfahren zur Berechnung von Tunnels in quellfähigem Gebirge und Kalibrierung an einem Versuchsbauwerk*. WBI-Print, Vol. 1(VGE Verlag GmbH).
- [35] Wittke, M. 2003. *Begrenzung der Quelldrücke durch Selbstabdichtung beim Tunnelbau in anhydritführendem Gebirge*. WBI-PRINT, Vol. 13(Verlag Glückauf GmbH).
- [36] Alonso, E. E., Olivella, S. 2008. *Modelling Tunnel Performance in Expansive Gypsum Claystone*. 12th International Conference of IACMAG. Goa, India. p. 891-910.
- [37] Oldecop, L., Alonso, E. 2012. *Modelling the degradation and swelling of clayey rocks bearing calcium-sulphate*. International Journal of Rock Mechanics and Mining Sciences, Vol. 54: p. 90-102.
- [38] Ramon, A. 2014. *Expansion mechanisms in sulphated rocks and soils*. Universitat Politècnica de Catalunya. p. 260.
- [39] Alonso, E. E., Ramon, A. 2013. *Heave of a railway bridge induced by gypsum crystal growth: field observations*. Geotechnique, Vol. 63(9): p. 707-719.
- [40] Ramon, A., Alonso, E. E. 2013. *Heave of a railway bridge: modelling gypsum crystal growth*. Geotechnique, Vol. 63(9): p. 720-732.
- [41] Alonso, E. E., Ramon, A. 2013. *Massive sulfate attack to cement-treated railway embankments*. Geotechnique, Vol. 63(10): p. 857-870.
- [42] Huder, J., Amberg, G. 1970. *Quellung in Mergel, Opalinuston und Anhydrit*. Schweizerische Bauzeitung, Vol. 88(43): p. 975-980.
- [43] ISRM 1989. *Suggested methods for laboratory testing of argillaceous swelling rocks*. Int. J. Rock Mech. Sci. and Geomech, Vol. 26: p. 415-426.

- [44] ISRM 1999. *Suggested methods for laboratory testing of swelling rocks*. Int. J. Rock Mech. Sci. and Geomech, Vol. 36: p. 291-306.
- [45] Pimentel, E. 1996. *Quellverhalten von diagenetisch verfestigtem Tonstein*. Veröffentlichungen des Institutes für Bodenmechanik und Felsmechanik der Universität Fridericiana in Karlsruhe, Heft 139.
- [46] Pimentel, E. Year. *Quellverhalten von Sedimentgesteinen - Neue Versuchstechniken*. In 3rd Colloquium "Rock Mechanics - Theory and Practice". 2006. Wien.
- [47] Van't Hoff, J. H., Armstrong, E. F., Hinrichsen, W., Wigert, F., Just, G. 1903. *Gips und Anhydrit*. Zeitschrift f. physik. Chemie, Vol. 45: p. 257-306.
- [48] Freyer, D., Voigt, W. 2003. *Crystallization and Phase Stability of CaSo₄ and CaSo₄ - Based Salts*. Monatshefte für Chemie, Vol. 134: p. 693-719.
- [49] Toriumi, T., Hara, R. 1938. *On the transition point of calcium sulphate in water and concentrated seawater*. Techn. Rep. Tohoku Imp. Univ, Vol. 12: p. 572-590.
- [50] Steiger, M. 2005. *Crystal growth in porous materials - II: Influence of crystal size on the crystallization pressure*. Journal of Crystal Growth: p. 470-481.
- [51] Scherer, G. W. 1999. *Crystallization in pores*. Cement and Concrete Research, Vol. 29(8): p. 1347-1358.
- [52] Flatt, R. J., Scherer, G. W. 2008. *Thermodynamics of crystallization stresses in DEF*. Cement and Concrete Research, Vol. 38(3): p. 325-336.
- [53] Freundlich, H. 1922. *Colloid & Capillary Chemistry*. Translated by H.S. Hatfield. Dutton and Company Publishers: New York: p. 883.
- [54] Raju, K., Atkinson, G. 1990. *Thermodynamics of 'scale' mineral solubilities. 3. Calcium sulfate in aqueous NaCl*. J. of Chem. and Engin. Data, Vol. 35: p. 361-367.
- [55] Paterson, S. M. 1973. *Non-hydrostatic thermodynamics and its geologic applications*. Reviews of Geophysics and Space Physics, Vol. 11(No. 2): p. 355-389.
- [56] Anderson, G. M. 1996. *Thermodynamics of Natural systems*. University of Toronto, John Wiley and Sons, Inc.
- [57] Dahlen, F. A. 1992. *Metamorphism of nonhydrostatically stressed rocks*. American Journal of Science, Vol. 292(3): p. 184-198.
- [58] Dewers, T., Ortoleva, J. P. 1989. *Mechano-chemical coupling in stressed rocks*. Geochimica et Cosmochimica Acta, Vol. 53: p. 1243-1258.
- [59] Millero, F. J. 1972. *The partial molar volume of electrolytes in aqueous solutions*. Water and Aqueous Solution, Wiley.
- [60] Scanlon, R. B., Andraski, J. B., Bilskie, J. 2002. *Miscellaneous methods for measuring matric or water potential*. In: Methods of Soil Analysis, Part 4, Physical Methods (eds Dane JH, Topp GC), Soil Science Society of America, Madison, WI: p. 643-670.
- [61] Yong, N. R., Warkentin, B. P. 1975. *Soil Properties and Behaviour*. Elsevier, Amsterdam.
- [62] Passioura, B. J. 1980. *The meaning of matric potential*. Journal of Experimental Botany, Vol. 31(No 123): p. 1161-1169.
- [63] Yong, N. R. 1999. *Soil suction and soil-water potentials in swelling clays in engineered clay barriers*. Engineering Geology, Vol. 54: p. 3-13.
- [64] Dormieux, L., Lemarchand, E., Coussy, O. 2003. *Macroscopic and micromechanical approaches to the modelling of osmotic swelling in clays*. Transport in Porous Media, Vol. 50: p. 75-91.
- [65] Atkins, P., De Paula, J. 2006. *Physical Chemistry, 8th Edition*. Oxford University Press.
- [66] Tuller, M., Or, D., Dudley, M. L. 1999. *Adsorption and capillary condensation in porous media: Liquid retention and interfacial configuration in angular pores*. Water Resources Research, Vol. 35: p. 1949-1964.
- [67] Philip, R. J. 1977. *Unitary approach to capillary condensation and adsorption*. The Journal of Chemical Physics, Vol. 66(No. 11): p. 5069-5075.
- [68] Chenevert, M. E. 1969. *Adsorptive pore pressure of argillaceous rocks*. Proc., II Symposium on Rock Mechanics, University of California, Berkeley: p. 599-627.
- [69] Derjaguin, B. V., Churaev, V. N., Muller, M. V. 1987. *Surface Forces*. Consult. Bur., New York.

- [70] Mitchell, J. K., Soga, K. 2005. *Fundamentals of Soil Behavior, 3rd edition*. John Wiley and Sons Inc. Publishers.
- [71] Low, P. F., Margheim, F. J. 1979. *The swelling of clay. I. Basic concepts and empirical equations*. Soil Sci. Soc. Am. J., Vol. 43: p. 473-481.
- [72] Steiger, M. 2005. *Crystal growth in porous materials - I: The crystallization pressure of large crystals*. Journal of Crystal Growth: p. 455-469.
- [73] Nielsen, E. A., Söhnle, O. 1971. *Interfacial tensions electrolyte crystal-aqueous solution, from nucleation data*. Journal of Crystal Growth, Vol. 11: p. 233-242.
- [74] Marsal, D. 1952. *Der Einfluss des Druckes auf das System CaSO₄-H₂O*. Heidelberger Beiträge zur Mineralogie and Petrographie, Vol. 3: p. 289-296.
- [75] MacDonald, G. J. F. 1953. *Anhydrite-gypsum equilibrium relations*. Am. J. of Science, Vol. 251: p. 884-898.
- [76] Kontrec, J., Kralj, D., Brečević, L. 2002. *Transformation of anhydrous calcium sulphate into calcium sulphate dihydrate in aqueous solutions*. Journal of Crystal Growth, Vol. 240(1-2): p. 203-211.
- [77] Marshall, W. L., Slusher, R. 1966. *Thermodynamics of calcium sulphate dihydrate in aqueous sodium chloride solutions, 0-110°C*. J. Phys. Chem., Vol. 70: p. 4015-4027.
- [78] Kelley, K. K., Southard, J. C., Anderson, C. T. 1941. *Thermodynamic properties of gypsum and its dehydration products*. U.S. Bur. Mines Tech. Paper, Vol. 625.
- [79] Posnjak, E. 1938. *The system CaSO₄*. Am. J. of Sc. 5th edition, Vol. 35-A: p. 247-272.
- [80] Zen, E.-A. 1965. *Solubility measurements in the system CaSO₄-NaCl-H₂O at 35°, 50° and 70°C and one atmosphere pressure*. Journal of Petrology, Vol. 6 Part 1: p. 124-164.
- [81] Kelley, K. K. 1960. *Contributions to the data on theoretical metallurgy, XIII. High-temperature heat-content, heat-capacity, and entropy data for the elements and inorganic compounds*. U.S. Bur. Mines Bull., Vol. 584.
- [82] Mullin, J. W. 2001. *Crystallization, 4th edition*. Butterworth-Heinemann.
- [83] Barton, A. F. M., Wilde, N. M. 1971. *Dissolution of polycrystalline samples of gypsum and orthorhombic forms of calcium sulphate by a rotating disc method*. Trans. Faraday Soc., Vol. 67: p. 3590-3597.
- [84] James, A. N., Lupton, A. R. R. 1978. *Gypsum and anhydrite in foundations of hydraulic structures*. Géotechnique, Vol. 28(No. 3): p. 249-272.
- [85] Liu, S. T., Nancollas, H. G. 1970. *The kinetics of crystal growth of calcium sulfate dihydrate*. Journal of Crystal Growth, Vol. 6: p. 281-289.
- [86] Smith, B. R., Sweett, F. 1971. *Crystallization of calcium sulfate dihydrate*. Journal of Colloid and Interface Science, Vol. 37(3): p. 612-618.
- [87] Appelo, C. A. J., Postma, D. 2005. *Geochemistry, groundwater and pollution, 2nd edn*. Rotterdam: A. A. Balkema.
- [88] Langbein, R., Peter, H., Schwahn, H. 1982. *Karbonat und Sulfatgesteine*. Deutscher Verlag für Grundstoffindustrie, Leipzig.
- [89] Murray, R. C. 1964. *Origin and diagenesis of gypsum and anhydrite*. Journal of Sedimentary Petrology, Vol. 34(No. 3): p. 512-523.
- [90] Azam, S., Abduljauwad, S. N., Al-Shayea, N. A., Al-Amoudi, O. S. B. 1998. *Expansive characteristics of gypsiferous/anhydritic soil formations*. Engineering Geology, Vol. 51: p. 89-107.
- [91] Azam, S. 2007. *Study on the swelling behaviour of blended clay-sand soils*. Geotechnical and Geological Engineering, Vol. 25: p. 369-381.
- [92] Pimentel, E., Anagnostou, G. 2010. *Langzeitquellversuche an anhydritführenden Gesteinen* Forschungsauftrag FGU 2006/001 auf Antrag des Bundesamtes für Strassen (ASTRA).
- [93] Böhringer, J., Jenni, J. P., Hürlimann, P., Resele, G., Grauer, R., Norbert, J. 1990. *Anhydritvorkommen als Wirtgestein für die Lagerung schwach- und mittelaktiver Abfälle dargestellt am Beispiel des Bois de la Glaive*. NAGRA, Technischer Bericht 88-15.
- [94] Müller, W. H., Briegel, U. 1977. *Experimentelle Untersuchungen an Anhydrit*. Bericht Nr. 2. Geol. Institut der ETH Zürich, Arbeitsgruppe Anhydrite der Nagra.
- [95] Amstad, C., Kovári, K. 2001. *Untertagbau in quellfähigem Fels ETHZ* Forschungsauftrag 52/94 auf Antrag des Bundesamtes für Strassen (ASTRA). IGT, ETH Zürich.

- [96] Wiesmann, E. 1914. *Über die Stabilität von Tunnelmauerwerk unter Berücksichtigung der Erfahrungen beim Bau des Hauenstein-Basistunnel.* Schweizerische Bauzeitung, Vol. 64(No. 3): p. 27-32.
- [97] Andrae, C. 1956. *Gebirgsdruck und Tunnelbau.* Schweizerische Bauzeitung, Vol. 74: p. 107-110.
- [98] Gassmann, J., Gysel, M., Schneider, J. F. 1979. *Anhydrit als Wirtgestein für die Endlagerung radioaktiver Abfälle in der Schweiz.* Technical Report Nagra, No. 12, Baden
- [99] Henke, K. F., Kaiser, W. 1975. *Zusammenfassung und Deutung der Ergebnisse in Bezug auf Sohlhebungen beim Tunnelbau im Gipskeuper. Durchführung eines felsmechanischen Grossversuches in der Nordröhre des Wagenburgtunnels in Stuttgart.* Schriftenhefte Strassenbau und Strassenverkehrstechnik, Vol. 184: p. 185-195.
- [100] Henke, K. F., Kaiser, W., Nagel, D. 1975. *Geomechanische Untersuchungen im Gipskeuper.* Durchführung eines felsmechanischen Grossversuches in der Nordröhre des Wagenburgtunnels in Stuttgart. Bundesminister für Verkehr, Abt. Strassenbau, Bonn: Bonn. p. 149-184.
- [101] Sahores, J. 1962. *Contribution à l'étude des phénomènes mécaniques accompagnant l'hydratation de l'anhydrite.* Université de Toulouse.
- [102] Madsen, F. T., Nüesch, R. 1990. *Langzeitquellenverhalten von Tongesteinen und tonigen Sulfatgesteinen.* Nagra.
- [103] Sievert, T., Wolter, A., Singh, N. B. 2005. *Hydration of anhydrit of gypsum (CaSo4.II) in a ball mill.* Cement and Concrete research: p. 623-630.
- [104] Bezjak, A., Jelenic, I. 1980. *On the determination of rate constants for hydration processes in cement pastes.* Cement and Concrete Research, Vol. 10: p. 553-563.
- [105] Pignat, C., Navi, P., Scrivener, K. 2005. *Simulation of cement paste microstructure hydration pore space characterization and permeability determination.* Materials and Structures, Vol. 38: p. 459-466.
- [106] Bishnoi, S., Scrivener, L. K. 2009. *Studying nucleation and growth kinetics of alite hydration using μ c.* Cement and Concrete Research, Vol. 2009: p. 849-860.
- [107] Fitts, C. R. 2002. *Groundwater science.* Amsterdam; Boston: Academic Press.
- [108] Bishnoi, S. 2008. *Vector modelling of hydrating cement microstructure and kinetics.* Dissertation No 4093, École Polytechnique Fédérale de Lausanne.
- [109] Serafeimidis, K., Anagnostou, G. 2012. *Simultaneous anhydrite dissolution and gypsum precipitation in a closed swelling rock system.* 46th US Rock Mechanics/ Geomechanics Symposium. Chicago, IL, USA.
- [110] Böhm, M., Devlinny, J., Jahani, F., Rosen, G. 1998. *On a moving-boundary system modeling corrosion in sewer pipes.* Applied Mathematics and Computation, Vol. 92: p. 247-269.
- [111] Li, Y. H., Gregory, S. 1974. *Diffusion of ions in sea water and in deep-sea sediments.* Geochimica et Cosmochimica Acta, Vol. 38: p. 703-714.
- [112] Neveux, L., Grgic, D., Carpentier, C., Pironon, J., Girard, J. P. 2014. *Influence of hydrocarbon injection on the compaction by pressure resolution of a carbonate rock: An experimental study under triaxial stresses.* Marine and Petroleum Geology, Vol. 55: p. 282-294.
- [113] Anagnostou, G. 1995. *Seepage flow around tunnels in swelling rock.* International Journal for Numerical and Analytical Methods in Geomechanics, Vol. 10: p. 705-724.
- [114] Anagnostou, G. 1995. *The influence of tunnel excavation on the hydraulic head.* International Journal for Numerical and Analytical Methods in Geomechanics, Vol. 19: p. 725-746.
- [115] Schaechterle, K. 1929. *Die Dichtung und Entwässerung des Schanztunnels bei Fichtenberg.* Die Bautechnik, Vol. Heft 40.
- [116] Erichsen, C., Kurz, G. 1996. *Rehabilitation of an old railway tunnel in swelling gypsum keuper.* Geotechnik, Vol. 19: p. 178-187.
- [117] Marsily, G. 1986. *Quantitative Hydrogeology.* Academic Press, Inc.
- [118] Bear, J. 1972. *Dynamics of Fluids in porous Media.* American Elsevier, New York.
- [119] Wolfram 2003. *The Mathematica Book, Fifth Edition.* Wolfram Media.

- [120] Lippmann, F. 1976. *Corrensite, a swelling clay mineral, and its influence on floor heave in tunnels in the Keuper formation*. Bulletin of the International Association of Engineering Geology, Vol. 13: p. 65-70.
- [121] Jordan, P. 1994. *Evaporite als Abscherhorizonte – Eine gefügekundlich-strukturgeologische Untersuchung am Beispiel der Nordschweizer Trias*. Beiträge zur geologischen Karte der Schweiz, Vol. 164.
- [122] Krause, H., Wurm, F. 1975. *Geologische Grundlagen und Untersuchungen zum Problem der Sohlhebungen in Keupertunneln Baden-Württembergs*. Strassenbau und Strassenverkehrstechnik, Vol. Heft 184: p. 7-41.
- [123] Krause, H. 1976. *Sulphate rocks in Baden-Württemberg and their importance in relation to civil engineering*. Bulletin of the International Association of Engineering Geology, Vol. 13: p. 45-49.
- [124] Kuhnenn, K., Lorscheider, W. 1979. *Sondierstollen mit Probestrecken für den Engelberg-Basistunnel der Autobahn Heilbronn-Stuttgart*. Berechnung, Erkundung und Entwurf von Tunneln und Felsbauwerken / Computation, Exploration and Design of Tunnels and Rock Structures. Springer Vienna. p. 147-171.
- [125] Prommersberger, G., Kuhnenn, K. 1989. *The Freudenstein Tunnel – Tunnel construction in swelling rocks*. Rapid Excavation and Tunneling Conference Los Angeles, California, June 11-14. p. 678-700.
- [126] Paul, A., Wichter, L. 1996. *Das Langzeitverhalten von Tunnelbauwerken im quellenden Gebirge - Neuere Messergebnisse vom Stuttgarter Wagenburgtunnel*. Taschenbuch für Tunnelbau p. 135-163.
- [127] Meyer, M. 2001. *Die Geologie des Adlertunnels*. Bull. angew. Geol., Vol. 6(Nr. 2): p. 199-208.
- [128] Kurz, G., Spang, J. 1984. *Instandsetzung und Erneuerung der Blähstrecke des Kappellesbergtunnels*. Bautechnik, Vol. Heft 11: p. 365-376.
- [129] Einstein, H. H. 2000. *Tunnels in Opalinus Clayshale - A review of Case Histories and New Developments*. Tunnel and Underground Space Technology, Vol. 15(1): p. 13-29.
- [130] Beck, D., Thullner, T. 1998. *Der Engelbergbasistunnel und der Umbau des Autobahndreiecks Leonberg*. Tiefbau, Vol. 10: p. 692-699.
- [131] Kirschke, D., Kuhnenn, K., Prommersberger, G. 1991. *Der Freudensteintunnel: Eine Herausforderung für den planenden Ingenieur*. Ingenieurbauwerke, DB Neubaustrecke Mannheim-Stuttgart, Vol. No. 8: p. 5-39.
- [132] Hauber, L. 1991. *Geologie des Bözbergtunnels*. N3: Bözberg- und Habsburgtunnel, Vol. Mitteilungen der Schweizerischen Gesellschaft für Boden- und Felsmechanik(Heft 123).
- [133] Schaeren, G., J., N. 1989. *Tunnel du Mont Terri et du Mont Russelin – La traversée des 'roches à risques': marnes et marnes à anhydrite*. Juradurchquerungen – aktuelle Tunnelprojekte im Jura Mitteilungen der Schweizerischen Gesellschaft für Boden- und Felsmechanik, (Heft 119).
- [134] Berdugo, I. R. 2007. *Tunnelling in sulphatic-bearing rocks – expansive phenomena*. Universitat Politècnica de Catalunya.
- [135] Medici, F., Rybach, L. 1995. *Geothermal map of Switzerland 1995 (heat flow density)*. Matériaux pour la Géologie de la Suisse, Vol. Geophysique Nr. 30.
- [136] Rolnick, L. S. 1954. *The stability of gypsum and anhydrite in the geologic environment*. MIT.
- [137] Lippmann, F., Schüle, F. 1975. *Mineralogische Untersuchungen an Keupergesteinen unter besonderer Berücksichtigung der Tonminerale*. Forschungsbericht Wagenburgtunnel: p. 119-148.
- [138] Fecker, E. Year. *Influence of swelling rock on tunnelling*. In *Bulletin of the International Association of Engineering Geology*. 1981.
- [139] Wichter, L. 1989. *Quellen anhydrithaltiger Tongesteine*. Bautechnik, Vol. 66(Heft 1): p. 1-6
- [140] Hauber, L., Jordan, P., Madsen, F., Nüesch, R., Vögtli, B. 2005. *Tonminerale und Sulfate als Ursache für druckhaftes Verhalten von Gesteinen – Ursachen und Wirkungen des Quellvorganges*. Forschungsauftrag ASTRA 1996/039 auf Antrag des Bundesamtes für Strassen (ASTRA).
- [141] Pimentel, E. 2007. *Quellverhalten von Gesteinen - Erkenntnisse aus Laboruntersuchungen*. Quellprobleme in der Geotechnik. Fribourg. p. 11-20.

- [142] Rauh, F. 2009. *Untersuchungen zum Quellverhalten von Anhydrit und Tongesteinen im Tunnelbau*. Münchner Geowissenschaftliche Abhandlungen, Vol. B(11): p. 110.
- [143] Röthlisberger, A. 2012. *MIP tests on gypsum Keuper samples from the Chienberg and Belchen Tunnel*. Internal laboratory test report, Institute for Geotechnical Engineering, ETH Zurich.
- [144] Leemann, A., Wyrzykowski, M. 2012. *MIP tests on Gypsum Keuper samples from the Chienberg and Belchen Tunnel*. Internal laboratory test report, EMPA
- [145] Chiaverio, F., Thut, A. 2010. *Chienberg Tunnel: Rehabilitation using yielding elements of the section in Keuper sediments affected by heave / . Chienbergtunnel: Instandsetzung der Hebungsstrecke im Gipskeuper mit Knautschkörpern*. Geomechanics and Tunnelling, Vol. 3(5): p. 573-582.
- [146] Huggenberger, P. 2014. *Personal communication*.
- [147] Flatt, J. R. 2002. *Salt damage in porous materials: how high supersaturations are generated*. Journal of Crystal Growth, Vol. 242: p. 435-454.
- [148] Scherer, W. G. 2002. *Factors affecting crystallization pressure*. International RILEM TC 186-ISA Workshop on Internal Sulfate Attack and Delayed Ettringite Formation. Villars, Switzerland. p. 139-154.
- [149] Scherer, G. W. 2004. *Stress from crystallization of salt*. Cement and Concrete Research, Vol. 34(9): p. 1613-1624.
- [150] Abell, A. B., Willis, K. L., Lange, D. A. 1999. *Mercury Intrusion Porosimetry and Image Analysis of Cement-Based Materials*. Journal of Colloid and Interface Science, Vol. 211(1): p. 39-44.
- [151] Moro, F., Böhni, H. 2002. *Ink-bottle effect in mercury intrusion porosimetry of cement-based materials*. Journal of Colloid and Interface Science, Vol. 246: p. 135-149
- [152] Renault, P. 1988. *Theoretical studies of mercury intrusion in some networks: testing the applicability of mercury intrusion in the size characterisation of the lacunar pore space of soil samples*. Transport in Porous media, Vol. 3: p. 529-547.
- [153] Kaufmann, J., Loser, R., Leemann, A. 2009. *Analysis of cement-bonded materials by multi-cycle mercury intrusion and nitrogen sorption*. Journal of Colloid and Interface Science, Vol. 336: p. 730-737.
- [154] Woodburn, J. A., Holden, J. C., Peter, P. 1993. *The Transistor Psychrometer: A New Instrument for Measuring Soil Suction*. American Society of Civil Engineers: New York. p. 91-102.
- [155] Mitaritonna, G., Pineda, J., Arroyo, M., Romero, E. 2009. *The effect of drying-wetting cycles on the seismic properties of an anisotropic claystone*. Forth Biot Conference on Poromechanics. DEStech Publications, Inc., PA. p. 286-293.
- [156] Mohajerani, M., Delage, P., Monfared, M., Tang, A. M., Sulem, J., Gatmiri, B. 2012. *On the Resaturation of Swelling Claystone*. In Unsaturated Soils: Research and Applications, Springer Berlin Heidelberg: p. 411-417.
- [157] Zhang, F., Xie, S. Y., Hu, D. W., Shao, J. F., Gatmiri, B. 2012. *Effect of water content and structural anisotropy on mechanical property of claystone*. Applied Clay Science, Vol. 69: p. 79-86.
- [158] Correns, C. W., Steinborn, W. 1939. *Experimente zur Messung und Erklärung der sogenannten Kristallisationskraft*. Z Krist (A), Vol. 101: p. 117-133.
- [159] Winkler, E. M., Singer, P. C. 1972. *Crystallization Pressure of Salts in Stone and Concrete*. Geological Society of America Bulletin, Vol. 83: p. 3509-3514.
- [160] Winkler, E. M. 1973. *Stone: Properties, durability in man's environment*. Springer Verlag.
- [161] Flückiger, A. 1994. *Anhydritquellung*. Rencontre Internationale des jeunes chercheurs en geologie appliquees. Lausanne. p. 103-107
- [162] Flückiger, A., Nüesch, R., Madsen, F. T. Year. *Anhydritquellung*. In *Berichte zur Jahrestagung Regensburg der Deutschen Ton und Tonmineralgruppe e.V.* 1994.
- [163] Steiner, W., Kaiser, K. P., Spaun, G. 2010. *Role of brittle fracture on swelling behaviour of weak rock tunnels: hypothesis and qualitative evidence*. Geomechanics and Tunnelling, Vol. 3: p. 583-596.
- [164] Washburn, E. W. 1926-1933. *International critical tables of numerical data, physics, chemistry and technology*. New York, Published for the National Research Council by McGraw-Hill

- [165] Blount, C. W., Dickson, F. W. 1973. *Gypsum-Anhydrite equilibria in systems CaSO₄-H₂O and CaCO₃-NaCl-H₂O*. Am. Mineralogist, Vol. 58: p. 323-331.
- [166] Merino, E., Dewers, T. 1998. *Implications of replacement for reaction-transport modeling*. Journal of Hydrology, Vol. 209: p. 137-146.
- [167] Klepetsanis, G. P., Koutsoukos, G. P. 1991. *Spontaneous precipitation of calcium sulfate at conditions of sustained supersaturation*. Journal of Colloid and Interface Science, Vol. 143(No.2): p. 299-308.
- [168] Fletcher, R. C., Merino, E. 2001. *Mineral growth in rocks: Kinetic-rheological models of replacement, vein formation, and syntectonic crystallization*. Geochimica et Cosmochimica Acta, Vol. 65(No. 21): p. 3733-3748.
- [169] Noher, H. P., Meyer, N. 2002. *Belchentunnel Versuchsdrainagegestollen, Beurteilung der Wasseranalysen*. Report 1510720.003 by Geotechnisches Institut AG.
- [170] Bachema 1995. *Chemische Untersuchung von Wasserproben Adlertunnel Bahn 2000* Several reports by "Institut Bachema AG, Analytische Laboratorien".
- [171] LPM 2000. *Wasseranalysen Chienberg Tunnel* Several reports by "Labor für Prüfung und Materialtechnologie".
- [172] Madsen, F. T., Flückiger, A., Hauber, L., Jordan, P., Voegtli, B. Year. *New investigations on swelling rocks in the Belchen tunnel, Switzerland*. In *Proceedings for the 8th International Congress on Rock Mechanics*. 1995. Tokyo, Japan.
- [173] Nüesch, R., Madsen, F. T., Steiner, W. Year. *Long time swelling of anhydritic rocks: Mineralogical and microstructural evaluation*. In *Proceedings for the 8th International Congress on Rock Mechanics*. 1995. Tokyo, Japan.
- [174] Vöggtli, B., Jordan, P. 1996. *Quelldruckentwicklung in Ton- und Sulfatgesteinen*. Schweizer Ingenieur und Architekt. p. 350-352.
- [175] Beiche, H. 1990. *Bemessung und Bau eines Tunnels in anhydridhaltigem Gebirge (B-14 Tunnel in Stuttgart)*. Geotechnik 27, Vol. Sonderheft, 9. Nationales Felsmechanik Symposium, Aachen: p. 208-215.
- [176] Kirschke, D. Year. *Laboratory and in situ swelling tests for the Freudenstein tunnel*. In *Proc. 6th International Congress Rock Mechanics*. 1987. Montreal, Canada.
- [177] Wahlen, R., Wittke, W. 2009. *Kalibrierung der felsmechanischen Kennwerte für Tunnelbauten in quellfähigem Gebirge*. Geotechnik 27, Vol. 32(Nr. 4): p. 226-233.
- [178] Kovári, K., Amstad, C., Fecker, E. 1986. *Freudensteintunnel, Versuchsstrecke U1, Mess- und Untersuchungsprogramm*. Bericht des IBETH – Fels- und Untertagbau ETH Zürich & der Gesellschaft für Baugeologie und Messtechnik mbH, Rheinstetten.
- [179] Kovári, K., Amstad, C., Anagnostou, G. 1988. *Design/construction methods – Tunnelling in swelling rock*. Proc. 29th U.S. Symposium on Rock Mechanics (USRMS). Minneapolis. p. 17-32.
- [180] Kovári, K. 1996. *NBS Mannheim-Stuttgart. Freudensteintunnel. Zwischenbericht zum Zustand der Tunnel aufgrund der Messungen im Untersuchungsstollen U1*.
- [181] Geotechnisches Ingenieurbüro Prof. Fecker & Partner GmbH. 2007. *Freudensteintunnel. Zusammenfassender Bericht Versuchsstrecke U1*. 64. Bericht zur geotechnischen Beratung.
- [182] Kovári, K. 2010. *Grossprojekt Stuttgart 21 Tunnelbau in quellfähigem Gebirge - Statische Untersuchung bestehender Tunnelbauwerke*. (unpublished report).
- [183] Kovári, K., Vogelhuber, M. Year. *Empirical Basis for the Design of Tunnel Linings in Swelling Rock containing Anhydrite*. In *World Tunnel congress 2014*. 2014. Foz do Iguaçu, Brazil.
- [184] Haines, P. J. 2002. *Principles of thermal analysis and calorimetry*. Royal society of chemistry.
- [185] TA Instruments 2015. *Thermal Analysis*. Available from: www.tainstruments.com.
- [186] Goldstein, J., Newbury, D. E., Joy, D. C., Lyman, C. E., Echlin, P., Lifshin, E., Sawyer, L., Michael, J. R. 2003. *Scanning electron microscopy and X-ray microanalysis*. New York : Kluwer. 689 S.
- [187] Young, R. A. 1995. *The Rietveld Method*. International Union of Crystallography Monographs. Oxford university press.
- [188] HORIBA 2015; Available from: www.horiba.com [cited 13.11.15].

- [189] Eshel, G., Levy, G. J., Mingelgrin, U., Singer, M. J. 2004. *Critical Evaluation of the Use of Laser Diffraction for Particle-Size Distribution Analysis*. Soil Science Society of America Journal, Vol. 68: p. 736-743.
- [190] Bundesverband der Gipsindustrie e.V. 2013. *Gips-Datenbuch*. Available from: <http://www.gips.de/service/download/publikationen/gips-datenbuch/>.
- [191] Richard Baker Harrison LTD 2011. *Polwhite E China Clay Data sheet*.
- [192] Imerys Performance & Filtration Minerals 2008. *Polwhite E. Data sheet*.
- [193] Kalkfabrik Netstal AG 2015. *KFN Technical Data Sheet nekafill 15*.
- [194] S. Benelux 2009. *Sikron M600 Technical Data*.
- [195] Weiss, A. 1958. *Über äquimolaren Kationenaustausch bei niedrig geladenen Inonenaustauschern*. Kolloid-Zeitschrift, Vol. 158(1): p. 22-28.
- [196] Jasmund, K., Lagaly, G. 1993. *Tonminerale und Tone : Struktur, Eigenschaften, Anwendungen, und Einsatz in Industrie und Umwelt*. Darmstadt: Steinkopff.
- [197] Van Olphen, H., Fripiat, J. 1979. *Data handbook for clay materials and other non-metallic minerals*. Oxford, England: Pergamon Press.
- [198] Meunier, A. 2005. *Clays*.
- [199] Thom, R., Sivakumar, R., Sivakumar, V., Murray, E. J., Mackinnon, P. 2007. *Pore size distribution of unsaturated compacted kaolin: the initial states and final states following saturation*. Geotechnique, Vol. 57(5): p. 469-474.
- [200] Amann, F., Ündül, Ö., Löw, S., Kaiser, P. K. 2013. *Fracture Processes and In-situ Fracture Observations in Gipskeuper* Forschungsauftrag ASTRA2011/006. Eidgenössisches Departement für Umwelt, Verkehr, Energie und Kommunikation UVEK, Bundesamt für Strassen.
- [201] AG, G. I., Pfirter, N. P. A. 2010. *Sanierungstunnel Belchen STB Bohrkampagne 2009 Laboruntersuchungen*.
- [202] Wu, R., Boyd, C. E. 1990. *Evaluation of Calcium Sulfate for Use in Aquaculture Ponds*. The Progressive Fish-Culturist, Vol. 52(1): p. 26-31.
- [203] Azimi, G., Papangelakis, V. G. 2011. *Mechanism and kinetics of gypsum-anhydrite transformation in aqueous electrolyte solutions*. Hydrometallurgy, Vol. 108(1-2): p. 122-129.
- [204] Dai, Z., Shi, W., Kan, A. T., Zhang, N., Tomson, M. B. *Improvement of Thermodynamic Modeling of Calcium Carbonate and Calcium Sulfates at High Temperature and High Pressure in Mixed Electrolytes*. Society of Petroleum Engineers.
- [205] Partridge, E. P., White, A. H. 1929. *The solubility of calcium sulfate from 0 to 200°*. Journal of the American Chemical Society, Vol. 51(2): p. 360-370.
- [206] Alimi, F., Gadri, A. 2004. *Kinetics and morphology of formed gypsum*. Desalination, Vol. 166: p. 427-434.
- [207] Mettler Toledo Intl. Inc. 2015. *SevenMulti*. Available from: www.mt.com.
- [208] Brezesinski, G., Mögel, H.-J. 1993. *Grenzflächen und Kolloide*. Heidelberg: Spektrum Akademischer Verlag.
- [209] Nesse, W. D. 1986. *Introduction to optical mineralogy*. New York: Oxford University Press.
- [210] Bontle, M., Nadiye-Tabbiruka, M. S. 2007. *Chemical and Thermal Characterization of a Clayey Material Found Near Gaborone Dam*. Journal of Applied Sciences and Environmental Management, Vol. 11(4): p. 4.

Projektabschluss



Schweizerische Eidgenossenschaft
Confédération suisse
Confederazione Svizzera
Confederaziun svizra

Eidgenössisches Departement für
Umwelt, Verkehr, Energie und Kommunikation UVEK
Bundesamt für Strassen ASTRA

FORSCHUNG IM STRASSENWESEN DES UVEK

Version vom 09.10.2013

Formular Nr. 3: Projektabschluss

erstellt / geändert am: 26.11.2015

Grunddaten

Projekt-Nr.: FGJ 2010/007

Projekttitel: Modellierung von anhydrithaltigen Tonsteinen

Enddatum: November 2015

Texte

Zusammenfassung der Projektergebnisse:

Mit dem vorliegenden Forschungsprojekt sollte der Kenntnisstand bezüglich folgender, dem Quellvorgang zugrunde liegenden Mechanismen verbessert werden: die Lösung des Anhydrits in Porenwasser, die Ausfällung von Gipskristallen aus der Lösung, die chemisch-mechanische Kopplung zwischen den Sulfaten und der Tonmatrix, die Sickerströmung und der diffusive und advective Ionentransport. Zu diesem Zweck wurde eine Serie von theoretischen und experimentellen Untersuchungen zu den Wechselwirkungen zwischen den chemischen Reaktionen, den Transportprozessen und dem mechanischen Verhalten durchgeführt.

Als erstes wurde ein thermodynamisches Modell entwickelt, das die Bedingungen erfasst, unter denen eine Umwandlung von Anhydrit in Gips stattfindet. Anders als bei bestehenden Modellen wurden dabei die einzelnen chemischen Reaktionen explizit berücksichtigt und der Einfluss der Tonphase und der Porengrösse kohärent erfasst. Mit Hilfe dieses thermodynamischen Modells wurden zwei Beobachtungen analysiert: das Vorkommen von Anhydrit (statt Gips) bei kleinen Überlagerungen im Gipskeuper und die im Verhältnis zum Kristallisationsdruck von Gips niedrigen Quelldrücke von anhydritführenden Tonsteinen. Die Analyse dieser Beobachtungen war aufschlussreich bezüglich der Rolle des Tons. Der grosse Unterschied zwischen dem Kristallisationsdruck des Gipses und den makroskopisch beobachteten Quelldrücken kann auf die mechanische Wechselwirkung zwischen den in den Poren wachsenden Kristallen und der umgebenden Tonmatrix, welche einen Puffer darstellt, zurückgeführt werden. Anhydrit ist trotz geringer Tiefenlage stabil, weil die Tonminerale die Aktivität des Porenwassers herabsetzen und somit die Löslichkeit des Gipses über jene des Anhydrits erhöhen. Dieses Ergebnis liefert eine plausible Erklärung für den Ablauf des Quellvorgangs anhydritführender Tonsteine und zeigt, dass der Unterbindung der Quellung des Tones für die Beherrschung der Quellproblematik eine Schlüsselrolle zukommt.

Zur Quantifizierung des Toneinflusses wurden zusätzliche Freiquellversuche mit natürlichen Proben aus dem Belchentunnel durchgeführt. Allerdings erlauben diese Versuche noch keine definitiven Schlussfolgerungen, da sie noch nicht abgeschlossen sind und ihre Ergebnisse, bedingt durch die natürliche Heterogenität des Materials, eine grosse Streuung aufweisen.

Zur Erfassung der Zeitabhängigkeit des Quellvorgangs wurden aus der Literatur bekannte kinetische Gleichungen übernommen und anhand der Modellierung eines geschlossenen Anhydrit-Gips-Wasser-Systems überprüft, für welches experimentelle Ergebnisse vorlagen. Die kinetischen Gleichungen wurden ferner in einem Modell implementiert, welches die Verzögerung der Anhydritlösung durch die im Zuge der Hydratation entstehende Gipschicht erfasst. Damit konnte die allgemeine Beobachtung erklärt werden, dass dickere Anhydritlagen nur sehr langsam quellen und deshalb für den Tunnelbau irrelevant sind. Die Modellprognosen stimmen mit den Ergebnissen von eigenen Versuchen an natürlichem Anhydrit überein, bei welchen die zeitliche Entwicklung der wachsenden Gipschicht gemessen wurde.

Zur Untersuchung des Zusammenspiels der chemischen Reaktion mit dem Ionentransport wurden gekoppelte Advektion-Diffusion-Reaktion-Berechnungen unter Berücksichtigung der oben erwähnten kinetischen Gleichungen durchgeführt. Die Simulationen zeigten, dass der Einfluss der Diffusion vernachlässigbar ist. Dasselbe gilt auch die Advektion betreffend, sofern die Sickergeschwindigkeiten niedrig sind, was in den wenig durchlässigen Tonsteinen des Gipskeupers üblicherweise der Fall ist. Somit kann in den meisten Fällen davon ausgegangen werden, dass die Umwandlung von Anhydrit in Gips einen topochemischen Prozess darstellt. Aufgrund dieser Erkenntnis konnte die Komplexität der mathematischen Erfassung der untersuchten physikalisch-chemischen Prozesse enorm reduziert und auf die sehr aufwändige experimentelle Untersuchung der hydraulisch-chemischen Wechselwirkungen verzichtet werden.

Die experimentellen Untersuchungen konzentrierten sich deshalb auf die chemisch-mechanischen Prozesse und insbesondere auf die Quantifizierung der Spannungen und Dehnungen infolge der Anhydrit-Gips-Umwandlung. Hierfür wurden Ödometerversuche an stark verdichteten Mischungen durchgeführt. Durch mineralogische Untersuchungen konnte eine deutliche Korrelation zwischen Quelldehnung und Fortschritt der Anhydritumwandlung festgestellt werden. Der an diesen Proben experimentell bestimmte Zusammenhang zwischen Quelldehnung und -druck lässt sich – analog zum bekannten Quellgesetz für Tonsteine – sehr gut durch eine Gerade im halblogarithmischen Diagramm approximieren. Dieses Ergebnis ist besonders bemerkenswert, da es sich hierbei um Dehnungen handelt, die nur infolge chemischer Reaktionen (ohne Tonquellung) entstehen.



Schweizerische Eidgenossenschaft
Confédération suisse
Confederazione Svizzera
Confederaziun svizra

Eidgenössisches Departement für
Umwelt, Verkehr, Energie und Kommunikation UVEK
Bundesamt für Strassen ASTRA

Zielerreichung:

Die Ziele des Projektes wurden erreicht indem wertvolle Erkenntnisse zur Rolle des Tons, zum Ablauf des Quellvorgangs in anhydritführenden Tonsteinen und zur Rolle der Transportprozesse gewonnen wurden, welche die Basis für weiterführende Untersuchungen darstellen.
Auch bezüglich des Zusammenhangs zwischen Quelldruck und -dehnung wurden wichtige Ergebnisse erhalten, welche aber noch keine definitive Schlussfolgerung erlauben, da die Versuche noch nicht abgeschlossen sind.

Folgerungen und Empfehlungen:

Die äusserst zeitaufwändigen experimentellen Untersuchungen zur Bestimmung des Zusammenhangs zwischen Quelledehnung und -druck sollen auch nach dem Abschluss dieses Forschungsprojekts fortgesetzt werden. Die im Rahmen des Forschungsprojekts gewonnenen Erkenntnisse werden bei der Formulierung eines kontinuumsmechanischen Modells berücksichtigt.

Publikationen:

Serafeimidis, K., Anagnostou, G. (2013): On the time-development of sulphate hydration in anhydritic swelling rocks. *Rock Mech. Rock Eng.*, 46, 619–634
Anagnostou, G., Serafeimidis, K., Vrakas A. (2014): On the occurrence of anhydrite in sulphatic claystones of the Gypsum Keuper. *Rock Mech. Rock Eng.*, 48, 1-13
Serafeimidis, K., Anagnostou, G. (2014): On the crystallization pressure of gypsum. *Env. Earth Sciences*, 72(12), 4985-4994
Serafeimidis, K., Anagnostou, G., Vrakas, A. (2014): Scale effects in relation to swelling pressure in anhydritic claystones. *Int. Symp. on Geomechanics from micro to macro*. University of Cambridge
Serafeimidis K. (2014): On the dissolution, precipitation and transport processes in sulphatic swelling rocks. *Diss. ETH Zürich Nr. 21707*
Serafeimidis K., Anagnostou G. (2015): The Solubilities and Thermodynamic Equilibrium of Anhydrite and Gypsum. *Rock Mech. Rock Eng.*, 48, 15-31
Huber T., Pimentel E., Anagnostou G. (2015): Experimental investigations for the modelling of chemo-mechanical processes in anhydritic rock. *Energy Procedia*, 76, 87-95

Der Projektleiter/die Projektleiterin:

Name: Anagnostou Vorname: Georgios

Amt, Firma, Institut: Institut für Geotechnik, ETH Zürich

Unterschrift des Projektleiters/der Projektleiterin:

FORSCHUNG IM STRASSENWESEN DES UVEK

Formular Nr. 3: Projektabschluss

Beurteilung der Begleitkommission:

Beurteilung:

Die Problematik des Anhydrit-Gips-Quellens ist für viele unterirdischen Infrastrukturen von grosser Bedeutung und wird trotz intensiver Forschung noch immer nicht ausreichend verstanden. Die vorliegende Forschungsarbeit liefert substantielle neue Erkenntnisse für verschiedene Aspekte des Phänomens. Von besonderer Bedeutung ist dabei die Wechselwirkung von Tonmineralien, Wasser und Anhydrit, da in der Natur Anhydrit-Gips Formationen sehr oft in Wechsellagerung mit Tonlagen vorkommen. Ebenfalls von grosser Wichtigkeit sind die Analysen zum Ionentransport in der Umwandlung von Anhydrit zu Gips, da die gewonnenen vertieften Einblicke die Modellbildung des Prozesses und dessen Bestätigung in Untersuchungen an Proben erlaubten.

Umsetzung:

Die durchgeführten Arbeiten waren ausserordentlich umfangreich und aufgrund der langsam ablaufenden Quellvorgänge zeitlich aufwändig. Die Komplexität der Phänomene und die Variabilität im geologischen Aufbau der quellfähigen Gesteine machten es schwierig, die entscheidenden Faktoren und ihr Einfluss zu identifizieren. Im Rahmen der Forschungsarbeit gelang es aber, die Ergebnisse der theoretischen und praktischen Arbeiten miteinander derart in Bezug zu setzen, dass die massgebenden Parameter erkannt, beschrieben und damit in ihrem Einfluss abgeschätzt werden konnten.

weitergehender Forschungsbedarf:

Die Forschungsarbeit hat grundlegende Erkenntnisse zu den massgebenden Parametern und ihres Einflusses auf den Quellprozesses geliefert. Dies erlaubt die ingenieurmässige Modellierung des Quellvorganges. Sie zeigten auch auf, wo Ansätze zu einer Beeinflussung des Vorganges liegen, die gegebenenfalls von erheblicher Auswirkung auf die bauliche

Einfluss auf Normenwerk:

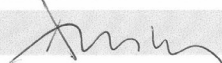
Die Forschungsarbeiten haben keinen unmittelbaren Einfluss auf Normen.

Der Präsident/die Präsidentin der Begleitkommission:

Name: Amberg Vorname: Felix

Amt, Firma, Institut: Amberg Engineering AG

Unterschrift des Präsidenten/der Präsidentin der Begleitkommission:



Verzeichnis der Berichte der Forschung im Strassenwesen

Bericht-Nr.	Projekt Nr.	Titel	Jahr
1507	FGU 2007/004	TBM Tunneling in Faulted and Folded Rocks	2015
1505	VSS 2006/509	Abdichtungssysteme und bitumenhaltige Schichten auf Betonbrücken - Initialprojekt	2014
1503	VSS 2006/515_OBF	Research Package on Bridge Deck Waterproofing Systems: EP5-Mechanisms of Blister Formation	2014
1502	VSS 2010/502	Road – landside interaction : Applications	2014
1501	VSS 2011/705	Grundlagen zur Anwendung von Lebenszykluskosten im Erhaltungsmanagement von Strassenverkehrsanlagen	2014
1500	ASTRA 2010/007	SURPRICE (Sustainable mobility through road user charging) - Swiss contribution: Equity effects of congestion charges and intra-individual variation in preferences	2015
1499	ASTRA 2011/010	Stauprognoseverfahren und -systeme	2014
1498	VSS 2011/914	Coordinated Ramp Metering Control with Variable Speed Limits for Swiss Freeways	2014
1497	VSS 2009/705	Verfahren zur Bildung von homogenen Abschnitten der Strassenverkehrsanlage für das Erhaltungsmanagement Fahrbahnen	2014
1496	VSS 2010/601	Einfluss von Lärmschutzwänden auf das Raumnutzungsverhalten von Reptilien	2014
1495	VSS 2009/703	Zusammenhang Textur und Griffigkeit von Fahrbahnen und Einflüsse auf die Lärmemission	2014
1494	VSS 2010/704	Erhaltungsmanagement der Strassen - Erarbeiten der Grundlagen und Schadenkataloge zur systematischen Zustandserhebung und -bewertung von zusätzlichen Objekten der Strassen	2014
1493	VSS 2006/001	Neue Methoden zur Beurteilung der Tieftemperatureigenschaften von bitumenhaltigen Bindemitteln	2014
1492	SVI 2004/029	Kombiniertes Verkehrsmittel- und Routenwahlmodell	2014
1491	VSS 2007/704	Gesamtbewertung von Kunstbauten	2014
1490	FGU 2004/002	Langzeit-Beständigkeit von Tunnel-Abdichtungssystemen aus Kunststoffen (Best TASK)	2014
1489	VSS 2006/516_OBF	Forschungspaket Brückenabdichtungen: EP6 - Anschlüsse von Brückenabdichtungen	2014
1488	SVI 2007/020	Methodik zur Nutzenermittlung von Verkehrsdosierungen	2014
1487	SVI 2008/001	Erfahrungsbericht Forschungsbündel	2014
1486	SVI 2004/005	Partizipation in Verkehrsprojekten	2014

Bericht-Nr.	Projekt Nr.	Titel	Jahr
1485	VSS 2007/401	Anforderungen an Anschlussfugensysteme in Asphaltdecken - Teil 1: Praxiserfahrung	2014
1484	FGU 2010/003	Misestimating time of collision in the tunnel entrance due to a disturbed adaptation	2014
1483	VSS 2005/452	Forschungspaket Recycling von Ausbauasphalt in Heissmischgut: EP1: Optimaler Anteil an Ausbauasphalt	2014
1482	ASTRA 2010/018	SURPRICE: Sustainable mobility through road user charges Swiss contribution: Comprehensive road user charging (RUC)	2015
1481	VSS 2001/702	Application des méthodes de représentation aux données routières	2014
1480	ASTRA 2008/004	Prozess- und wirkungsorientiertes Management im betrieblichen Strassenunterhalt Modell eines siedlungsübergreifenden Unterhalts	2014
1479	ASTRA 2005/004	Entscheidungsgrundlagen & Empfehlungen für ein nachhaltiges Baustoffmanagement	2014
1478	VSS 2005/455	Research Package on Recycling of Reclaimed Asphalt in Hot Mixes - EP4: Evaluation of Durability	2014
1477	VSS 2008/503	Feldversuch mit verschiedenen Pflästerungen und Plattendecken	2014
1476	VSS 2011/202	Projet initial pour la conception multi-usagers des carrefours	2014
1475	VSS 1999/125	Ringversuch "Eindringtiefe eines ebenen Stempels, statische Prüfung an Gussasphalt"	2014
1474	VSS 2009/704	Wechselwirkung zwischen Aufgrabungen, Zustand und Alterungsverhalten im kommunalen Strassennetz-Entwicklung eines nachhaltigen Aufgrabungsmanagement	2014
1473	VSS 2011/401	Forschungspaket "POLIGRIP - Einfluss der Polierbarkeit von Gesteinskörnungen auf die Griffigkeit von Deckschichten - Initialprojekt"	2014
1472	SVI 2010/003	Einfluss der Verlässlichkeit der Verkehrssysteme auf das Verkehrsverhalten	2014
1471	ASTRA 2008/011	Strategien zum wesensgerechten Einsatz der Verkehrsmittel im Güterverkehr Forschungspaket UVEK/ASTRA - Synthese	2014
1470	VSS 2011/907	Initialprojekt für ein Forschungspaket "Kooperative Systeme für Fahrzeug und Strasse"	2014
1469	VSS 2008/902	Untersuchungen zum Einsatz von Bewegungssensoren für fahrzeitbezogene Verkehrstelematik-Anwendungen	2014
1468	VSS 2010/503	Utilisation des géostructures énergétiques pour la régulation thermique et l'optimisation énergétique des infrastructures routières et ouvrages d'art	2014
1467	ASTRA 2010/021	Sekundärer Feinstaub vom Verkehr	2014
1466	VSS 2010/701	Grundlagen zur Revision der Normen über die visuelle Erhebung des Oberflächenzustands	2014
1465	ASTRA 2000/417	Erfahrungen mit der Sanierung und Erhaltung von Betonoberflächen	2014
1462	ASTRA 2011/004	Ermittlung der Versagensgrenze eines T2 Norm-Belages mit der mobiles	2014

Bericht-Nr.	Projekt Nr.	Titel	Jahr
		Grossversuchsanlage MLS10	
1460	SVI 2007/017	Nutzen der Verkehrsinformation für die Verkehrssicherheit	2014
1459	VSS 2002/501	Leichtes Fallgewichtsgesetz für die Verdichtungskontrolle von Fundationsschichten	2014
1458	VSS 2010/703	Umsetzung Erhaltungsmanagement für Strassen in Gemeinden - Arbeitshilfen als Anhang zur Norm 640 980	2014
1457	SVI 2012/006	Forschungspaket VeSPA Teilprojekt 5: Medizinische Folgen des Strassenunfallgeschehens	2014
1456	SVI 2012/005	Forschungspaket VeSPA Teilprojekt 4: Einflüsse des Wetters auf das Strassenunfallgeschehen	2014
1455	SVI 2012/004	Forschungspaket VeSPA Teilprojekt 3: Einflüsse von Fahrzeugeigenschaften auf das Strassenunfallgeschehen	2014
1454	SVI 2012/003	Forschungspaket VeSPA Teilprojekt 2: Einflüsse von Situation und Infrastruktur auf das Strassenunfallgeschehen: Phase 1	2014
1453	SVI 2012/002	Forschungspaket VeSPA Teilprojekt 1: Einflüsse von Mensch und Gesellschaft auf das Strassenunfallgeschehen: Phase 1	2014
1452	SVI 2012/001	Forschungspaket VeSPA: Synthesebericht Phase 1	2014
1451	FGU 2010/006	Gasanalytik zur frühzeitigen Branddetektion in Tunneln	2013
1450	VSS 2002/401	Kaltrecycling von Ausbauphosphat mit bituminösen Bindemitteln	2014
1449	ASTRA 2010/024	E-Scooter - Sozial- und naturwissenschaftliche Beiträge zur Förderung leichter Elektrofahrzeuge in der Schweiz	2013
1448	SVI 2009/008	Anforderungen der Güterlogistik an die Netzinfrastruktur und die langfristige Netzentwicklung in der Schweiz. Forschungspaket UVEK/ASTRA "Strategien zum wesensgerechten Einsatz der Verkehrsmittel im Güterverkehr der Schweiz", Teilprojekt C	2014
1447	SVI 2009/005	Informationstechnologien in der zukünftigen Gütertransportwirtschaft Forschungspaket UVEK/ASTRA "Strategien zum wesensgerechten Einsatz der Verkehrsmittel im Güterverkehr der Schweiz", Teilprojekt E	2013
1446	VSS 2005/454	Forschungspaket Recycling von Ausbauphosphat in Heissmischgut: EP3: Stofffluss- und Nachhaltigkeitsbeurteilung	2013
1445	VSS 2009/301	Öffnung der Busstreifen für weitere Verkehrsteilnehmende	2013
1444	VSS 2007/306	Verkehrsqualität und Leistungsfähigkeit von Anlagen des leichten Zweirad- und des Fussgängerverkehrs	2013
1443	VSS 2007/305	Verkehrsqualität und Leistungsfähigkeit des strassengebundenen ÖV	2013
1442	SVI 2010/004	Messen des Nutzens von Massnahmen mit Auswirkungen auf den Langsamverkehr -	2013

Bericht-Nr.	Projekt Nr.	Titel	Jahr
		Vorstudie	
1441_2	SVI 2009/010	Zielsystem im Güterverkehr. Forschungspaket UVEK/ASTRA Strategien zum wesensgerechten Einsatz der Verkehrsmittel im Güterverkehr der Schweiz - Teilprojekt G	2013
1441_1	SVI 2009/010	Effizienzsteigerungspotenziale in der Transportwirtschaft durch integrierte Bewirtschaftungsinstrumente aus Sicht der Infrastrukturbetreiber Synthese der Teilprojekte B3, C, D, E und F des Forschungspakets Güterverkehr anhand eines Zielsystems für den Güterverkehr	2013
1440	SVI 2009/006	Benchmarking-Ansätze im Verkehrswesen	2013
1439	SVI 2009/002	Konzept zur effizienten Erfassung und Analyse der Güterverkehrsdaten Forschungspaket UVEK/ASTRA Strategien zum wesensgerechten Einsatz von Verkehrsmitteln im Güterverkehr der Schweiz TP A	2013
1438_2	SVI 2009/011	Ortsbezogene Massnahmen zur Reduktion der Auswirkungen des Güterverkehrs - Teil 2. Forschungspaket UVEK/ASTRA Strategien zum wesensgerechten Einsatz der Verkehrsmittel im Güterverkehr der Schweiz TP H	2013
1438_1	SVI 2009/011	Ortsbezogene Massnahmen zur Reduktion der Auswirkungen des Güterverkehrs - Teil 1. Forschungspaket UVEK/ASTRA Strategien zum wesensgerechten Einsatz der Verkehrsmittel im Güterverkehr der Schweiz TP H	2013
1437	VSS 2008/203	Trottoirüberfahrten und punktuelle Querungen ohne Vortritt für den Langsamverkehr	2013
1436	VSS 2010/401	Auswirkungen verschiedener Recyclinganteile in ungebundenen Gemischen	2013
1435	FGU 2008/007_OBF	Schadstoff- und Rauchkurzschlüsse bei Strassentunneln	2013
1434	VSS 2006/503	Performance Oriented Requirements for Bituminous Mixtures	2013
1433	ASTRA 2010/001	Güterverkehr mit Lieferwagen: Entwicklungen und Massnahmen Forschungspaket UVEK/ASTRA Strategien zum wesensgerechten Einsatz der Verkehrsmittel im Güterverkehr der Schweiz TP B3	2013
1432	ASTRA 2007/011	Praxis-Kalibrierung der neuen mobilen Grossversuchsanlage MLS10 für beschleunigte Verkehrslastsimulation auf Strassenbelägen in der Schweiz	2013
1431	ASTRA 2011/015	TeVeNOx - Testing of SCR-Systems on HD-Vehicles	2013
1430	ASTRA 2009/004	Impact des conditions météorologiques extrêmes sur la chaussée	2013
1429	SVI 2009/009	Einschätzungen der Infrastrukturnutzer zur Weiterentwicklung des Regulativs Forschungspaket UVEK/ASTRA Strategien zum wesensgerechten Einsatz der Verkehrsmittel im Güterverkehr der Schweiz TP F	2013
1428	SVI 2010/005	Branchenspezifische Logistikkonzepte und Güterverkehrsaufkommen sowie deren Trends Forschungspaket UVEK/ASTRA Strategien zum wesensgerechten Einsatz der Verkehrsmittel im Güterverkehr der Schweiz TP B2	2013

Bericht-Nr.	Projekt Nr.	Titel	Jahr
1427	SVI 2006/002	Begegnungszonen - eine Werkschau mit Empfehlungen für die Realisierung	2013
1426	ASTRA 2010/025_OBF	Luftströmungsmessung in Strassentunneln	2013
1425	VSS 2005/401	Résistance à l'altération des granulats et des roches	2013
1424	ASTRA 2006/007	Optimierung der Baustellenplanung an Autobahnen	2013
1423	ASTRA 2010/012	Forschungspaket: Lärmarme Beläge innerorts EP3: Betrieb und Unterhalt lärmarmen Beläge	2013
1422	ASTRA 2011/006_OBF	Fracture processes and in-situ fracture observations in Gipskeuper	2013
1421	VSS 2009/901	Experimenteller Nachweis des vorgeschlagenen Raum- und Topologiemodells für die VM-Anwendungen in der Schweiz (MDATrafo)	2013
1420	SVI 2008/003	Projektierungsfreiräume bei Strassen und Plätzen	2013
1419	VSS 2001/452	Stabilität der Polymere beim Heisseinbau von PmB-haltigen Strassenbelägen	2013
1418	VSS 2008/402	Anforderungen an hydraulische Eigenschaften von Geokunststoffen	2012
1417	FGU 2009/002	Heat Exchanger Anchors for Thermo-active Tunnels	2013
1416	FGU 2010/001	Sulfatwiderstand von Beton: verbessertes Verfahren basierend auf der Prüfung nach SIA 262/1, Anhang D	2013
1415	VSS 2010/A01	Wissenslücken im Infrastrukturmanagementprozess "Strasse" im Siedlungsgebiet	2013
1414	VSS 2010/201	Passive Sicherheit von Tragkonstruktionen der Strassenausstattung	2013
1413	SVI 2009/003	Güterverkehrsintensive Branchen und Güterverkehrsströme in der Schweiz Forschungspaket UVEK/ASTRA Strategien zum wesensgerechten Einsatz der Verkehrsmittel im Güterverkehr der Schweiz Teilprojekt B1	2013
1412	ASTRA 2010/020	Werkzeug zur aktuellen Gangliniennorm	2013
1411	VSS 2009/902	Verkehrstelematik für die Unterstützung des Verkehrsmanagements in ausserordentlichen Lagen	2013
1410	VSS 2010/202_OBF	Reduktion von Unfallfolgen bei Bränden in Strassentunneln durch Abschnittsbildung	2013
1409	ASTRA 2010/017_OBF	Regelung der Luftströmung in Strassentunneln im Brandfall	2013
1408	VSS 2000/434	Viellissement thermique des enrobés bitumineux en laboratoire	2012
1407	ASTRA 2006/014	Fusion des indicateurs de sécurité routière : FUSAIN	2012
1406	ASTRA 2004/015	Amélioration du modèle de comportement individuel du Conducteur pour évaluer la sécurité d'un flux de trafic par simulation	2012
1405	ASTRA 2010/009	Potential von Photovoltaik an Schallschutzmassnahmen entlang der Nationalstrassen	2012

Bericht-Nr.	Projekt Nr.	Titel	Jahr
1404	VSS 2009/707	Validierung der Kosten-Nutzen-Bewertung von Fahrbahn-Erhaltungsmassnahmen	2012
1403	SVI 2007/018	Vernetzung von HLS- und HVS-Steuerungen	2012
1402	VSS 2008/403	Witterungsbeständigkeit und Durchdrückverhalten von Geokunststoffen	2012
1401	SVI 2006/003	Akzeptanz von Verkehrsmanagementmassnahmen-Vorstudie	2012
1400	VSS 2009/601	Begrünte Stützgitterböschungssysteme	2012
1399	VSS 2011/901	Erhöhung der Verkehrssicherheit durch Incentivierung	2012
1398	ASTRA 2010/019	Environmental Footprint of Heavy Vehicles Phase III: Comparison of Footprint and Heavy Vehicle Fee (LSVA) Criteria	2012
1397	FGU 2008/003_OBF	Brandschutz im Tunnel: Schutzziele und Brandbemessung Phase 1: Stand der Technik	2012
1396	VSS 1999/128	Einfluss des Umhüllungsgrades der Mineralstoffe auf die mechanischen Eigenschaften von Mischgut	2012
1395	FGU 2009/003	KarstALEA: Wegleitung zur Prognose von karstspezifischen Gefahren im Untertagbau	2012
1394	VSS 2010/102	Grundlagen Betriebskonzepte	2012
1393	VSS 2010/702	Aktualisierung SN 640 907, Kostengrundlage im Erhaltungsmanagement	2012
1392	ASTRA 2008/008_009	FEHRL Institutes WIM Initiative (Fiwi)	2012
1391	ASTRA 2011/003	Leitbild ITS-CH Landverkehr 2025/30	2012
1390	FGU 2008/004_OBF	Einfluss der Grundwasserströmung auf das Quellverhalten des Gipskeupers im Belchentunnel	2012
1389	FGU 2003/002	Long Term Behaviour of the Swiss National Road Tunnels	2012
1388	SVI 2007/022	Möglichkeiten und Grenzen von elektronischen Busspuren	2012
1387	VSS 2010/205_OBF	Ablage der Prozessdaten bei Tunnel-Prozessleitsystemen	2012
1386	VSS 2006/204	Schallreflexionen an Kunstbauten im Strassenbereich	2012
1385	VSS 2004/703	Bases pour la révision des normes sur la mesure et l'évaluation de la planéité des chaussées	2012
1384	VSS 1999/249	Konzeptuelle Schnittstellen zwischen der Basisdatenbank und EMF-, EMK- und EMT-DB	2012
1383	FGU 2008/005	Einfluss der Grundwasserströmung auf das Quellverhalten des Gipskeupers im Chienbergtunnel	2012
1382	VSS 2001/504	Optimierung der statischen Eindringtiefe zur Beurteilung von harten Gussasphaltsorten	2012
1381	SVI 2004/055	Nutzen von Reisezeiteinsparungen im Personenverkehr	2012

Bericht-Nr.	Projekt Nr.	Titel	Jahr
1380	ASTRA 2007/009	Wirkungsweise und Potential von kombinierter Mobilität	2012
1379	VSS 2010/206_OBF	Harmonisierung der Abläufe und Benutzeroberflächen bei Tunnel-Prozessleitsystemen	2012
1378	SVI 2004/053	Mehr Sicherheit dank Kernfahrbahnen?	2012
1377	VSS 2009/302	Verkehrssicherheitsbeurteilung bestehender Verkehrsanlagen (Road Safety Inspection)	2012
1376	ASTRA 2011/008_004	Erfahrungen im Schweizer Betonbrückenbau	2012
1375	VSS 2008/304	Dynamische Signalisierungen auf Hauptverkehrsstrassen	2012
1374	FGU 2004/003	Entwicklung eines zerstörungsfreien Prüfverfahrens für Schweissnähte von KDB	2012
1373	VSS 2008/204	Vereinheitlichung der Tunnelbeleuchtung	2012
1372	SVI 2011/001	Verkehrssicherheitsgewinne aus Erkenntnissen aus Datapooling und strukturierten Datenanalysen	2012
1371	ASTRA 2008/017	Potenzial von Fahrgemeinschaften	2011
1370	VSS 2008/404	Dauerhaftigkeit von Betonfahrbahnen aus Betongranulat	2011
1369	VSS 2003/204	Rétention et traitement des eaux de chaussée	2012
1368	FGU 2008/002	Soll sich der Mensch dem Tunnel anpassen oder der Tunnel dem Menschen?	2011
1367	VSS 2005/801	Grundlagen betreffend Projektierung, Bau und Nachhaltigkeit von Anschlussgleisen	2011
1366	VSS 2005/702	Überprüfung des Bewertungshintergrundes zur Beurteilung der Strassengriffigkeit	2010
1365	SVI 2004/014	Neue Erkenntnisse zum Mobilitätsverhalten dank Data Mining?	2011
1364	SVI 2009/004	Regulierung des Güterverkehrs Auswirkungen auf die Transportwirtschaft Forschungspaket UVEK/ASTRA Strategien zum wesensgerechten Einsatz der Verkehrsmittel im Güterverkehr der Schweiz TP D	2012
1363	VSS 2007/905	Verkehrsprognosen mit Online -Daten	2011
1362	SVI 2004/012	Aktivitätenorientierte Analyse des Neuverkehrs	2012
1361	SVI 2004/043	Innovative Ansätze der Parkraumbewirtschaftung	2012
1360	VSS 2010/203	Akustische Führung im Strassentunnel	2012
1359	SVI 2004/003	Wissens- und Technologietransfer im Verkehrsbereich	2012
1358	SVI 2004/079	Verkehrsanbindung von Freizeitanlagen	2012
1357	SVI 2007/007	Unaufmerksamkeit und Ablenkung: Was macht der Mensch am Steuer?	2012
1356	SVI 2007/014	Kooperation an Bahnhöfen und Haltestellen	2011

Bericht-Nr.	Projekt Nr.	Titel	Jahr
1355	FGU 2007/002	Prüfung des Sulfatwiderstandes von Beton nach SIA 262/1, Anhang D: Anwendbarkeit und Relevanz für die Praxis	2011
1354	VSS 2003/203	Anordnung, Gestaltung und Ausführung von Treppen, Rampen und Treppenwegen	2011
1353	VSS 2000/368	Grundlagen für den Fussverkehr	2011
1352	VSS 2008/302	Fussgängerstreifen (Grundlagen)	2011
1351	ASTRA 2009/001	Development of a best practice methodology for risk assessment in road tunnels	2011
1350	VSS 2007/904	IT-Security im Bereich Verkehrstelematik	2011
1349	VSS 2003/205	In-Situ-Abflussversuche zur Untersuchung der Entwässerung von Autobahnen	2011
1348	VSS 2008/801	Sicherheit bei Parallelführung und Zusammentreffen von Strassen mit der Schiene	2011
1347	VSS 2000/455	Leistungsfähigkeit von Parkieranlagen	2010
1346	ASTRA 2007/004	Quantifizierung von Leckagen in Abluftkanälen bei Strassentunneln mit konzentrierter Rauchabsaugung	2010
1345	SVI 2004/039	Einsatzbereiche verschiedener Verkehrsmittel in Agglomerationen	2011
1344	VSS 2009/709	Initialprojekt für das Forschungspaket "Nutzensteigerung für die Anwender des SIS"	2011
1343	VSS 2009/903	Basistechnologien für die intermodale Nutzungserfassung im Personenverkehr	2011
1342	FGU 2005/003	Untersuchungen zur Frostkörperbildung und Frosthebung beim Gefrierverfahren	2010
1341	FGU 2007/005	Design aids for the planning of TBM drives in squeezing ground	2011
1340	SVI 2004/051	Aggressionen im Verkehr	2011
1339	SVI 2005/001	Widerstandsfunktionen für Innerorts-Strassenabschnitte ausserhalb des Einflussbereiches von Knoten	2010
1338	VSS 2006/902	Wirkungsmodelle für fahrzeugseitige Einrichtungen zur Steigerung der Verkehrssicherheit	2009
1337	ASTRA 2006/015	Development of urban network travel time estimation methodology	2011
1336	ASTRA 2007/006	SPIN-ALP: Scanning the Potential of Intermodal Transport on Alpine Corridors	2010
1335	VSS 2007/502	Stripping bei lärmindernden Deckschichten unter Überrollbeanspruchung im Labormassstab	2011
1334	ASTRA 2009/009	Was treibt uns an? Antriebe und Treibstoffe für die Mobilität von Morgen	2011
1333	SVI 2007/001	Standards für die Mobilitätsversorgung im peripheren Raum	2011
1332	VSS 2006/905	Standardisierte Verkehrsdaten für das verkehrsträgerübergreifende Verkehrsmanagement	2011

Bericht-Nr.	Projekt Nr.	Titel	Jahr
1331	VSS 2005/501	Rückrechnung im Strassenbau	2011
1330	FGU 2008/006	Energiegewinnung aus städtischen Tunneln: Systemevaluation	2010
1329	SVI 2004/073	Alternativen zu Fussgängerstreifen in Tempo-30-Zonen	2010
1328	VSS 2005/302	Grundlagen zur Quantifizierung der Auswirkungen von Sicherheitsdefiziten	2011
1327	VSS 2006/601	Vorhersage von Frost und Nebel für Strassen	2010
1326	VSS 2006/207	Erfolgskontrolle Fahrzeugrückhaltesysteme	2011
1325	SVI 2000/557	Indices caractéristiques d'une cité-vélo. Méthode d'évaluation des politiques cyclables en 8 indices pour les petites et moyennes communes.	2010
1324	VSS 2004/702	Eigenheiten und Konsequenzen für die Erhaltung der Strassenverkehrsanlagen im überbauten Gebiet	2009
1323	VSS 2008/205	Ereignisdetektion im Strassentunnel	2011
1322	SVI 2005/007	Zeitwerte im Personenverkehr: Wahrnehmungs- und Distanzabhängigkeit	2008
1321	VSS 2008/501	Validation de l'oedomètre CRS sur des échantillons intacts	2010
1320	VSS 2007/303	Funktionale Anforderungen an Verkehrserfassungssysteme im Zusammenhang mit Lichtsignalanlagen	2010
1319	VSS 2000/467	Auswirkungen von Verkehrsberuhigungsmassnahmen auf die Lärmimmissionen	2010
1318	FGU 2006/001	Langzeitquellversuche an anhydritführenden Gesteinen	2010
1317	VSS 2000/469	Geometrisches Normalprofil für alle Fahrzeugtypen	2010
1316	VSS 2001/701	Objektorientierte Modellierung von Strasseninformationen	2010
1315	VSS 2006/904	Abstimmung zwischen individueller Verkehrsinformation und Verkehrsmanagement	2010
1314	VSS 2005/203	Datenbank für Verkehrsaufkommensraten	2008
1313	VSS 2001/201	Kosten-/Nutzenbetrachtung von Strassenentwässerungssystemen, Ökobilanzierung	2010
1312	SVI 2004/006	Der Verkehr aus Sicht der Kinder: Schulwege von Primarschulkindern in der Schweiz	2010
1311	VSS 2000/543	VIABILITE DES PROJETS ET DES INSTALLATIONS ANNEXES	2010
1310	ASTRA 2007/002	Beeinflussung der Luftströmung in Strassentunneln im Brandfall	2010
1309	VSS 2008/303	Verkehrsregelungssysteme - Modernisierung von Lichtsignalanlagen	2010
1308	VSS 2008/201	Hindernisfreier Verkehrsraum - Anforderungen aus Sicht von Menschen mit Behinderung	2010

Bericht-Nr.	Projekt Nr.	Titel	Jahr
1307	ASTRA 2006/002	Entwicklung optimaler Mischgüter und Auswahl geeigneter Bindemittel; D-A-CH - Initialprojekt	2008
1306	ASTRA 2008/002	Strassenglätte-Prognosesystem (SGPS)	2010
1305	VSS 2000/457	Verkehrserzeugung durch Parkieranlagen	2009
1304	VSS 2004/716	Massnahmenplanung im Erhaltungsmanagement von Fahrbahnen	2008
1303	ASTRA 2009/010	Geschwindigkeiten in Steigungen und Gefällen; Überprüfung	2010
1302	VSS 1999/131	Zusammenhang zwischen Bindemittleigenschaften und Schadensbildern des Belages?	2010
1301	SVI 2007/006	Optimierung der Strassenverkehrsunfallstatistik durch Berücksichtigung von Daten aus dem Gesundheitswesen	2009
1300	VSS 2003/903	SATELROU Perspectives et applications des méthodes de navigation pour la télématique des transports routiers et pour le système d'information de la route	2010
1299	VSS 2008/502	Projet initial - Enrobés bitumineux à faibles impacts énergétiques et écologiques	2009
1298	ASTRA 2007/012	Griffigkeit auf winterlichen Fahrbahnen	2010
1297	VSS 2007/702	Einsatz von Asphaltbewehrungen (Asphalteinlagen) im Erhaltungsmanagement	2009
1296	ASTRA 2007/008	Swiss contribution to the Heavy-Duty Particle Measurement Programme (HD-PMP)	2010
1295	VSS 2005/305	Entwurfsgrundlagen für Lichtsignalanlagen und Leitfaden	2010
1294	VSS 2007/405	Wiederhol- und Vergleichspräzision der Druckfestigkeit von Gesteinskörnungen am Haufwerk	2010
1293	VSS 2005/402	Détermination de la présence et de l'efficacité de dope dans les bétons bitumineux	2010
1292	ASTRA 2006/004	Entwicklung eines Pflanzenöl-Blockheizkraftwerkes mit eigener Ölmühle	2010
1291	ASTRA 2009/005	Fahrmuster auf überlasteten Autobahnen Simultanes Berechnungsmodell für das Fahrverhalten auf Autobahnen als Grundlage für die Berechnung von Schadstoffemissionen und Fahrzeitgewinnen	2010
1290	VSS 1999/209	Conception et aménagement de passages inférieurs et supérieurs pour piétons et deux-roues légers	2008
1289	VSS 2005/505	Affinität von Gesteinskörnungen und Bitumen, nationale Umsetzung der EN	2010
1288	ASTRA 2006/020	Footprint II - Long Term Pavement Performance and Environmental Monitoring on A1	2010
1287	VSS 2008/301	Verkehrsqualität und Leistungsfähigkeit von komplexen ungesteuerten Knoten: Analytisches Schätzverfahren	2009

Bericht-Nr.	Projekt Nr.	Titel	Jahr
1286	VSS 2000/338	Verkehrsqualität und Leistungsfähigkeit auf Strassen ohne Richtungstrennung	2010
1285	VSS 2002/202	In-situ Messung der akustischen Leistungsfähigkeit von Schallschirmen	2009
1284	VSS 2004/203	Evacuation des eaux de chaussée par les bas-cotés	2010
1283	VSS 2000/339	Grundlagen für eine differenzierte Bemessung von Verkehrsanlagen	2008
1282	VSS 2004/715	Massnahmenplanung im Erhaltungsmanagement von Fahrbahnen: Zusatzkosten infolge Vor- und Aufschub von Erhaltungsmaßnahmen	2010
1281	SVI 2004/002	Systematische Wirkungsanalysen von kleinen und mittleren Verkehrsvorhaben	2009
1280	ASTRA 2004/016	Auswirkungen von fahrzeuginternen Informationssystemen auf das Fahrverhalten und die Verkehrssicherheit Verkehrspsychologischer Teilbericht	2010
1279	VSS 2005/301	Leistungsfähigkeit zweistreifiger Kreisel	2009
1278	ASTRA 2004/016	Auswirkungen von fahrzeuginternen Informationssystemen auf das Fahrverhalten und die Verkehrssicherheit - Verkehrstechnischer Teilbericht	2009
1277	SVI 2007/005	Multimodale Verkehrsqualitätsstufen für den Strassenverkehr - Vorstudie	2010
1276	VSS 2006/201	Überprüfung der schweizerischen Ganglinien	2008
1275	ASTRA 2006/016	Dynamic Urban Origin - Destination Matrix - Estimation Methodology	2009
1274	SVI 2004/088	Einsatz von Simulationswerkzeugen in der Güterverkehrs- und Transportplanung	2009
1273	ASTRA 2008/006	UNTERHALT 2000 - Massnahme M17, FORSCHUNG: Dauerhafte Materialien und Verfahren SYNTHESE - BERICHT zum Gesamtprojekt "Dauerhafte Beläge" mit den Einzelnen Forschungsprojekten: - ASTRA 200/419: Verhaltensbilanz der Beläge auf Nationalstrassen - ASTRA 2000/420: Dauerhafte Komponenten auf der Basis erfolgreicher Strecken - ASTRA 2000/421: Durabilité des enrobés - ASTRA 2000/422: Dauerhafte Beläge, Rundlaufversuch - ASTRA 2000/423: Griffigkeit der Beläge auf Autobahnen, Vergleich zwischen den Messergebnissen von SRM und SCRIM - ASTRA 2008/005: Vergleichsstrecken mit unterschiedlichen oberen Tragschichten auf einer Nationalstrasse	2008
1272	VSS 2007/304	Verkehrsregelungssysteme - behinderte und ältere Menschen an Lichtsignalanlagen	2010
1271	VSS 2004/201	Unterhalt von Lärmschirmen	2009
1270	VSS 2005/502	Interaktion Strasse Hangstabilität: Monitoring und Rückwärtsrechnung	2009
1269	VSS 2005/201	Evaluation von Fahrzeugrückhaltesystemen im Mittelstreifen von Autobahnen	2009
1268	ASTRA 2005/007	PM10-Emissionsfaktoren von Abriebspartikeln des Strassenverkehrs (APART)	2009

Bericht-Nr.	Projekt Nr.	Titel	Jahr
1267	VSS 2007/902	MDAinSVT Einsatz modellbasierter Datentransfernormen (INTERLIS) in der Strassenverkehrstelematik	2009
1266	VSS 2000/343	Unfall- und Unfallkostenraten im Strassenverkehr	2009
1265	VSS 2005/701	Zusammenhang zwischen dielektrischen Eigenschaften und Zustandsmerkmalen von bitumenhaltigen Fahrbahnbelägen (Pilotuntersuchung)	2009
1264	SVI 2004/004	Verkehrspolitische Entscheidungsfindung in der Verkehrsplanung	2009
1263	VSS 2001/503	Phénomène du dégel des sols gélifs dans les infrastructures des voies de communication et les pergélisols alpins	2006
1262	VSS 2003/503	Lärmverhalten von Deckschichten im Vergleich zu Gussasphalt mit strukturierter Oberfläche	2009
1261	ASTRA 2004/018	Pilotstudie zur Evaluation einer mobilen Grossversuchsanlage für beschleunigte Verkehrslastsimulation auf Strassenbelägen	2009
1260	FGU 2005/001	Testeinsatz der Methodik "Indirekte Vorauserkundung von wasserführenden Zonen mittels Temperaturdaten anhand der Messdaten des Lötschberg-Basistunnels	2009
1259	VSS 2004/710	Massnahmenplanung im Erhaltungsmanagement von Fahrbahnen - Synthesebericht	2008
1258	VSS 2005/802	Kaphaltestellen Anforderungen und Auswirkungen	2009
1257	SVI 2004/057	Wie Strassenraumbilder den Verkehr beeinflussen Der Durchfahrtswiderstand als Arbeitsinstrument bei der städtebaulichen Gestaltung von Strassenräumen	2009
1256	VSS 2006/903	Qualitätsanforderungen an die digitale Videobild-Bearbeitung zur Verkehrsüberwachung	2009
1255	VSS 2006/901	Neue Methoden zur Erkennung und Durchsetzung der zulässigen Höchstgeschwindigkeit	2009
1254	VSS 2006/502	Drains verticaux préfabriqués thermiques pour la consolidation in-situ des sols	2009
1253	VSS 2001/203	Rétention des polluants des eaux de chaussées selon le système "infiltrations sur les talus". Vérification in situ et optimisation	2009
1252	SVI 2003/001	Nettoverkehr von verkehrintensiven Einrichtungen (VE)	2009
1251	ASTRA 2002/405	Incidence des granulats arrondis ou partiellement arrondis sur les propriétés d'adhérence des bétons bitumineux	2008
1250	VSS 2005/202	Strassenabwasser Filterschacht	2007
1249	FGU 2003/004	Einflussfaktoren auf den Brandwiderstand von Betonkonstruktionen	2009
1248	VSS 2000/433	Dynamische Eindringtiefe zur Beurteilung von Gussasphalt	2008
1247	VSS 2000/348	Anforderungen an die strassenseitige Ausrüstung bei der Umwidmung von Standstreifen	2009

Bericht-Nr.	Projekt Nr.	Titel	Jahr
1246	VSS 2004/713	Massnahmenplanung im Erhaltungsmanagement von Fahrbahnen: Bedeutung Oberflächenzustand und Tragfähigkeit sowie gegenseitige Beziehung für Gebrauchs- und Substanzwert	2009
1245	VSS 2004/701	Verfahren zur Bestimmung des Erhaltungsbedarfs in kommunalen Strassennetzen	2009
1244	VSS 2004/714	Massnahmenplanung im Erhaltungsmanagement von Fahrbahnen - Gesamtnutzen und Nutzen-Kosten-Verhältnis von standardisierten Erhaltungsmassnahmen	2008
1243	VSS 2000/463	Kosten des betrieblichen Unterhalts von Strassenanlagen	2008
1242	VSS 2005/451	Recycling von Ausbauasphalt in Heissmischgut	2007
1241	ASTRA 2001/052	Erhöhung der Aussagekraft des LCPC Spurbildungstests	2009
1240	ASTRA 2002/010	L'acceptabilité du péage de congestion : Résultats et analyse de l'enquête en Suisse	2009
1239	VSS 2000/450	Bemessungsgrundlagen für das Bewehren mit Geokunststoffen	2009
1238	VSS 2005/303	Verkehrssicherheit an Tagesbaustellen und bei Anschlüssen im Baustellenbereich von Hochleistungsstrassen	2008
1237	VSS 2007/903	Grundlagen für eCall in der Schweiz	2009
1236	ASTRA 2008/008_07	Analytische Gegenüberstellung der Strategie- und Tätigkeitsschwerpunkte ASTRA-AIPCR	2008
1235	VSS 2004/711	Forschungspaket Massnahmenplanung im EM von Fahrbahnen - Standardisierte Erhaltungsmassnahmen	2008
1234	VSS 2006/504	Expérimentation in situ du nouveau drainomètre européen	2008
1233	ASTRA 2000/420	Unterhalt 2000 Forschungsprojekt FP2 Dauerhafte Komponenten bitumenhaltiger Belagsschichten	2009
665	AGB 2011/001	Wirksamkeit und Prüfung der Nachbehandlungsmethoden von Beton	2014
664	AGB 2009/005	Charges de trafic actualisées pour les dalles de roulement en béton des ponts existants	2014
663	AGB 2003/014	Seismic Safety of Existing Bridges	2014
662	AGB 2008/001	Seismic Safety of Existing Bridges - Cyclic Inelastic Behaviour of Bridge Piers	2014
661	AGB 2010/002	Fatigue limit state of shear studs in steel-concrete composite road bridges	2014
660	AGB 2008/002	Indirekt gelagerte Betonbrücken - Sachstandsbericht	2014
659	AGB 2009/014	Suizidprävention bei Brücken: Follow-Up	2014
658	AGB 2006/015_OBF	Querkraftwiderstand vorgespannter Brücken mit ungenügender Querkraftbewehrung	2014
657	AGB 2003/012	Brücken in Holz: Möglichkeiten und Grenzen	2013

Bericht-Nr.	Projekt Nr.	Titel	Jahr
656	AGB 2009/015	Experimental verification of integral bridge abutments	2013
655	AGB 2007/004	Fatigue Life Assessment of Roadway Bridges Based on Actual Traffic Loads	2013
654	AGB 2005-008	Thermophysical and Thermomechanical Behavior of Cold-Curing Structural Adhesives in Bridge Construction	2013
653	AGB 2007/002	Poinçonnement des pontsdalles précontraints	2013
652	AGB 2009/006	Detektion von Betonstahlbrüchen mit der magnetischen Streufeldmethode	2013
651	AGB 2006/006_OBF	Instandsetzung und Monitoring von AAR-geschädigten Stützmauern und Brücken	2013
650	AGB 2005/010	Korrosionsbeständigkeit von nichtrostenden Betonstählen	2012
649	AGB 2008/012	Anforderungen an den Karbonatisierungswiderstand von Betonen	2012
648	AGB 2005/023 + AGB 2006/003	Validierung der AAR-Prüfungen für Neubau und Instandsetzung	2011
647	AGB 2004/010	Quality Control and Monitoring of electrically isolated post-tensioning tendons in bridges	2011
646	AGB 2005/018	Interactin sol-structure : ponts à culées intégrales	2010
645	AGB 2005/021	Grundlagen für die Verwendung von Recyclingbeton aus Betongranulat	2010
644	AGB 2005/004	Hochleistungsfähiger Faserfeinkornbeton zur Effizienzsteigerung bei der Erhaltung von Kunstbauten aus Stahlbeton	2010
643	AGB 2005/014	Akustische Überwachung einer stark geschädigten Spannbetonbrücke und Zustandserfassung beim Abbruch	2010
642	AGB 2002/006	Verbund von Spanngliedern	2009
641	AGB 2007/007	Empfehlungen zur Qualitätskontrolle von Beton mit Luftpermeabilitätsmessungen	2009
640	AGB 2003/011	Nouvelle méthode de vérification des ponts mixtes à âme pleine	2010
639	AGB 2008/003	RiskNow-Falling Rocks Excel-basiertes Werkzeug zur Risikoermittlung bei Steinschlagschutzgalerien	2010
638	AGB2003/003	Ursachen der Rissbildung in Stahlbetonbauwerken aus Hochleistungsbeton und neue Wege zu deren Vermeidung	2008
637	AGB 2005/009	Détermination de la présence de chlorures à l'aide du Géoradar	2009
636	AGB 2002/028	Dimensionnement et vérification des dalles de roulement de ponts routiers	2009
635	AGB 2004/002	Applicabilité de l'enrobé drainant sur les ouvrages d'art du réseau des routes nationales	2008
634	AGB 2002/007	Untersuchungen zur Potenzialfeldmessung an Stahlbetonbauten	2008

Bericht-Nr.	Projekt Nr.	Titel	Jahr
633	AGB 2002/014	Oberflächenschutzsysteme für Betontragwerke	2008
632	AGB 2008/201	Sicherheit des Verkehrssystem Strasse und dessen Kunstbauten Testregion - Methoden zur Risikobeurteilung Schlussbericht	2010
631	AGB 2000/555	Applications structurales du Béton Fibré à Ultra-hautes Performances aux ponts	2008
630	AGB 2002/016	Korrosionsinhibitoren für die Instandsetzung chloridverseuchter Stahlbetonbauten	2010
629	AGB 2003/001 + AGB 2005/019	Integrale Brücken - Sachstandsbericht	2008
628	AGB 2005/026	Massnahmen gegen chlorid-induzierte Korrosion und zur Erhöhung der Dauerhaftigkeit	2008
627	AGB 2002/002	Eigenschaften von normalbreiten und überbreiten Fahrbahnübergängen aus Polymerbitumen nach starker Verkehrsbelastung	2008
626	AGB 2005/110	Sicherheit des Verkehrssystems Strasse und dessen Kunstbauten: Baustellensicherheit bei Kunstbauten	2009
625	AGB 2005/109	Sicherheit des Verkehrssystems Strasse und dessen Kunstbauten: Effektivität und Effizienz von Massnahmen bei Kunstbauten	2009
624	AGB 2005/108	Sicherheit des Verkehrssystems / Strasse und dessen Kunstbauten / Risikobeurteilung für Kunstbauten	2010
623	AGB 2005/107	Sicherheit des Verkehrssystems Strasse und dessen Kunstbauten: Tragsicherheit der bestehenden Kunstbauten	2009
622	AGB 2005/106	Rechtliche Aspekte eines risiko- und effizienzbasierten Sicherheitskonzepts	2009
621	AGB 2005/105	Sicherheit des Verkehrssystems Strasse und dessen Kunstbauten Szenarien der Gefahrenentwicklung	2009
620	AGB 2005/104	Sicherheit des Verkehrssystems Strasse und dessen Kunstbauten: Effektivität und Effizienz von Massnahmen	2009
619	AGB 2005/103	Sicherheit des Verkehrssystems / Strasse und dessen Kunstbauten / Ermittlung des Netzrisikos	2010
618	AGB 2005/102	Sicherheit des Verkehrssystems Strasse und dessen Kunstbauten: Methodik zur vergleichenden Risikobeurteilung	2009
617	AGB 2005/100	Sicherheit des Verkehrssystems Strasse und dessen Kunstbauten Synthesebericht	2010
616	AGB 2002/020	Beurteilung von Risiken und Kriterien zur Festlegung akzeptierter Risiken in Folge aussergewöhnlicher Einwirkungen bei Kunstbauten	2009